**AFRL-RB-WP-TR-2009-3112**

# AERONAUTICAL SCIENCES ADVANCED STUDIES PROGRAM
## Delivery Order 0002: Plasma Modeling Program

**Thomas M. Weeks, James Menart, Joseph Shang, Hong Yan, Sergey Surzhikov, and Domenic D'Ambrosio**

**Universal Technology Corporation**

**APRIL 2009**
**Interim Report**

**STINFO COPY**

**AIR FORCE RESEARCH LABORATORY**
**AIR VEHICLES DIRECTORATE**
**WRIGHT-PATTERSON AIR FORCE BASE, OH 45433-7542**
**AIR FORCE MATERIEL COMMAND**
**UNITED STATES AIR FORCE**

# NOTICE AND SIGNATURE PAGE

This report was cleared for public release by the USAF 88th Air Base Wing (88 ABW) Public Affairs Office (PAO) and is available to the general public, including foreign nationals. Copies may be obtained from the Defense Technical Information Center (DTIC) (http://www.dtic.mil).

AFRL-RB-WP-TR-2009-3112 HAS BEEN REVIEWED AND IS APPROVED FOR PUBLICATION IN ACCORDANCE WITH ASSIGNED DISTRIBUTION STATEMENT.

\*//Signature//                                            //Signature//

ROGER KIMMEL                                    CHRISTOPHER P. GREEK
Project Engineer                                     Chief
Aerodynamic Configuration Branch        Aerodynamic Configuration Branch
Aeronautical Sciences Division               Aeronautical Sciences Division

//Signature//

CARL TILMANN
Technical Advisor
Aerodynamic Configuration Branch
Aeronautical Sciences Division

| REPORT DOCUMENTATION PAGE | | *Form Approved*<br>*OMB No. 0704-0188* |
|---|---|---|

The public reporting burden for this collection of information is estimated to average 1 hour per response, including the time for reviewing instructions, searching existing data sources, searching existing data sources, gathering and maintaining the data needed, and completing and reviewing the collection of information. Send comments regarding this burden estimate or any other aspect of this collection of information, including suggestions for reducing this burden, to Department of Defense, Washington Headquarters Services, Directorate for Information Operations and Reports (0704-0188), 1215 Jefferson Davis Highway, Suite 1204, Arlington, VA 22202-4302. Respondents should be aware that notwithstanding any other provision of law, no person shall be subject to any penalty for failing to comply with a collection of information if it does not display a currently valid OMB control number. **PLEASE DO NOT RETURN YOUR FORM TO THE ABOVE ADDRESS**.

| 1. REPORT DATE *(DD-MM-YY)*<br>April 2009 | 2. REPORT TYPE<br>Interim | 3. DATES COVERED *(From - To)*<br>03 June 2004 – 22 April 2009 | |
|---|---|---|---|
| 4. TITLE AND SUBTITLE<br>AERONAUTICAL SCIENCES ADVANCED STUDIES PROGRAM<br>Delivery Order 0002: Plasma Modeling Program | | | 5a. CONTRACT NUMBER<br>F33615-03-D-3307-0002 |
| | | | 5b. GRANT NUMBER |
| | | | 5c. PROGRAM ELEMENT NUMBER<br>0602201 |
| 6. AUTHOR(S)<br>Thomas M. Weeks (Universal Technology Corporation)<br>James Menart, Joseph Shang, and Hong Yan (Wright State University)<br>Sergey Surzhikov (Russian Academy of Science)<br>Domenic D'Ambrosio (Polytechnic Institute of Torino) | | | 5d. PROJECT NUMBER<br>A074 |
| | | | 5e. TASK NUMBER |
| | | | 5f. WORK UNIT NUMBER<br>0B |
| 7. PERFORMING ORGANIZATION NAME(S) AND ADDRESS(ES)<br>**By:**<br>Wright State University<br>--------------------------------------------------------<br>Russian Academy of Science<br>--------------------------------------------------------<br>Polytechnic Institute of Torino | **For:**<br>Universal Technology Corporation<br>1270 N. Fairfield Road<br>Dayton, OH 45432-2600 | | 8. PERFORMING ORGANIZATION REPORT NUMBER |
| 9. SPONSORING/MONITORING AGENCY NAME(S) AND ADDRESS(ES)<br>Air Force Research Laboratory<br>Air Vehicles Directorate<br>Wright-Patterson Air Force Base, OH 45433-7542<br>Air Force Materiel Command<br>United States Air Force | | | 10. SPONSORING/MONITORING AGENCY ACRONYM(S)<br>AFRL/RBAA |
| | | | 11. SPONSORING/MONITORING AGENCY REPORT NUMBER(S)<br>AFRL-RB-WP-TR-2009-3112 |

**12. DISTRIBUTION/AVAILABILITY STATEMENT**
Approved for public release; distribution unlimited.

**13. SUPPLEMENTARY NOTES**
PAO Case Number: 88ABW 2009-3804, 31 Aug 2009. Report contains color.

**14. ABSTRACT**
The Aeronautical Sciences Division, Air Vehicles Directorate, Air Force Research Laboratory (AFRL/RBA) completed a program including modeling and experimental work of the effect of plasmas on air flows. Heating, magnetohydrodynamic (MHD) and electrodynamic (EHD) effects are considered. The direct current plasmas are normal or abnormal glow discharges and the alternating current plasmas are dielectric barrier discharges. Each of these plasma types has actuating effects in different flow regimes. In addition to plasma effects, the phenomenon of pure heating was studied. Path finding numerical simulations of weakly ionized airflows in a hypersonic flow have been successfully accomplished. The research results from this modeling work consist of a basic formulation of the magneto-aerodynamic equations, a plasma model based on the drift-diffusion theory, numerical algorithm development, and computational results. In addition, detailed computer models of the effect of energy deposition on supersonic flow have been developed and utilized. Innovative experimental investigations were carried out in the Mach 5 wind tunnel facility located at Wright Patterson Air Force Base and in the CAPEC Lab (Center for Advanced Power and Energy Conversion) at Wright State University that resulted in a number of new findings and a number of diagnostic tools being developed. All these efforts directly supported the research efforts at AFRL/RB in plasma flow control. *See alternate Abstract on reverse* →

**15. SUBJECT TERMS**
Plasma-based flow, heat deposition, transition, MHD, glow discharges, supersonics, hypersonics.

| 16. SECURITY CLASSIFICATION OF: | | | 17. LIMITATION OF ABSTRACT:<br>SAR | 18. NUMBER OF PAGES<br>264 | 19a. NAME OF RESPONSIBLE PERSON (Monitor)<br>Roger Kimmel |
|---|---|---|---|---|---|
| **a. REPORT**<br>Unclassified | **b. ABSTRACT**<br>Unclassified | **c. THIS PAGE**<br>Unclassified | | | 19b. TELEPHONE NUMBER *(Include Area Code)*<br>N/A |

**Standard Form 298 (Rev. 8-98)**
Prescribed by ANSI Std. Z39-18

**14. ABSTRACT**

This document is the final report for a project entitled "Plasma Modeling Program". The technical work period for this project was from July 1, 2004 to December 31, 2008. The project includes 10 separate tasks.

This work includes modeling and experimental work of the effect of plasmas on air flows. Heating, magnetohydrodynamic (MHD) and electrodynamic (EHD) effects are considered. Direct current plasmas and alternating current plasmas are studied. The direct current plasmas are normal or abnormal glow discharges and the alternating current plasmas are dielectric barrier discharges. Each of these plasma types has actuating effects in different flow regimes. In addition the effect of pure heating is studied.

Path finding numerical simulations of weakly ionized airflows in a hypersonic flow have been successfully accomplished. The research results from this modeling work consist of a basic formulation of the magneto-aerodynamic equations, a plasma model based on the drift-diffusion theory, numerical algorithm development, and computations. All these efforts directly supported the research efforts in computational magneto-fluid-dynamics and experimental investigations in the Mach 5 hypersonic wind tunnel at AFRL/RB.

Innovative experimental investigations were carried out in the Mach 5 wind tunnel facility located at Wright Patterson Air Force Base and in the CAPEC Lab (Center for Advanced Power and Energy Conversion) at Wright State University as part of this funded work. The experiments carried out in the Mach 5 wind tunnel facility involved MHD concepts for flow control, while those carried out at Wright State involved DBD concepts for flow control. The experiments at Wright State were carried out using borrowed equipment from AFRL/RB. These experiments produced a number of new findings on plasmas for flow control, as well as a number of new diagnostic tools.

Detailed computer models of the effect of energy deposition on supersonic flow have been developed and utilized. These models are unsteady, three dimensional models that capture the effects of energy deposition on complex shock structures and boundary layers for supersonic flow. These computations show conclusively that drag reduction can be achieved with energy deposition upstream of a body traveling at supersonic speeds. They also show that the location and size of this energy deposition affect the efficiency of such a scheme for reducing drag.

# TABLE OF CONTENTS

# TABLE OF CONTENTS

# TABLE OF CONTENTS

# LIST OF FIGURES

# LIST OF TABLES

# PREFACE

# ACKNOWLEDGEMENTS

## 1.0 SUMMARY

This report presents the work completed under the Plasma Modeling contract. Work was done in four basic areas: modeling of plasmas, experimental investigations of MHD flow interactions, experimental investigations of DBD plasmas, and computational investigations of supersonic flow control by heat addition. Each of these four topics is described in a separate section of this report. There were a total of 10 tasks under this effort, all of which have been completed. This work includes modeling and experimental work of the effect of plasmas on air flows. Heating, magnetohydrodynamic (MHD) and electrodynamic (EHD) effects are considered. Direct current plasmas and alternating current plasmas are studied. The direct current plasmas are normal or abnormal glow discharges and the alternating current plasmas are dielectric barrier discharges. Each of these plasma types has actuating effects in different flow regimes.

A great deal of information on these plasma types utilized for flow control has been acquired because of this research work. This project has been extremely productive producing 42 published papers, a large number of national presentations, a national best paper award from the AIAA Plasmadynamics and Lasers Technical Committee, one Master's student, and one Ph.D. student. In addition work done by four undergraduate students was funded as part of this grant. Because of this work a number of computer codes have been developed, a number of diagnostic tools have been developed, the AFRL/RB Mach 5 wind tunnel facility underwent a number of improvements, a large volume of results have been published, and a large number of presentations have been made at both the local and national levels. The volume of work completed in the technical work period funded by this grant, July 1, 2004 to December 31, 2008, is large. This grant has produced results that have guided the field of MHD during this time period.

## 2.0   INTRODUCTION

This document is the final report for a project entitled "Plasma Modeling Program". The technical work period for this project was from July 1, 2004 to December 31, 2008. The project includes 10 separate tasks.

This work includes modeling and experimental work of the effect of plasmas on air flows. Heating, magnetohydrodynamic (MHD), and electrodynamic (EHD) effects are considered. Direct current plasmas and alternating current plasmas are studied. The direct current plasmas are normal or abnormal glow discharges and the alternating current plasmas are dielectric barrier discharges. Each of these plasma types has actuating effects in different flow regimes.  In addition the effects of preheating are studied.

This final report is broken into four main parts. Section 3 discusses the work done as part of Tasks 1, 3, and 5, Section 4 discusses the work done as part of Tasks 2 and 4, Section 5 discusses the work done as part of Task 7, and lastly Section 6 discusses the work done as part of Tasks 6, 6.5, 8 and 10. Each of these parts has its own introduction and its own summary. Each section is broken into subsections and up to two levels of subsections below these. A great deal of work is discussed in this final report, because a great deal of work was performed as part of this project. The number of innovations, ideas, and research findings that resulted as part of this project is large. In addition, a number of mathematical models were developed, computer programs written, experimental equipment developed, and diagnostic tools developed during the course of this AFRL funded research.

## 3.0   PLASMA MODELING

Section 3 of this report presents path finding numerical simulations of weakly ionized plasmas in high-speed airflows. This research consists of a basic formulation of the magneto-aerodynamic equations, development of a plasma model based on the drift-diffusion theory, development of a numerical algorithm, and production of results utilizing these computer models. All of the modeling efforts presented in Section 3 of this report directly supported the research initiative for magneto-fluid-dynamics at AFRL/RB. Section 3 of this report covers Tasks 1, 3, and 5 of the Plasma Modeling Program.

In order to directly support the AFRL/RB research activity in hypersonic magnetohydrodynamics (MHD), the present research develops both internal and external, path-finding simulations of high-speed, weakly ionized airflows. Since the principal plasma generation process used at AFRL/RB in a Mach 5 MHD wind tunnel is based on the direct current plasma discharge, the present plasma modeling is limited to DC discharges where the dominate mechanism of plasma production is electron collisions. Electrons gain energy from an externally applied electric field and then create more electrons through inelastic collisions.

Section 3 of this report is divided into three main subsections. In the first subsection the basic model development is discussed. As part of this development process a plasma generated between two parallel electrodes is simulated first. While the goal of this work is to couple a plasma with a high-speed airflow, modeling the plasma in this parallel plate configuration without flow was a wise place to start this plasma modeling activity. In Section 3.2 of this report, a two-dimensional model of MHD flow between parallel plates is developed. This model is the precursor for the three-dimensional model discussed in Section 3.3 of this part of the report.

## 3.1   Model Development for Parallel Electrodes and External Flow over a Wing

### 3.1.1   Introduction

In most magneto-aerodynamic applications for flow control, even in the hypersonic regime, the degree of ionization is still relatively low to produce a strong magneto-aerodynamic interaction (Shang, 2001). However, the charged particle number density can be significantly elevated by surface plasmas via the electron collision process (Mitchner and Kruger, 1973). The plasma generated by this ionization process is best described as a multi-fluid model consisting of electro-positive, electro-negative, and heavy neutral particles. To increase the performance of plasmas for flow control, an externally applied strong magnetic field has been imposed to introduce an additional Lorentz force. It was therefore critical and timely for the present task to have focused research in this area of plasma modeling and to share research results with personnel at AFRL. An equally critical area for computational modeling and simulation of the magneto-aerodynamic interaction is satisfying the divergence free condition for a consistent electrical field. This physical requirement of a numerical simulation is achievable by solving the Poisson equation with stiff source terms and discontinuous boundary conditions.

To support the USAF mission and to accelerate the basic scientific exchange, this research effort is extended to include world-class scientists. Task one of the Plasma Modeling Program is concentrated on the three basic scientific issues mentioned in the above paragraph. The first element addresses the multi-fluid model of a direct current discharge in electro-positive and electro-negative gas. The second element investigates the theory of a quasi-neutral gas discharge plasma in a magnetic field. The third element is focused on numerical solutions of the Poisson

equation with stiff source terms and discontinuous boundary conditions. Finally this work demonstrates a viable application by simulating plasma control on an airfoil. This is the fourth element which simulates subsonic and supersonic flow around a NACA-0012 airfoil with a localized surface gas discharge.

### 3.1.2 Element 1 - Multi-Fluid Model of Direct Current Discharge in Electro-Positive and Electro-Negative Gas

Theory and results of a numerical study of a two-dimensional glow discharge in a crossed magnetic field are presented in papers by Surzhikov and Shang, (2003a) and Surzhikov and Shang (2003b). The theory is based on the drift-diffusion theory of charged particles, and takes into account near electrode regions that have a space charge. This theory allows predictions coordinated with available experimental data for glow discharges, which can be used in various aerospace applications and laser physics. These parameters are: concentration of electrons and ions in the positive column and near the electrode regions, electrical conductivity of the weakly ionized gas of the glow discharge, electrical potential distribution in the gas discharge gap, current density on the electrodes, and total current through an external electrical circuit, which includes ohmic resistance and a power supply generated EMF. The developed theory predicts parameters of the glow discharge coupled with parameters of the external electric circuit.

Numerical simulations (Surzhikov and Shang, 2003a, Surzhikov and Shang 2003b) demonstrate an influence of the gas pressure, the EMF of the power supply, the magnetic field induction, the geometry of the gas discharge gap, the coefficient of secondary electronic emission, and heating effects on the electrodynamics of the glow discharge. These numerical studies enlarged our knowledge of possibilities to use these kinds of discharges for aerospace applications, and these models could be used for predictive purposes. However, many models presented in the literature are oriented for electro-positive gases, namely for molecular nitrogen ($N_2$). However, it is well known that the most significant gas for aerospace application is air, which is an electro-negative gas, due to the high activity of oxygen molecules to attach electrons.

This study presents development of the drift-diffusion-drift of a glow discharge in a crossed magnetic field (Surzhikov and Shang, 2003a) for electro-negative gases. The drift-diffusion model of a DCD (direct-current-discharge) with a magnetic field in an electro-negative gas is based on the momentum conservation equations for electrons (e), positive ions (+), and negative ions (−) in a background fluid which consists of neutral (n) particles (Lifshits and Pitaevskii, 1979):

$$m_e n_e \frac{\partial \mathbf{u}_e}{\partial t} + m_e n_e \left( \mathbf{u}_e \cdot \nabla \right) \mathbf{u}_e = -\nabla p_e + \frac{m_e n_e \mathbf{F}_e}{m_e} - \boldsymbol{\tau}_e - e n_e \left( \mathbf{E} + \frac{1}{c} \left[ \mathbf{u}_e \mathbf{B} \right] \right) - m_e n_e \nu_{en} \left( \mathbf{u}_e - \mathbf{u}_n \right)$$

$$- m_e n_e \nu_{e+} \left( \mathbf{u}_e - \mathbf{u}_+ \right) - m_e n_e \nu_{e-} \left( \mathbf{u}_e - \mathbf{u}_- \right) , \tag{1}$$

$$M_+ n_+ \frac{\partial \mathbf{u}_+}{\partial t} + M_+ n_+ \left( \mathbf{u}_+ \cdot \nabla \right) \mathbf{u}_+ = -\nabla p_+ + \frac{M_+ n_+ \mathbf{F}_+}{m_+} - \boldsymbol{\tau}_+ + e n_+ \left( \mathbf{E} + \frac{1}{c} \left[ \mathbf{u}_+ \mathbf{B} \right] \right) - M_+ n_+ \nu_{+e} \left( \mathbf{u}_+ - \mathbf{u}_e \right)$$

$$- M_+ n_+ \nu_{+n} \left( \mathbf{u}_+ - \mathbf{u}_n \right) - M_+ n_+ \nu_{+-} \left( \mathbf{u}_+ - \mathbf{u}_- \right) , \tag{2}$$

and
$$M_- n_- \frac{\partial \mathbf{u}_-}{\partial t} + M_- n_- \left( \mathbf{u}_- \cdot \nabla \right) \mathbf{u}_- = -\nabla p_- + \frac{M_- n_- \mathbf{F}_-}{m_-} - \boldsymbol{\tau}_- - e n_- \left( \mathbf{E} + \frac{1}{c} \left[ \mathbf{u}_- \mathbf{B} \right] \right) - M_- n_- \nu_{-e} \left( \mathbf{u}_- - \mathbf{u}_e \right)$$

4

$$-M_-n_-\nu_{-n}\left(\mathbf{u}_- -\mathbf{u}_n\right)-m_-n_-\nu_{-+}\left(\mathbf{u}_- -\mathbf{u}_+\right)$$ (3)

where $\tau_\alpha = -\mathbf{i}\dfrac{\partial p_{\alpha,i,m}}{\partial x_m} - \mathbf{j}\dfrac{\partial p_{\alpha,j,m}}{\partial x_m} - \mathbf{k}\dfrac{\partial p_{\alpha,k,m}}{\partial x_m}$ is the vector (component of tensor) of the viscous stress (summing on repeated symbols is presumed) and $\alpha=(e,+,-,n)$; $\mathbf{F}_\alpha$ is the volume mass force for the fluid $\alpha$; $m_e$ and $M_e$ are the masses of the electron and positive and negative ions; $n_\alpha$ is the volume concentration of species $\alpha$; $\mathbf{u}_\alpha$ is the averaged velocity of species $\alpha$; $p_\alpha$ is the pressure of species $\alpha$; $p_{\alpha,(i,j,k),m}$ is the component of the stress tensor; $e$ is the charge of an electron; $c$ is the speed of light; $\mathbf{E}=\mathbf{i}E_x + \mathbf{j}E_y$ is the vector of the electro-static field; $\mathbf{B}=\mathbf{k}B_z$ is the magnetic induction, and $\nu_{\alpha\beta}$ is the frequency of collision of species $\alpha$ and $\beta$.

The electron-neutral collision frequency can be estimated by the following approximations (Gershaman et al., 1984):

$$\nu_{eN_2} = 2.5\times10^{-11} n_{N_2} T_e \left(1+9.3\times10^{-3}\sqrt{T_e}\right),\ \mathrm{s}^{-1},$$

$$\nu_{eO_2} = 1.5\times10^{-10} n_{O_2}\sqrt{T_e}\left(1+4.2\times10^{-2}\sqrt{T_e}\right),\ \mathrm{s}^{-1},$$ (4)

and
$$\nu_{eO} = 2.8\times10^{-10} n_O \sqrt{T_e}\ ,\ \mathrm{s}^{-1}.$$

If it is possible to introduce an effective electric field, then one can formulate a final system of equations of the drift-diffusion model of an electro–negative, weakly–ionized gas discharge in a magnetic field:

$$\frac{\partial n_e}{\partial t} + \frac{\partial}{\partial x}\left(-\mu_e n_e E_{e,x} - \frac{D_e}{1+b_e^2}\frac{\partial n_e}{\partial x}\right) + \frac{\partial}{\partial y}\left(-\mu_e n_e E_{e,y} - \frac{D_e}{1+b_e^2}\frac{\partial n_e}{\partial y}\right) = \alpha(E)\left|\Gamma_e\right| - \beta_e n_+ n_e - \nu_a n_e + k_d n_n n_-$$ (5)

$$\frac{\partial n_+}{\partial t} + \frac{\partial}{\partial x}\left(+\mu_+ n_+ E_{+,x} - \frac{D_+}{1+b_+^2}\frac{\partial n_+}{\partial x}\right) + \frac{\partial}{\partial y}\left(+\mu_+ n_+ E_{+,y} - \frac{D_+}{1+b_+^2}\frac{\partial n_+}{\partial y}\right) = \alpha(E)\left|\Gamma_e\right| - \beta_e n_+ n_e - \beta_- n_- n_+$$ (6)

$$\frac{\partial n_-}{\partial t} + \frac{\partial}{\partial x}\left(-\mu_- n_- E_{-,x} - \frac{D_-}{1+b_-^2}\frac{\partial n_-}{\partial x}\right) + \frac{\partial}{\partial y}\left(-\mu_- n_- E_{-,y} - \frac{D_-}{1+b_-^2}\frac{\partial n_-}{\partial y}\right) = \nu_a n_e - k_d n_n n_- - \beta_- n_- n_+$$ (7)

$$\frac{\partial^2\varphi}{\partial x^2} + \frac{\partial^2\varphi}{\partial y^2} = 4\pi e(n_e + n_- - n_+)$$ (8)

and
$$\mathbf{E} = -\mathrm{grad}\,\varphi$$ (9)

where the components of the effective electric field can be calculated (Surzhikov and Shang, 2003a).

To numerically integrate this system of equations, equations (5) through (7), it is necessary to define coefficients which characterize the processes of physical kinetics in an electro–negative weakly–ionized gas:

1. The attachment frequency is defined as $v_a = (\alpha_a/p)v_{dr} \cdot p$, where $\alpha_a/p$ is the attachment coefficient, which is borrowed from Brown (1966) for air and $v_{dr}$ is the drift velocity of electrons. The following relation fits this coefficient $\alpha_a/p = 0.005$ 1/cm·torr for $E/p < 40$ volt/cm·torr and $\alpha_a/p = 0.005 + \left[(E/p) - 40\right] \cdot 0.35 \times 10^{-3}$ 1/cm·torr for $E/p > 40$ volt/cm·torr.

2. The coefficient of ion–ion recombination is estimated for the reaction $N_2^+ + O_2^- \rightarrow N_2 + O_2$, and it is assumed that $\beta_- = 1.6 \times 10^{-7}$ cm$^3$/s.

3. The detachment coefficient is estimated as $k_d = 10^{-14}$ cm$^3$/s.

4. Coefficients of ionization $\alpha(E)$ and recombination $\beta_e$ were taken as

$$\frac{\alpha}{p} = A \exp\left[-\frac{B}{(E/p)}\right]$$ 1/cm·torr and $\beta_e = 2 \times 10^{-7}$ cm$^3$/s, where $A = 12$ (cm·torr)$^{-1}$ and

$B = 342$ volt/cm·torr as in our previous study (Surzhikov and Shang 2003a, Surzhikov and Shang, 2003b) for nitrogen. It should be noted that for weakly ionized air the following formulas are more acceptable (Shang, 2002a):

$$\left(\frac{\alpha}{p}\right)_{air} = A_{air} \exp\left[-\frac{B_{air}}{(E/p)}\right]$$ (cm·torr)$^{-1}$ where $A_{air} = 15$ (cm·torr)$^{-1}$ and $B_{air} = 365$

volt/cm·torr for $(E/p) \in [100 \div 800]$ volt/cm·torr or $\left(\dfrac{\alpha}{p}\right)_{air} = 1.17 \times 10^{-4}\left(\dfrac{E}{p} - 32.2\right)^2$

(cm·torr)$^{-1}$ for $(E/p) \in [44 \div 176]$ volt/cm·torr.

Boundary conditions for charged particles and an electrical potential between parallel plate electrodes are formulated as:

$$y = 0: \quad \frac{\partial n_i}{\partial y} = 0, \quad \Gamma_e = \gamma\Gamma_i, \quad \varphi = 0; \qquad\qquad y = 0: \quad \frac{\partial n_i}{\partial y} = 0, \quad \Gamma_e = \gamma\Gamma_i, \qquad \varphi = 0;$$

$$y = H: \quad n_i = 0, \quad \frac{\partial n_e}{\partial y} = 0, \quad \varphi = \frac{V}{E}; \qquad y = H: \quad n_i = 0, \quad \frac{\partial n_e}{\partial y} = \frac{\partial n_-}{\partial y} = 0, \quad \varphi = \frac{V}{E};$$

$$x = 0: \quad \frac{\partial n_e}{\partial x} = \frac{\partial n_i}{\partial x} = \frac{\partial \varphi}{\partial x} = 0; \qquad x = 0: \quad \frac{\partial n_e}{\partial x} = \frac{\partial n_i}{\partial x} = \frac{\partial \varphi}{\partial x} = 0;$$

$$x = L: \quad \frac{\partial n_e}{\partial x} = \frac{\partial n_i}{\partial x} = \frac{\partial \varphi}{\partial x} = 0. \qquad x = L: \quad \frac{\partial n_e}{\partial x} = \frac{\partial n_i}{\partial x} = \frac{\partial \varphi}{\partial x} = 0.$$

$$y = 0: \quad \frac{\partial n_+}{\partial y} = \frac{\partial n_-}{\partial y} = 0, \quad \Gamma_e = \gamma\Gamma_+, \quad \varphi = 0,$$

$$y = H: \quad n_+ = 0, \quad \frac{\partial n_e}{\partial y} = \frac{\partial n_-}{\partial y} = 0, \quad \varphi = V,$$

$$x = 0: \quad \frac{\partial n_e}{\partial y} = \frac{\partial n_+}{\partial y} = \frac{\partial n_-}{\partial y} = \frac{\partial \varphi}{\partial y} = 0,$$

and $$x = L: \quad \frac{\partial n_e}{\partial y} = \frac{\partial n_+}{\partial y} = \frac{\partial n_-}{\partial y} = \frac{\partial \varphi}{\partial y} = 0,$$ (10)

where $\gamma$ is the coefficient of secondary electronic emission and $V$ is the voltage drop in the discharge gap. A quasi-neutral plasma cloud of a half-spherical form near to the cathode of the glow discharge is used as the initial condition.

Numerical results have been obtained from theory and typical simulation results are presented in Figure 1. The numerical simulation method for solving equations (5) through (7) with boundary conditions (10) is presented in Surzhikov and Shang (2003a) and Surzhikov and Shang (2003b).
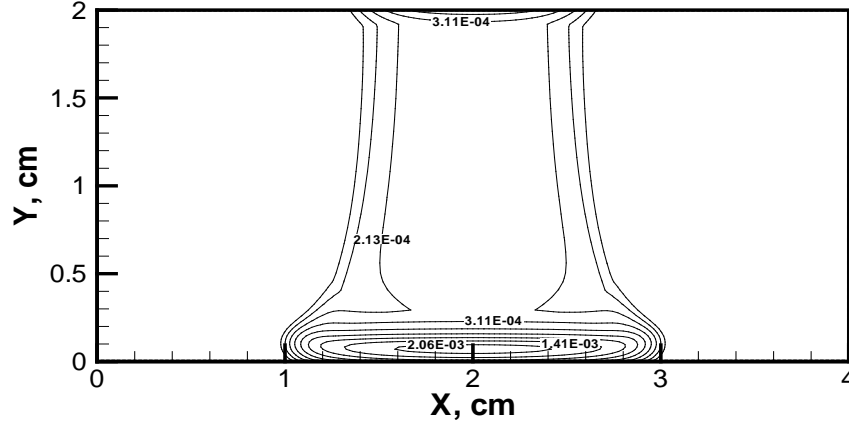


**Figure 1.  Negative Ion Contours in the Gas Discharge Gap at** $p = 5$ **torr,** $E = 2000$ **Volt for an Electro-Negative Gas with** $n_- = 10^9$ **cm$^{-3}$**

### 3.1.3   Element 2 - Theory of Quasi-Neutral Gas Discharge Plasma in Magnetic Field

The classical quasi-neutral model of a DCD is based on the following two equations (Brown, 1966; Raizer, 1991; Von Engel et al., 1932):

$$\frac{\partial n}{\partial t} + \mathrm{div}\left(\mathbf{V}n\right) = \mathrm{div}\left(D_a \mathrm{grad}n\right) + \dot{\omega}_e, \tag{11}$$

and
$$\mathrm{div}\,\mathbf{j} = 0, \tag{12}$$

where $D_a$ is the coefficient of ambipolar diffusion, $\mathbf{V}$ is the velocity of gas flow, $n$ is the volume concentration of charge particles ($n_e \approx n_+ \approx n$), $\mathbf{j}$ is the current density vector, and $\dot{\omega}_e = \alpha\left(E\right)\left|\mathbf{\Gamma}_e\right| - \beta_e n_+ n_e = \alpha\left(E\right)\left|\mathbf{\Gamma}_e\right| - \beta_e n^2$ is the source term defined in element 1 for the more general case of electro-negative gases.

Let us prove the validity of these equations within the framework of some assumptions. If densities $n_e$ and $n_+$ are not low, a considerable space charge is formed as a result of charge separation, which is due to large differences between mobilities of the electrons and the much heavier ions. As a result the generated polarization field impedes further charge separation. Charge separation and the field adjust to each other so that the field restrains the run-away electrons which pulls the heavy ions, making them diffuse as a team. This diffusion is known as *ambipolar* diffusion (Mitchner and Kruger, 1973).

Let us turn to the general expressions for charge particle fluxes (see Element 1), and at the beginning let us neglect a magnetic field,

7

$$\mathbf{\Gamma}_e = -\mu_e n_e \mathbf{E} - D_e \operatorname{grad} n_e , \tag{13}$$

and
$$\mathbf{\Gamma}_+ = +\mu_+ n_+ \mathbf{E} - D_e \operatorname{grad} n_+ . \tag{14}$$

To determine the electric field one should consider Poisson's equation,

$$\operatorname{div}\mathbf{E} = 4\pi e \left( n_+ - n_e \right) . \tag{15}$$

In the presence of a homogeneous external electric field, equation (15) gives the polarization field $\mathbf{E}$. Now one can estimate a typical scale of quasi-neutrality, i.e. the Debye radius,

$$r_{\mathrm{D}} = \sqrt{\frac{kT_e}{4\pi e^2 n_e}} = 6.88 \sqrt{\frac{T_e\,[\mathrm{K}]}{n_e\,\left[\mathrm{cm}^{-3}\right]}} .$$

For the conditions under consideration of $T_e = 11610\,\mathrm{K}$ and $n_e = 10^{11}\,\mathrm{cm}^{-3}$ the Debye length is $r_{\mathrm{D}} \cong 3.4 \times 10^{-4}\,\mathrm{cm}$. This means that inside an infinite plasma volume one can use the ambipolar approach at a scale $L > r_D$, say at $L \sim 10^{-2}\,\mathrm{cm}$.

If we let the separation of charges be small on a scale $L$ then

$$n_- = 10^9 \;;\qquad \left| n_+ - n_e \right| \ll n_e \approx n_+ \approx n . \tag{16}$$

For the separation to not grow appreciably, the electron and ion fluxes must be almost equal. Let us consider one direction

$$\Gamma_{e,x} \approx \Gamma_{+,x} , \tag{17}$$

where

$$\Gamma_{e,x} \approx -\mu_e E_x n - D_e \frac{\partial n}{\partial x} , \tag{18}$$

and
$$\Gamma_{+,x} \approx +\mu_+ E_x n - D_+ \frac{\partial n}{\partial x} . \tag{19}$$

In order to eliminate the polarization field from expressions (18) and (19) we divide the first by $\mu_e$, the second by $\mu_+$, and add the results giving

$$\frac{\Gamma_{e,x}}{\mu_e} + \frac{\Gamma_{+,x}}{\mu_+} = -\frac{D_e}{\mu_e}\frac{\partial n}{\partial x} - \frac{D_+}{\mu_+}\frac{\partial n}{\partial x}$$

or

$$\Gamma_x \frac{\mu_e + \mu_+}{\mu_e \mu_+} = -\left( \frac{D_e}{\mu_e} + \frac{D_+}{\mu_+} \right) \frac{\partial n}{\partial x}$$

or

$$\Gamma_x = -\frac{\mu_+ D_e + \mu_e D_+}{\mu_e + \mu_+} \frac{\partial n}{\partial x} . \tag{20}$$

So, we find that the flux of charge particles of both signs is written in the standard form for diffusion (Hoh, 1962; Chen, 1974),

$$\Gamma_x = -D_a \frac{\partial n}{\partial x}, \quad D_a = \frac{\mu_+ D_e + \mu_e D_+}{\mu_e + \mu_+}$$

(21)

with an effective coefficient $D_a$, the ambipolar diffusion coefficient.

To close the description of the quasi-neutral model of a DCD (Brown, 1966; Raizer, 1991; Von Engel et al., 1932) we define the value of the current density

$$\mathbf{j} = e(\mathbf{\Gamma}_+ - \mathbf{\Gamma}_e) = e\left[\mathbf{e}_x(\Gamma_{+,x} - \Gamma_{e,x}) + \mathbf{e}_y(\Gamma_{+,y} - \Gamma_{e,y})\right]$$

(22)

where $\mathbf{e}_x$ and $\mathbf{e}_y$ are the unit coordinate vectors. Components of the charge particle fluxes must be derived from the following expressions (see Element 1):

$$\Gamma_{e,x} = -\mu_e n_e E_{e,x} - \frac{D_e}{1+b_e^2}\frac{\partial n_e}{\partial x} + \frac{b_e}{1+b_e^2}D_e\frac{\partial n_e}{\partial y},$$

(23)

$$\Gamma_{+,x} = +\mu_+ n_+ E_{+,x} - \frac{D_+}{1+b_+^2}\frac{\partial n_+}{\partial x} - \frac{b_+}{1+b_+^2}D_+\frac{\partial n_+}{\partial y},$$

(24)

$$\Gamma_{e,y} = -\mu_e n_e E_{e,y} - \frac{D_e}{1+b_e^2}\frac{\partial n_e}{\partial y} - \frac{b_e}{1+b_e^2}D_e\frac{\partial n_e}{\partial x},$$

(25)

and

$$\Gamma_{+,y} = +\mu_+ n_+ E_{+,y} - \frac{D_+}{1+b_+^2}\frac{\partial n_+}{\partial y} + \frac{b_+}{1+b_+^2}D_+\frac{\partial n_+}{\partial x},$$

(26)

where

$$E_{e,x} = \frac{E_x - b_e E_y}{1+b_e^2}, \qquad E_{e,y} = \frac{E_y - b_e E_x}{1+b_e^2},$$

(27)

and

$$E_{+,x} = \frac{E_x + b_+ E_y}{1+b_+^2}, \qquad E_{+,y} = \frac{E_y - b_+ E_x}{1+b_+^2}.$$

(28)

In view of the fact that $n_e \approx n_+ \approx n$, one can project the total current density vector on the coordinate axis and introduce an effective electronic mobility and an effective electronic diffusion coefficient. The charge particle fluxes are approximated very well by the following formulas

$$\mathbf{\Gamma}_e = -\tilde{\mu}_e n\mathbf{E} - \tilde{D}_e \mathrm{grad} n$$

(29)

and

$$\mathbf{\Gamma}_+ = +\mu_+ n\mathbf{E} - D_+ \mathrm{grad} n .$$

(30)

Then

$$\mathbf{j} = e(\mathbf{\Gamma}_+ - \mathbf{\Gamma}_e) = e\left[(\mu_+ + \tilde{\mu}_e)n\mathbf{E} + (\tilde{D}_e - D_+)\mathrm{grad} n\right].$$

(31)

9

The total electric field can be determined from

$$\mathbf{E} = \frac{\mathbf{j}}{en\left(\mu_+ + \tilde{\mu}_e\right)} - \frac{\tilde{D}_e - D_+}{n\left(\mu_+ + \tilde{\mu}_e\right)}\,\mathrm{grad}\,n \;. \tag{32}$$

Finally the possibility of obtaining expressions for charge particle fluxes in the quasi-neutral approximation is realized. The electric field equation, equation (32), is used in equations (29) and (30) giving

$$\boldsymbol{\Gamma}_e = -\frac{\mathbf{j}}{e}\cdot\frac{\tilde{\mu}_e}{\tilde{\mu}_e + \mu_+} - \tilde{D}_a \nabla n \;, \tag{33}$$

and

$$\boldsymbol{\Gamma}_+ = +\frac{\mathbf{j}}{e}\cdot\frac{\mu_+}{\tilde{\mu}_e + \mu_+} - \tilde{D}_a \nabla n \;, \tag{34}$$

where

$$\tilde{D}_a = \frac{\tilde{\mu}_e D_+ + \mu_+ \tilde{D}_e}{\mu_+ + \tilde{\mu}_e}\;. \tag{35}$$

Note that relations (33) and (34) can be rewritten in terms of $\mu_e^*$:

$$\boldsymbol{\Gamma}_e = -\frac{\mathbf{j}}{e}\mu_e^* - \mu_e^* D_a \nabla n \;, \tag{36}$$

and

$$\boldsymbol{\Gamma}_+ = +\frac{\mathbf{j}}{e}\cdot\frac{\mu_+}{\tilde{\mu}_e + \mu_+} - \mu_e^* D_a \nabla n \;. \tag{37}$$

As a result, the quasi-neutral model of the DCD in a magnetic field can be formulated as follows

$$\frac{\partial n}{\partial t} + \mathrm{div}\left(\mathbf{V}n\right) = \mathrm{div}\left(\mu_e^* D_a \mathrm{grad}\,n\right) + \dot{\omega}_e \;, \tag{38}$$

and

$$\mathrm{div}\left[\left(\mu_+ + \tilde{\mu}_e\right)n\mathbf{E} + \left(\tilde{D}_e - D_+\right)\mathrm{grad}\,n\right] = 0 \;, \tag{39}$$

where

$$\tilde{\mu}_e = \frac{\mu_e}{1+b_e^2}\;,\quad \mu_e^* = \frac{\mu_e + \mu_+}{\left(1+b_e^2\right)\mu_+ + \mu_e} \cong \frac{\mu_e}{\left(1+b_e^2\right)\mu_+ + \mu_e} \tag{40}$$

and

$$\tilde{D}_e = \frac{D_e}{1+b_e^2}\;. \tag{41}$$

Note that equation (39) is used for calculation of the total electric field $\mathbf{E}$ and equation (38) is used for calculation of the concentration of charge particles. The source term in equation (38) must be modified to account for the presence of a magnetic field,

$$\dot{\omega}_e = \left(\frac{\alpha}{p^*}\right) p^* E \frac{\mu_e\left(p^*\right)}{1+b_e^2} - \beta n^2 . \tag{42}$$

Here we used the definition of ionization frequency as

$$\nu_i = \left(\frac{\alpha}{p^*}\right) \cdot v_{e,d} = \frac{\alpha}{p} \mu_e E , \tag{43}$$

where $\dfrac{\alpha}{p^*}$ is the first Townsend coefficient and $p^*$ is the effective pressure.

### 3.1.4 Element 3 - Numerical Solution of the Poisson Equation with Stiff Source Term and Discontinuous Boundary Conditions

Poisson's equation appears in many magneto-fluid dynamics models where it is possible to define an electric potential (D'Ambrosio and Giodana, 2004; Gaitonde, 2004). In particular, it is present in the low magnetic Reynolds number approximation of magneto-fluid dynamics as a modified form of the electric charge conservation equation and in the drift-diffusion theory of a gas discharge plasma where it used to enforce Gauss' law for electric fields (Gaitonde, 2004). In addition, for moderate to high magnetic Reynolds number models, when the magnetic induction equation must be solved, a Poisson equation is also used in projection schemes for maintaining the $\nabla \cdot \mathbf{B} = 0$ constraint (Gaitonde, 200; Brackbill and Barnes, 1980; Toth, 2000).

Frequently, especially in the first two cases cited above, the boundary conditions that accompany Poisson's equation can be very severe. For instance, if electrodes are present at the wall, the electric potential varies very rapidly in a very small region close the electrodes, so that stretched meshes are necessary there. Moreover, the boundary conditions are discontinuous when passing from an electrically conducting wall to a dielectric surface. All these aspects make the numerical solution of Poisson's equation for magneto-fluid dynamic applications a delicate aspect of the global numerical solution of the considered model.

The present effort will focus on the description of numerical methods for the efficient and accurate solution of Poisson's equation in two-dimensions as it appears in typical magneto-fluid dynamics applications and on the discussion of the obtained results. To this aim, a model equation is considered that presents the same difficulties that would be encountered in practical applications. Different relaxation techniques will be used, starting from the Gauss-Seidel scheme, to the Successive Over-Relaxation (SOR) scheme and up to the Alternate Direction Implicit (ADI) scheme. All these numerical methods are applied to a multi-block finite volume discretization of the computational domain. The discussion on the efficiency and the accuracy of the different techniques will be based upon numerical tests carried out on various configurations, from the simple two-facing-electrodes setup, to the more complex airfoil-with-electrodes geometry.

A model Poisson equation is derived that possesses characteristics similar to those encountered in realistic problems near an electrode, with particular reference to drift-diffusion theory (Surzhikov and Shang, 2003a, Surzhikov and Shang, 2003a). We start with the assumption that the electron and the ion number densities can be described by Boltzmann distributions:

$$n_e = n_o \, exp(e\varphi/kT_e) \tag{44}$$

11

and
$$n_i = n_o \, exp(e\varphi/kT_i) \, , \tag{45}$$

where $n_o$ is the ambient charge particle number density.

Recall that Poisson's equation can be obtained for an electric field that is irrotational and can be defined by a potential function

$$-\nabla \cdot (\nabla\varphi) = -\nabla^2 \varphi = e/\varepsilon_0 (n_i - n_e) \, . \tag{46}$$

If we expand in a series the exponential functions that appear in equations (44) and (45) and retain only the leading term, we have:

$$-\nabla \cdot (\nabla\varphi) = -\nabla^2 \varphi = e^2 n_o/\varepsilon_0(1/kT_i + 1/kT_e) \varphi + O(\varphi^2) \, . \tag{47}$$

Using the definition of the Debye length,

$$\lambda_D = (\varepsilon_o \kappa T/ne^2)^{1/2} \, ,$$

and making no distinction between the two different Debye lengths, but simply defining an average Debye length, the final form of our model Poisson equation is

$$\nabla \cdot (\nabla\varphi) = \nabla^2 \varphi = \varphi/\lambda_D^2 \, . \tag{48}$$

The Debye length, which we will assume to be constant, is numerically very small with respect to the typical scale of the problems considered.

As we are interested in numerically solving this equation using a finite volume method, we write it in integral form:

$$\iint \nabla\varphi \cdot \mathbf{n} \, ds - \iiint \varphi/\lambda_D^2 \, dV = 0 \, . \tag{49}$$

Depending on the nature of the considered surface, we can have different boundary conditions:

$$\text{on the cathode;} \qquad \varphi = 0 \, ,$$
$$\text{on the anode;} \qquad \varphi = V_c, \tag{50}$$

and $\qquad$ on a dielectric wall; $\quad \nabla\varphi \cdot \mathbf{n} = 0 \, .$

At the connection between an electrode and the dielectric wall, the boundary conditions are discontinuous. In the numerical solution of equation (49), this fact may create perturbations that destabilize the system. The investigation of such a problem is one of the subjects of the present research activity.

To acquire some preliminary insight into the problem, we reduce Poisson's equation to 1D and find its solution. Luckily, an analytical solution exists for the 1D problem:

$$\varphi(y) = A \, exp \, (y/\lambda_D) + B \, exp \, (-y/\lambda_D) \tag{51}$$

Constants A and B are to be determined by enforcing the boundary conditions. Here, we initially assume the cathode is at $y=0$ and the anode is at $y=L$. By satisfying the boundary conditions, the analytical solution becomes

$$\varphi(y) = V_c \, sinh(y/\lambda_D)/ \, sinh(L/\lambda_D) \, . \tag{52}$$

As $\lambda_D$ is typically of the order of magnitude of $10^{-7}$ m and the distance between two electrodes, $L$, is typically $10^{-1}$ m, numerical problems arise as the functions $sinh(10^6)$ need special treatment.

This problem was removed by a simple independent variable transformation to provide an appropriate physical scale.

To solve equation (48) numerically, we introduce an artificial time-dependent term that modifies the original equation as follows:

$$-\partial\varphi/\partial t + \partial^2\varphi/\partial y^2 - 1/\lambda_D^2\ \varphi = 0 \tag{53}$$

We used the "-" sign in front of the pseudo time-derivative for stability considerations that will be made clear later. If we discretize the above equation according to an implicit scheme, and we consider an equally spaced grid, we obtain a second order spatial accurate scheme and it is a simple tridiagonal system that can be easily solved.

Note that if an explicit scheme were used, the stability condition would be such that if a "+" sign were placed before the pseudo time-derivative in equation (53), then the explicit scheme would have been unconditionally unstable. This explains the choice of the "-" sign in the model equation. Such a choice is not important if one adopts an implicit scheme, which is unconditionally stable whatever the sign in front of the pseudo time-derivative.

In order to retain second order accuracy at the boundaries, Dirichlet boundary conditions, such as those at the anode and at the cathode, require special treatment. In particular, we adopted a one-sided difference approximation for the second order derivative for $\varphi$.

The final system that we obtain has the form:

$$[A]\ \Delta\varphi = R \tag{54}$$

where $[A]$ is a tridiagonal matrix and $R$ is a column vector.

A comparison between analytical and numerical results for the 1D problem is shown in Figures 2 and 3 for characteristic length ratios $\lambda_D/L=10^{-4}$ and $\lambda_D/L=10^{-5}$, respectively. The computational grids are composed of 100 points and are strongly refined close to the electrodes. Exponential stretching was used, with a minimum distance from the wall equal to $\Delta y_o/L=5\cdot10^{-6}$ for $\lambda_D/L=10^{-4}$ and $\Delta y_o/L=5\cdot10^{-7}$ for $\lambda_D/L=10^{-5}$.
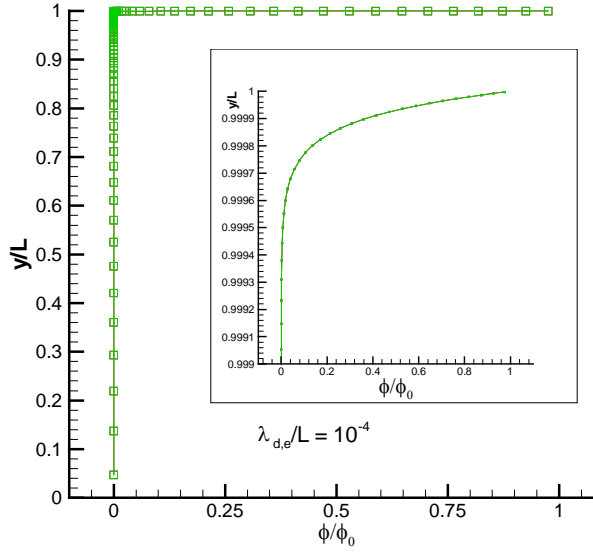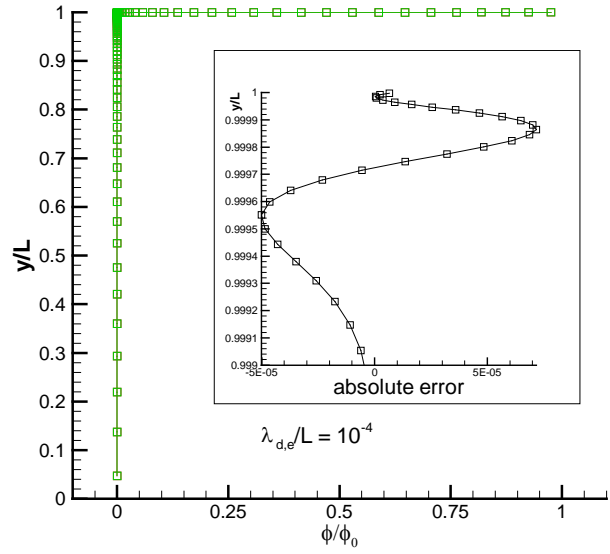
Potential function φ(y) at top electrode                Absolute value of numerical error

**Figure 2.  Analytic and Numerical Solution of 1-D Poisson Equation, $\lambda_D/L = 10^{-4}$**
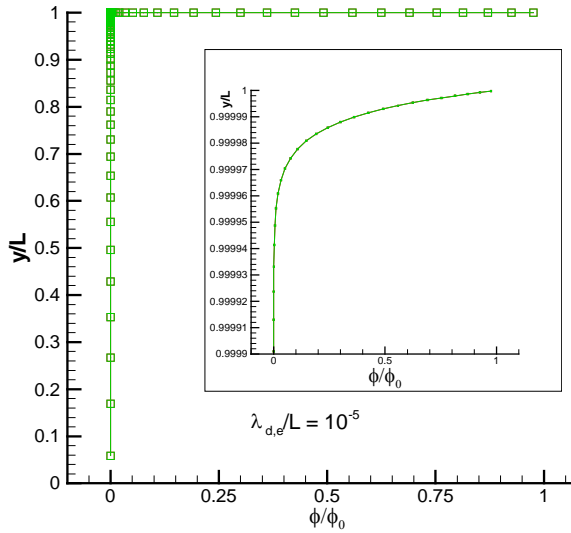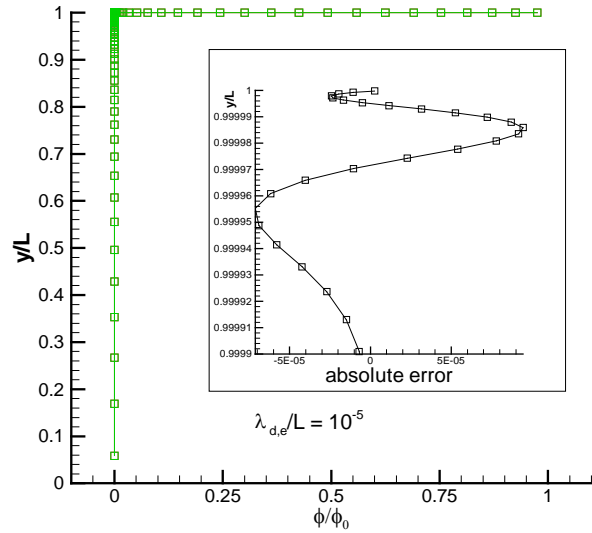


Potential function φ(y) at top electrode                Absolute value of numerical error

**Figure 3.  Analytic and Numerical Solution of 1-D Poisson Equation, $\lambda_D/L = 10^{-5}$**

The two-dimensional Poisson equation is solved using relaxation methods. Therefore, an artificial time-dependent term is added to equation (49), leading to the following equation:

$$\iiint \partial\varphi/\partial t + \iint \nabla\varphi \cdot \mathbf{n} \, ds + \iiint \varphi/\lambda_D^2 \, dV = 0 \, . \tag{55}$$

The discretized form of equation (55), in general, is given by

$$\frac{\Delta\phi_{N,M}}{\Delta t}\Delta V_{N,M} - \sum_{s=1}^{4} \left[ (\nabla\phi)_s^{K+\ell} \cdot \mathbf{n}_s \right]_{N,M} (\Delta S_s)_{N,M} + \frac{1}{\lambda_{D,e}^2}\phi_{N,M}^{K+\ell}\Delta V_{N,M} = 0 \tag{56}$$

14

If $L=0$, then an explicit method is adopted, while for $L=1$ or $L=1/2$, the integration method is implicit.

In order to compute the gradient of $\varphi$ at each cell surface s, we build secondary staggered cells around each primary cell surface, as shown in Figure 4.
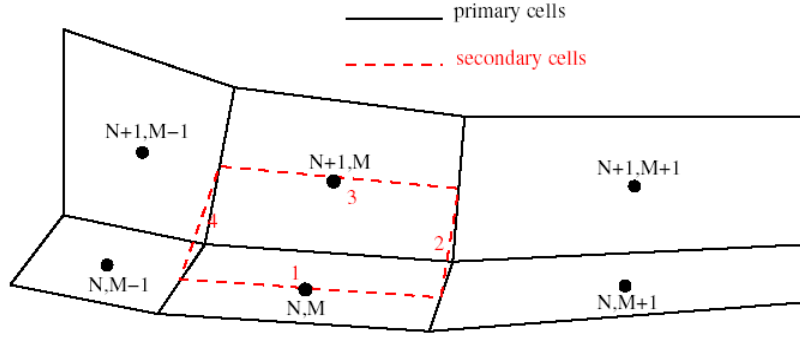


Figure 4.  Staggered Cells for Derivatives Calculation at Primary Cells

By writing the diffusive fluxes that appear in equation (55) as

$$[(\nabla\varphi)_s \cdot \mathbf{n}_s]_{N,M}(\Delta S_s)_{N,M} = F_s$$

equation (56) finally becomes

$$\frac{\Delta\phi_{N,M}}{\Delta t}\Delta V_{N,M} - \left(F^{K+\ell}_{N+1/2,M} + F^{K+\ell}_{N-1/2,M} + F^{K+\ell}_{N,M+1/2} + F^{K+\ell}_{N,M-1/2}\right) + \frac{1}{\lambda^2_{D,e}}\phi^{K+\ell}_{N,M}\Delta V_{N,M} = 0 \qquad (57)$$

The boundary conditions for the two-dimensional problem are separated into two groups for the electrode and dielectric surfaces. At the electrodes the electric potential, $\varphi$, is prescribed. Thus, a flux exists on the electrode's surface, given by:

$$F_{el} = (\nabla\varphi)_{el} \cdot \mathbf{n}_{el} \Delta S_{el}, \qquad (58)$$

where the subscript *el* stands for electrode. Provided the cells are not excessively distorted at the wall, we can obtain $(\nabla\varphi)_{el}$ with second order accuracy, which was obtained assuming that $\varphi$ behaves as a second order polynomial passing through adjacent cells.

The dielectric wall boundary condition is very simple:

$$F_{ds} = (\nabla\varphi)_{ds} \cdot \mathbf{n}_{ds} \Delta S_{ds} = 0 , \qquad (59)$$

where the subscript *ds* stands for dielectric surface. Note that in this case the wall flux does not depend upon the value of $\varphi$ in the interior points.

A comparative study of solving schemes is performed in the present effort to assess the relative numerical efficiency for solving Poisson's equation with a stiff source term and discontinuous boundary conditions. For the present purpose, the Gauss-Seidel, successive over relaxation (SOR), and alternating-directions implicit (ADI) algorithms were chosen to solve the discretized equations. These numerical procedures are described below:

Gauss-Seidel Scheme:

The Gauss-Seidel relaxation scheme makes use of the updated values of the fluxes $F$ as soon as they become available. The numerical procedure can be written as follows:

$$\Delta\phi_{N,M} = \frac{\Delta t}{\Delta V_{N,M}} \left( F^K_{N+1/2,M} + F^\star_{N-1/2,M} + F^K_{N,M+1/2} + F^\star_{N,M-1/2} \right) - \frac{1}{\lambda^2_{D,e}} \phi^K_{N,M} \Delta t$$

(60)

$$\phi^{K+1}_{N,M} = \phi^K_{N,M} + \Delta\phi_{N,M}$$

SOR Scheme:

The SOR scheme is very similar to the Gauss-Seidel scheme. The difference in equation (60) is

$$\phi^{K+1}_{N,M} = \phi^K_{N,M} + \omega\Delta\phi_{N,M}$$, 

(61)

where ω is called the relaxation parameter. This method is convergent only if $0 < \omega < 2$. Only over-relation ($1 < \omega < 2$) can give faster convergence than the Gauss-Seidel method. For any specific problem, an optimal choice of $\omega$ can be found.

ADI Scheme:

The alternative-directions implicit method is an example of an operator splitting method. In this case, we choose to split the operator in the two grid directions $N$ and $M$. Then, we difference the time-dependent equation (57) implicitly in two fractional steps as follows:

$$\frac{\Delta\phi'_{N,M}}{\Delta t/2} \Delta V_{N,M} - \left( F^{K+1/2}_{N+1/2,M} + F^{K+1/2}_{N-1/2,M} + F^K_{N,M+1/2} + F^K_{N,M-1/2} \right) + \frac{1}{\lambda^2_{D,e}} \phi^{K+1/2}_{N,M} \Delta V_{N,M} = 0$$

$$\frac{\Delta\phi''_{N,M}}{\Delta t/2} \Delta V_{N,M} - \left( F^{K+1/2}_{N+1/2,M} + F^{K+1/2}_{N-1/2,M} + F^{K+1}_{N,M+1/2} + F^{K+1}_{N,M-1/2} \right) + \frac{1}{\lambda^2_{D,e}} \phi^{K+1}_{N,M} \Delta V_{N,M} = 0$$

(62)

The typical form of the two matrices related to the two sweeps of the ADI scheme are composed of smaller tridiagonal blocklets, one for each $N$ or $M$ line of grid cells.

The numerical code built in the present research activity has been extended to multi-block domain discretization. The concept of multi-block domain discretization is useful when dealing with complex grids, but it becomes necessary when dealing with airfoils. In fact, any O-type or C-type grid will contain at least two matching interfaces.

When the computational domain is discretized using a multi-block approach, the Jacobian matrices of the ADI scheme are no longer tridiagonal, as new elements appear that take into account the dependence of the flux across the boundary of a certain block with respect to the values of the dependent variables in an adjacent block. However, it is still possible to transform the ADI matrices with non-tridiagonal terms into tridiagonal matrices by merging those blocklets that are connected one to the other and operating with row and column permutations on them. This is equivalent to solving each couple of connected $N$ or $M$ lines as a single line.

16

Two-dimensional results for two different geometrical configurations will be presented. The first configuration is a flat plate with two electrodes placed side by side. The second one is a symmetric NACA-0015 airfoil with two electrodes put in the trailing edge region.

Though it will not be shown here, a normalized residual was also monitored. The normalized residual is the residual divided by the source term of Poisson's equation. It was taken into consideration because it was observed that the source term might be large, in which case a large local residual might result in the difference of two large numbers (the Laplacian and the source term). However, monitoring the convergence history using the normalized residual did not have an effect on the final conclusions made about the convergence properties of the numerical schemes.

In this test case, two electrodes are placed side by side on the surface of a flat plate made of dielectric material. The Debye length is set to $\lambda_D = 10^{-4}$ m. The geometric setup and the computational grid are composed of 216 cells along the plate wall and of 94 cells normal to it. The grid is stretched in the normal direction at the flat plate wall and in the tangential direction in the electrode regions. Dielectric wall boundary conditions are enforced everywhere except at the electrodes. The electric potential is set to -40 V for the left electrode and to +20 V for the right electrode. The result of the computation is shown in Figure 5.
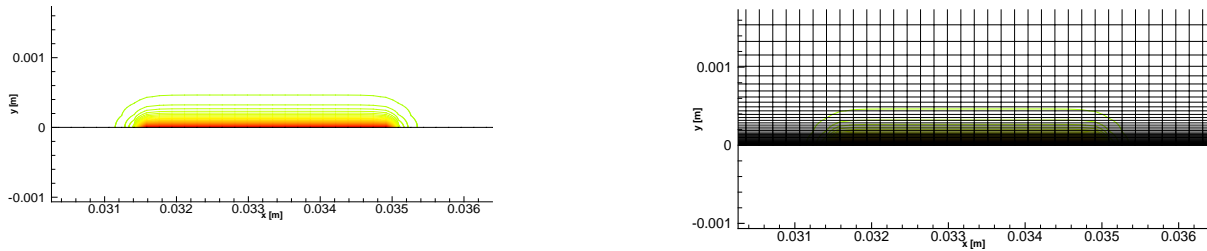


**Figure 5. Electrodes Embedded in a Dielectric Flat Plate**

The convergence history demonstrated the superiority of the ADI scheme for this case. Using the SOR scheme, which is more efficient than the Gauss-Seidel scheme, the average residual used for convergence was still equal to $4.8 \times 10^{-5}$ after 60850 iterations and 5250 s of CPU time on a Pentium IV - 2.2 GHz machine. The relaxation factor used was $\omega = 1.8$. For this case, the best value for $\omega$ is somewhere between 1.8 and 1.9. Note that the grid is stretched at the wall and at the electrodes, but it is uniform elsewhere. This may explain why the optimal $\omega$ is close to the optimal value for an equally spaced grid. Conversely, the ADI scheme converged to a value of the average residual lower than $10^{-8}$ after 18 iterations and 4.54 s of CPU time.

As no appreciable difference was detected between solutions with different average residuals of $O(10^{-5})$ and $O(10^{-8})$, we remark that it may not be necessary to seek excessively converged solutions, at least in the case of the model Poisson equation.
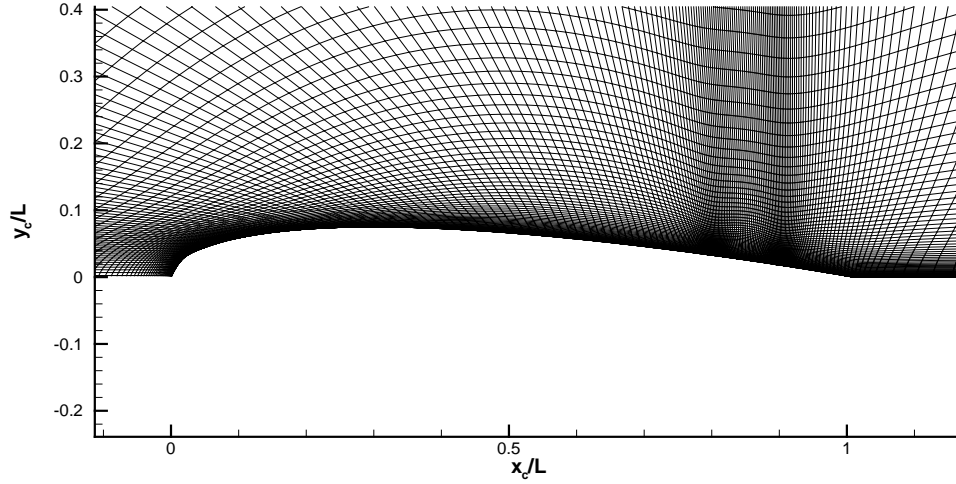
**Figure 6. Components of Electrical Potential over the Electrodes on NACA 0015 Airfoil**

In the present test case, a NACA 0015 airfoil is considered, with two electrodes placed side by side in the trailing edge region. The Debye length, $\lambda_D$, is equal to $10^{-4}$ m, while the airfoil chord is set to $L = 0.2$ m. At the left electrode, the boundary condition for the electric potential is $\varphi = -40$ V, while it is $\varphi = 0$ V for the right electrode. The grid, which is very similar to one that could be used for CFD computations, is finely clustered at the wall and in the electrode regions. Progressively enlarged views of the mesh are displayed in Figure 6. Note the clustering of the grid near the electrodes, and in particular at the outer boundaries of the electrodes. The solution obtained is shown in Figure 7. The characteristic features are similar to those of the previous test case. Appreciable changes in the value of $\varphi$ are present in the near electrode region only and vanish at a distance on the order of magnitude of the Debye length.
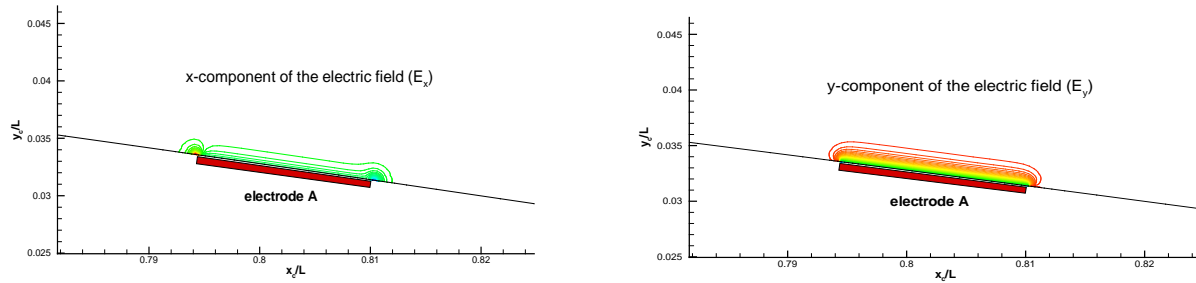


**Figure 7. Components of Electrical Potential over the Electrodes on NACA 0015 Airfoil**

In Figure 7, the computed values of $\varphi$, $E_x$ and $E_y$ at the first cell center away from the wall are presented. As in the previous test case, $E_x$ and $E_y$ plots are characterized by peaks in the areas between the electrode and the dielectric wall. As stated previously, such behavior might have a numerical origin and should be investigated through a grid convergence study.

The iteration convergence history of the present test case is shown in the root-mean-square residual (RES). Here, the maximum allowed CFL number was 300 and the choice of the "CFL ramp", that is the variation of the CFL number from an initial value to the final one, was very delicate.

In Figure 8, the different curves show the convergence history for the same test case computed starting with an initial constant CFL number of 50. The only difference between the plots, some

of which represent a non-convergent iteration history, is in the number of iterations during which the initial CFL number value was kept constant and in the number of iterations in which the initial CFL value was linearly increased up to the final one. Slight variations of these two parameters may transform a convergent computation into a divergent one. The values of local CFL numbers are used to garner evidence where the instability that leads to divergence is triggered. The plots represent the location of the maximum local residual in the grid direction $N$, normal to the wall, and in the grid direction $M$, tangential to wall, see equation (61). Considering it is possible to see that, when the residual decreases and, thus, the computation converges, the maximum local residual is located in the middle of the electrode ($M$=108-109) and goes away from the electrode wall ($N$ increases). Conversely, immediately before divergence occurs, the location of the maximum local residual shifts to $N$=1-2 and $M$=109-110, which is at the junction between electrode A and the dielectric wall. Thus, the discontinuities in the wall boundary conditions seem to be very critical for the iteration convergence of the numerical solution.
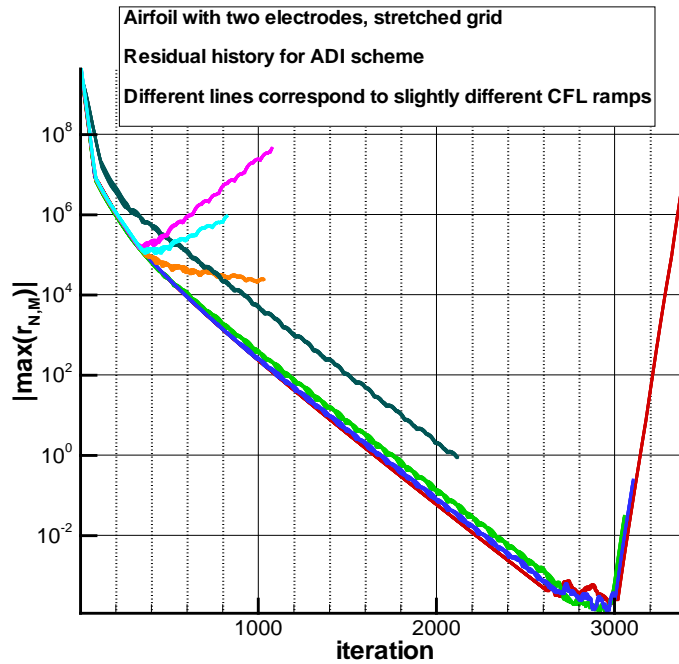


**Figure 8. Convergence History of Solution with Different CFL Values**

In short, a multiblock, finite volume code for solving the model Poisson equation has been implemented. This code can use the Gauss-Seidel, the SOR, and the ADI relaxation schemes. All schemes have been implemented using a multi-block domain discretization. Numerical experiments have demonstrated that the ADI scheme is definitely superior, in terms of convergence rate, with respect to the Gauss-Seidel and the SOR schemes.

### 3.1.5 Element 4 - Subsonic and Supersonic Flow around Airfoil NACA-0012 with Localized Surface Discharge

As an illustration for bench marking the present investigations of the plasma modeling for flow control, the formulation of a multi-fluid model of plasma and an efficient numerical procedure for solving the electrodynamic equations are integrated to simulate a direct current discharge on a lift surface. For the present purpose, there is no attempt made to enhance aerodynamic

performance of the lifting device, but rather to focus on the newly developed ability for simulating the magneto-aerodynamic interaction.

In Figure 9, physical and computational fluid dynamic models of a localized surface gas discharge in subsonic and supersonic flows around a NACA-0012 airfoil are presented. The simulated flow field spans a Mach number range from a subsonic Mach number of 0.2 to a supersonic Mach of 2.0. The model contains coupled Navier-Stokes equations and electrodynamic equations for a gas discharge plasma in generalized curvilinear coordinates. A physical statement of the problem includes the continuous surface discharge with an electromotive force (EMF) generated by a power supply and ohmic resistance in the external electric circuit between the cathode and anode, which are located on the top surface of the aerodynamic profile (Figure 10). The basic objective of the problem is solving the coupled gas dynamic and electrodynamic equations, and analyzing the effect of the localized surface discharge on pressure and temperature distributions over boundary surfaces of the airfoil.
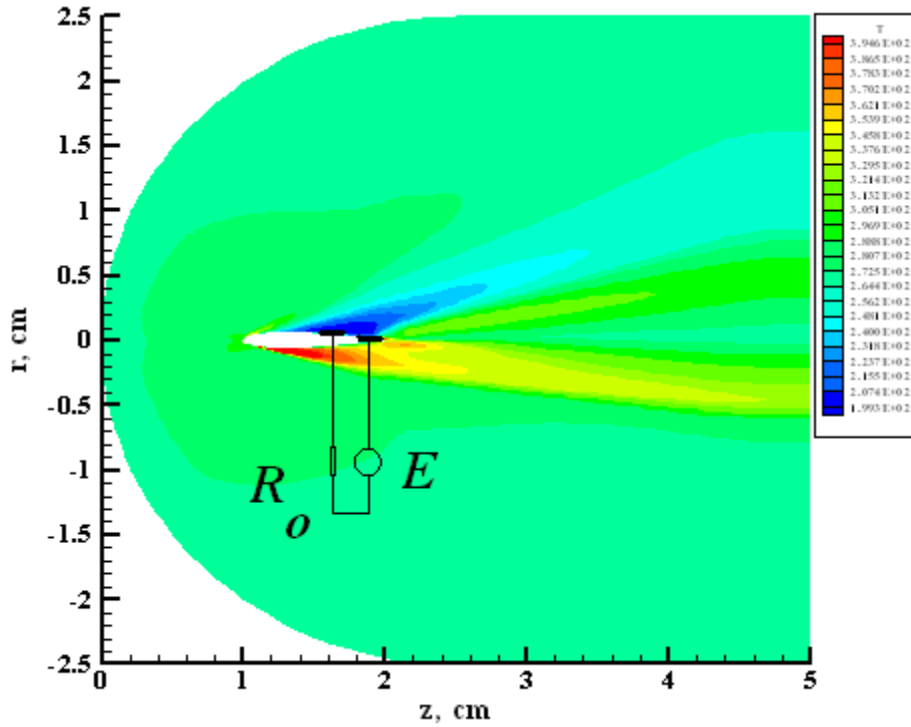


Figure 9.  Sketch of the Glow Discharge on Airfoil
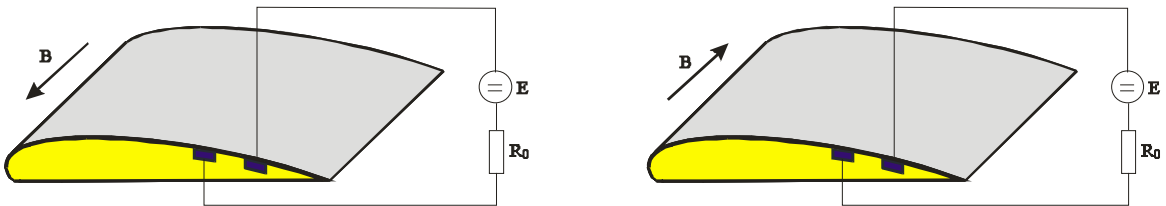


Figure 10.  Electrode Configuration and Magnetic Field Polarity

20

The governing equations of the magneto-aerodynamic interaction can be given as:

$$\frac{\partial \rho}{\partial t} + \mathrm{div}\left(\rho \mathbf{V}\right) = 0 \,, \tag{63}$$

$$\frac{\partial \rho u}{\partial t} + \mathrm{div}\left(\rho u \mathbf{V}\right) = -\frac{\partial p}{\partial x} - \frac{2}{3}\frac{\partial}{\partial x}\left(\mu \,\mathrm{div}\mathbf{V}\right) + \frac{\partial}{\partial y}\left[\mu\left(\frac{\partial u}{\partial y} + \frac{\partial v}{\partial x}\right)\right] + 2\frac{\partial}{\partial x}\left(\mu \frac{\partial u}{\partial x}\right)\,, \tag{64}$$

$$\frac{\partial \rho v}{\partial t} + \mathrm{div}\left(\rho v \mathbf{V}\right) = -\frac{\partial p}{\partial y} - \frac{2}{3}\frac{\partial}{\partial y}\left(\mu \,\mathrm{div}\mathbf{V}\right) + \frac{\partial}{\partial x}\left[\mu\left(\frac{\partial u}{\partial y} + \frac{\partial v}{\partial x}\right)\right] + 2\frac{\partial}{\partial y}\left(\mu \frac{\partial v}{\partial y}\right)\,, \tag{65}$$

$$\rho c_p \frac{\partial T}{\partial t} + \rho c_p \mathbf{V}\,\mathrm{grad}T + p\,\mathrm{div}\mathbf{V} = \mathrm{div}\left(\lambda\,\mathrm{grad}T\right) + Q_\Sigma \,, \tag{66}$$

$$\frac{\partial n}{\partial t} + \mathrm{div}\left(n\mathbf{V}\right) = \mathrm{div}\left(D_a \mathrm{grad}n\right) + n_{\;i}\left(\frac{E}{N}\right) - \beta n^2 \,, \tag{67}$$

and
$$\mathrm{div}\left(n\mu_e \mathrm{grad}\varphi - D_e \mathrm{grad}n\right) = 0 \,, \tag{68}$$

where $x$, $y$ are the Cartesian coordinates, $\mathbf{V} = (u,v)$ is the velocity and its components on the Cartesian coordinates, $\rho, p$ are the density and pressure, $\mu$ is the viscosity coefficient, $c_p$ is the heat capacity at constant pressure, $T$ is the temperature, $\lambda$ is the heat conduction coefficient, $n$ is the volume concentration of charged particles, $D_a$ is the ambipolar diffusion coefficient, $v_i$ is the coefficient of electron-neutral impact ionization, and $\varphi$ is the electric potential which is connected to the intensity of the electric field by the following relation, $\mathbf{E} = -\mathrm{grad}\varphi$.

The boundary conditions for the investigated problem are straightforward. For the aerodynamic variables, the velocity components approach the freestream value at the far field and vanish at the airfoil surface. The temperature and density of the fluid medium are set to the surface value at the airfoil and attain the asymptote at the far field. The pressure, however, must satisfy the vanishing gradient condition at the airfoil surface. For the electromagnetic variables, the zero gradient charged particle condition is applied together with a specified electrical potential value on the cathode. On the dielectric surface the charge particle density must be zero and the outward normal gradient of the electrical field potential is set to zero.

The governing equations cast in flux vector form become:

$$\frac{\partial \mathbf{f}}{\partial t} + \frac{\partial \mathbf{E}}{\partial \xi} + \frac{\partial \mathbf{F}}{\partial \eta} = \frac{\partial \mathbf{E}_v}{\partial \xi} + \frac{\partial \mathbf{F}_v}{\partial \eta} + \frac{\partial}{\partial \xi}\left(v^{(\xi)}\frac{\partial \mathbf{f}}{\partial \xi}\right) + \frac{\partial}{\partial \eta}\left(v^{(\eta)}\frac{\partial \mathbf{f}}{\partial \eta}\right) + \mathbf{\Phi} \tag{69}$$

or

$$\frac{\partial \mathbf{f}}{\partial t} + \frac{\partial U\mathbf{f}}{\partial \xi} + \frac{\partial \mathbf{E}_p}{\partial \xi} + \frac{\partial V\mathbf{f}}{\partial \eta} + \frac{\partial \mathbf{F}_p}{\partial \eta} = \frac{\partial \mathbf{E}_v}{\partial \xi} + \frac{\partial \mathbf{F}_v}{\partial \eta} + \frac{\partial}{\partial \xi}\left(v^{(\xi)}\frac{\partial \mathbf{f}}{\partial \xi}\right) + \frac{\partial}{\partial \eta}\left(v^{(\eta)}\frac{\partial \mathbf{f}}{\partial \eta}\right) + \mathbf{\Phi} \tag{70}$$

21

where

$$\mathbf{f} = \frac{1}{J}\begin{bmatrix} \rho \\ \rho u \\ \rho v \end{bmatrix}, \qquad \mathbf{E}_p = \frac{1}{J}\begin{bmatrix} 0 \\ \xi_x p \\ \xi_y p \end{bmatrix}, \qquad \mathbf{F}_p = \frac{1}{J}\begin{bmatrix} 0 \\ \eta_x p \\ \eta_y p \end{bmatrix}, \tag{71}$$

The coefficients of the artificial dissipation, $v(\varepsilon)$ and $v(\eta)$, can be found in Edwards and Liou (1998).

The numerical procedure adopted is a version of the MUSCL approximation with artificial dissipation for possible shock wave resolution (Edwards and Liou, 1998). The general MUSCL approximation can be written in the following form:

$$U_R = U_{j+1} - \frac{1}{4}\left[(1-\kappa)\nabla_1 + (1+\kappa)\nabla_2\right]_{j+1} \tag{72}$$

$$(\Delta_2)_j = \min \bmod\left[(U_{j+1} - U_j); \beta(U_j - U_{j-1})\right],$$
$$(\Delta_1)_j = \min \bmod\left[(U_j - U_{j-1}); \beta(U_{j+1} - U_j)\right], \tag{73}$$

$$\min \bmod (x, y) = \text{sign}(x) \cdot \max\left\{0, \min\left[x \cdot \text{sign}(y); y \cdot \text{sign}(x)\right]\right\} \tag{74}$$

and

$$1 \le \beta \le \frac{3-\kappa}{1-\kappa}, \quad \kappa = \frac{1}{3}.$$

The Kolgan MUSCL approximation has also been used for the present computation:

$$U_L = U_j + \frac{1}{2}\min \bmod\left(U_j - U_{j-1}; U_{j+1} - U_j\right) \tag{75}$$

$$U_R = U_{j+1} - \frac{1}{2}\min \bmod\left(U_{j+1} - U_j; U_{j+2} - U_{j+1}\right), \tag{76}$$

and

$$\min \bmod (a,b) = \begin{cases} a, & \text{at } (ab) > 0, \quad |a| < |b|, \\ b, & \text{at } (ab) > 0, \quad |a| \ge |b|, \\ 0, & \text{at } (ab) < 0. \end{cases} \tag{77}$$

Similarly, approximations for $a_{ij}$ were also used for the present calculations

$$a^{(1)}_{i,j+1/2} = \sqrt{\gamma \frac{p_{i,j+1/2}}{\rho_{i,j+1/2}}}, \tag{78}$$

where

$$p_{i,j+1/2} = \frac{1}{2}\left(p_{i,j} + p_{i,j+1}\right), \quad \rho_{i,j+1/2} = \frac{1}{2}\left(\rho_{i,j} + \rho_{i,j+1}\right), \text{ and } a^{(2)}_{i,j+1/2} = \frac{1}{2}\left(a_{i,j} + a_{i,j+1}\right). \tag{79}$$

In Figure 11, the pressure contour around the NACA-0012 airfoil at a free-stream Mach number of 0.2, a DCD electrical field intensity of 700 volts, and a Joule heating parameter of 0.2 is depicted. The surface plasma is seen to exert a significant perturbation to the pressure field around the lifting device. The pressure rise over the electrodes extends upstream to reach the stagnation point of the airfoil. However, the effect is much more pronounced at the trailing edge region of the airfoil and its wake region far downstream. It should also be pointed out that the energy input to the surface plasma is truly small, less than 60 watts.
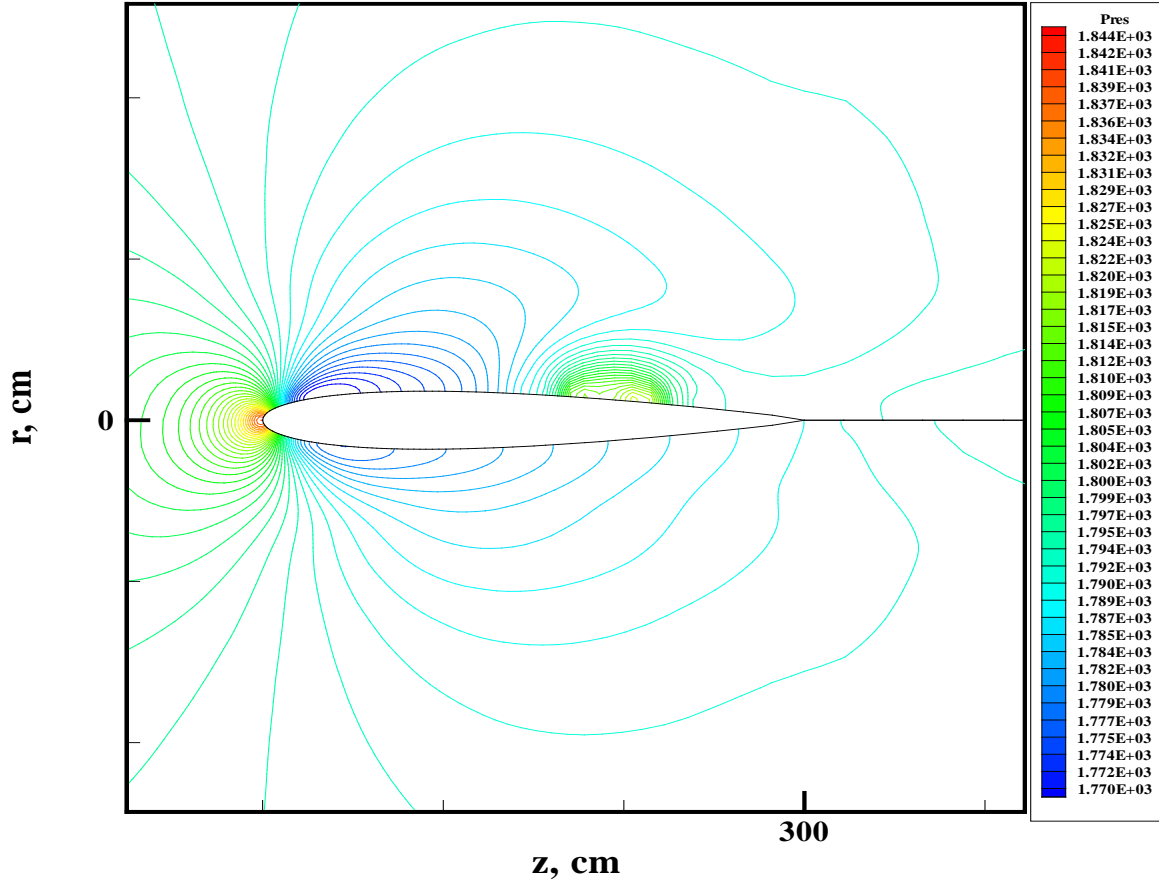


Figure 11. Pressure Contours for NACA-0012 Airfoil $M = 0.2$ and Re $= 2500$; DCD with $E = 700$ V, $\eta = 0.2$

The local perturbation by the electromagnetic force to the flow field is strongly contrasted by comparing the calculated pressure coefficient distributions with and without the surface plasma discharge. This fact is made obvious in Figure 12.

The temperature contours of the NACA-0012 airfoil at a simulated Mach number of 2.0 and an angle of attack of 10 degrees are presented in Figure 13. The surface plasma is sustained by an electrical field intensity of 700 V. The volumetric Joule heating provides an extensive heat source over the airfoil surface and produces a profound effect to the flow field structure.

For small amounts of energy input, the concentration of charged particles is mostly clustered over the electrodes (See Figure 14). The level of electron or ion concentration is on the order of magnitude of $10^{10}$ per cubic centimeter and the degree of ionization is merely $10^{-6}$. However, the impact by the surface plasma to the flow field around the NACA-0012 airfoil is profound.

23
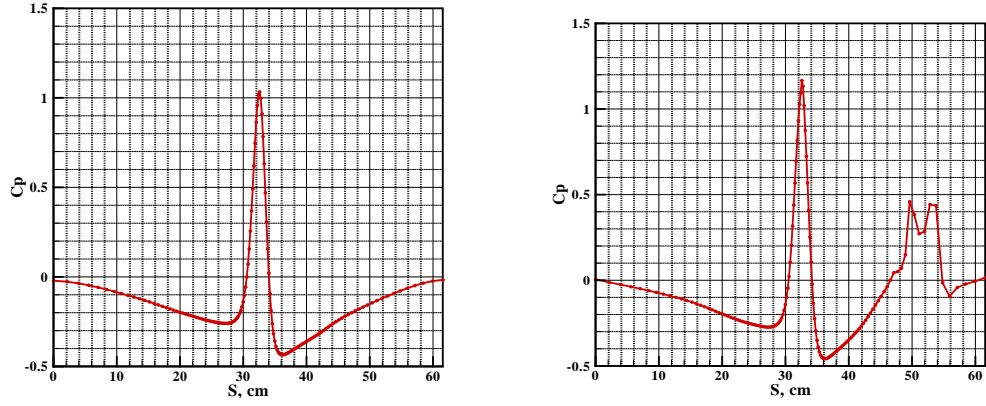
Figure 12. Comparison of Pressure Coefficients with/without Surface Plasma Discharge
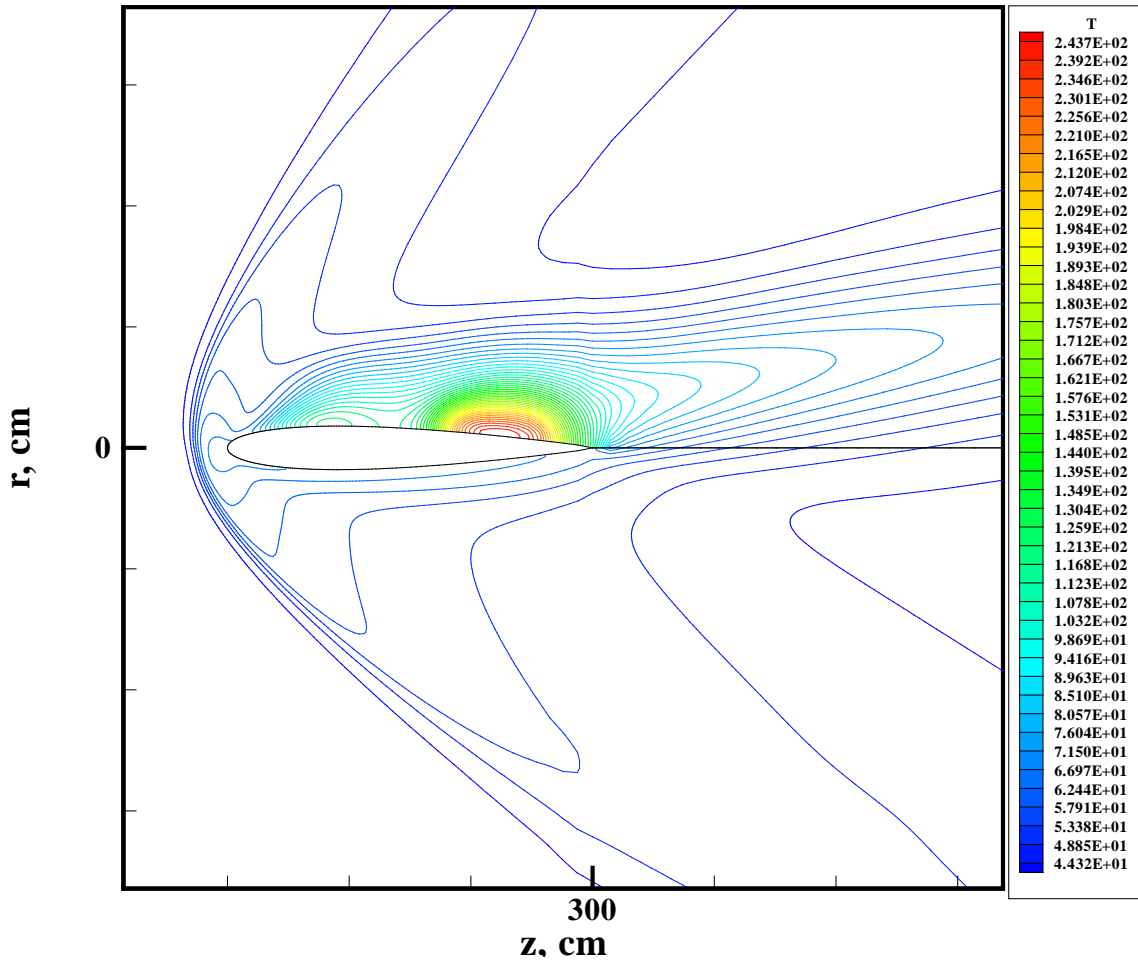


Figure 13. Temperature Contours of NACA-0012 at $M$=2 and Re = 1000, $\alpha$= 10$^o$, and E=700 V

### 3.1.6  Summary

Drift diffusion modeling of direct current discharges in an electro-negative gas with an external magnetic field has been developed and numerically studied. This model is realized in a two-dimensional parallel plate electrode configuration. Near-electrode layers of charged volumes are taken into account in this model. The quasi-neutral approximation of the model is developed and presented in this section of this report. A numerical study was performed for air at a pressures of 5 to 10 torr and for a power supply EMF of 2 kV. Induction of an external magnetic field was varied between the limits of $B = \pm 0.05$ T.
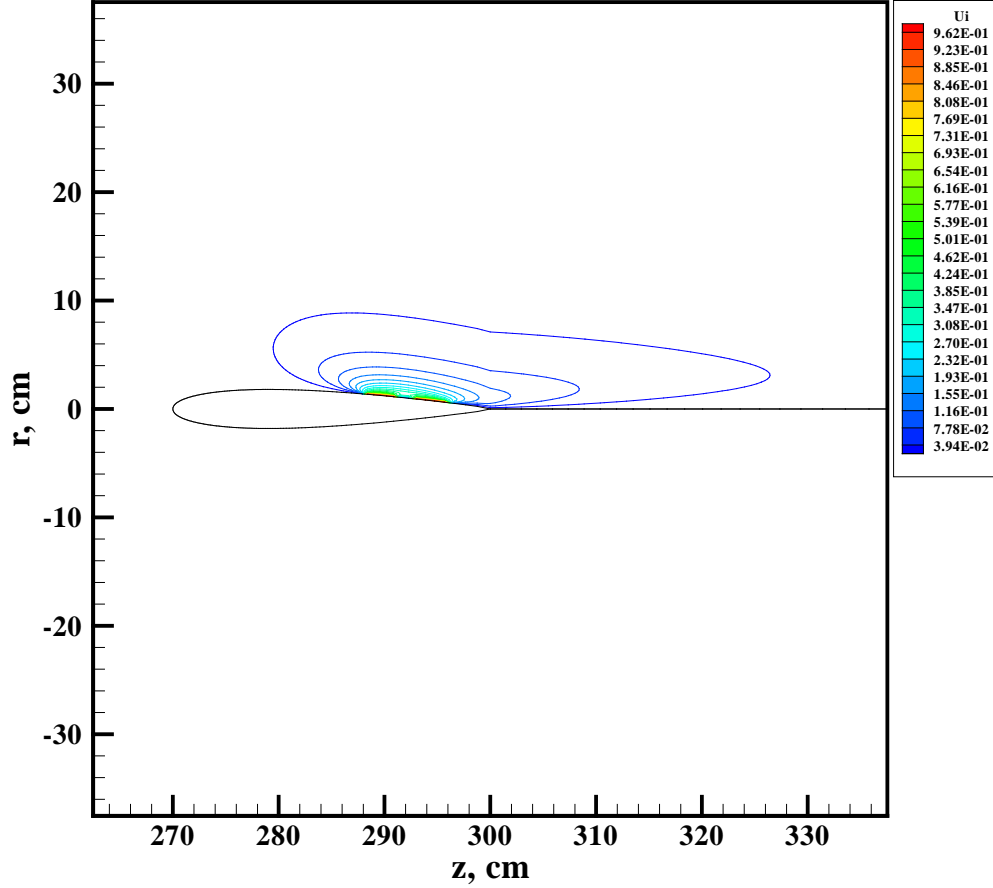
Figure 14.  Concentration of Charge Particles, $10^{10}$ cm$^{-3}$, for NACA-0012 at $M=2$ and Re = 1000, $\alpha = 10^{o}$, and E=700 V

The model for a quasi-neutral plasma in an external magnetic field has also been developed. It is shown that charge particle flux in the quasi-neutral approximation with an external magnetic field can be written in the form $\Gamma = -\mu_e^* D_a \mathrm{grad}\, n$, where $\mu_e^*$ is the coefficient taking into account magnetic fields. It is also shown, that up to a magnetic field of 0.2 T one can neglect magnetic field effects in the calculation of the ambipolar diffusion flux.

A multi-block, finite volume code for solving the model Poisson equation has been accomplished. The code can use the Gauss-Seidel, the SOR, and the ADI relaxation schemes. Numerical experiments have demonstrated that the ADI scheme is superior, in terms of convergence rate, with respect to the Gauss-Seidel and the SOR schemes. If rectangular cells are

25

used, the ADI scheme converges exceptionally fast in the presence of a discontinuous boundary condition between electrodes and dielectric surfaces.

A strong grid refinement seems to be necessary where discontinuous boundary conditions of the type electrode/dielectric wall are present. This fact may present a problem in practical applications, where the electrode region is small with respect to the overall length scale of the problem. A possible solution could be to use embedded grid refinement coupled with multi-grid relaxations in the electrode regions. This will allow for a relatively uniform grid refinement where it is necessary.

Physical and computational fluid dynamic models of localized surface gas discharges in subsonic and supersonic flows around a NACA-0012 airfoil are numerically studied. The model is based on coupled momentum equations, energy conservation equation, and electrodynamic equations for a gas-discharge, quasi-neutral plasma in curvilinear coordinates. An external electric circuit with electromotive force produced by a power supply and ohmic resistance, as well as an external magnetic field, have been taken into account. The electromagnetic forces have shown a profound impact on the flow field structure around a lifting device.

## 3.2   Model Development for Two-Dimensional Flow in a Channel

### 3.2.1   Introduction

Recent analyses of the potential application of a gas discharge plasma and magneto-aerodynamic technology in applied aerodynamic research has shown that the magneto-aerodynamic actuator has promise (Shang, 2001). From the realistic point of view, the prospects of global modification of the flow field around aircraft and inside energetic devices like scramjets are remote. But the opportunity of the local modification of weakly ionized gas flows has already been shown in experimental and computational studies (See Element 1 and Shang, 2001; Shang et al. 2002; Shang, 2002a; George et al., 2002; Poggie and Gaitonde, 2002; Corke et al., 2002). Therefore, significant effort needs to be devoted to theoretical and numerical simulation models of the interaction of weakly ionized gas flows with external electric and magnetic fields. The efficiency of the impulse and energy transfer from the charge particles to the neutral components of the gas flow also needs to be investigated (Candler and Kelly, 1999; Josyula, 2002; Wegener and Buzyna, 1969). Supersonic weakly ionized gas flows in curvilinear channels are considered in this section. These conditions closely resemble the experimental conditions at the AFRL/RB hypersonic MHD channel.

Physical and computational fluid dynamic models of DCD's in supersonic flows in curvilinear and planar channels with external magnetic fields are presented. It is assumed that the DCD exists in two possible configurations. The first configuration is a DCD between a sectionalized cathode on the bottom surface of the channel and solid anode on the top surface of the channel (Figure 15a). This configuration of the DCD was numerically studied in Surzhikov and Shang (2003c). A localized bump on the bottom surface of the channel was taken into account. The second configuration of the DCD has the electrodes, both cathode and anode, on the same surface (Figure 15b). This model allows one to take into account any number of such coupled sections of electrodes.
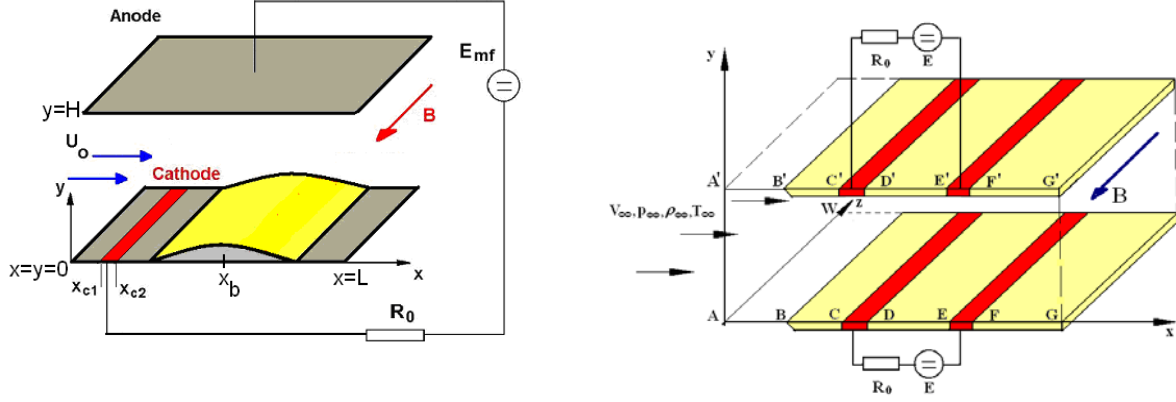
**Figure 15. Schematic of Curvilinear (a) and Plane (b) Gas Discharge Channels**

Numerical simulation results for weakly ionized nitrogen flows at a Mach number of $M_0 = 4 - 6$ inside the planar, two-dimensional channel with and without a magnetic field are presented. It is shown by numerical simulations that a glow discharge and transverse magnetic field can be adopted as a control mechanism in different aero-applications.

### 3.2.2 Mathematical Model

The physical statement of the problem includes consideration of a viscous and heat conducting weakly ionized gas flow in a curvilinear channel with a DCD and transverse external magnetic field. The continuous glow discharge with electromotive force (EMF) of $E = 300$ volts is applied between the sectionalized cathode, which is located before a 10% bump on the bottom surface of the channel (Figure 15a), and a continuous anode on the top surface of the channel.

The general objective of the problem under consideration is a self-consistent solution of the gas dynamic and electrodynamic equations. These equations are then used to analyze the effect of a glow discharge and external magnetic field on the pressure and temperature distributions on the boundary surfaces of the channel.

#### 3.2.2.1 Governing Equations

The system of governing equations includes the following:

$$\frac{\partial \rho}{\partial t} + \operatorname{div}(\rho \mathbf{V}) = 0 \tag{80}$$

$$\frac{\partial \rho u}{\partial t} + \operatorname{div}(\rho u \mathbf{V}) = -\frac{\partial p}{\partial x} - \frac{2}{3}\frac{\partial}{\partial x}(\mu \operatorname{div}\mathbf{V}) + \frac{\partial}{\partial y}\left[\mu\left(\frac{\partial u}{\partial y} + \frac{\partial v}{\partial x}\right)\right] + 2\frac{\partial}{\partial x}\left(\mu \frac{\partial u}{\partial x}\right) \tag{81}$$

$$\frac{\partial \rho v}{\partial t} + \operatorname{div}(\rho v \mathbf{V}) = -\frac{\partial p}{\partial y} - \frac{2}{3}\frac{\partial}{\partial y}(\mu \operatorname{div}\mathbf{V}) + \frac{\partial}{\partial x}\left[\mu\left(\frac{\partial u}{\partial y} + \frac{\partial v}{\partial x}\right)\right] + 2\frac{\partial}{\partial y}\left(\mu \frac{\partial v}{\partial y}\right) \tag{82}$$

$$\rho c_p \frac{\partial T}{\partial t} + \rho c_p \mathbf{V}\operatorname{grad}T - \mathbf{V}\operatorname{grad}(p) = \operatorname{div}(\lambda \operatorname{grad}T) + q \tag{83}$$

$$\frac{\partial n}{\partial t} + \text{div}(n\mathbf{V}) = \text{div}(D_a \text{grad} n) + n\nu_i\left(\frac{E}{N}\right) - \beta n^2 \tag{84}$$

and
$$\text{div}(n\mu_e \text{grad}\varphi - D_a \text{grad} n) = 0, \tag{85}$$

where $x$, $y$ are the Cartesian coordinates; $\mathbf{V} = (u,v)$ is the velocity and its projections on the Cartesian axis; $\rho$, $p$ are the density and pressure; $\mu$ is the viscosity coefficient; $c_p$ is the specific heat capacity at constant pressure; $T$ is the temperature; $\lambda$ is the heat conduction coefficient; $n$ is the volume concentration of charged particles (the problem is considered in the quasi-neutral approach, therefore $n = n_i = n_e$, where $n_i, n_e$ are the concentrations of ions and electrons); $D_a, D_e$ are the ambipolar and electron diffusion coefficients; $\nu_i$ is the coefficient of electron-neutral impact ionization; $\mu_e$ is the electron mobility, $\beta$ is the coefficient of electron-ion recombination; $\varphi$ is the electric potential, which is connected to the intensity of the electric field by the following relation $\mathbf{E} = -\text{grad}\varphi$; $N$ is the concentration of neutral particles; $E = |\mathbf{E}|$; and $q$ is the heat release power of the discharge.

### 3.2.2.2 Boundary and Initial Conditions

Boundary conditions for equations (80) through (85) are (see Figure 15):

$$x = 0: \quad \begin{array}{l} u = u_0, \quad v = 0, \quad T = T_0, \\ \\ p = p_0, \quad \rho = \rho_0, \quad n = n_0, \quad \dfrac{\partial \varphi}{\partial x} = 0 \end{array} \tag{86}$$

$$x = L: \quad \frac{\partial u}{\partial x} = \frac{\partial v}{\partial x} = \frac{\partial T}{\partial x} = \frac{\partial n}{\partial x} = \frac{\partial \rho}{\partial x} = \frac{\partial \varphi}{\partial x} = 0 \tag{87}$$

$$y = 0: \quad u = v = 0, \quad T = T_w, \quad \frac{\partial p}{\partial n_y} = 0 \tag{88}$$

$x_{c,1} \le x \le x_{c,2}$ (cathode section):

$$\frac{\partial n}{\partial y} = 0, \quad \varphi = V_c \tag{89}$$

$x < x_{c,1}, \quad x > x_{c,2}$ (dielectric surface):

$$n = 10^{-5} n_0, \quad \frac{\partial \varphi}{\partial n_y} = 0 \; ; \tag{90}$$

$$y = H: \quad u = v = 0, \quad T = T_w, \quad \frac{\partial p}{\partial y} = 0; \tag{91}$$

and
$$\frac{\partial n}{\partial y} = 0, \quad \varphi = \text{Emf}. \tag{92}$$

Here $n_0$ is the typical concentration of charged particles in a positive column ($n_0 \sim 10^{10}\,\text{cm}^{-3}$), $V_c$ is the cathode potential relative to a zero level (ground), and $n_y$ is the local normal to the bottom surface.

It is necessary to formulate an equation for an external electric circuit,

$$IR_0 + V_c = EMF, \tag{93}$$

from which a cathode voltage drop can be determined. Here $R_0$ is the ballast resistance, $I$ is the total current in the circuit, which can be calculated as

$$I = \int_0^L (\mathbf{jn})_c \, dx = \int_0^L (\mathbf{jn})_a \, dx, \tag{94}$$

where $\mathbf{n}$ is the unit vector normal to the cathode (c) and anode (a) surface, and $\mathbf{j}$ is the current density.

### 3.2.2.3 Constitutive Relationships

The constitutive relationships for the gas-dynamic equations (for $N_2$) are:

$$\mu_m = 2.6710^{-5}\sqrt{M_A T}\,\frac{1}{\sigma^2 \Omega^{(2,2)*}} \text{ is the viscosity coefficient},$$

$$\sigma = 3.68\,\mathring{A}, \quad \Omega^{(2,2)*} = 1.157\left(T^*\right)^{-0.1472},$$

and
$$T^* = \frac{T}{\left(\varepsilon/k\right)}, \quad \left(\varepsilon/k\right) = 71.4,$$

where
$$\lambda = 8.334 \times 10^{-4}\sqrt{\frac{T}{M_A}}\,\frac{\left(0.115 + 0.354\dfrac{c_p}{R_0}M_A\right)}{\sigma^2 \Omega^{(2,2)*}} \tag{95}$$

is the coefficient of molecular heat conductivity, $c_p = 8.317\dfrac{7}{2}\dfrac{1}{M_A}$, $\rho = \dfrac{p}{T}\dfrac{M_A}{R_0}$, $M_A = 28$

g/mole, and $R_0 = 8.314 \times 10^7$ erg/(mole K).

The constitutive relationships for the electro-dynamical equations are:

$$\nu_i = \left(\frac{\alpha}{p^*}\right)p^* E\mu_e\left(p^*\right), \quad \left(\frac{\alpha}{p^*}\right) = A\exp\left[-\frac{B}{\left(E/p^*\right)}\right], \tag{96}$$

$$p^* = p\frac{293}{T}, \quad D_e = \mu_e\left(p^*\right)T_e, \quad D_+ = \mu_+\left(p^*\right)T_+, \tag{97}$$

$$\mu_e\left(p^*\right)=4.2\times10^5\frac{1}{p^*}, \quad \mu_+\left(p^*\right)=1450\frac{1}{p^*}, \tag{98}$$

and
$$\beta=2\times10^{-7} \text{ cm}^3\big/\text{s}, \quad T_e=11610 \text{ K}, \quad A=12\,(\text{cm}\cdot\text{torr})^{-1}, \tag{99}$$

where $B=342$ volt/(cm·torr), $N=0.954\times10^{19}\left(p/T\right)$ is the concentration of the neutral particles, and $\mu_+$ is the mobility of the ions.

The constitutive relationships also provide the calculation of the heat release in a gas due to Joule heating,

$$q=\eta\left(\mathbf{j}\cdot\mathbf{E}\right)=1.6\times10^{-19}\eta\left[nE^2\left(\mu_++\mu_e\right)+\left(D_e-D_+\right)\mathbf{E}\,\text{grad}n\right], \tag{100}$$

and the effect of a magnetic field on the gasdynamic structure, $F_B=\chi\left(\mathbf{jB}\right)$, where $\eta$ is the efficiency of heating ($\eta\sim0.1\div0.3$) and $\chi$ is the efficiency of impulse transfer ($\chi=0.1\div1.0$).

### 3.2.3 Numerical Procedures

### 3.2.3.1 Gas Dynamic Part of the Problem

The Navier-Stokes equations in a curvilinear coordinate system, $\xi=\xi\left(x,y\right)$ and $\eta=\eta\left(x,y\right)$, are formulated as

$$\frac{\partial\mathbf{f}}{\partial t}+\frac{\partial\mathbf{E}}{\partial\xi}+\frac{\partial\mathbf{F}}{\partial\eta}=\frac{\partial\mathbf{E}_v}{\partial\xi}+\frac{\partial\mathbf{E}_v}{\partial\eta}+\mathbf{\Phi}, \tag{101}$$

where
$$\mathbf{f}=\frac{1}{J}\begin{bmatrix}\rho\\\rho u\\\rho v\end{bmatrix}, \tag{102}$$

$$\mathbf{E}=\frac{1}{J}\begin{bmatrix}\rho U\\\rho uU+\xi_x p\\\rho vU+\xi_y p\end{bmatrix}, \tag{103}$$

$$\mathbf{F}=\frac{1}{J}\begin{bmatrix}\rho V\\\rho uV+\eta_x p\\\rho vV+\eta_y p\end{bmatrix}, \tag{104}$$

$$\mathbf{E}_v=\frac{1}{J\cdot\text{Re}}\begin{bmatrix}0\\\xi_x\tau_{xx}+\xi_y\tau_{xy}\\\xi_x\tau_{xy}+\xi_y\tau_{yy}\end{bmatrix}, \tag{105}$$

$$\mathbf{F}_v = \frac{1}{J \cdot \mathrm{Re}} \begin{bmatrix} 0 \\ \eta_x \tau_{xx} + \eta_y \tau_{xy} \\ \eta_x \tau_{xy} + \eta_y \tau_{yy} \end{bmatrix}, \tag{106}$$

$$\boldsymbol{\Phi} = \alpha \begin{bmatrix} -\dfrac{\rho v}{yJ} + f_{m,x} \\[2ex] \dfrac{\tau_{xy}}{yJ\,\mathrm{Re}} - \dfrac{\rho u v}{yJ} + f_{m,y} \\[2ex] \dfrac{2\mu}{\mathrm{Re}}\left[\dfrac{\partial}{\partial \xi}\left(\dfrac{\xi_y v}{yJ}\right) + \dfrac{\partial}{\partial \eta}\left(\dfrac{\eta_y v}{yJ}\right)\right] - \dfrac{\rho v^2}{yJ} \end{bmatrix}, \tag{107}$$

$$U = \xi_x u + \xi_y v, \qquad V = \eta_x u + \eta_y v,$$

$$\tau_{xx} = J\mu\left\{2\left[\left(\frac{\xi_x u}{J}\right)_\xi + \left(\frac{\eta_x u}{J}\right)_\eta\right] - \frac{2}{3}\left[\left(\frac{U}{J}\right)_\xi + \left(\frac{V}{J}\right)_\eta + \alpha\frac{v}{yJ}\right]\right\},$$

$$\tau_{xy} = J\mu\left[\left(\frac{U^*}{J}\right)_\xi + \left(\frac{V^*}{J}\right)_\eta\right],$$

and

$$\tau_{yy} = J\mu\left\{2\left[\left(\frac{\xi_y v}{J}\right)_\xi + \left(\frac{\eta_y v}{J}\right)_\eta\right] - \frac{2}{3}\left[\left(\frac{U}{J}\right)_\xi + \left(\frac{V}{J}\right)_\eta + \alpha\frac{v}{yJ}\right]\right\}.$$

The quantities $f_{m,x}$, $f_{m,y}$ are the components of the magnetic force (formulas for calculation of these functions will be presented later); $U^* = \xi_y u + \xi_x v$, $V^* = \eta_y u + \eta_x v$; $\alpha = 0$ for the plane case, $\alpha = 1$ for axisymmetric case; $\xi = \xi(x, y)$, $\eta = \eta(x, y)$ are the suitable curvilinear coordinates; $\tau_{xx}, \tau_{xy}, \tau_{yy}$ are the viscous stress tensor components; $\mathrm{Re} = \rho_0 u_0 H / \mu_0$ is the Reynolds number; $\xi_x = \partial\xi/\partial x$, $\xi_y = \partial\xi/\partial y$, $\eta_x = \partial\eta/\partial x$, $\eta_y = \partial\eta/\partial y$; and $J = \xi_x \eta_y - \xi_y \eta_x$ is the Jacobian of the grid transformation.

The energy conservation equation is formulated relative to temperature, i.e. in the non-conservative form:

$$\rho\frac{c_p}{J}\frac{\partial T}{\partial t} + \rho c_p\frac{U}{J}\frac{\partial T}{\partial \xi} + \rho c_p\frac{V}{J}\frac{\partial T}{\partial \eta} = \frac{1}{\mathrm{Re}\,\mathrm{Pr}}\frac{\partial}{\partial \xi}\left[\lambda\frac{(\xi_x^2 + \xi_y^2)}{J}\frac{\partial T}{\partial \xi}\right] + \frac{1}{\mathrm{Re}\,\mathrm{Pr}}\frac{\partial}{\partial \eta}\left[\lambda\frac{(\eta_x^2 + \eta_y^2)}{J}\frac{\partial T}{\partial \eta}\right] +$$

$$+\frac{1}{\mathrm{Re}\,\mathrm{Pr}}\frac{\partial}{\partial\xi}\left[\lambda\frac{\left(\xi_x\eta_x+\xi_y\eta_y\right)}{J}\frac{\partial T}{\partial\eta}\right]+\frac{1}{\mathrm{Re}\,\mathrm{Pr}}\frac{\partial}{\partial\eta}\left[\lambda\frac{\left(\xi_x\eta_x+\xi_y\eta_y\right)}{J}\frac{\partial T}{\partial\xi}\right]+$$

$$+\alpha\frac{1}{\mathrm{Re}\,\mathrm{Pr}}\frac{\lambda}{yJ}\left(\xi_y\frac{\partial T}{\partial\xi}+\eta_y\frac{\partial T}{\partial\eta}\right)+\left(\frac{Q_\Sigma}{J}\right)\frac{L_0}{\rho_0 u_0 c_{p_0} T_0}, \qquad (108)$$

where $\mathrm{Pr}=\mu_0 c_{p_0}/\lambda_0$ is the Prandtl number. Index "0" is used here for functions and parameters in the undisturbed flow.

Function $Q_\Sigma$ on the right-hand side of equation (108) contains a source term describing a heat deposit in the flow

$$\frac{Q_\Sigma}{J}=\frac{Q_{rad}}{J}+\frac{Q_p}{J}+\frac{Q_\mu}{J}, \qquad (109)$$

where $Q_{rad}$ is the heat release power due to thermal radiation processes and/or Joule heating, $Q_p$ is the heat release power due to compressibility of the gas flow, and $Q_\mu$ is the heat release power due to viscous dissipation.

The last two terms are presented in the following form

$$\frac{Q_p}{J}=\left[U\left(\frac{p}{J}\right)_\xi+V\left(\frac{p}{J}\right)_\eta\right] \qquad (110)$$

and

$$\frac{Q_\mu}{J}=\mu J\left\{2\left[\left(\frac{\xi_x u}{J}\right)_\xi+\left(\frac{\eta_x u}{J}\right)_\eta\right]^2+2\left[\left(\frac{\xi_y v}{J}\right)_\xi+\left(\frac{\eta_y v}{J}\right)_\eta\right]^2+\right.$$

$$\left.+\left[\left(\frac{U^*}{J}\right)_\xi+\left(\frac{V^*}{J}\right)_\eta\right]^2-\frac{2}{3}\left[\left(\frac{U}{J}\right)_\xi+\left(\frac{V}{J}\right)_\eta+\alpha\frac{v}{yJ}\right]^2\right\}\cdot\frac{1}{\mathrm{Re}}+2\alpha\mu J\left(\frac{v}{yJ}\right)^2\frac{1}{\mathrm{Re}}. \qquad (111)$$

Radiation heat transfer processes are omitted in this work. Therefore the term $Q_{rad}$ includes only the Joule heating

$$Q_{\mathrm{Joule}}=\eta\left(\mathbf{j}\cdot\mathbf{E}\right)=\eta en\mu_e\left(\mathbf{E}\cdot\mathbf{E}\right), \qquad (112)$$

where $\eta$ is the part of the Joule dissipation which goes to heating of the gas (another part goes to the excitation of the vibrational molecular states). It is known from laser physics that for molecular nitrogen $\eta\sim 0.15\div 0.3$, $\mathbf{j}$ is the current density, $\mathbf{E}$ is the electric field intensity, and the electron charge is $e=1.6\times 10^{-19}$ Coulombs. Note that we have omitted the ambipolar diffusion part of the current density.

### 3.2.3.2  Electromagnetic Part of the Problem

The configuration of the external electric circuit and magnetic field is shown in Figures 15a and 15b (cases with the magnetic field direction inverted will also be considered).

As mentioned above, see equations (84) and (85), electrodynamic equations are formulated in the quasi-neutral drift-diffusion approach for the glow discharge plasma in a gas flow. These equations can be presented in the following form:

$$\frac{\partial \mathbf{f}_M}{\partial t} + \frac{\partial \mathbf{E}_M}{\partial \xi} + \frac{\partial \mathbf{F}_M}{\partial \eta} = \frac{\partial \mathbf{E}_{D,M}}{\partial \xi} + \frac{\partial \mathbf{F}_{D,M}}{\partial \eta} + \mathbf{Q}_M \qquad (113)$$

where

$$\mathbf{f}_M = \begin{bmatrix} n \\ \varphi \end{bmatrix}, \qquad (114)$$

$$\mathbf{E}_M = \begin{bmatrix} nU \\ J \\ 0 \end{bmatrix}, \qquad (115)$$

$$\mathbf{F}_M = \begin{bmatrix} nV \\ J \\ 0 \end{bmatrix}, \qquad (116)$$

$$\mathbf{E}_{D,M} = \begin{bmatrix} D_a \dfrac{\left(\xi_x^2 + \xi_y^2\right)}{J} \dfrac{\partial n}{\partial \xi} + D_a \dfrac{\left(\xi_x \eta_x + \xi_y \eta_y\right)}{J} \dfrac{\partial n}{\partial \eta} \\[2mm] n\mu_e \dfrac{\left(\xi_x^2 + \xi_y^2\right)}{J} \dfrac{\partial \varphi}{\partial \xi} + n\mu_e \dfrac{\left(\xi_x \eta_x + \xi_y \eta_y\right)}{J} \dfrac{\partial \varphi}{\partial \eta} \end{bmatrix}, \qquad (117)$$

$$\mathbf{F}_{D,M} = \begin{bmatrix} D_a \dfrac{\left(\eta_x^2 + \eta_y^2\right)}{J} \dfrac{\partial n}{\partial \eta} + D_a \dfrac{\left(\xi_x \eta_x + \xi_y \eta_y\right)}{J} \dfrac{\partial n}{\partial \xi} \\[2mm] n\mu_e \dfrac{\left(\eta_x^2 + \eta_y^2\right)}{J} \dfrac{\partial \varphi}{\partial \eta} + n\mu_e \dfrac{\left(\xi_x \eta_x + \xi_y \eta_y\right)}{J} \dfrac{\partial \varphi}{\partial \xi} \end{bmatrix}, \qquad (118)$$

$$\mathbf{Q}_M = \begin{bmatrix} n\nu_i - \beta n^2 + \alpha \dfrac{D_a}{yJ}\left( \xi_y \dfrac{\partial n}{\partial \xi} + \eta_y \dfrac{\partial n}{\partial \eta} \right) - \alpha \dfrac{n\upsilon}{yJ} \\[2mm] Q_{M,\varphi} \end{bmatrix}, \qquad (119)$$

and 
$$Q_{M,\varphi} = -D_a \frac{\left(\xi_x^2 + \xi_y^2\right)}{J} \frac{\partial n}{\partial \xi} - D_a \frac{\left(\xi_x \eta_x + \xi_y \eta_y\right)}{J} \frac{\partial n}{\partial \eta} -$$

$$-D_a \frac{\left(\eta_x^2 + \eta_y^2\right)}{J} \frac{\partial n}{\partial \eta} - D_a \frac{\left(\xi_x \eta_x + \xi_y \eta_y\right)}{J} \frac{\partial n}{\partial \xi} - \alpha \frac{D_a}{yJ} \left(\xi_y \frac{\partial n}{\partial \xi} + \eta_y \frac{\partial n}{\partial \eta}\right). \tag{120}$$

For calculation of the Joule heating and projections of the magnetic force $\mathbf{F}_M$ the following formulas are used:

$$Q_J = \eta e n \mu_e E^2 = \eta e n \mu_e \left(E_x^2 + E_y^2\right) = \eta e n \mu_e \left[\left(\frac{\partial \varphi}{\partial x}\right)^2 + \left(\frac{\partial \varphi}{\partial y}\right)^2\right], \tag{121}$$

$$\mathbf{F}_M = [\mathbf{j} \cdot \mathbf{B}] = \begin{vmatrix} \mathbf{e}_x & \mathbf{e}_y & \mathbf{e}_z \\ j_x & j_y & j_z \\ 0 & 0 & B \end{vmatrix} = \mathbf{e}_x \left(j_y B\right) - \mathbf{e}_y \left(j_x B\right), \tag{122}$$

$$f_{M,x} = j_y B = B n \mu_e \left[\frac{\partial}{\partial \xi}\left(\frac{\xi_y}{J}\varphi\right) + \frac{\partial}{\partial \eta}\left(\frac{\eta_y}{J}\varphi\right)\right], \tag{123}$$

and
$$f_{M,y} = -j_x B = -B n \mu_e \left[\frac{\partial}{\partial \xi}\left(\frac{\xi_y}{J}\varphi\right) + \frac{\partial}{\partial \eta}\left(\frac{\eta_y}{J}\varphi\right)\right], \tag{124}$$

where, as mentioned above, we omit components of the current density related to the ambipolar diffusion.

Dimensions, which are used in our computational code, are:

1) The Current density

$$j = e n \mu_e E, \frac{A}{cm^3}, \tag{125}$$

where $e = 1.6 \times 10^{-19}$ Coul, $[n] = \frac{1}{cm^3}$, $[\mu_e] = \frac{cm^2}{s \cdot Volt}$, $[E] = \frac{Volt}{cm}$.

2) The Joule heating

$$Q_J = \eta e n \mu_e E^2, \frac{W}{cm^3}. \tag{126}$$

3) The magnetic force

$$f_M \sim 10^5 \chi e n \mu_e EB, \frac{g}{cm \cdot s^2}, \tag{127}$$

where $[B] = T$.

34

### 3.2.3.3 Components of the Current Density and Intensity of the Electric Field Near to the Channel Surfaces

The boundary condition which is used for a curvilinear surface has the following form:

$$(\mathbf{n} \cdot \mathrm{grad}\psi) = 0, \tag{128}$$

where $\psi = \{\varphi, n\}$. This boundary condition may be rewritten in the form

$$\omega_x \frac{\partial \psi}{\partial x} + \omega_y \frac{\partial \psi}{\partial y} = 0, \tag{129}$$

where $\omega_x, \omega_y$ are the directional cosines' of a normal $\mathbf{n}$ to a surface. Then the general form of the boundary condition can be written in the following form:

$$\omega_x J \frac{\partial}{\partial \xi}\left(\frac{\xi_x}{J}\psi\right) + \omega_x J \frac{\partial}{\partial \eta}\left(\frac{\eta_x}{J}\psi\right) + \omega_y J \frac{\partial}{\partial \xi}\left(\frac{\xi_y}{J}\psi\right) + \omega_y J \frac{\partial}{\partial \eta}\left(\frac{\eta_y}{J}\psi\right) = 0. \tag{130}$$

It is possible to simplify this boundary condition in some cases. For example, for the cathode section and for the anode there is an obvious additional condition

$$\frac{\partial \psi}{\partial \xi} = 0.$$

Sometimes it is possible to use the approximation of a weakly curvilinear surface, $\omega_x \approx 0, \quad \omega_y \approx 1$.

### 3.2.4 Numerical Simulation Method

To solve the problem formulated above we developed a numerical simulation method which has the following two peculiar properties:

1) The energy conservation equation is formulated in non-conservative form.

2) Each computing stage (which corresponds to one time-step) is divided into two sub-stages. The first stage is the integration of the Navier-Stokes equations by the explicit method. The second stage is the integration of the equations of conservation energy and continuity of charged particles in an electric field using an implicit technique.
   Calculations were performed on a unique, non-homogeneous grid $\{\xi, \eta\}$.

### 3.2.4.1 Gas Dynamic Part of the Problem

At the gas-dynamic stage of the computation process the following system of equations are numerically integrated:

$$\frac{\partial \mathbf{f}_M}{\partial t} + \frac{\partial \mathbf{E}_M}{\partial \xi} + \frac{\partial \mathbf{F}_M}{\partial \eta} = \frac{\partial \mathbf{E}_v}{\partial \xi} + \frac{\partial \mathbf{F}_v}{\partial \eta} + \mathbf{\Phi} \tag{131}$$

or

35

$$\frac{\partial \mathbf{f}}{\partial t} + \frac{\partial U \mathbf{f}}{\partial \xi} + \frac{\partial \mathbf{E}_p}{\partial \xi} + \frac{\partial V \mathbf{f}}{\partial \eta} + \frac{\partial \mathbf{F}_p}{\partial \eta} = \frac{\partial \mathbf{E}_v}{\partial \xi} + \frac{\partial \mathbf{F}_v}{\partial \eta} + \mathbf{\Phi} \qquad (132)$$

where

$$\mathbf{f} = \frac{1}{J}\begin{bmatrix} \rho \\ \rho u \\ \rho v \end{bmatrix}, \quad \mathbf{E}_p = \frac{1}{J}\begin{bmatrix} 0 \\ \xi_x p \\ \xi_y p \end{bmatrix}, \quad \mathbf{F}_p = \frac{1}{J}\begin{bmatrix} 0 \\ \eta_x p \\ \eta_y p \end{bmatrix}. \qquad (133)$$

This system of gas-dynamic equations was solved by the van-Leer second order splitting method (van Leer, 1979).

### 3.2.4.2  Finite-Difference Scheme for Energy Conservation Equation

The energy conservation equation is integrated relative to a temperature that is in a non-conservative form. Several finite-difference schemes were created by the integro-interpolation method. An example of one of them is presented below.

Let us integrate the energy conservative equation in the following form

$$\frac{\rho c_p}{J}\frac{\partial T}{\partial t} + \frac{\rho c_p U}{J}\frac{\partial T}{\partial \xi} + \frac{\rho c_p V}{J}\frac{\partial T}{\partial \eta} = RHS \qquad (134)$$

for an elementary volume, which is shown in Figure 16. The volume of this elementary volume is
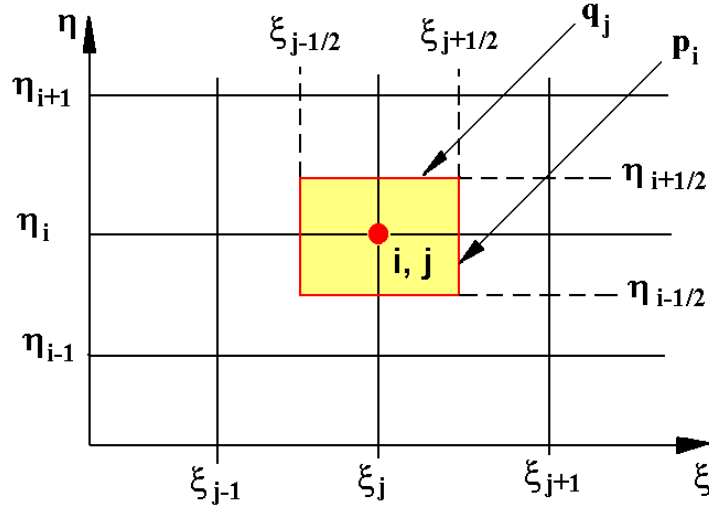


Figure 16.  Calculation Grid Elementary Volume

$$Vol_{i,j} = \int\limits_{\xi_{j-1/2}}^{\xi_{j+1/2}} d\xi \int\limits_{\eta_{j-1/2}}^{\eta_{j+1/2}} d\eta = \left(\xi_{j+1/2} - \xi_{j-1/2}\right)\left(\eta_{j+1/2} - \eta_{j-1/2}\right) = p_i q_j. \qquad (135)$$

Then, for example, the second term on the left-side of equation (134) becomes

$$I_\xi = \int\limits_{\xi_{j-1/2}}^{\xi_{j+1/2}} \int\limits_{\eta_{j-1/2}}^{\eta_{j+1/2}} \left\{ \frac{\rho c_p}{J} \frac{\partial T}{\partial \xi} \right\} d\xi d\eta =$$

$$= p_i \left[ \left( \frac{\rho c_p U T}{J} \right)_{i,j+1/2} - \left( \frac{\rho c_p U T}{J} \right)_{i,j-1/2} \right] - p_i T_{i,j} \int\limits_{\xi_{j-1/2}}^{\xi_{j+1/2}} \frac{\partial}{\partial \xi} \left( \frac{\rho c_p U}{J} \right) d\xi , \qquad (136)$$

or

$$I_\xi = p_i \left[ b_R^+ \left( \frac{\rho c_p}{J} T \right)_{i,j} + b_R^- \left( \frac{\rho c_p}{J} T \right)_{i,j+1} - b_L^+ \left( \frac{\rho c_p}{J} T \right)_{i,j-1} - b_L^- \left( \frac{\rho c_p}{J} T \right)_{i,j} \right] -$$

$$- p_i T_{i,j} \left[ b_R^+ \left( \frac{\rho c_p}{J} \right)_{i,j} + b_R^- \left( \frac{\rho c_p}{J} \right)_{i,j+1} - b_L^+ \left( \frac{\rho c_p}{J} \right)_{i,j-1} - b_L^- \left( \frac{\rho c_p}{J} \right)_{i,j} \right] =$$

$$= p_i \left\{ T_{i,j} \left[ b_L^+ \left( \frac{\rho c_p}{J} \right)_{i,j-1} - b_R^- \left( \frac{\rho c_p}{J} \right)_{i,j+1} \right] + T_{i,j+1} b_R^- \left( \frac{\rho c_p}{J} \right)_{i,j+1} - T_{i,j-1} b_L^+ \left( \frac{\rho c_p}{J} \right)_{i,j-1} \right\} , \qquad (137)$$

where

$$b_R^\pm = \frac{1}{2} \left( U_{i,j+1/2} \pm \left| U_{i,j+1/2} \right| \right), \; b_L^\pm = \frac{1}{2} \left( U_{i,j-1/2} \pm \left| U_{i,j-1/2} \right| \right).$$

Integration in the $\eta$-direction is carried out by analogy. The final five-point scheme has the following form:

$$A_{i,j} T_{i-1,j}^{n+1} + B_{i,j} T_{i+1,j}^{n+1} + A_{i,j}^* T_{i,j-1}^{n+1} + B_{i,j}^* T_{i,j+1}^{n+1} - C_{i,j} T_{i,j}^{n+1} + F_{i,j} = 0 , \qquad (138)$$

where

$$A_{i,j} = \frac{a_L^+ \left( \rho c_v / J \right)_{i-1,j}}{p_i} , \quad B_{i,j} = -\frac{a_R^- \left( \rho c_v / J \right)_{i+1,j}}{p_i} , \qquad (139)$$

$$A_{i,j}^* = \frac{b_L^+ \left( \rho c_v / J \right)_{i,j-1}}{q_j} , \quad B_{i,j}^* = -\frac{b_R^- \left( \rho c_v / J \right)_{i,j+1}}{q_j} , \qquad (140)$$

$$C_{i,j} = A_{i,j} + B_{i,j} + A_{i,j}^* + B_{i,j}^* + \left( \frac{\rho c_v}{J} \right)_{i,j} \frac{1}{\tau} , \qquad (141)$$

and

$$a_R^\pm = \frac{1}{2} \left( V_{i+1/2,j} \pm \left| V_{i+1/2,j} \right| \right), \; a_L^\pm = \frac{1}{2} \left( V_{i-1/2,j} \pm \left| V_{i-1/2,j} \right| \right),$$

where $\tau$ is the time-step, $I = 1,2\ldots,NI$, and $j=1,2\ldots NJ$.

The finite-difference scheme for the electrodynamic equations was created by analogy.

### 3.2.5 Results

The hypersonic flow of molecular nitrogen ($N_2$) in a flat channel is considered (Figure 15b). A gas stream with parameters $V_\infty, \rho_\infty, p_\infty, T_\infty$ enters into the channel from the left. Electrodes are placed on both surfaces of the channel as shown in Figure 15b. Each pair of the electrodes has its own external electric circuit with EMF power supply producing a voltage of $E$, and a ballast resistance of $R_0$. The calculation domain $AA'G'G$ includes a region of the unperturbed gas stream $AA'B'B$ and an area of internal flow between two surfaces $BG$ and $B'G'$. Coordinates of the electrodes on the lower and upper surfaces of the channel are identical ($x_C = x_{C'}, \ x_D = x_{D'}, \cdots$). Electric parameters of the two external electric circuits ($E, R_0$) also are identical. It should be noted that assuming identical electrode configurations for the lower and upper surfaces of the channel allows the computer models to be checked for solution symmetry. Examples of performance and the default of the symmetry requirements is presented below.

The external magnetic field $B$ is taken into account in some calculation cases. In these cases the analysis of the influence of volumetric Lorentz' forces acting on the weakly ionized gas of a surface DCD on the gas dynamics of the channel was performed. One possible direction of the magnetic field is shown in Figure 15a. It is necessary to note that the magnetic field will exert a contrary influence on the parameters of the viscid-inviscid interaction near the walls. Near to one of the walls the magnetic volumetric force will act away from the wall, while near to the other wall the magnetic volumetric force will act into the surface.

A finite-difference grid was produced that contains regions of node concentrations near to leading edges of the channel surfaces ($x_B, x_{B'}$), in the boundary layer along the surfaces, and near to the locations of the electrodes. An example of a grid used is shown in Figures 17 through 19.
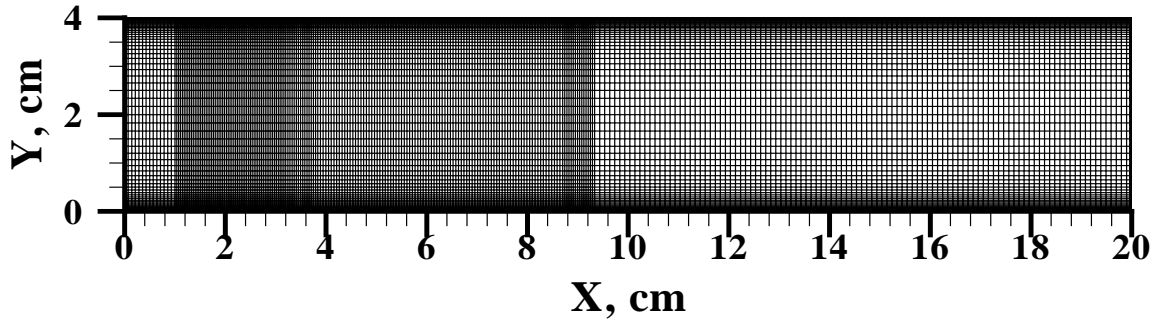


Figure 17. Calculation Grid Number 1

The grid used in the calculations of the first variant (see Table 1) is shown in Figure 17. Figures 18 and 19 show more detail of the structure of the grid. The grid used in the calculation of the second variant (see Table 1) is shown in Figure 20. Figures 21 and 22 show more detail of the structure of the grid.

Calculations were performed using two different models of an external electric circuit. In the first model the requirement of constancy of the EMF of the power supply ($E = \text{const}$) was assumed. In this case the voltage drop in the discharge gap, $V_{dc}$, was predicted by the numerical process. In the second variant the requirement of consistency of the total current through the

discharge gap, or similarly, the requirement of a constant voltage drop across the gap ($V_{dc}$ = const) was set.
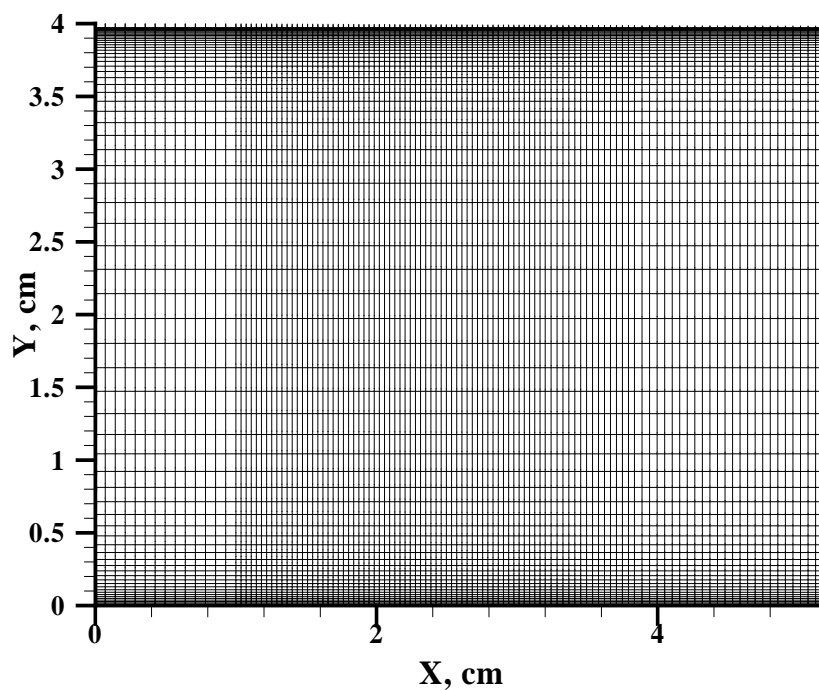


Figure 18. Fragment of the Calculation Grid Number 1
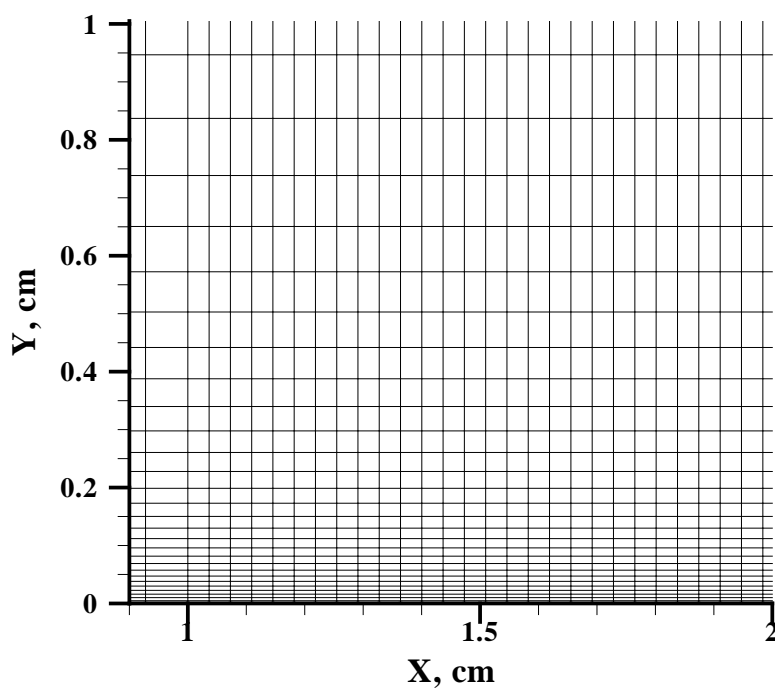


Figure 19. Segment of the Calculation Grid Number 1

Table 1. Geometry of Electrodes

| Variant Number | | $x_C$, cm | $x_D$, cm | $x_E$, cm | $x_F$, cm |
|---|---|---|---|---|---|
| 1 | $H$=4.0 cm, $E$=1400 V Altitude = 40 km | 3.2 | 3.84 | 5.0 | 5.7 |
| 2 | $H$=4.0 cm, $E$=1000 V Altitude = 35 km | 2.0 | 3.0 | 4.0 | 5.0 |
| 3 | $H$=4.0 cm, $E$=700 V Altitude = 40 km | 1.5 | 2.0 | 4.0 | 5.0 |
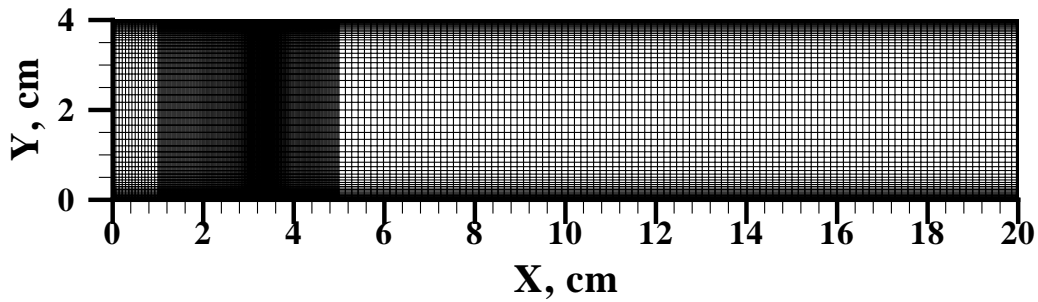


Figure 20. Calculation Grid Number 2
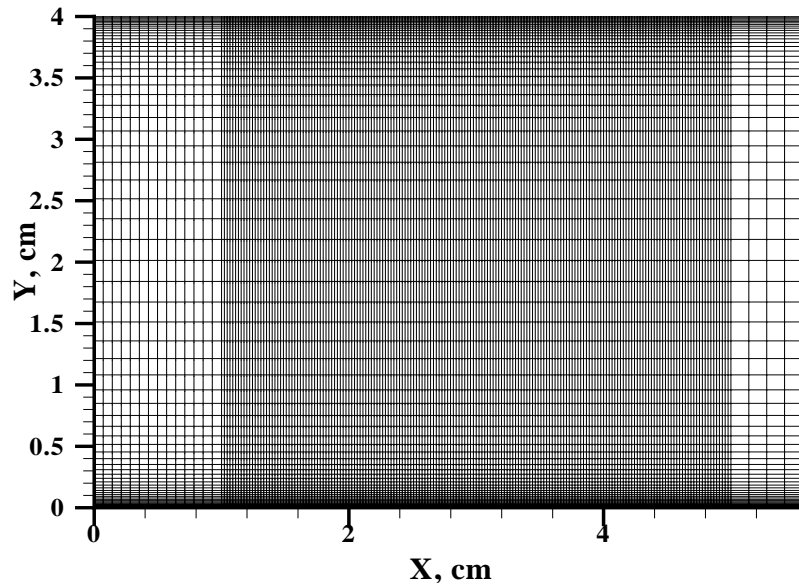


Figure 21. Segment of the Calculation Grid Number 2

40
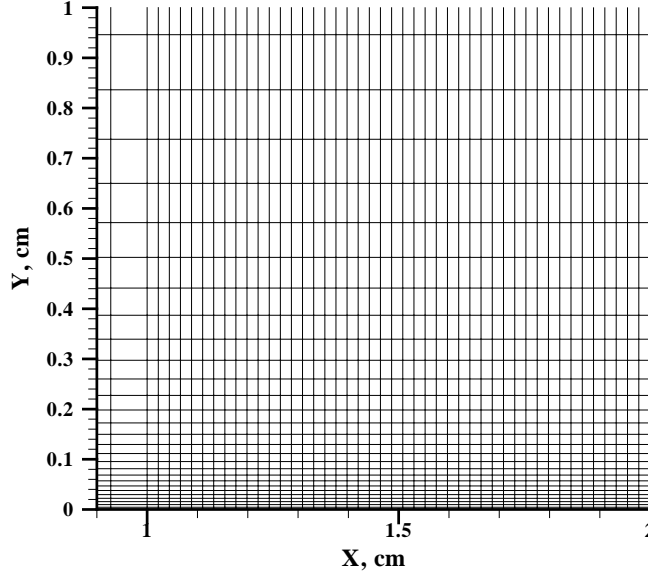
**Figure 22. Segment of the Calculation Grid Number 2**
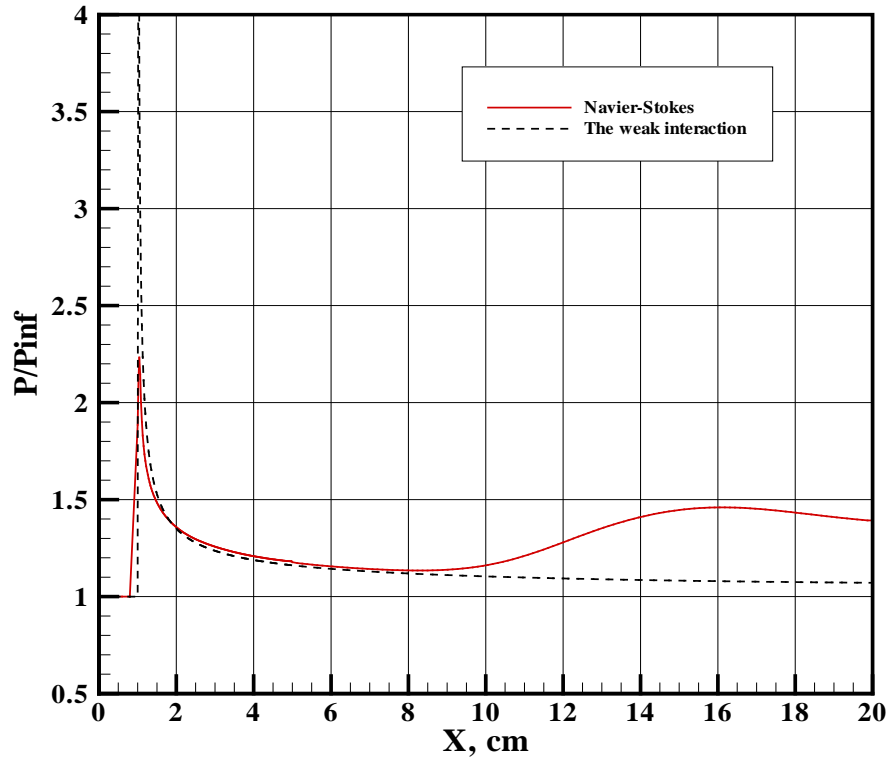


**Figure 23. Pressure Distribution along Bottom Surface; Case 1: Altitude = 40 km, $H$ = 4.0 cm, $M$ = 4, No DCD**

Numerical simulation results for the first calculation case (Case 1, Variant 1 in Table 1) without a surface discharge are shown in Figures 23 through 28. Distributions of the pressure along the lower and upper surfaces (Figures 23 and 24) confirm good performance of symmetry properties of the solution. The pressure distribution predicted by the asymptotic theory of the viscid-inviscid interaction (Hayes and Probstein, 1959) is also shown in Figure 23. It is visible that the

numerically predicted pressure distribution near the leading edge of the streamline surface coincides with the asymptotic theory (except in the immediate vicinity of the leading edge, where the solution obtained is within the limits of a model of a continuous medium, which is not adequate to the physics of the phenomenon). Growth of the pressure at $x > 9$ cm is related to the influence of the head shock wave impinging from the upper surface.

Distributions of the aerodynamic coefficients $c_p$ and $c_f$ along the lower surface are shown in Figure 25. As with the pressure distributions, two areas are clearly visible in these figures: the first one, where the gasdynamic field is formed only by the leading edge ($x < 9$ cm), and the second one, where there is an influence of a shock coming from the upper plate. Isolines of Mach number, pressure, and density (Figures 26 through 28) give common representations of the features of the hypersonic flow in a flat channel. Two shock waves generated by the leading edges of the flat plates interact among themselves and generate a complex system of shock-wave interactions in the channel that appear as oscillating pressures in a longitudinal direction. Areas of increased pressure between the two plates are also observed (Figure 27).
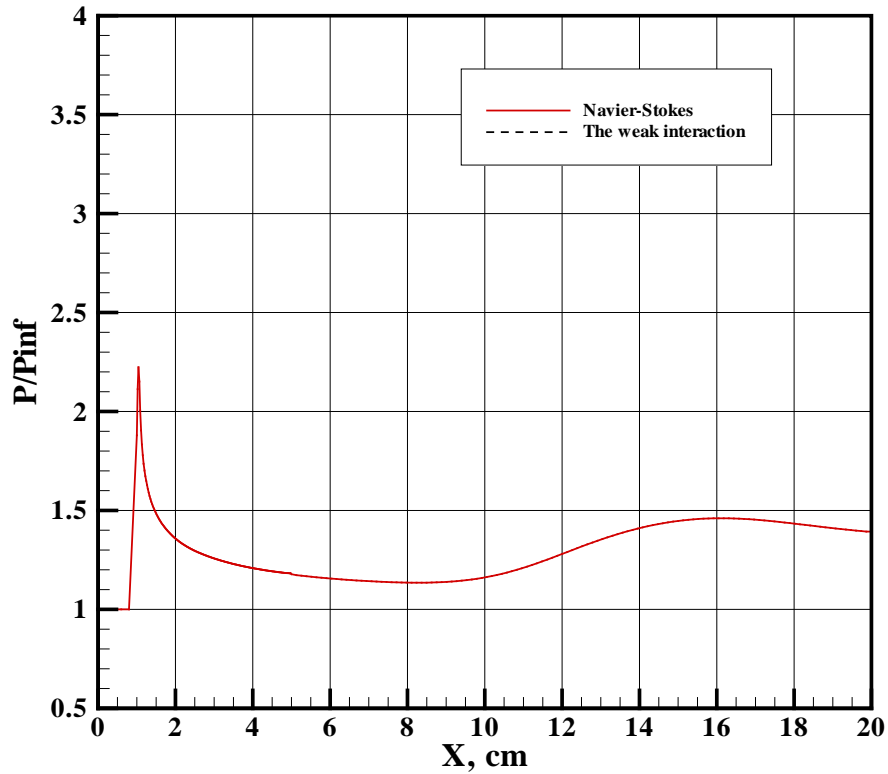


Figure 24.  Pressure Distribution along Top Surface; Case 1:  Altitude = 40 km, $H$ = 4.0 cm, $M$ = 4, No DCD
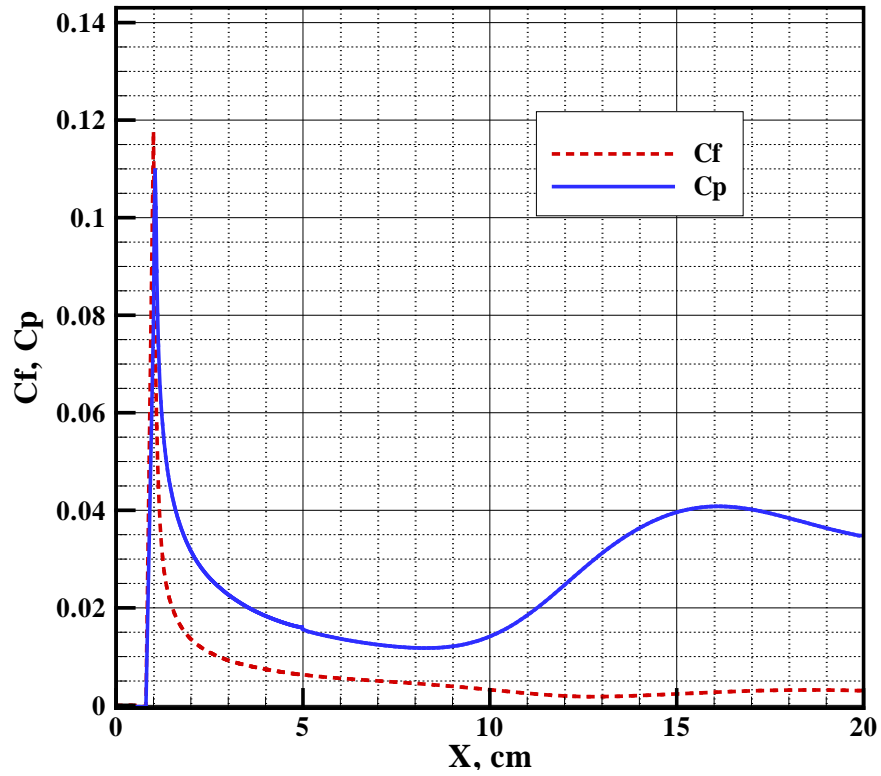
Figure 25. Aerodynamic Coefficients; Case 1: Altitude = 40 km, *H* = 4.0 cm, *M* = 4, No DCD
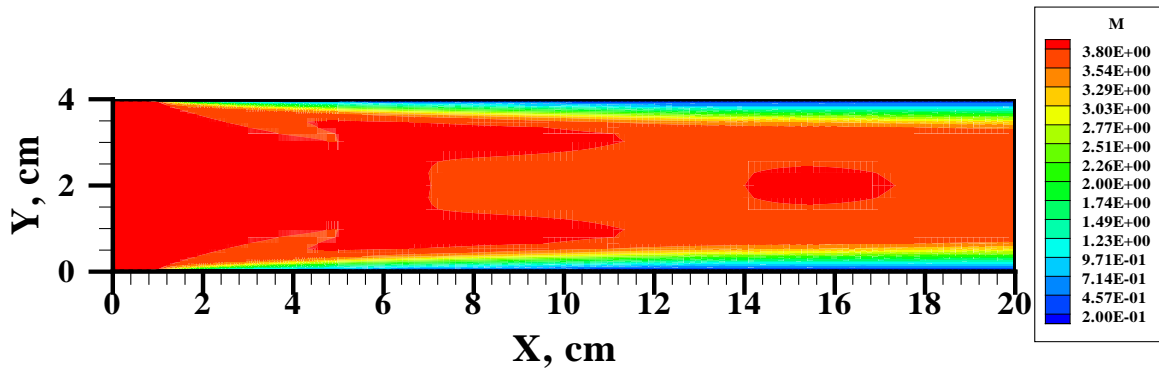


Figure 26. Mach Number; Case 1: Altitude = 40 km, *H* = 4.0 cm, *M* = 4, No DCD
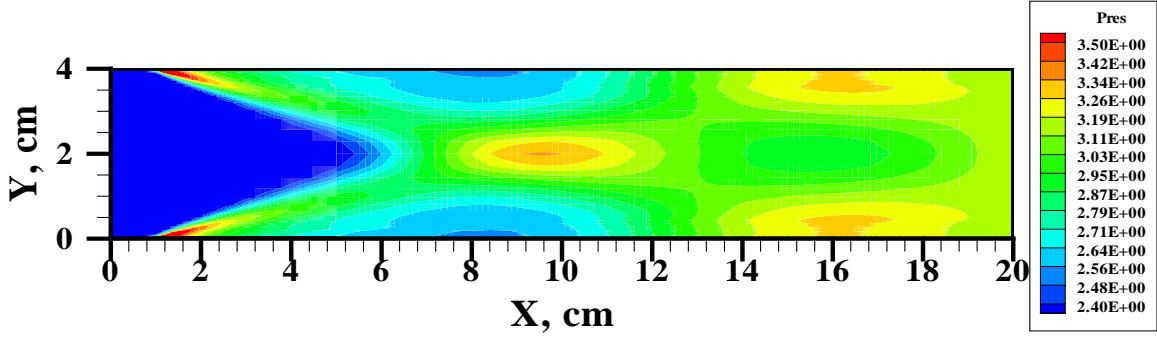
Figure 27. Pressure In Torr; Case 1: Altitude = 40 km, *H* = 4.0 cm, *M* = 4, No DCD
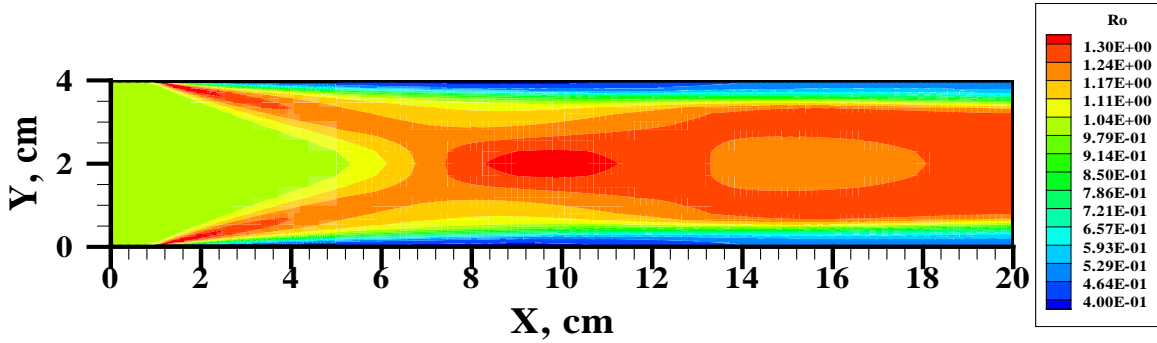


Figure 28. Density, ρ/ρ∞, Case 1: Altitude = 40 km, *H* = 4.0 cm, *M* = 4, No DCD

In the second calculation case (Case 2, Variant 1 in Table 1) a glow discharge exists between the electrodes in the mode $E = 1400$ V=constant. Predicted total current through the discharge gap is $I = 0.11$ A and the voltage drop is $V_{dc} = 262$ V.

The distribution of the pressure along the surfaces for this case is shown in Figures 29 and 30. The numerical simulation results demonstrate good satisfaction of the symmetry properties. Appreciable pressure growth is observed in this case near to the inter-electrode gap due to the surface discharge. It also affects the pressure distribution at $x > 9$, where the pressure is observed to increase more as compared to Case 1.
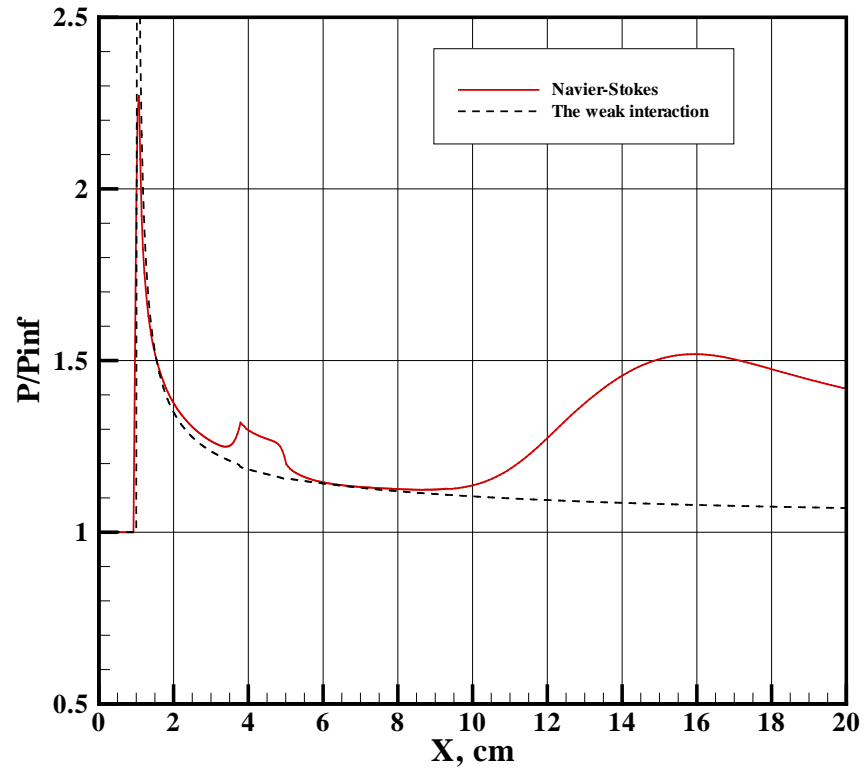
Figure 29.  Pressure Distribution along Lower Surface; Case 2:  Altitude = 40 km, $H = 4.0$ cm, $M = 4$, $E = 1400$ V
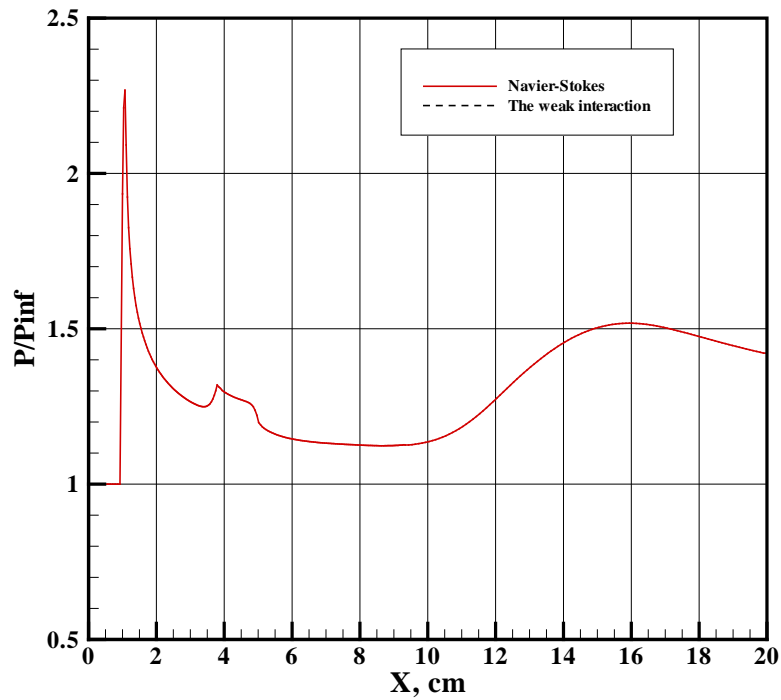


Figure 30.  Pressure Distribution along Upper Surface; Case 2:  Altitude = 40 km, $H = 4.0$ cm, $M = 4$, $E = 1400$ V
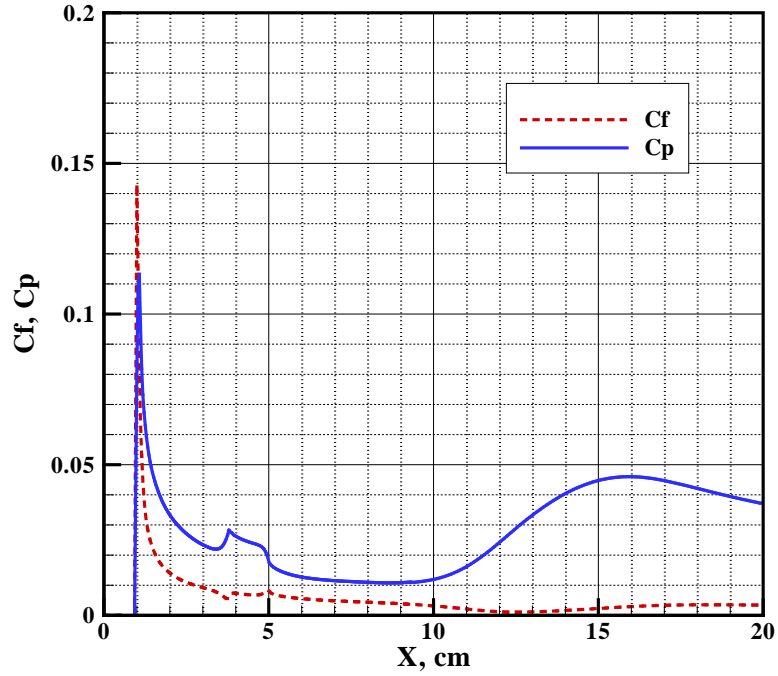
Figure 31. Aerodynamic Coefficients; Case 2: Altitude = 40 km, $H$ = 4.0 cm, $M$ = 4, $E$ = 1400 V
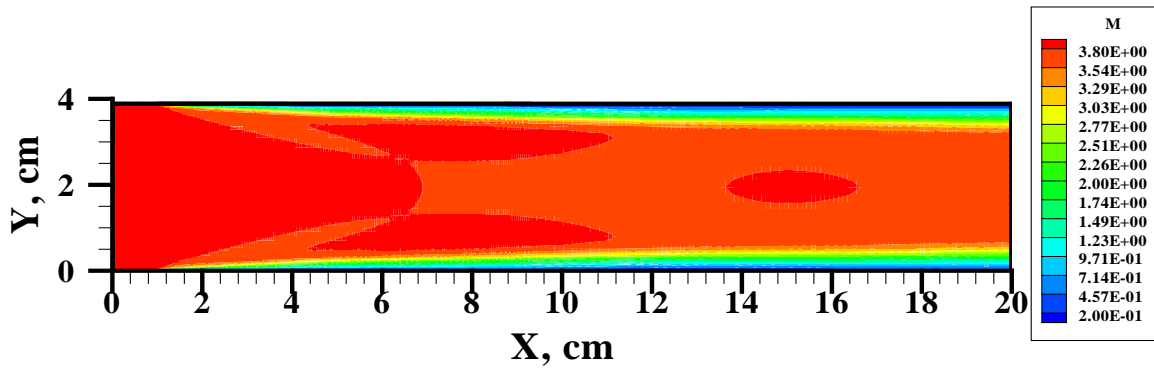


Figure 32. Mach Number Case 2: Altitude = 40 km, $H$ = 4.0 cm, $M$ = 4, $E$ = 1400 V
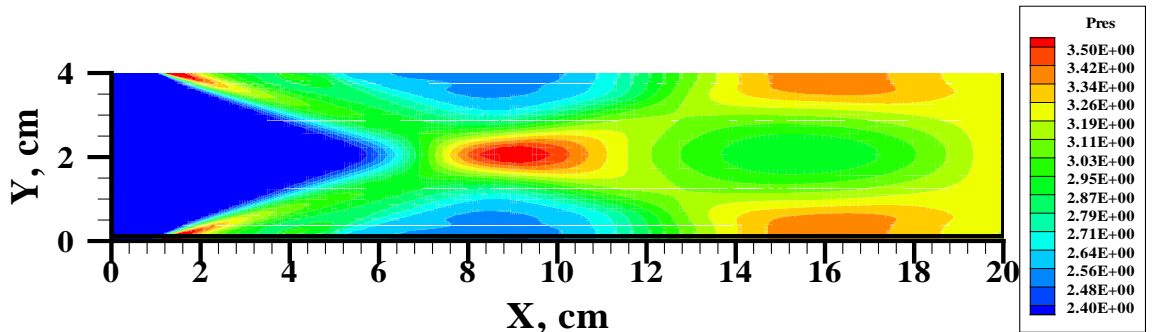


Figure 33. Pressure in Torr; Case 2: Altitude = 40 km, $H$ = 4.0 cm, $M$ = 4, $E$ = 1400 V
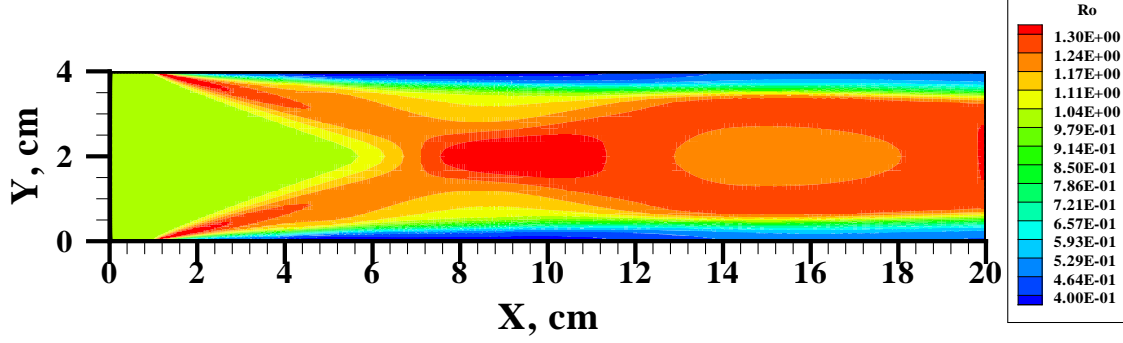
**Figure 34.** Density, $\rho/\rho_\infty$; Case 2: Altitude = 40 km, $H$ = 4.0 cm, $M$ = 4, $E$ = 1400 V

Distributions of aerodynamic coefficients $c_p$ and $c_f$ along the lower surface are shown in Figure 31. There is a small inhomogeneity in the distribution of the coefficient $c_f$ near to the surface discharge. This inhomogeneity increases with increasing total current through the discharge. Mach number distributions for the case with a DCD are almost the same as the case without a DCD (compare Figure 26 with no DCD and Figure 32 with DCD). However, the pressure distributions for these two cases differ significantly (compare Figure 27 with no DCD and Figure 33 with DCD). The density distribution is shown in Figure 34. For convenience of the comparison these figures are presented with an identical scale.

In the third calculation case (Case 3, Variant 3 in Table 1) a rise in the pressure above the surface discharge, near to the leading edge of the streamlined plates, is observed (Figures 35 and 36). Note that requirements of the solution symmetry are well satisfied in this case also. Total current through the discharge in this case achieves $I = 0.605$ A; this is considerably higher than in the previous calculation case.

This high of a total current causes relatively large gas heating and results in the pressure increasing. It is remarkable, that such a high pressure near to the leading edge of the plates has a smaller degree of influence on the induced pressure at $x > 6$ cm. It is substantially related to the location of the electrodes in the vicinity of the leading edges. Nevertheless, appreciable changes in distributions of the Mach number, pressure, and density are visible in Figures 37 through 39 when compared to the previous calculation case. Here it is necessary to note the important feature of numerical simulations in a mode $V_{dc} = \text{const}$. It is well known, that computing models of glow discharges can be used for prediction of electrodynamic parameters in a weakly ionized gas for total currents through the discharge up to ~ 10 mA. For these conditions a heating of the neutral gas is insufficient for changing the gas chemical composition. Otherwise, at sufficiently high currents, high temperatures and chemical transformations are observed. In the case under consideration, an unrealistic temperature, in the frame of the model of a weakly ionized gas, is observed above the electrodes (see Figure 40). This illustrates that at high total currents the calculation model should be changed.
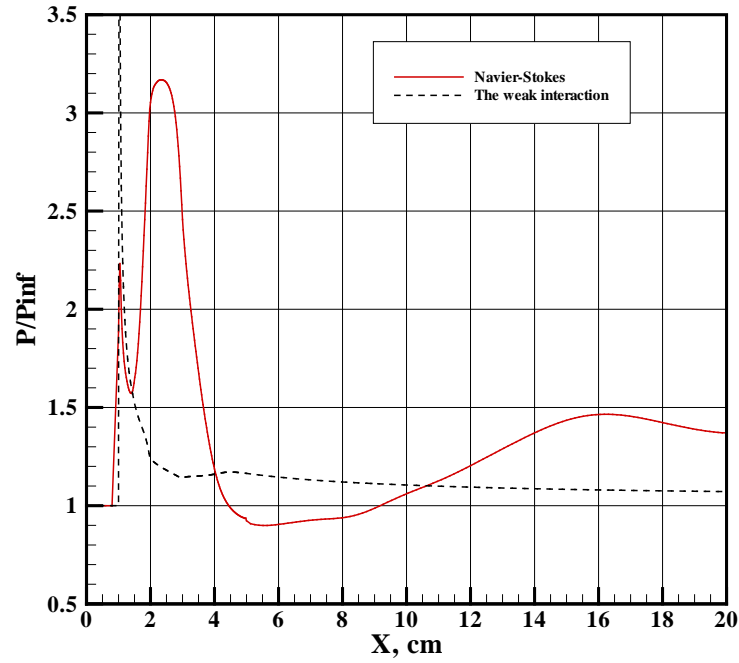
Figure 35.  Pressure Distribution along Lower Surface; Case 3:  Altitude = 40 km, $H$ = 4.0 cm, $M$ = 4,  $V$ = 700 V = Constant
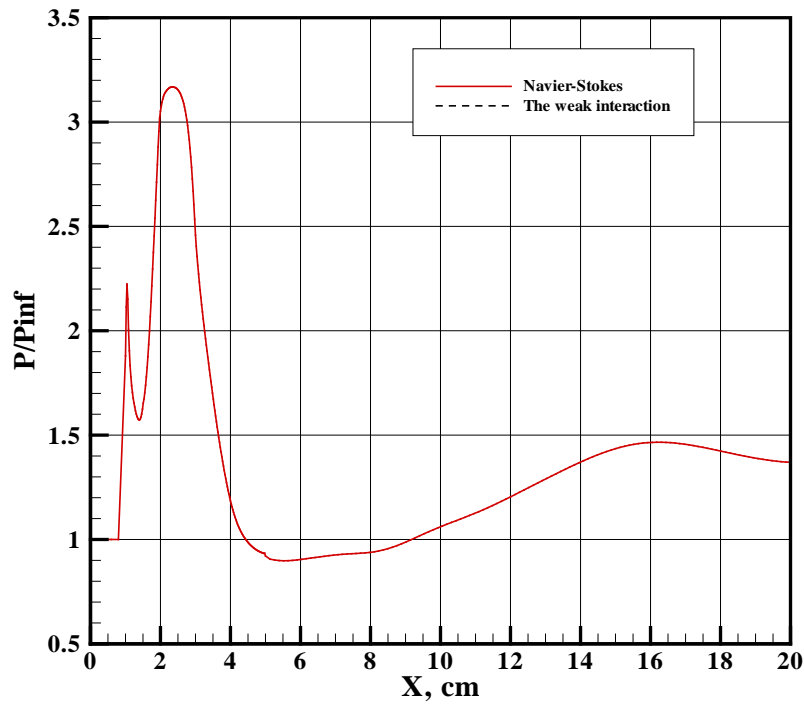


Figure 36.  Pressure Distribution along Upper Surface; Case 3:  Altitude = 40 km, $H$ = 4.0 cm, $M$ = 4,  $V$ = 700 V = Constant
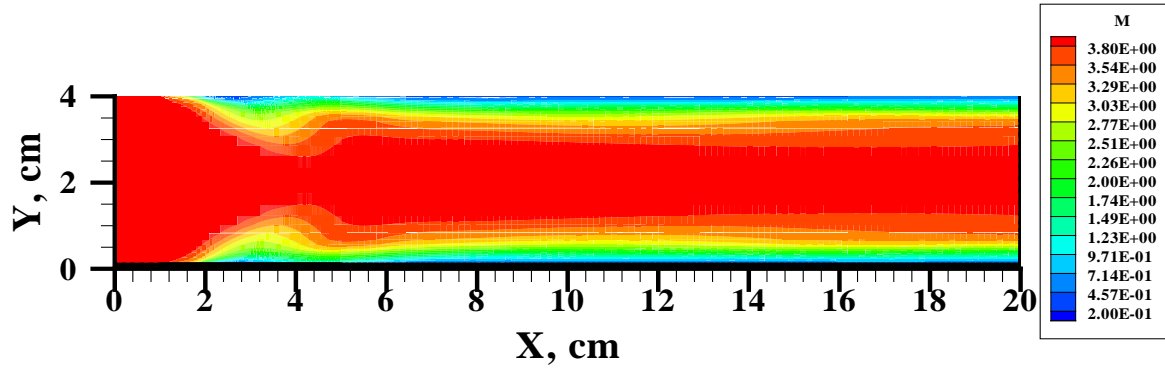
Figure 37.  Mach Number; Case 3:  Altitude = 40 km, $H$ = 4.0 cm, $M$ = 4, $V$ = 700 V = Constant
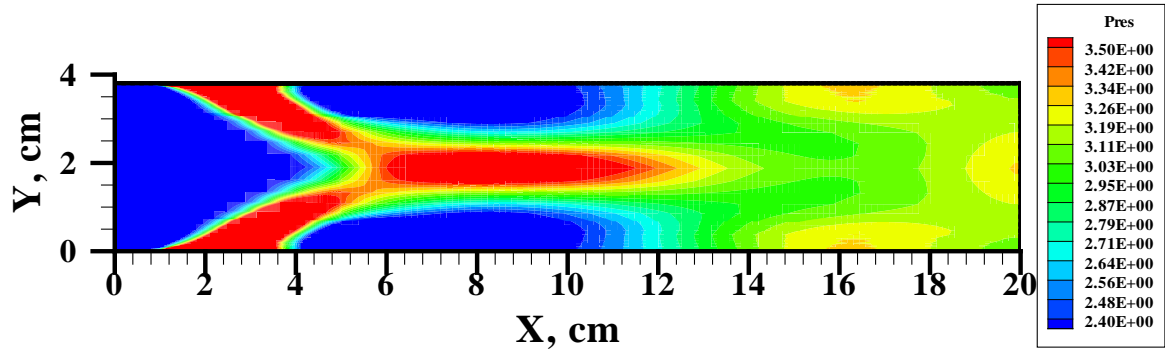


Figure 38.  Pressure in Torr; Case 3:  Altitude = 40 km, $H$ = 4.0 cm, $M$ = 4, $V$ = 700 V = Constant
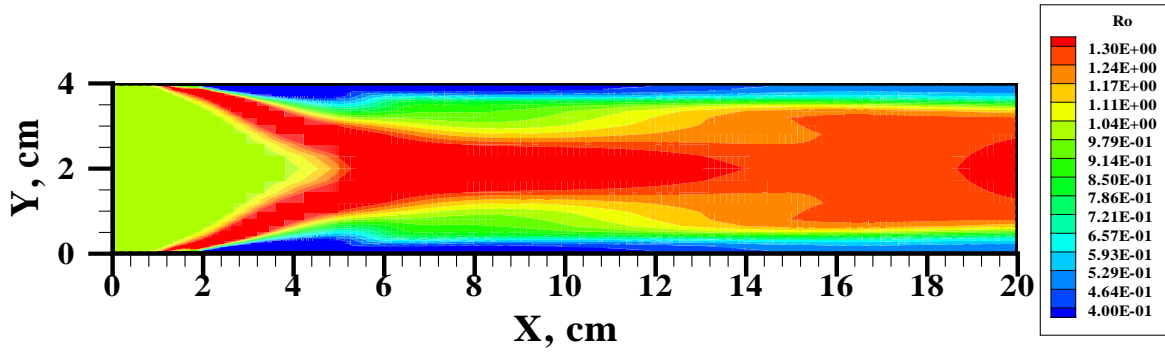


Figure 39.  Density, $\rho/\rho_\infty$; Case 3:  Altitude = 40 km, $H$ = 4.0 cm, $M$ = 4, $V$ = 700 V = Constant
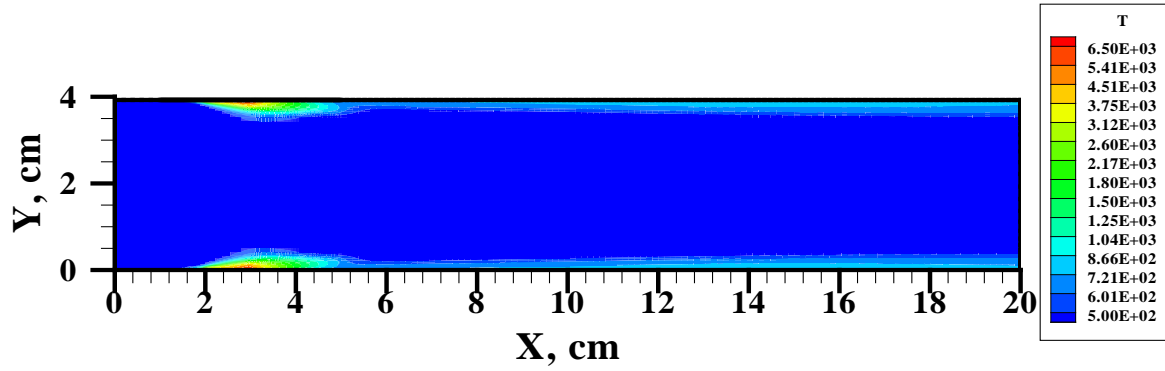
Figure 40.  Temperature in Kelvin; Case 3:  Altitude = 40 km, $H$ = 4.0 cm, $M$ = 4, $V$ = 700 V = Constant

In the fourth calculation case (Case 4, Variant 2 in Table 1, and Variant 2 in Table 2) calculations were performed without taking into account a glow discharge. Numerical simulation results are shown in Figures 41 through 46. These figures show pressure distributions along the lower and upper surfaces, aerodynamic coefficients on the lower surface, isolines of Mach number, pressures, and densities. These data will be used below for comparison with calculation cases taking into account a gas discharge.

Table 2.  Parameters of a Gas Freestream

| Variant No. | $p_\infty$ , erg/cm$^3$ | $\rho_\infty$ , g/cm$^3$ | $T_\infty$ , K | $V_\infty$ , m/s | $M$ |
|---|---|---|---|---|---|
| 1 | $2.96 \times 10^3$ | $4.00 \times 10^{-6}$ | 257 | 1285 | 4 |
| 2 | $5.80 \times 10^3$ | $8.28 \times 10^{-6}$ | 244 | 1879 | 6 |

The fifth calculation case (Case 5) is the same as Case 4, but has a discharge with $V_{dc} = 1$ kV=constant. An appreciable high pressure above the electrode gap is observed in this case (Figures 47 through 48). The aerodynamic coefficients are shown in Figure 49. Note that the requirements of symmetry are still well satisfied. There is an appreciable effect of the high pressure above the electrodes on the pressure distribution at $x > 14$ cm, where the influence of a shock wave coming from the opposite surface has appeared. Nevertheless, a pressure field in the central part of the channel, at $10 < x < 18$ cm, has a little increment (see Figure 51). There is also an appreciable change in the distribution of the Mach number and density profiles (see Figures 50 and 52). Total current through the discharge gap in this case is $I = 0.7$ A, and the peak concentration of charged particles reaches $n \sim 7.8 \times 10^{11} \, \text{cm}^{-3}$.

50
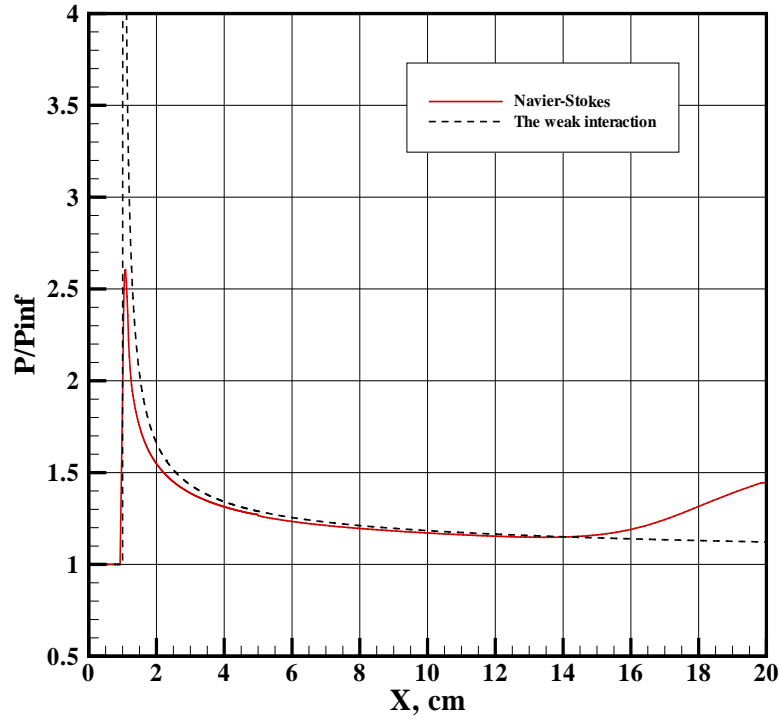
Figure 41.  Pressure Distribution along Lower Surface; Case 4:  Altitude = 35 km,
$H$ = 4.0 cm, $M$ = 6, No DCD
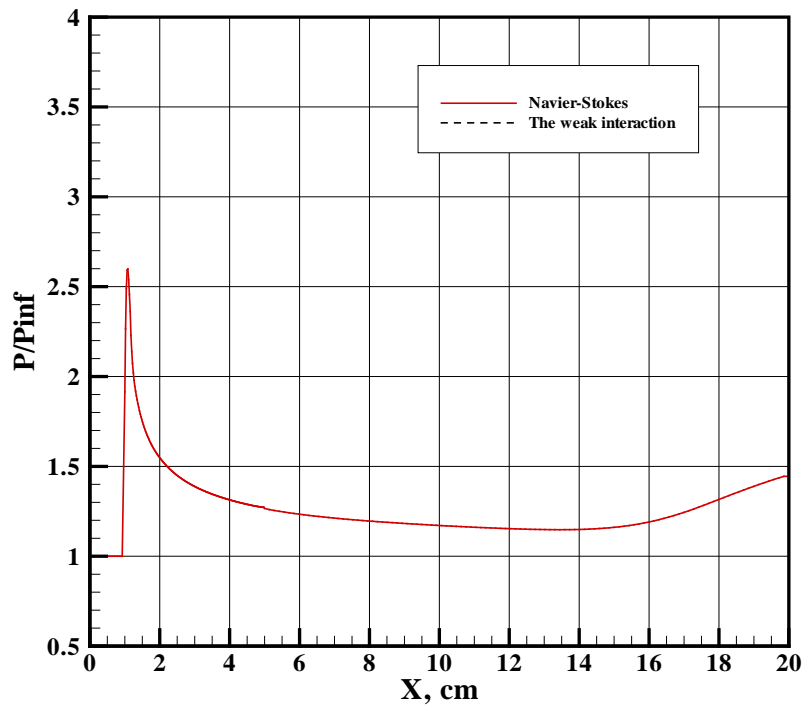


Figure 42.  Pressure Distribution along Upper Surface; Case 4:  Altitude = 35 km,
$H$ = 4.0 cm, $M$ = 6, No DCD
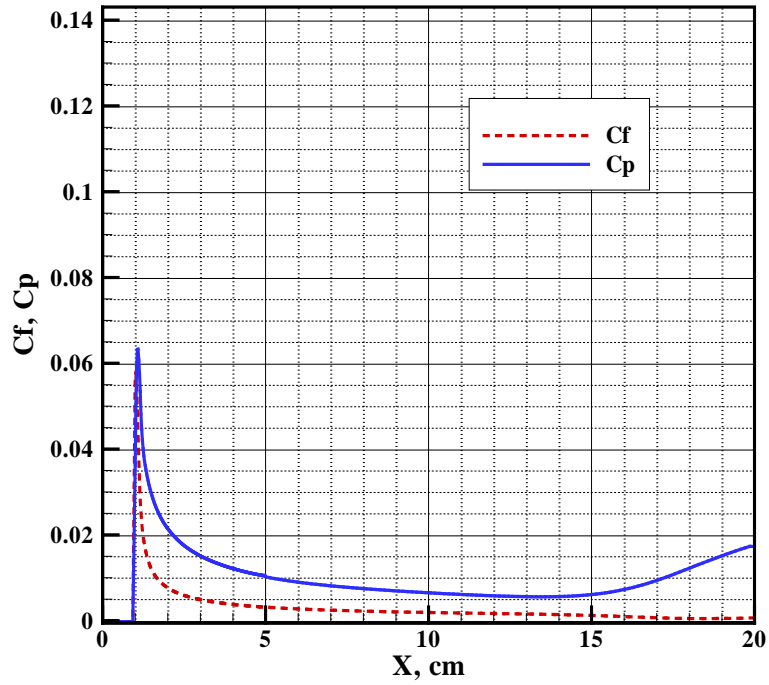
Figure 43. Aerodynamic Coefficients; Case 4: Altitude = 35 km, $H$ = 4.0 cm, $M$ = 6, No DCD
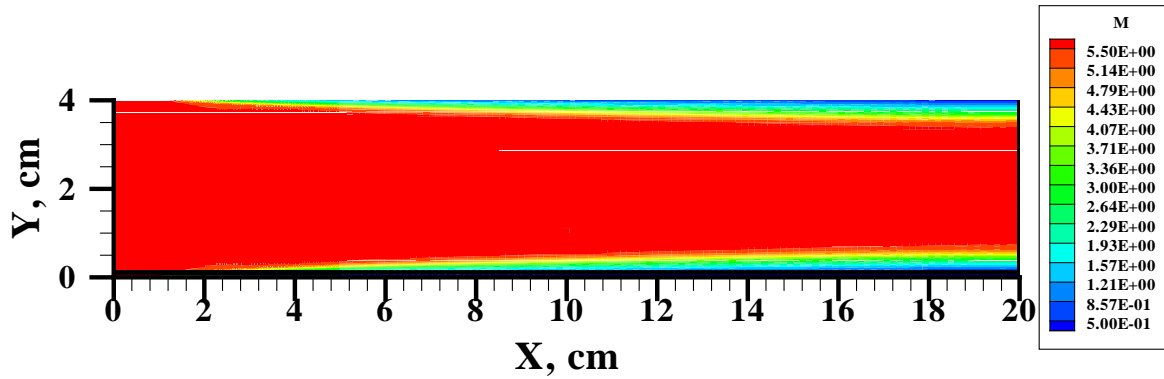


Figure 44. Mach Number; Case 4: Altitude = 35 km, $H$ = 4.0 cm, $M$ = 6, No DCD
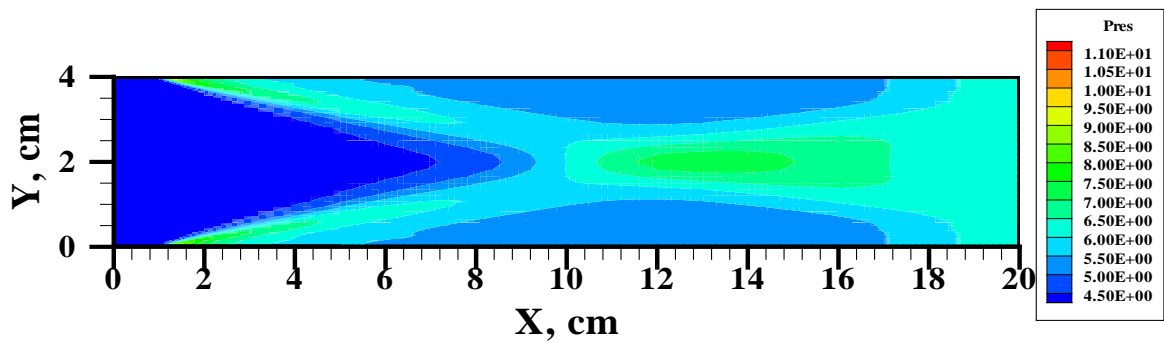


Figure 45. Pressure in Torr; Case 4: Altitude = 35 km, $H$ = 4.0 cm, $M$ = 6, No DCD

52
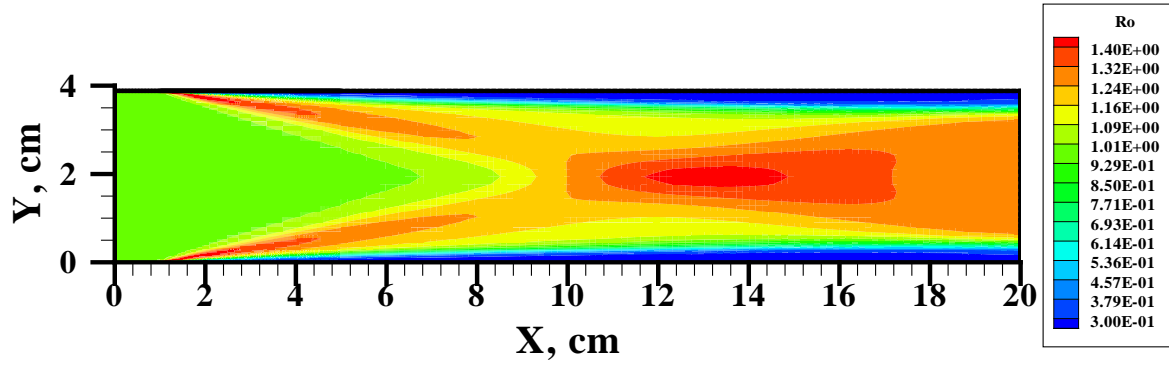
Figure 46. Density, $\rho/\rho_\infty$; Case 4: Altitude = 35 km, $H$ = 4.0 cm, $M$ = 6, No DCD
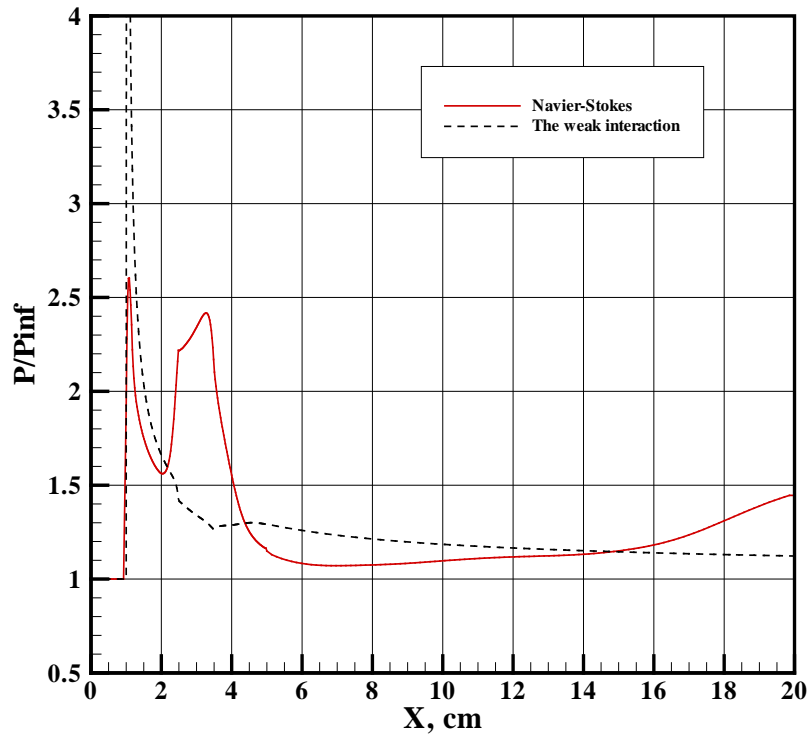


Figure 47. Pressure Distribution along Lower Surface; Case 5: Altitude = 35 km, $M$ = 6, $V$ = 1000 V = Constant
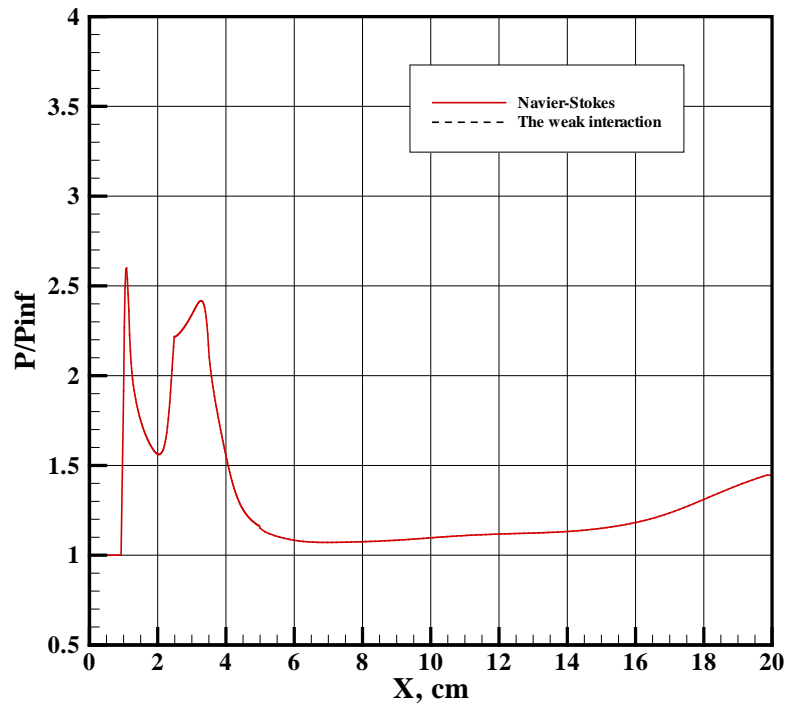
Figure 48. Pressure Distribution along Upper Surface; Case 5: Altitude = 35 km, $M = 6$,
$V = 1000$ V = Constant
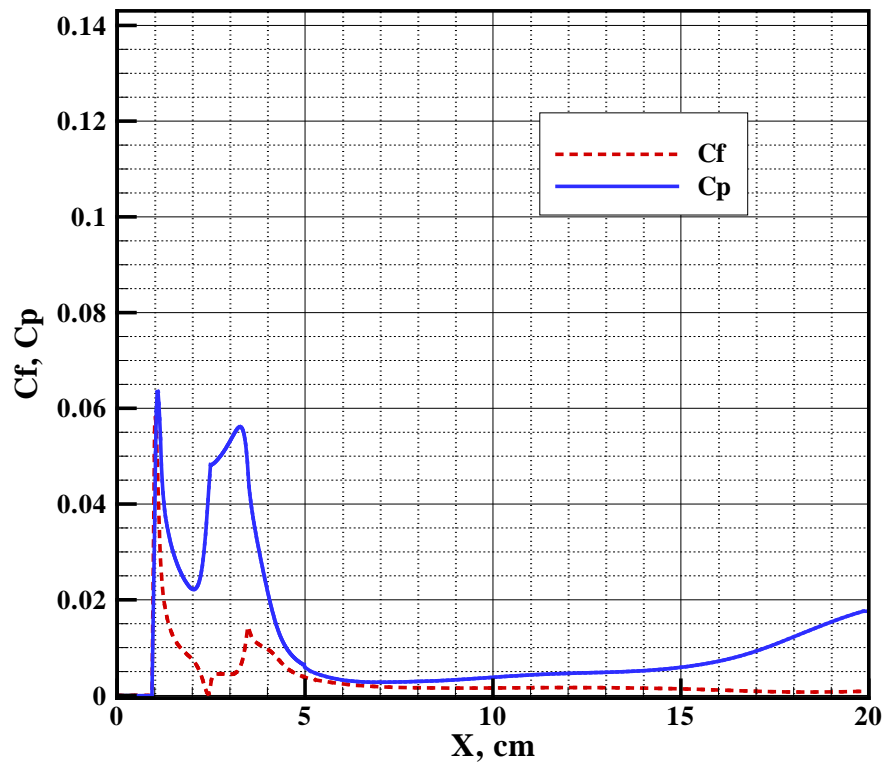


Figure 49. Aerodynamic Coefficients; Case 5: Altitude = 35 km, $M = 6$,
$V = 1000$ V = Constant
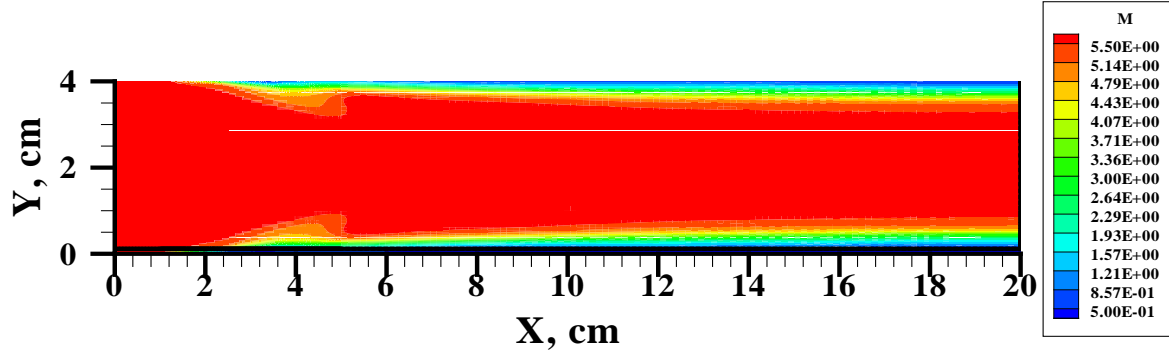
**Figure 50.** Mach Number; Case 5: Altitude = 35 km, *M* = 6, *V* = 1000 V = Constant

A representation of the numerical convergence of the iterative process for charge particle concentrations is given in Figure 53. It should be noted, that in the mode of $E = \text{const}$ the typical number of iterations is from $10^4$ to $10^5$.
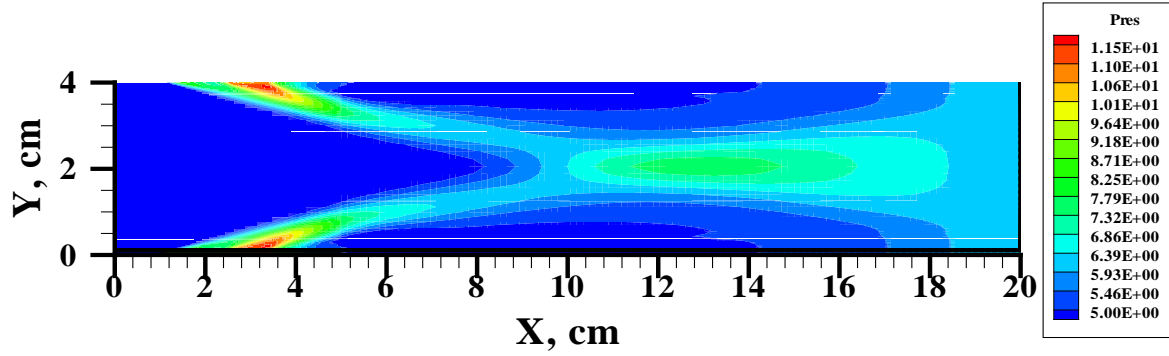


**Figure 51.** Pressure in Torr; Case 5: Altitude = 35 km, *M* = 6, *V* = 1000 V = Constant
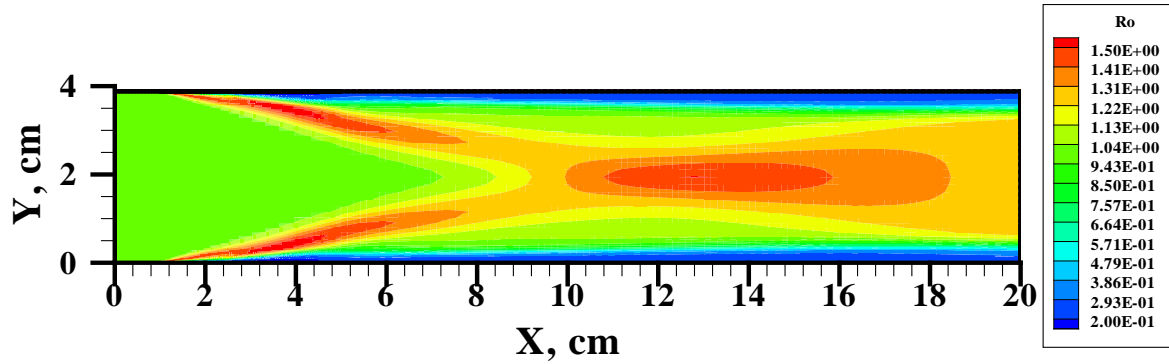


**Figure 52.** Density, $\rho/\rho_\infty$; Case 5: Altitude = 35 km, *M* = 6, *V* = 1000 V = Constant
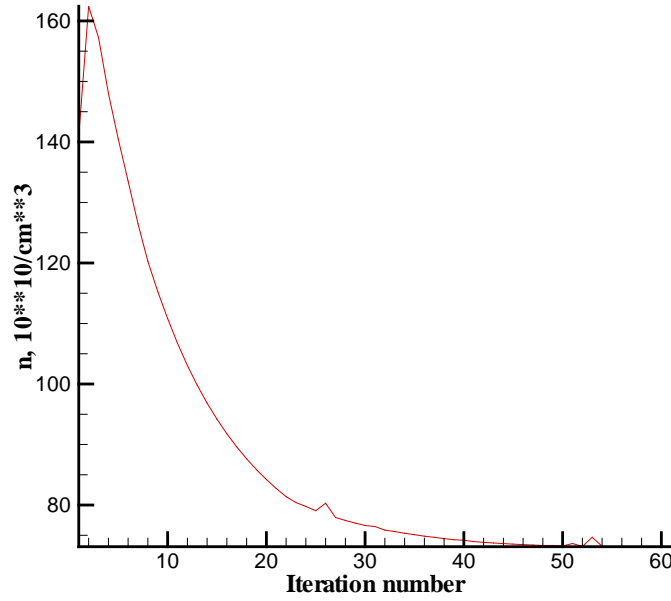
**Figure 53. Convergence History for Charge Particles**

In the last case studied (Case 6, Variant 2 in Table 1, and Variant 2 in Table 2) an external magnetic field ($B_z = 0.2\,\text{T}$) is taken into account. These results are shown in Figures 54 through 58. The direction of the magnetic field in the lower and upper half-spaces of the calculation domain is set opposite. Because of the magnetic field an anisotropy of the solutions is observed (see Figures 54 and 55).

Preliminary numerical simulation results show appreciable increase in the gas pressure above the inter-electrode gap and in the center of the channel for $9 < x < 15$ cm, this confirms the initial assumption about the opportunity to use a magnetic field as an additional control factor for gas flow.

### 3.2.6 Summary

A computer model for the coupled direct current discharge and gasdynamics for hypersonic internal flows within a flat channel with a surface gas discharge has been developed. This model is based on the combined solutions of the Navier-Stokes equations and equations describing electrodynamic processes in a quasi-neutral plasma.

Numerical simulation results for molecular nitrogen ($N_2$) gas flows with Mach numbers from four to six and at conditions of the unperturbed gas stream corresponding to altitudes in the earth's atmosphere of 35 and 40 km are presented.

These calculations of hypersonic internal gas flows have shown that the use of a surface gas discharge on both surfaces of a gasdynamic channel leads to appreciable modification of the flow field. There may be a place for use of this phenomenon in hypersonic flight.
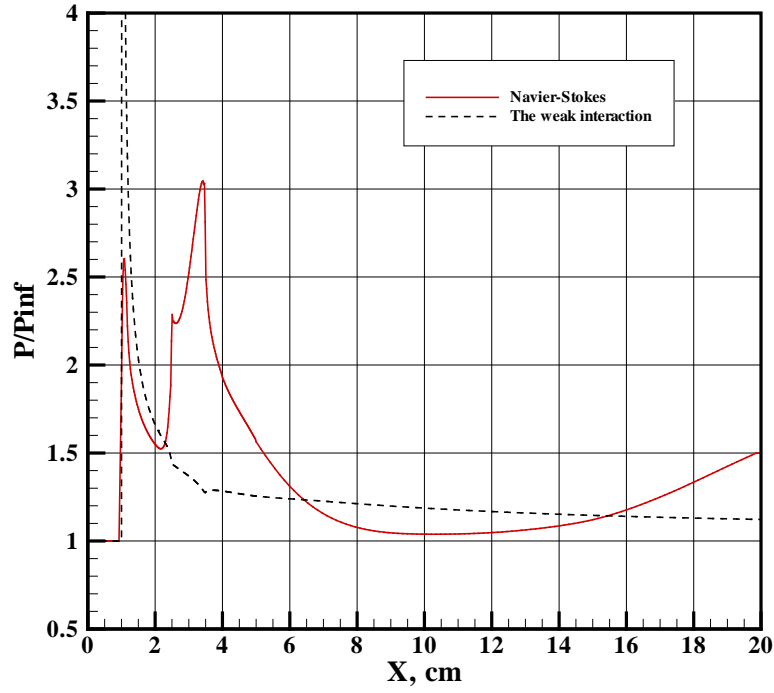
Figure 54.  Pressure Distribution along Lower Surface; Case 6:  Altitude = 35 km, $H = 4.0$ cm, $M = 6$, $V = 1000$ V = const, $B_z = 0.2$ T
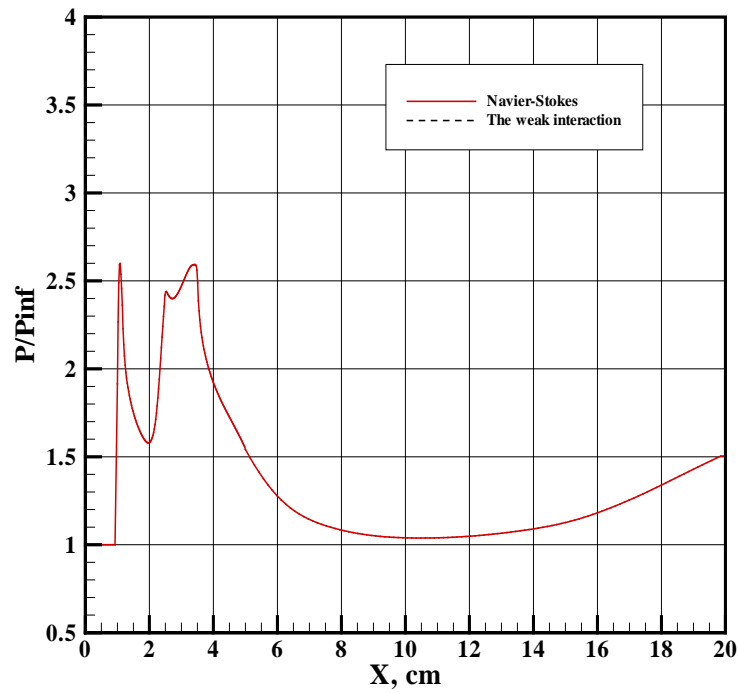


Figure 55.  Pressure Distribution along Upper Surface; Case 6:  Altitude = 35 km, $H = 4.0$ cm, $M = 6$, $V = 1000$ V = const, $B_z = 0.2$ T
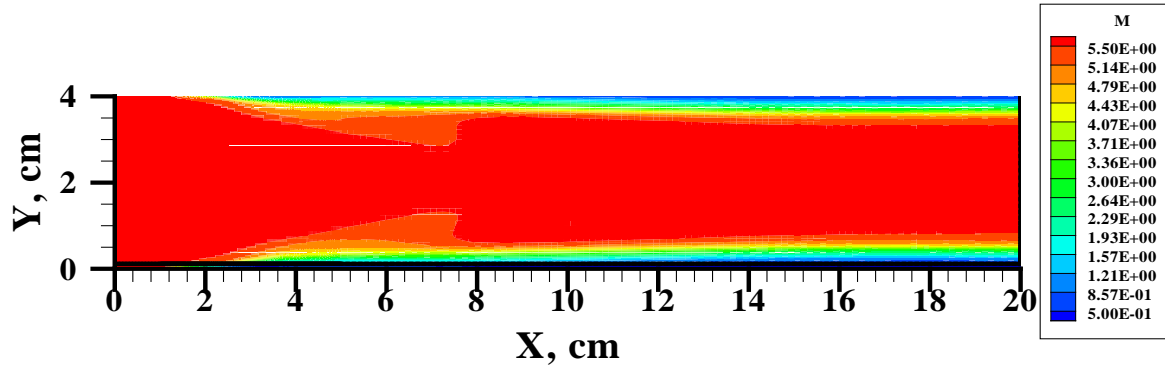
Figure 56. Mach Number; Case 6: Altitude = 35 km, $H$ = 4.0 cm, $M$ = 6, $V$ = 1000 V = const, $B_z$ = 0.2 T
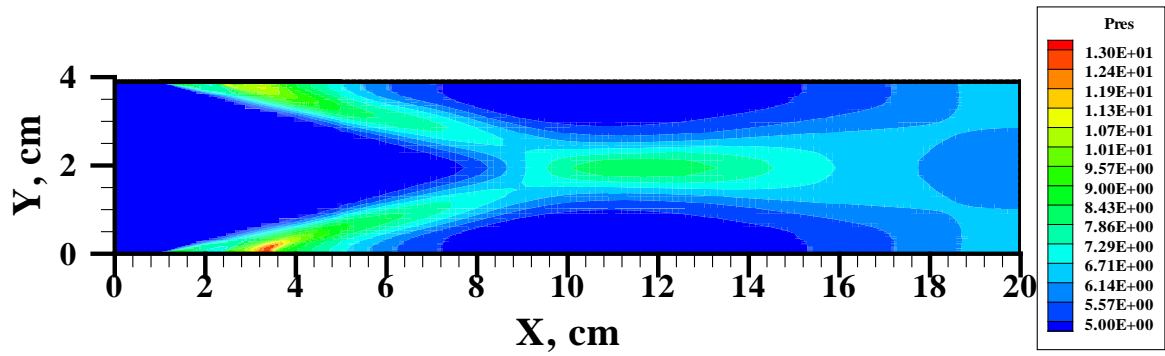


Figure 57. Pressure in torr; Case 6: Altitude = 35 km, $H$ = 4.0 cm, $M$ = 6, $V$ = 1000 V = const, $B_z$ = 0.2 T
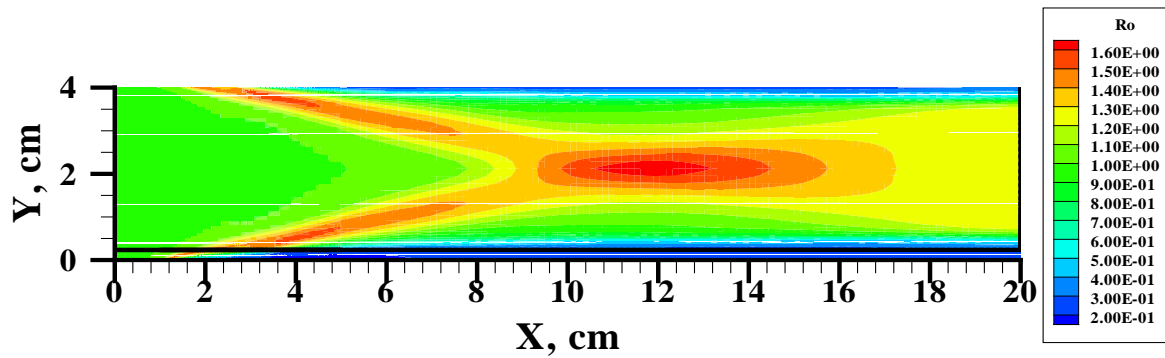


Figure 58. Density, $\rho/\rho_\infty$; Case 6: Altitude = 35 km, $H$ = 4.0 cm, $M$ = 6, $V$ = 1000 V = const, $B_z$ = 0.2 T

### 3.3  Model Development for Three-Dimensional Flow in a Rectangular Channel

### 3.3.1  Introduction

In order to accelerate the technical transfer from basic research to practical applications, it is critical to quantify the usable high pressure plateau generated by the plasma actuator and to define the operable envelope. More importantly, a solid database must be established and validated for engineering design and practical applications. However, the physical phenomenon of magnetoaerodynamic interactions is unsteady and tends to be three dimensional, thus drastically increasing the complexity of the measuring technique. Most surface plasma actuators adopted in flow control must operate in the abnormal discharge mode in that it is not possible to maintain a steady discharge (Menart et al, 2003b; Kimmel et al., 2004a; Raizer, 1991; Mitchner and Kruger, 1973). In this mode of the gas discharge, the plasma electrical current exhibits a random oscillation up to the kilohertz range. Furthermore, the magnetohydrodynamic (MHD) channel at AFRL/RB is severely limited in size and thus tested models and measuring instruments must be small. At the present time, the measurements are restricted to pitot pressure surveys, Schlieren photography, and spectral data. These shortcomings must be compensated with side-by-side three-dimensional computing simulations.

For the present purpose, the computational simulation becomes an interpreter of experimental measurements. The computed results are first calibrated against the measured data to establish the error band. The validated pitot pressure data ensures the accuracy of the static and stagnation pressure profiles obtained from the numerical model and required for analysis and evaluation. The entire flow is replicated by the three-dimensional computational simulation solving the magneto-fluid-dynamic equations with a physically based model of two-temperatures and three plasma species (neutral particles, electrons, and ions) (Gaitonde, 2003; MacCormack, 2003).

This section presents numerical simulation results on the physical gas dynamics and physics of glow discharges in a three-dimensional square channel. The main part of this subsection contains results of a numerical simulation of the electro-gas-dynamic structure inside a hypersonic inlet with glow discharges existing between sectionalized electrodes located on opposing surfaces. In this section of this report, results in only two directions are shown, vertical and flow directions. The vertical direction is the direction that goes across the flow channel between the electrodes. In Section 4 of this report results will be presented for the third dimension. Section 4 will present results at different flow cross sections. In addition, Section 4 of this report will present comparisons to experimental measurements.

### 3.3.2  Governing Equations

The governing equations of the numerical simulation consist of the magneto-fluid-dynamic equations at the low Magnetic Reynolds number, $Re_m = \mu_m \sigma u L$, limit (Mitchner and Kruger, 1973). For the experimental condition, the Magnetic Reynolds number is $8.48 \times 10^{-6}$. The governing equations in vector notation for a three-dimensional case are:

$$\partial \rho / \partial t + \nabla \cdot (\rho \mathbf{u}) = 0 , \tag{142}$$

$$\partial \rho \mathbf{u} / \partial t + \nabla \cdot (\rho \mathbf{u}\mathbf{u} - \boldsymbol{\tau}) = \mathbf{J} \times \mathbf{B} , \tag{143}$$

and
$$\partial \rho e / \partial t + \nabla \cdot (\rho e \mathbf{u} - \mathbf{q} - \mathbf{u} \cdot \boldsymbol{\tau}) = \mathbf{E} \cdot \mathbf{J} . \tag{144}$$

In these equations, as well as all the equations in this section of the report, a bold quantity is a vector quantity. This resultant governing partial differential equation system is identical to the

Navier-Stokes equations, except with non-zero source terms. Therefore the initial values and boundary conditions, as well as the numerical procedure, are directly usable from the cumulative knowledge of the CFD discipline (Shang, 2005b).

The added electromagnetic effect of the flow is primarily derived from the electrically conducting medium. For most plasma actuators used for flow control, the weakly ionized gas is generated by electron collisions (Raizer, 1991). For the present purpose, the only required information for numerical simulation are the properties of the weakly ionized gas so that the electrical field intensity, $\mathbf{E}$, and electrical current density, $\mathbf{J}$, in the basic formulation, equations (143) and (144) can be determined. These inputs of a numerical simulation define the physical fidelity of the simulation and are the focus of the proposed research activity.

The technical approach used in this work, which is based on first principles of physics, is readily available in Surzhikov and Shang (2004) and Shang (2005b). The electrodynamics of the plasma generation via electron collisions has been modeled by the drift-diffusion theory, including a rational treatment of the surface electrical charge. From this system of equations, plasma properties, such as the charge particle densities, electrical current density, electromagnetic field intensity, and electrical conductivity can be determined.

The governing equations of a plasma in the drift diffusion formulation for a three-dimensional geometry are:

$$\partial n_e/\partial t + \nabla \cdot \mathbf{\Gamma}_e = \alpha(E,p) \, |\mathbf{\Gamma}_e| - \beta \, n_+ n_e , \tag{145}$$

$$\partial n_+/\partial t + \nabla \cdot \mathbf{\Gamma}_+ = \alpha(E,p) \, |\mathbf{\Gamma}_e| - \beta \, n_+ n_e , \tag{146}$$

$$\mathbf{\Gamma}_e = -D_e \nabla n_e - n_e \mu_e \mathbf{E} , \tag{147}$$

and
$$\mathbf{\Gamma}_+ = -D_+ \nabla n_+ + n_+ \mu_+ \mathbf{E} . \tag{148}$$

In the above formulation, $\alpha\,(E,\,p)$ and $\beta$ are the first Townsend ionization coefficient and recombination coefficient, $\mu_e$ and $\mu_+$ are the electron and ion mobility, and $D_e$ and $D_+$ are the electron and ion diffusion coefficients. The electrical current density that appears in the low magnetic Reynolds number approximation is computed using

$$\mathbf{J} = e(\mathbf{\Gamma}_+ - \mathbf{\Gamma}_e) . \tag{149}$$

A compatible electrical field intensity, $E$, throughout the discharge domain is obtained by satisfying the charge conservation equation derived from the generalized Ampere's law and Gauss's law of electrical field intensity,

$$\partial \rho_e/\partial t + \nabla \cdot \mathbf{J} = 0 . \tag{150}$$

This equation can be further simplified in the globally neutral plasma by introducing an electrical potential function, $\mathbf{E} = -\nabla \phi$. The electrical field intensity is then the solution of the well-known Poisson equation of plasmadynamics,

$$\nabla^2 \phi = -\rho_e/\varepsilon . \tag{151}$$

The initial values and boundary conditions of the plasma model for a numerically stable procedure have been found through a series of sustained research efforts discussed in Shang and Surzhikov (2005), Shang et al. (2005b), Shang et al. (2006a), Surzhikov and Shang (2004), and Shang (2005b). A key element in determining the boundary conditions is specifying the electron number density on the cathode for the secondary emission phenomenon. This physical

requirement is met by requiring the normal component of the electron flux at the cathode to be proportional to the ion counterpart,

$$\mathbf{\Gamma}_e \cdot \mathbf{n} = \gamma\, \mathbf{\Gamma}_+ \cdot \mathbf{n} \tag{152}$$

where $\gamma$ is the secondary emission coefficient. This coefficient depends on the material of the cathode and intensity of the electrical field. Raizer (1991) has extensively investigated the influence of $\gamma$ on the structure of the gas discharge. For direct current discharges in nitrogen, a value from 0.01 to 0.1 is recommended. A range of the secondary emission coefficients for direct current glow discharges has been used in a large group of numerical simulations (Surzhikov and Shang, 2004; Shang, 2005b). The values of $\gamma$ from 0.1 to 0.3 actually improve the computation stability, and the agreement between computed results and experimental data justifies their adaptation.

This developed and validated plasma model is implemented into the magneto-fluid-dynamic equations for low Magnetic Reynolds number flows. In order to improve the computational efficiency, the iterative convergence is accelerated through a multi-grid technique using a three-level mesh sequencing (Shang et al., 2006b). In essence, the present work is focused on improved physical fidelity and numerical efficiency of computational simulations in direct support of the MHD channel operation and revolutionary technology development in the Air Vehicles Directorate, Air Force Research Laboratory.

### 3.3.3  Results

Physical and computational fluid dynamic models of a direct current discharge (DCD) in a hypersonic inlet with plasma induced compression is applied for analysis of experimental data (Shang et al, 2006a, Shang et al., 2006b). The developed computing model allows us to simulate a DCD in hypersonic gas flows in two possible configurations. The first one is the DCD between a sectionalized cathode on the bottom surface of the channel and a solid anode on the top surface of the channel. This configuration of the DCD in a hypersonic flow was numerically studied in Shang et al. (2006b).

The second configuration of the DCD installs electrodes (cathode and anode) on the upper and lower surface (see Figure 59), and the developed model allows taking into account any number of such coupled sections of electrodes. To describe aerodynamic structure in the hypersonic inlet a three-dimensional numerical simulation model has been developed. This three-dimensional model can be adapted for modeling the electrodynamic and aerodynamic interaction in hypersonic inlet channels of practical geometry. A cylindrical geometry is modeled in Section 4.5 of this report. Many of the three-dimensional results from this model are shown in Section 4.4 of this report. A more detailed description of this computing model, which was developed by Surzhikov and Shang, is presented in Surzhikov and Shang (2004), Shang (2005b), and Shang et al (2006b).
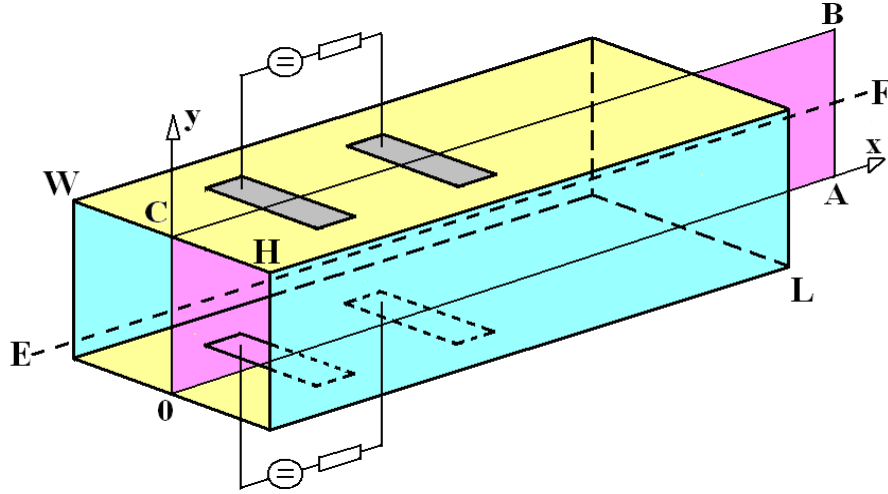
**Figure 59. Schematic of Electrode Arrangement in a Rectangular Inlet**

The general objective of the numerical study performed in this work is the analysis of a relation between the electrodynamic and aerodynamic phenomena through the Joule heating process. Therefore a major portion of the research results are concentrated on the volumetric heating and the amplification of the electromagnetic perturbation by the viscous-inviscid interaction.

All numerical simulations were conducted under identical operating conditions of the nominal Mach 5 plasma channel at AFRL/RB at the operating condition of a Mach number of 5.15, a stagnation pressure of 370 torr (49.33 kPa), a stagnation temperature of 270 K, and a free-stream Reynolds number, based on the model length, of $1.078 \times 10^5$. The freestream in the test chamber can be characterized as $U_\infty = 676$ m/s, $p_\infty = 78.38$ pascal, $T_\infty = 45$ K, and $\rho_\infty = 0.636 \times 10^{-3}$ kg/m$^3$. A couple of electromotive forces (EMF) are simulated to assess the electron collision process. Numerical results are computed for two EMFs, 500 and 700 volts across the electrodes.

Figures 60 through 66 summarize the numerical simulation results for the inlet of a direct current discharge of $V_C = 500$ V. It is assumed that the dielectric surface of the channel and surfaces of the electrodes are cooled and maintained at a temperature of $T_w = 300$ K.

The key mechanism of the magneto-aerodynamic compression in the inlet channel is the local heating of the gas medium. Isolines of the Joule thermal heating are shown in Figure 60. It is distinctly visible near the edges of the electrodes where the area of increased plasma current takes place. This electrical energy dissipation from electric current flow in the plasma leads to the strong change of the flow field structures of the gas stream.

For the electron collision processes for plasma generation, the electrical potential within the rectangular inlet and across the cathodes and anodes is depicted in Figure 61. The high voltage domains over the anodes are clearly displayed. The applied electric field actually extends over the entire interior of the rectangular inlet. The interaction of the electric potential across the channel from each pair of the electrodes on the sidewalls is also easily recognizable.
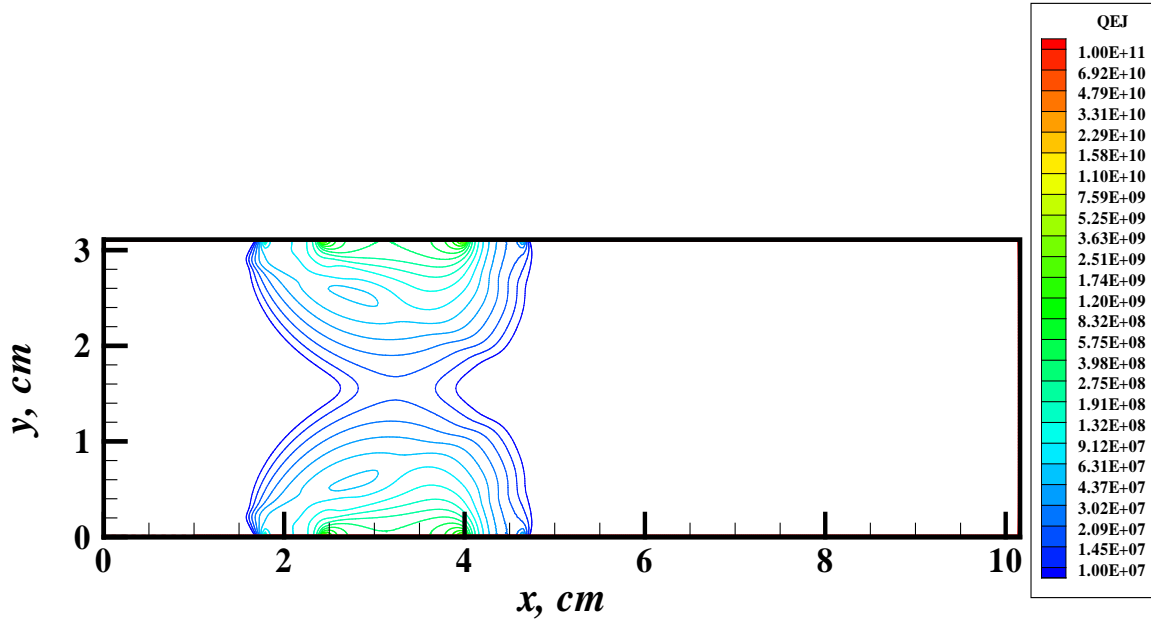
Figure 60. Joule Heating Contours; $E$=500 volt, $T_w$ = 300 K, and $\eta$ = 0.1
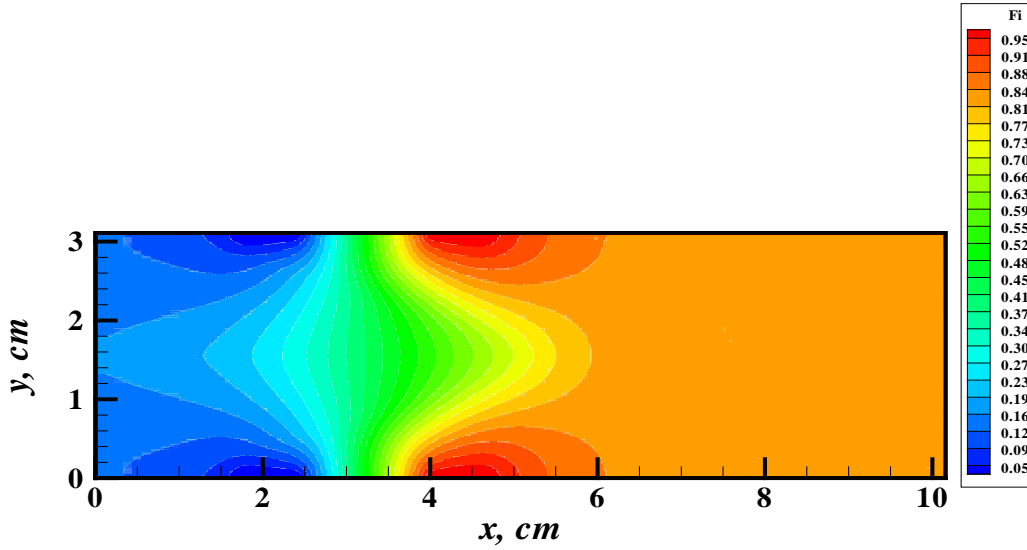


Figure 61. Electric Potential Distribution; $E$=500 volt, $T_w$ = 300 K and $\eta$ = 0.1

The distribution of electric current density inside the discharge is given in Figure 62. The greatest quantity of the current density is clustered near the edges of electrodes. Such distribution of current density generates areas of the greatest power of thermal emission, also in the vicinity of the edges of the electrodes. Higher current density is also promoted by a sharp growth of the intensity of the electric field near the edges of the electrodes. Distributions of nondimensional electric field intensities on the inlet surfaces are seen in Figure 61. Near the sharp edges of the electrodes the electric field intensity increases greater than three times that of the rest of the electrode surface. To determine a dimensional quantity of the electric field from this figure it is necessary to use a conversion constant of $E/H$ =160.77 V/cm.
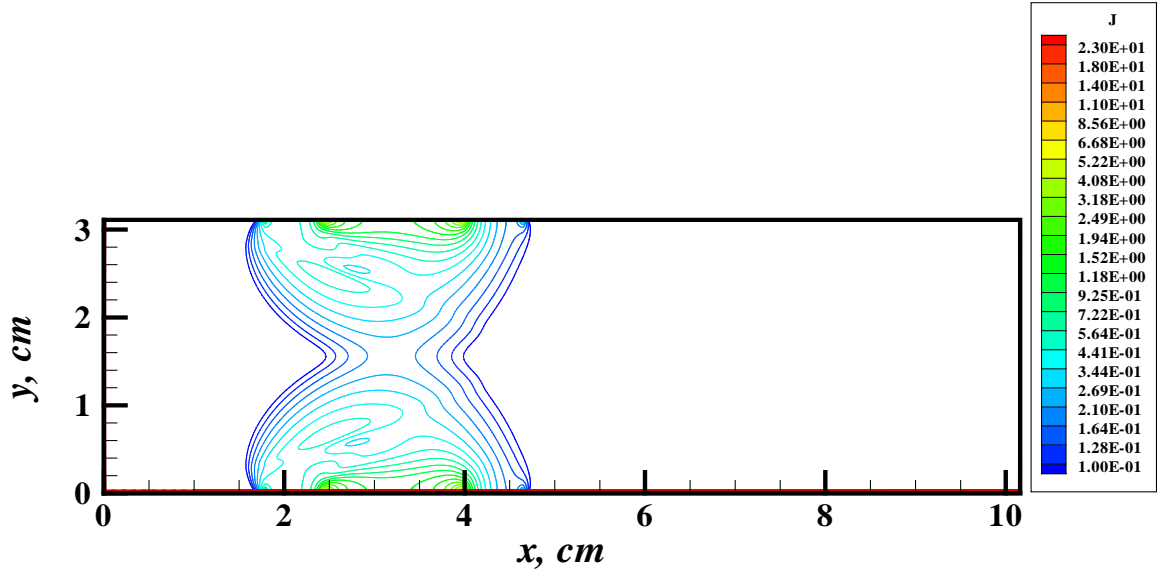
**Figure 62. Current Density (in A/cm$^2$), E=500 volt, T$_w$ = 300 K; $\eta$ = 0.1**

In the areas of the intensive electric field, the ionization processes are greatly enhanced, therefore at the edges of the electrodes increased electron concentrations are observed. This behavior is identical to both sets of electrodes on opposite sidewalls. The distribution of electron concentrations over the entire calculation domain is presented in Figure 63. The normalized contours are based upon a reference value of $10^{10}$/cm$^3$.

The current density of the direct current discharge is the net balance of the flux density of electrons and ions. Only in the areas near the electrode does the electric current density indicate a high concentration. The present numerical simulation actually captures the physics. From these calculations, the electric current flows mainly between the cathode and anode. In order to create a Lorentz force to accelerate the gas stream or to generate an outward flow disturbance from the sidewalls, a transverse magnetic field is required. In fact, the present investigation offers a unique insight for intensifying the magneto-aerodynamic interaction for high-speed flow control.
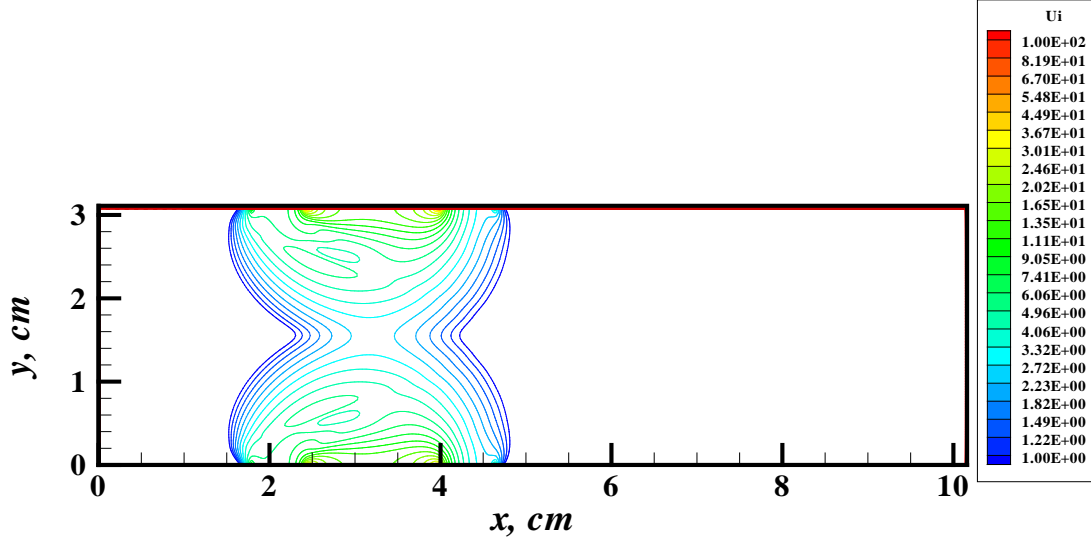
Figure 63. Electron Concentration $n_e/n_o$; $E$=500 volt, $T_w$ = 300 K; $\eta$ = 0.1, and $n_o = 10^{10}$ cm$^{-3}$
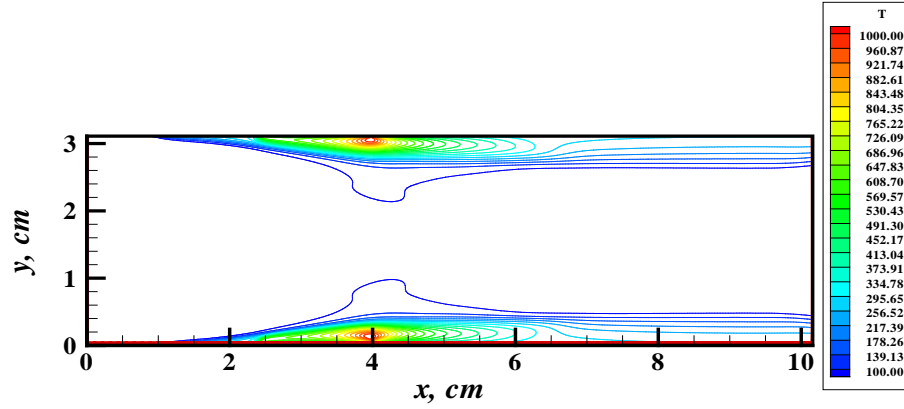


Figure 64. Temperature Contours; $E$=500 volt, $T_w$ = 300 K; and $\eta$ = 0.1

It is obvious in Figure 64 that high local temperature regions are closely associated with the intense plasma activity at the electrodes. It should be stressed that because surfaces of the channel are cooled, the high-temperature spot is observed inside the gas stream, instead of on the surface. In fact this location is on the outer edge of the cathode layer. This physical characteristic is the direct consequence of the energy dissipation of an electric current transmitting in a semi-conducting medium such as the weakly ionized gas in the rectangular inlet. The heat addition to the boundary layer over the sidewalls increases the displacement thickness to act as a flow diverter which in turn produces a plasma induced compression.

Figure 65 presents the pressure distribution in the inlet channel. The plasma discharges engender additional growth of the displacement thickness of the sidewall boundary layer. The outward flow deflection toward the inviscid core triggers compression waves that coalesce into a pair of oblique shock waves that act as a side compression on the flow coming into the inlet. The net result is an increased static pressure from this magneto-aerodynamic interaction. The plasma induced compression waves have a steepened oblique wave angle to intercept each other

upstream ($x \sim 5$ cm) of the location where this occurs in the flow with a deactivated direct current discharge. The compression shock waves can produce a static pressure rise on the sidewall that attains twice the value of a constant cross-section rectangular inlet.
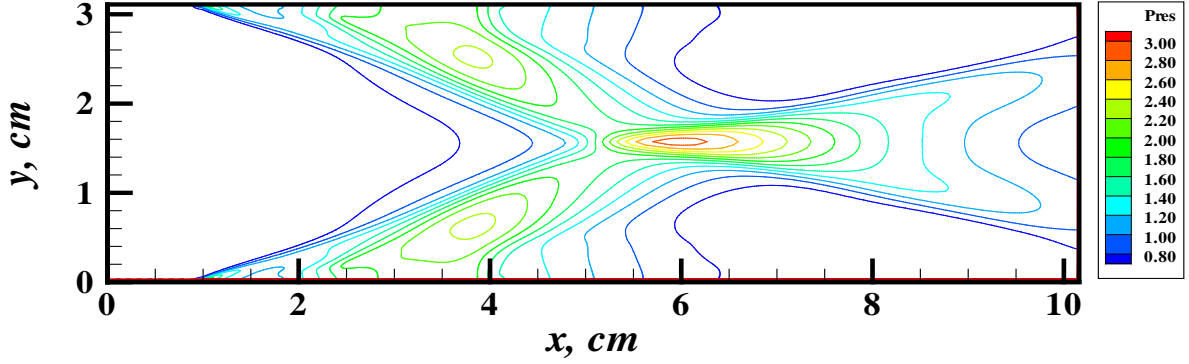


Figure 65. Pressure Contours in Torr; $E = 500$ volt and $T_w = 300$ K
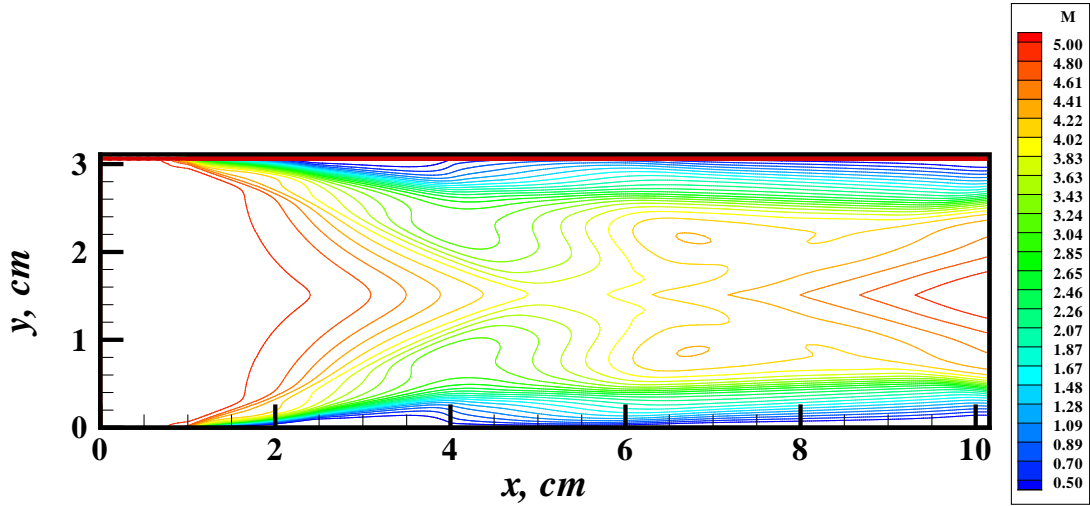


Figure 66. Mach Number Contours; $E$=500 volt and $T_w = 300$ K

It is observed in Figure 66, that the plasma discharge generates a sharp local change in pressure that leads to an appreciable change of the aerodynamic coefficients. However, there is a rather large change in the pressure coefficient, $C_p$, but not the skin-friction coefficient $C_f$. The relatively small change in the skin-friction is incurred by the mutual cancellation of the rise and fall of the surface shear in the adverse and favorable pressure domains. It is also noted, that an appreciable change of pressure entails significant inhomogeneities over the entire flow field within the inlet. The induced perturbation to the flow field is illustrated by the Mach number contours shown in Figure 66.

As mentioned previously, the presence of the local areas of thermal emission near the electrodes leads to a strong heating of the inner region of the boundary layer over the inlet sidewalls. The convective heat flux distribution on the interior surfaces of the inlet have been computed; the results are fully substantiated by early experimental research findings (Shang et al., 2006a).

The qualitative features of a plasma discharge inside a hypersonic inlet remain the same with the change of the key driving mechanism of the applied electric field intensity. The quantification of the interaction of a gas discharge with the gas stream is not only dependent on the discharge characteristics, but also on the surface temperature of the channel and electrodes. In particular, the electrode surface temperature plays a significant role in intensifying the magneto-aerodynamic interaction.

Figures 67 through 71 present the calculations of the identical inlet, but with an increased voltage drop between the electrodes to $V_c = 700$ V. To keep the present investigation systematic, the inlet surface temperature is kept the same as in the previous case. In other words, the plasma is only generated by a stronger externally applied electric field intensity.

With the increased voltage drop between the electrodes, $V_c$, all electrodynamic functions are further amplified by the viscous-inviscid interaction caused by the Joule heating (see Figure 68 for concentrations of charged particles and Figure 69 for electric current densities). All these magnetoaerodynamic interactions lead to an increase in local temperature by a greater Joule heating as shown in Figure 70. A strengthened inlet electromagnetic compression is also seen in Figure 71.
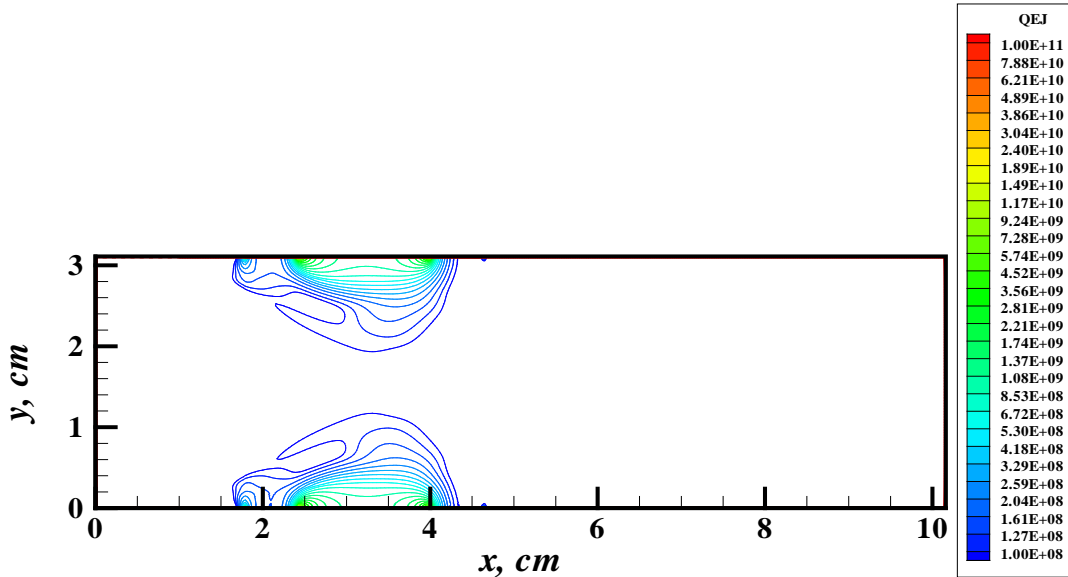


**Figure 67. Joule Heating; $E$=700 volt, $T_w = 600$ K, and $\eta = 0.1$**

As it was already mentioned, the main reason for perturbation of all aerodynamic structures is the local heating of the gas by a plasma discharge. The energy conversion can be controlled by the coefficient of the Joule thermal emission ($\eta$=0.1). The amount of energy transfer is prescribed by this parameter, as it has been detailed in previous efforts (Surzhikov and Shang, 2004; Shang, 2005b). Numerical simulation results for the case at a higher electric potential of 700 V and the identical Joule thermal emission is depicted in Figure 67. At a higher cathode fall, the Joule heating expands to include the upstream edges of the cathode in comparison with the lower electric potential of 500 V (Figure 60). These results once again confirm the necessity to devise adequate thermo-physics and kinetic models of gas heating in a plasma discharge.

A main feature of the increased electric field intensity is the additional charge particles, both ions and electrons in the field of collision. The normalized electron number density normalized by a reference number of $10^{10}$ per cubic centimeter is given in Figure 68. As it will be discussed shortly, the visible intensity of the magnetoaerodynamic interaction does not appreciably increase. This is because the heating of the gas has more volumetric character and the force exerted on the flow stream becomes more distributed.

There are strong inhomogeneous electric fields near the electrodes like that appearing in Figure 61. This drastic varying electric potential generates an inhomogeneous electron concentration above the electrodes and the local character of volumetric heat release in the gas. Isolines of electron concentration and current density are shown in Figures 68 and 69 respectively.

For the case of constant and lower temperature surfaces of 300 K, the highest current density of the direct current discharge is observed over the electrodes (see Figure 69), and as a consequence, the strongest influence of a plasma discharge on the flow field structure is reached at that location. Computational results fully substantiate this observation and receive direct support from experimental data (Shang et al., 2006a).
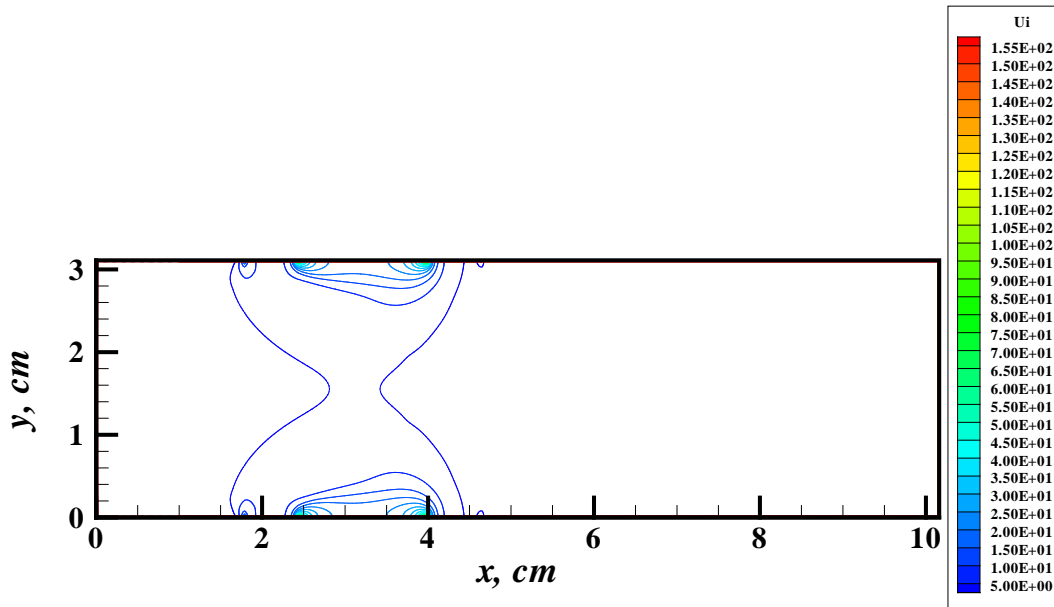


Figure 68. Electron Concentration $n_e/n_o$; $E$=700 Volt, $T_w$ = 300 K, $\eta$ = 0.1, and $n_o = 10^{10}$ cm$^{-3}$
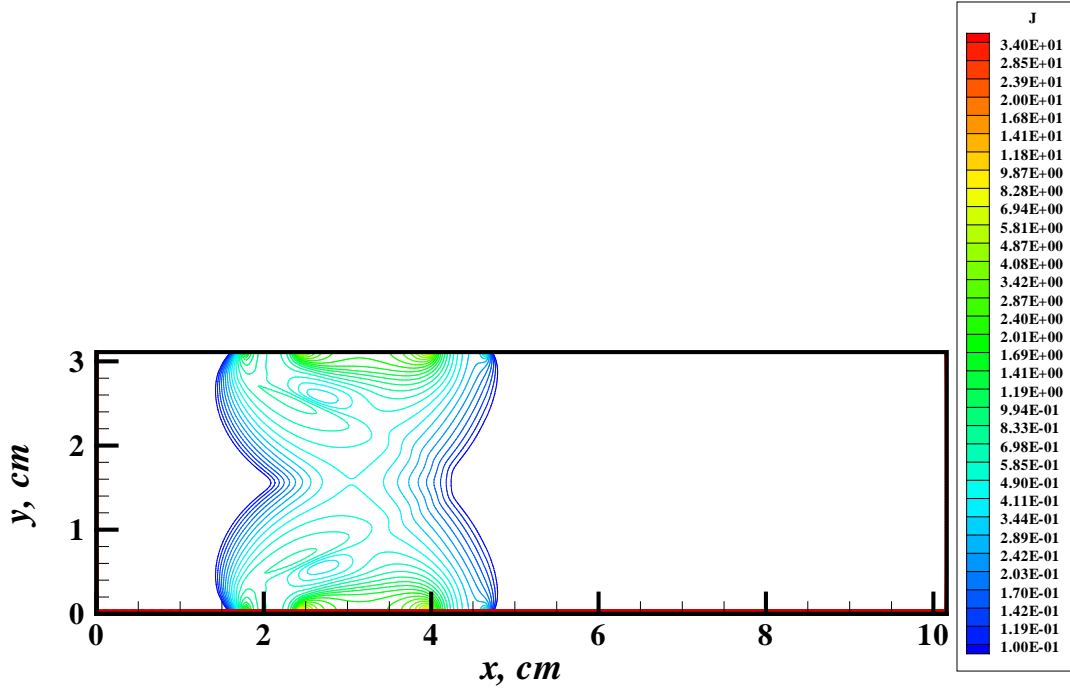
Figure 69. Current Density in A/cm$^2$; $E$=700 volt, T$_w$ = 300 K, and $\eta$ = 0.1
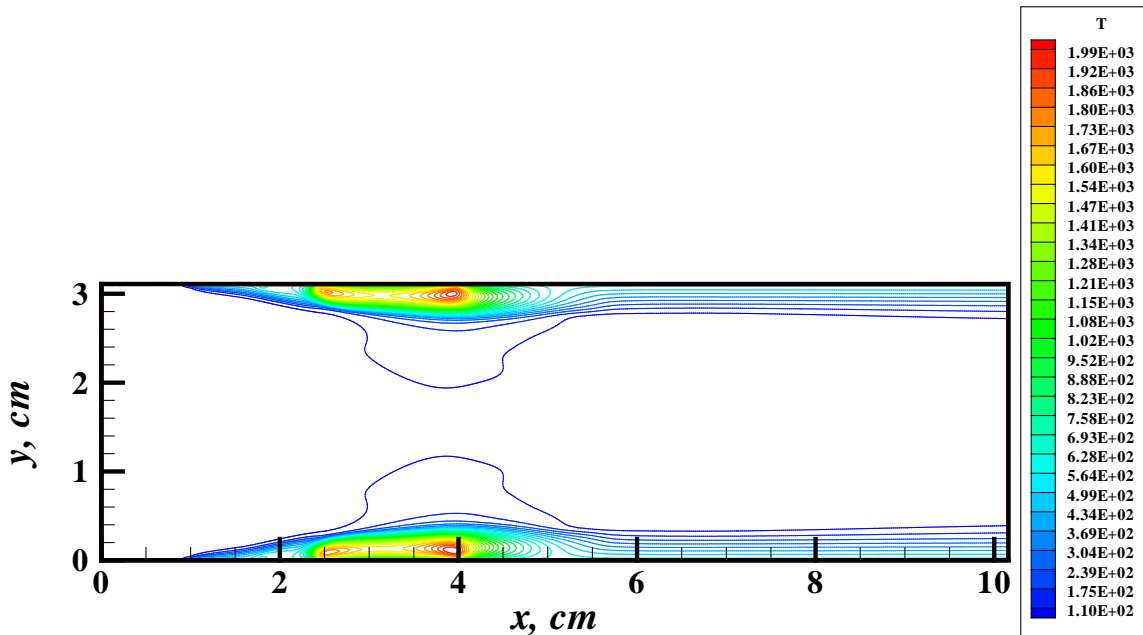


**Figure 70. Temperature in the Inlet in Kelvin; $E$=700 volt, T$_w$ = 600 K, and $\eta$ = 0.1**

The current density of the surface plasma discharge is presented in Figure 69 for the higher electric field intensity of 700 V. At the higher applied electric field intensity, a low current is flowing between the electrodes across the hypersonic inlet. This interference is also noticed at the lower applied electric field intensity. In short, for the range of externally applied electric

fields studied, the surface plasma discharge retains essentially the similar key features. However, the heat transfer through the higher discharge electric current density increases significantly in direct contrast to the lower plasma surface discharge. Additional hot spots now appear at the leading and trailing edge of the cathode. These high temperature regions are concentrated mostly over the plasma sheath, but still deeply embedded within the inner portion of the boundary layers over the inlet sidewalls. The maximum temperature from the computing simulation attains 1200 K, unfortunately there are no available experimental data for verification.

To investigate the influence of a localized plasma discharge on flow field structure of a hypersonic inlet, a special analysis of two calculations was performed. In one case all electrodes on both surfaces of the inlet were heated to a temperature of $T_w = 600$ K, to mimic the electrode surface temperature from experimental observations (see Figure 70), while the inlet dielectric surfaces were heat isolated (Menart et al, 2003b; Kimmel et al., 2004a). The plasma discharge was not activated. In the second group of calculations, a plasma discharge at $E = 800$ V, $I = 32.6$ mA, $R_0 = 20$ kohm, and $\eta = 0.1$ was conducted. The aerodynamic structure inside the hypersonic inlet with heated electrodes, but deactivated direct current discharge, is different than the magnetoaerodynamic interaction. A plasma discharge produces perceptible changes in the flow field structure within the inlet channel. General reasons for these wide variations are volumetric regions of heated gas above heated electrodes. The computed results show that the plasma discharge generates additional pressure from the compression waves, but does not alter the total friction coefficient.
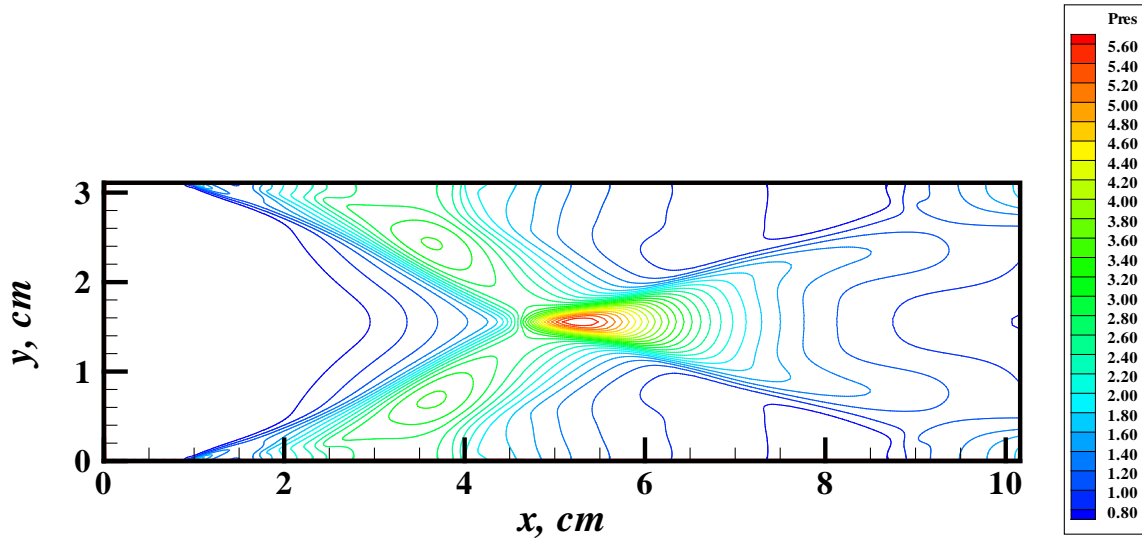


Figure 71. Pressure Distribution in Torr; $E = 700$ volt and $T_w = 300$ K

The pressure distribution of the magneto-aerodynamic interaction at the Mach number of 5.15 that duplicates the experimental condition in the hypersonic plasma channel of AFRL is presented in Figure 71. In this presentation, the induced oblique shock waves by the plasma surface discharged are clearly demonstrated by the interdisciplinary computing simulation using a drift-diffusion weakly ionized gas model. The computed pitot pressure results have good agreement with data. The direct comparison of the pitot pressure profile indicates a maximum discrepancy as low as 4.7% and is fully supported by an independent calculation published recently (Shang et al., 2006b) by the same authors.

70

### 3.3.4  Summary

The computing simulations describing the interaction of an electro-discharge and a high-speed flow within a hypersonic inlet has been successfully applied for analyzing a set of path-finding experimental data. The interdisciplinary computing simulation is based on the coupled solutions of the Navier -Stokes equations and equations describing electrodynamic processes in a quasi-neutral plasma.

Numerical results for the partially ionized air at a Mach number $M = 5.15$ and parameters of $V_\infty = 676$ m/s, $\rho_\infty = 0.636 \times 10^{-5}$ g/cm$^3$, $p_\infty = 783.7$ pascal, $T_\infty = 45$ for the unperturbed gas stream are presented. Different direct current discharge conditions were conducted to bracket the uncertainty of the experimental conditions. The numerical results indicate a similar discharge pattern and a range of magnetoaerodynamic interactions for the different conditions.

The hypersonic inlet calculations with direct current discharge showed that the use of surface gas discharges on the top and bottom of an inlet channel leads to appreciable additional compression in the flow field. A general agreement has been reached with an independent computational investigation using a different numerical algorithm, and more importantly good agreement has been reached with experimental measurements from the hypersonic plasma channel of AFRL. The future application of this phenomenon in practical aero-physics is interesting.

## 4.0　EXPERIMENTAL INVESTIGATION OF MHD FLOW INTERACTIONS

Section 4 of this report covers the experimental portion of the Plasma Modeling contract work. Some numerical calculation results that support the experimental work are also presented here. They are presented in this section, instead of Section 3, because they are compared to the experimentally obtained values. A number of very interesting experiments were done as part of this work. In addition, a number of diagnostic tools for magneto-fluid-dynamics research in the Mach 5 wind tunnel at WPAFB have been developed. Section 4 of this report covers Tasks 2 and 4 of the Plasma Modeling Program.

The diagnostic tools developed as part of this work are a small, high speed pitot pressure probe and two different types of force measurement devices that can determine the change in lift and drag on a body caused by plasma discharges and magnetic fields. The first three subsections of this section of this report are organized around these three diagnostic tools which were developed as part of this work. These diagnostic tools were used to investigate different aspects of the plasma, magnetic field, flow field interaction. The last two subsections in Section 4 of this report present measured and computational results for flow in a channel altered by plasma discharges. Section 4.4 deals with a square channel, while Section 4.5 deals with a round channel.

## 4.1　High Speed Pitot Pressure Measurements over a Flat Plate

### 4.1.1　Introduction

At this time it is known that a plasma discharge applied to a high speed flow will alter the characteristics of that flow (Kuo and Bivolaru 2003, Leonov et al. 2003, Leonov et al. 2002; Leonov et al. 2001; Samimy et al., 2004; Kolesnichenko et al., 2004; Menart et al., 2004a; Menart et al., 2004b; Kimmel et al., 2004a; Shneider et al., 2003; Knight, 2003). The reason for this alteration is the direct heating of the gas by the plasma discharge. It is also known at this time that the application of a magnetic field to a high-speed flow with a plasma discharge further alters the flow field (Bityurin et al., 2003; Bobashev et al., 2004; Staats et al., 2000; Bityurin et al, 2004; Borghi et al., 2004; Meyer et al., 2004; Takizawa et al., 2004; Forghi et al., 2004; Shang et al., 2004; Knight, 2004; Shang, 2001; Shang, 2002b; Menart et al., 2003b; Kimmel et al., 2004b). In this case, however, the physical reason why this alteration takes place is more uncertain. It also needs to be noted that a plasma interacting with the electric fields required to generate the plasma can alter flow fields. This has been shown to be an effective means of modifying low speed flows by Roth (2000) and Corke et al. (2004). The types of plasmas that use the electrohydrodynamics phenomena are called dielectric barrier discharges. In this section a pulsed DC discharge with exposed electrodes is used in a high speed flow environment, and thus the plasma effects should be thermal in nature. In addition, a magnetic field is applied to obtain magneto-fluid-dynamic interactions. Investigations into dielectric barrier discharges (DBDs) that operate on an electrohydrodynamic interaction are the topic of Section 5 of this report.

Depending on how the discharge is applied, two different mechanisms of heating can be present. The quickest acting of these mechanisms is direct Joule heating of the air by the current running through the plasma discharge. The ionized air offers resistance to the current passing through it and thus there is a Joule heating effect. In this report Joule heating is the volumetric heating of the air flow. The other type of heating caused by the plasma discharge is an indirect mechanism. This indirect mechanism is the plasma heating of the model and the electrodes located within the

model. If heat is going to the model and the electrodes, less heat is available to heat the air. After a short period of time, heat from the model and the electrodes can be released back into the air flow. This mechanism will be referred to as surface heating of the air flow. This heating mechanism is slower than the volumetric heating mechanism. Menart et al. (2004a) and Kimmel et al. (2004a) have presented results showing that both of these heating mechanisms are showing themselves for long time frames. In this work the plasma effects will be studied on short time frames.

In addition to looking at the heating effects of a plasma on the hypersonic flow field, this work will look at the magnetic field effects when a magnetic field is applied to a hypersonic flow with a plasma. Even though a number of investigators have studied magnetic fields, it is still not understood exactly how the magnetic field alters the high speed flow field when there is a plasma discharge. From theory (Mitchner and Kruger, 1973) and from experimental work done by Menart et al. (2003b) it is known that there are two possible mechanisms by which a magnetic field can affect the flow field in a hypersonic wind tunnel with a plasma discharge. If it is accepted that a plasma alters a hypersonic flow by heating, then it must be realized that anything that alters the plasma will alter the heating affect. A reasonable name for this effect would be the "indirect Lorentz force effect". That is, the magnetic field alters the plasma, which in turn means the heating within the discharge changes, which in turn alters the flow field. This has been shown to occur by Menart et al. (2003b).

The other Lorentz force effect that is of great interest to investigators in the MHD discipline, as applied to high-speed air flows, is what will be referred to as the "direct Lorentz force effect". The direct Lorentz force effect is where the magnetic field applies a force to the plasma, which in turn transmits this force to the flow field. This happens independent of the plasma heating. Up to this time there are few investigators who have claimed to be able to demonstrate this effect in their experiments. A couple of experimental groups who indicate that they have a direct Lorentz force effect are Meyer et al. (2004) and Zaidi et al. (2006). Meyer et al. (2004) show the Lorentz force effect when a magnetic field is applied to a Mach 3 flow with an RF and DC discharge. These investigators show that the Lorentz force changes the density fluctuation spectrum in a supersonic flow. Zaidi et al. (2006) use a magnetic field to accelerate a plasma discharge through a high speed flow, which in turns supplies momentum to the high speed flow. They call this plasma discharge configuration a "snowplow". In this work experimental data and observation will indicate that the indirect Lorentz force mechanism is at work; however, no proof is given to show whether a direct Lorentz force is present or not. At this time there is no doubt that there is a Lorentz force applied to the plasma discharge. This is obvious from experimental observations (Menart et al., 2003b) and from looking at the Lorentz force equation (Griffiths, 1981). It is also reasonable to assume that there is a direct Lorentz force effect. The question is, is this direct Lorentz force significant?

A primary result shown in this section of this report is that a Mach 5 flow responds in less than a few milliseconds to the application of a plasma discharge. The response of the flow should be on the order of the residence time of the air in the discharge. Utilizing freestream conditions the residence time can be calculated to be 0.1 ms. In the boundary layer, the flow is much slower on average, and the residence time should be larger. Another physical phenomenon studied in this paper is the effect of pulsing a discharge at different frequencies.

### 4.1.2   Experimental Facility

To carry out this work a piezoresistive pressure sensor chip is used. This pressure sensor is a relatively small, temperature compensated sensor that works at low pressures. A fraction of a torr differential pressure can be sensed at pressures less than a torr. The full scale differential pressure range of the sensor used in this work is 41 torr with an accuracy of ±0.021 torr. In the past, a pitot probe with a Baratron type absolute pressure transducer was used. The response time of this pitot probe assembly was a little less than 1 second. The response time of the Baratron type pitot probe was slow because a long tube, 89 cm, was required to connect the tube located in the Mach 5 flow to the pressure transducer. The pressure transducer had to be kept outside the flow field because of its large size. It is very difficult to find small size pressure transducers that are capable of measuring pressures in the 0 to 40 torr range. To speed up this measurement a pressure transducer small enough to be placed in the flow field without causing too much blockage to the Mach 5 flow had to be found. The pressure transducer found turns out to be a piezoresistive pressure sensor chip attached to a ceramic substrate that is 1.3 cm long by 1.5 cm wide by 0.5 cm thick. This size transducer can be placed behind the model or behind the strut connected to the *x-y-z* translator mechanism, so that very little blockage of the flow occurs. A small tube is run from the piezoresistive pressure sensor chip on a substrate to a location above the plate where a pitot probe pressure measurement is desired. The location where the pressure is sensed by the pitot probe will be referred to as the tap location. Because this tube is so much shorter than the tube used originally, the time response of this pitot probe is greatly enhanced. Based on data taken as part of this work, it appears this new pitot probe can respond to pressure changes on the time frame of a few milliseconds. This is more than a two orders-of-magnitude improvement over the old pitot probe system.

No response time data of the piezoresistive pressure sensor chip is available from the manufactures. It must be remembered that the response of the pitot probe assembly is a function of more than just the response of the piezoresistive pressure sensor chip. The length of tubing from the chip to the measurement location has a large effect on the pitot probe response. In addition, experimental work indicates the response time is a function of the velocity of the flow in which the pitot probe is being used. For static pressures the response can be rather slow, while for high speed flows the response is faster. This is due to a capacitive effect of the tube connecting the measurement location to the piezoresistive pressure sensor chip.

Two arrangements of pitot probes with the piezoresistive pressure sensor chips were utilized in this work. Both of these arrangements are shown in Figure 72. The first arrangement is where the pitot probe is attached to an *x-y-z* translator mechanism. The actual piezoresistive pressure sensor chip cannot be seen in Figure 72 because it is located just out of the picture attached to the strut that connects to the *x-y-z* translator mechanism. As can be seen in Figure 72 the actual sensing portion of the tube is made of a stainless steel tube that has an inside diameter of 1.8 mm and outside diameter of 2.3 mm. To protect the piezoresistive pressure sensor chip from the plasma discharge the stainless steel tube is connected to the piezoresistive pressure sensor chip with Tygon tubing. The total length of tubing from the tap location to the piezoresistive pressure sensor chip is 7.6 cm. The second pitot probe utilized was attached to the model. In Figure 72 this is the probe in the back with the tube running downward. Just like the first fast pitot probe discussed, this pitot probe is made of stainless steel and there is Tygon tubing between the stainless steel tubing and the piezoresistive pressure sensor chip. The inside diameter on the stainless steel tube is 1.1 mm and the outside diameter is 1.6 mm. The length of the tube is

10 cm. This pitot probe had to be used when the electromagnet is in operation. As shown in Figure 73, the electromagnet, the object in the center of the picture, is placed right over the test section of the wind tunnel. When this is done the *x-y-z* translator mechanism needs to be removed from the tunnel, otherwise the magnet will not fit over the test section of the wind tunnel.



Figure 72.  Flat Plate Model with Translator Mounted Pitot Probe and Model Mounted Pitot Probe
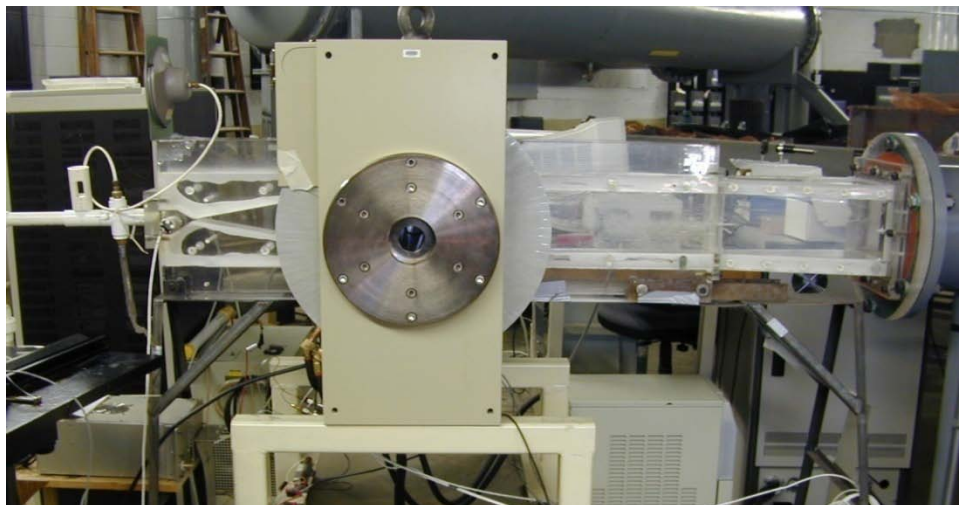


Figure 73.  Mach 5 Wind Tunnel with an Electromagnet

The electrical signal from the piezoresistive pressure sensor chip is sent to an amplifier and then to a National Instruments M-Series high speed data acquisition board. All the data in this section of the report was sampled at a rate of 12,500 samples per second. This means the pitot probe pressure, discharge voltage, and the discharge current were sampled every 80 μs. The voltage readings were taken at the two electrodes using a voltage divider to reduce the voltage across the electrodes by a factor of 445. This was done to protect the data acquisition equipment. The current was measured just before the grounded electrode by simply measuring the voltage across

a 43 ohm resistor. These means of measuring the current and the voltage have response times much quicker than the 80 µs at which the data is sampled.
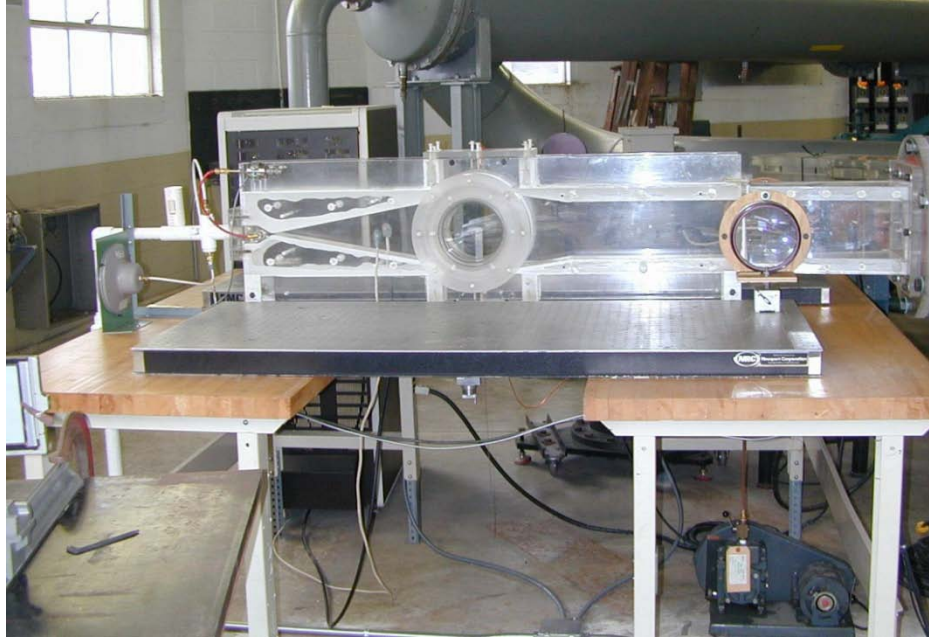


**Figure 74. Mach 5 Wind Tunnel without Electromagnet**

The wind tunnel in which these measurements are taken is shown in Figure 74 without the electromagnetic and in Figure 73 with the electromagnet. The acrylic plastic tunnel shown in this figure is a nominal Mach 5, hypersonic wind tunnel that is supplied with dried air from high-pressure bottles located outside of the building where the wind tunnel is located. While the nominal Mach number of the wind tunnel is Mach 5, the centerline Mach number of the wind tunnel at the test section was measured to be 5.15 without any model located in the tunnel. The test section is 38.6 x 17.8 x 7.4 cm (flow direction x height direction x spanwise direction) in size and it is located at the exit from the supersonic nozzle. In Figure 74 the test section is where the circular portal is located. The undisturbed core of the flow in the test section is about 15 cm high by 3.8 cm in the spanwise direction. For the results presented in this section the hypersonic wind tunnel is run at a stagnation pressure of 450 torr. This results in a static pressure of 0.8 torr at the test section. The stagnation temperature of the air entering the wind tunnel varies depending on the outdoor air temperature. Typically the stagnation temperature at the inlet to the nozzle of the wind tunnel is around 270 K. This number can vary by as much as 15 K. A stagnation temperature of 270 K results in a static air temperature of 42 K in the test section. Even though this temperature is well below the liquefaction temperature of nitrogen at atmospheric pressure, the nitrogen stays in the gaseous state because of the low static pressure at the test section of the wind tunnel. The back pressure at the tunnel exit is maintained between 5 to 8 torr by a 2800 m$^3$ vacuum tank and a number of vacuum pumps. This wind tunnel has the very desirable feature of being able to be run continuously. A more detailed description of this wind tunnel can be found in Shang et al. (2003).

Magnetic fields are produced with a water cooled GMW electromagnet. This magnet is capable of generating a steady state magnetic field up to 0.9 tesla between 25 cm diameter poles spaced 15.8 cm apart. Through the center of the poles are 5.1 cm diameter holes so the plasma discharge

on top of the model may be viewed from the front and back of the tunnel. Higher magnetic fields can be generated if the poles are brought closer together; however, this is not possible in this experimental setup as the test section of the wind tunnel is placed between the poles of the magnet. The placement of the magnet on the wind tunnel can be seen in Figure 73. The applied magnetic field is orientated so the field lines run spanwise across the wind tunnel. The plasma discharge is orientated so most of the current travel is aligned with the flow direction. This means the magnetic field is perpendicular to most of the current motion.

The model placed in the wind tunnel can be described as a flat plate with a sharp leading edge (see Figures 72 and 75). The leading edge constitutes half a wedge. This model is 0.6 cm thick, 5.1 cm wide in the spanwise direction, and 10.2 cm long in the flow direction. The model is made of a machinable fiberglass.
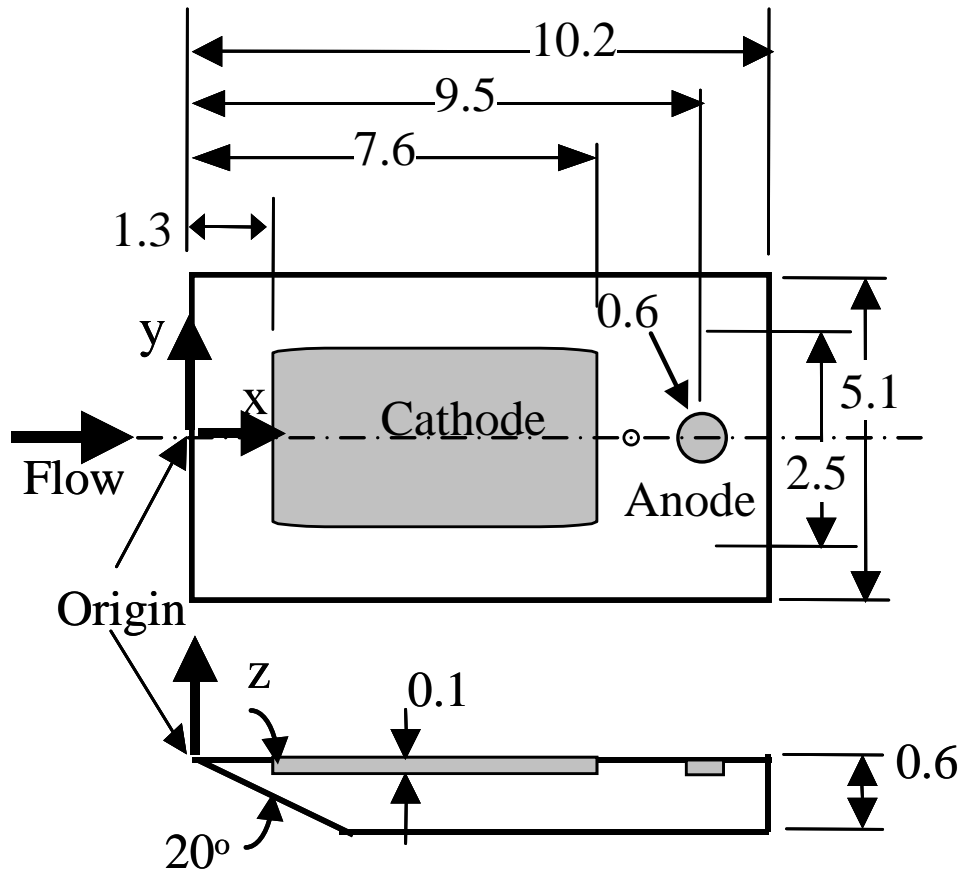


**Figure 75. Dimensions for Flat Plate Model (all dimensions are in cm)**

Embedded into the flat surface of the model are two electrodes used to generate a plasma discharge. These electrodes are made of copper and they are placed flush with the surface of the model. The large upstream electrode is the cathode and the small downstream electrode is the anode. These can be switched, but the discharge is much more constricted when this is done.

Two types of power supplies were used to generate the results presented in this section of the report. All of the plasma results without a magnetic field were generated with a TREK high voltage power amplifier. This power supply is capable of delivering 5000 volts and 80 mA of current at frequencies up to 75 kHz. This device takes a voltage signal from a digital-to-analog

National Instruments data acquisition card and amplifies it by a factor of 1000. Thus square waves, sine waves, or other sorts of waves can be delivered by this power supply. In this work square waves are used to pulse the discharge on and off. The waves delivered by this device are voltage waves. The output voltage of this power amplifier is what is controlled. This causes difficulties when dealing with plasma discharges, which should be current controlled devices. For this reason the output current signals sometimes do not look like square waves, even when a very nice square wave is entered into the power amplifier. Even the voltage signals do not come out as square waves at times. This behavior is caused by the current-voltage characteristics of the plasma discharge. The power amplifier has a control for setting the peak output current. This option is used in this work.

For the magnetic field results a Universal Voltronics DC electrical power supply was used. This power supply is capable of delivering 800 mA of current and 10,000 volts of electrical potential. The output from the power supply can be set to a specified current or a specified voltage. This power supply was operated in a current-stabilized mode. A typical discharge at 80 mA of current and approximately 700 volts is shown in Figure 76. Since the power supply was set to operate in the current-stabilized mode, the current remained constant and the voltage fluctuated to maintain this current.
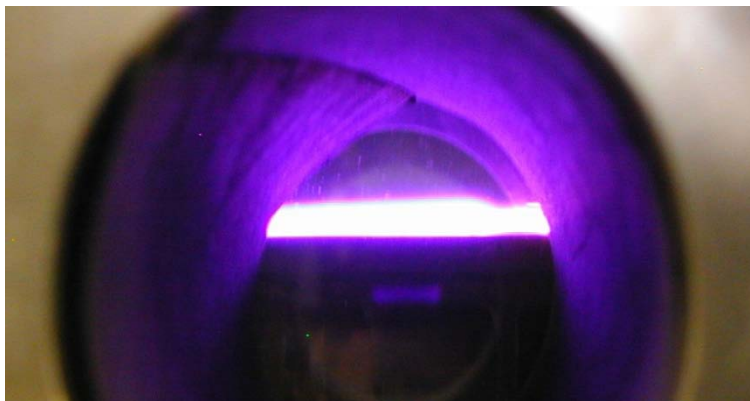


**Figure 76. Steady 80 mA Discharge in Mach 5 Flow**

To obtain a current square wave with the Universal Voltronics DC power supply an electrically controlled switch was placed between the power supply and the plasma discharge. This switch was turned off and on by the data acquisition system generating a square wave current signal to the plasma discharge. This could only be done with good success at low frequencies. For the most part the discharge was pulsed at 4 Hz with this device.

### 4.1.3 Results

The results subsection is separated into three lower level subsections. The first presents measured results that provide an indication of the amount of noise in the pitot probe measurements. The second presents the results of applying a plasma discharge to a Mach 5 flow with no magnetic field. The third gives a few results with a magnetic field applied to the plasma discharge in the Mach 5 flow. Most of the results presented in this paper are for the plasma discharge without any magnetic field applied. The reason for this is the noise problems that occurred in the measurements when a magnetic field was applied. For this reason the results with a magnetic field applied are more difficult to interpret and to draw conclusions from than those without the magnetic field and there are fewer results with the magnetic field.

The general procedure used to obtain data in this work was to turn the plasma on and off at a known frequency and look at the response of the pitot probe to the applied discharge. The discharge was turned off and on by means of a power amplifier or by means of a computer controlled switch. The difference in the pitot probe signal between the plasma on and the plasma off is one of the results sought. All the results shown in this work use the power amplifier and the larger diameter pitot probe that is located on the *x-y-z* translator, except for the magnetic field results. The magnetic field results used the slightly smaller diameter pitot probe attached to the model itself.

The results presented in this subsection are the pitot probe pressure, discharge current, and discharge voltage as a function of time. The discharge current is the key parameter indicating when the discharge is on, putting energy into the air flow.

### 4.1.3.1   Noise Study

Before applying any magnetic field or plasma discharge to the Mach 5 flow, pitot probe measurements of the still air and of the Mach 5 flow were made. These measurements are shown in Figures 77 and 78 respectively. These two measurements provide an estimate of the electronic noise in the pitot probe and data acquisition system and the amount of flow noise in the Mach 5 wind tunnel. As can be seen from Figure 77 there is 0.15 torr amplitude electrical noise in the pitot probe system and data acquisition system with occasional 0.5 torr jumps. On average the amplitude of the electrical noise is 0.4% of the full scale of the pitot probe. The measured pitot probe results in Figure 77 are centered around zero because this pitot probe makes differential pressure measurements. When there is no flow the reference pressure is the same as that at the tap location of the pitot probe. Figure 78 illustrates a rather large increase in the noise detected by the pitot probe when the tunnel flow is on. The amplitude of this noise is 1 torr. Since there are no other electrical components, except the pitot probe and the data acquisition system being operated during the collection of these results, this noise is probably due to the flow noise in the tunnel. The results shown in Figure 78 were taken upstream of the leading edge of the plate.

The electrical noise generated by the plasma which is detected by the pitot probe is shown in Figure 79. These results were obtained with the tap location of the pitot probe located 0.6 cm upstream of the leading edge and 0.5 cm above the upper surface of the model. At this location the effects of the 40 mA discharge on the flow field should be null. Thus changes seen in the pitot probe results can be attributed to the electrical interactions between the pitot probe and the discharge. When the tap location of the pitot probe is placed upstream of the model, as done here, some of the tubing used to connect the tap location to the piezoresistive pressure sensor chip is directly in the discharge. The piezoresistive pressure sensor chip is located about 4 cm above the discharge. The measured pitot pressures in Figure 79 indicate that the plasma discharge does add to the noise detected by the pitot probe. The frequency at which the discharge is turned on and off in a square wave fashion is 10 Hz. The on current is 40 mA and the on voltage is -440 volts. The amplitude of the oscillations in the current is 2 mA and the oscillations in the voltage are 15 volts on average. It is these oscillations in the discharge voltage and current that are causing the pitot probe to oscillate 0.75 torr above the oscillations caused by the flow noise. When the discharge is off the amplitude of the noise in the pitot probe pressures is 0.75 torr and when the discharge is on the amplitude in the noise is about 1.5 torr.
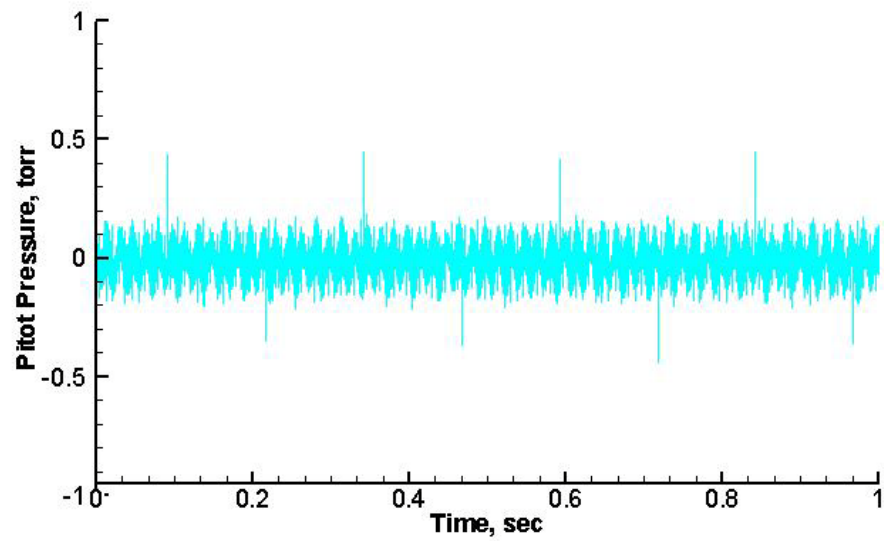
Figure 77.  Pitot Probe Measurements in Mach 5 Wind Tunnel with No Flow
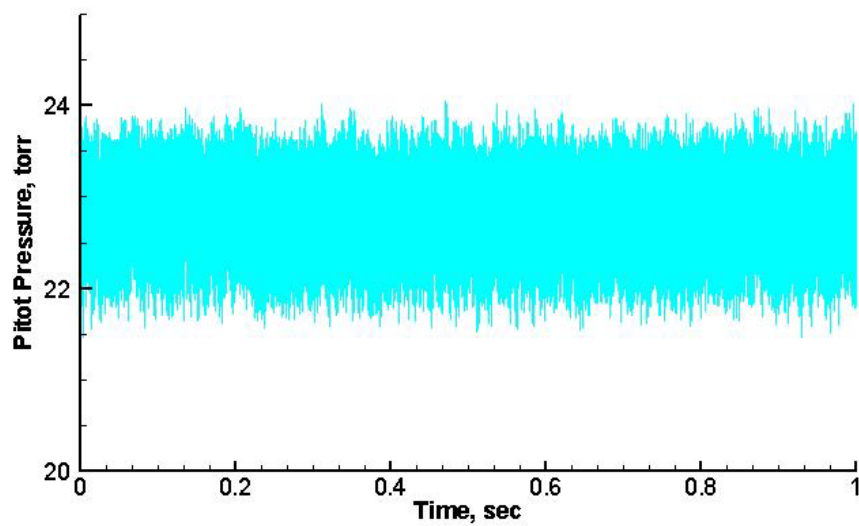


Figure 78.  Pitot Probe Measurements in Mach 5 Wind Tunnel with the Air Flow On
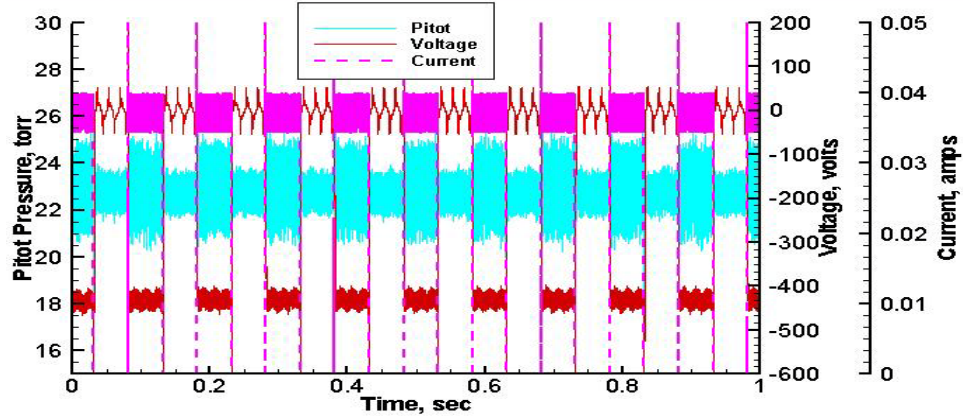
**Figure 79. Measured Results for a Mach 5 Flow with a 40 mA Discharge that is Oscillated at 10 Hz**

The important point to notice about the pitot probe pressures presented in Figure 79 is that the oscillating behavior of the results with the plasma on and the results with the plasma off are centered around the same average value. While it is not presented here, this can plainly be seen when the curve is mathematically smoothed. This means that the plasma discharge noise does not offset the pitot probe measurements. This is important because this work is looking for average offsets of the pitot pressure between the case when the plasma is on and the case when the plasma is off.

### 4.1.3.2 Plasma Effects

The first plasma effect that is investigated is the response of the flow field and the pitot probe to varying pulsing frequencies of the discharge. The frequencies checked in this work are 5, 10, 20, 40, 80, 160, 320, 640, 1280, 2560 and 10,000 Hz. For these tests the power amplifier is utilized along with the pitot probe located on the *x-y-z* translator. All pitot pressure measurements are made at a location 7.6 cm downstream of the leading edge of the plate along the spanwise centerline and 0.5 cm above the upper surface. This puts the probe just downstream of the cathode. Examples of these measurements in their unaltered form for 5, 40, 160, and 2560 Hz are shown in Figures 80 through 83. The time scales are adjusted for each of these plots so that the waveforms can be seen more clearly. The conditions for the results shown in these figures are the same except for the frequency at which the plasma discharge is pulsed. The plasma on current is set to 80 mA by adjusting the current limit of the power amplifier.

The general effect of increasing the plasma pulsing frequency from 5 to 40 Hz on the measured pitot probe pressures is that differences between the plasma off and plasma on values shrink a little. The plasma off values tend to decrease and the plasma on pitot pressures tend to increase slightly or stay relatively constant; thus a decrease in the difference seen between the two situations. This can be seen more clearly in Table 3 where the average plasma off pitot pressure, the average plasma on pitot pressure, and the percent difference between the two is given. Up to 80 Hz the average plasma off values continue to decrease while the plasma on values tend to remain constant. Above 80 Hz the plasma off values continue to decrease and the plasma on values increase somewhat. The interesting trend is that the percent difference between the two results goes negative. Up to an 80 Hz pulsing frequency the plasma off pitot pressures are higher than the plasma on pitot pressures. This trend can be seen in Figures 80 and 81. For 160 Hz and higher the average plasma off pressure is less than the average plasma on pressure. This trend is

somewhat evident in Figures 82 and 83. The pitot probe pressures in Figures 82 and 83 show no sign of reaching a steady value during any of the pulses.
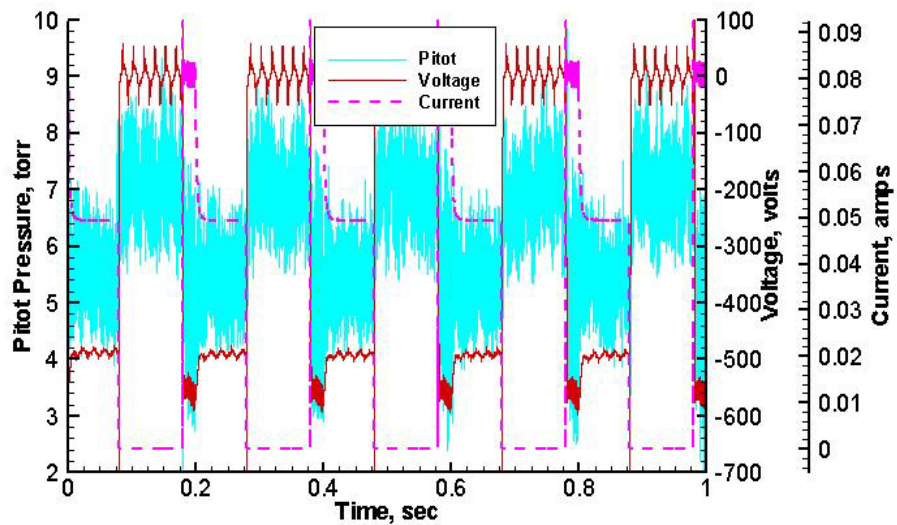


**Figure 80.  Measured Results for a Mach 5 Flow with an 80 mA Discharge that is Oscillated at 5 Hz**
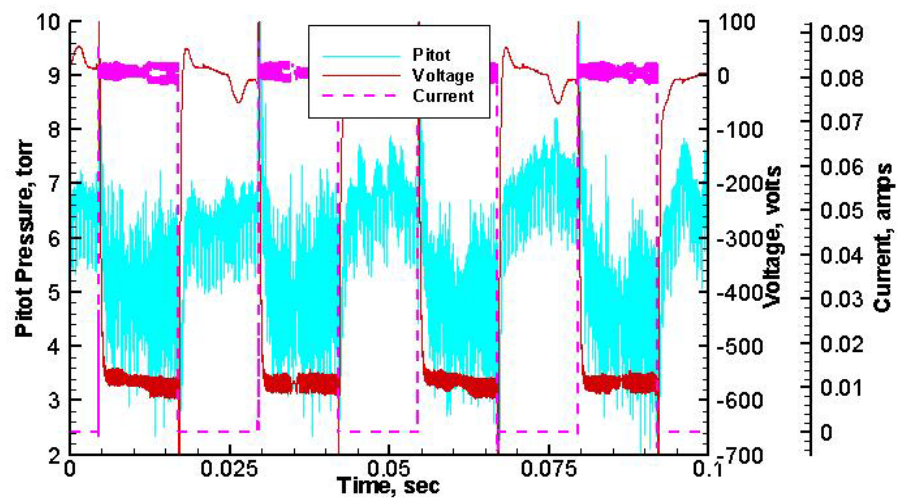


**Figure 81.  Measured Results for a Mach 5 Flow with an 80 mA Discharge that is Oscillated at 40 Hz**
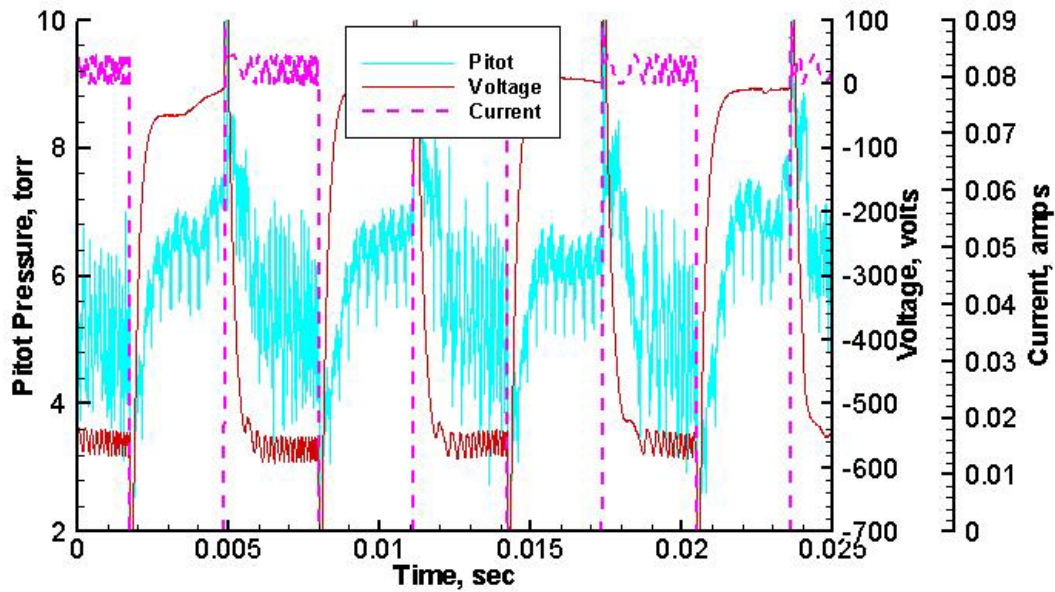
**Figure 82. Measured Results for a Mach 5 Flow with an 80 mA Discharge that is Oscillated at 160 Hz**
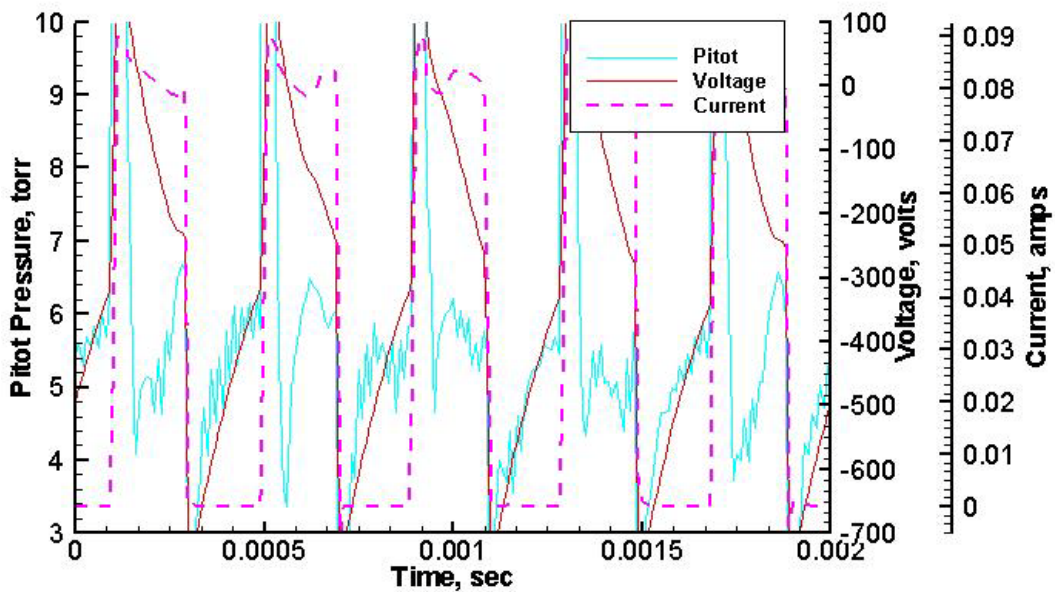


**Figure 83. Measured Results for a Mach 5 Flow with an 80 mA Discharge that is Oscillated at 2560 Hz**

The trends explicitly presented in Table 3 are probably a result of the limits of the ability of the pitot probe to respond to quick changes in the flow field. At an 80 Hz plasma pulsing frequency the time which the plasma is on for any given cycle is 6.25 ms. This means the pitot probe must respond to the changes in the flow field caused by turning the plasma off in less than 6.25 ms. For the 160 Hz case shown in Figure 82 the time that the plasma is on for any given cycle is 3.13 ms. It may be that the pitot probe results in Figure 82 are reaching some sort of a steady

value. However, it can certainly be said that the pitot probe pressures in Figure 83 are not reaching a steady value. The results in Table 3 show the average pitot pressure over all the half cycles with the plasma off in the second column and the average over all the half cycles with the plasma on in the third column. This means the pitot probe time response will gradual show itself in these results as the plasma pulsing frequency increases.

**Table 3.  Tabulated Average Values of the Pitot Pressure with the Plasma on and the Plasma off for Different Plasma Pulsing Frequencies**

| Plasma Frequency (Hz) | 0 mA Pitot Pressure (torr) | 80 mA Pitot Pressure (torr) | % Difference |
|---|---|---|---|
| 5 | 7.3 | 5.3 | 27.2 |
| 10 | 7.3 | 5.3 | 27.3 |
| 20 | 7.0 | 5.3 | 24.3 |
| 40 | 6.5 | 5.1 | 21.5 |
| 80 | 6.2 | 5.3 | 14.3 |
| 160 | 5.7 | 5.9 | -4.21 |
| 320 | 5.0 | 6.4 | -28.6 |
| 640 | 4.3 | 6.6 | -51.6 |
| 1280 | 3.9 | 5.9 | -53.3 |
| 2560 | 3.0 | 5.9 | -99.2 |
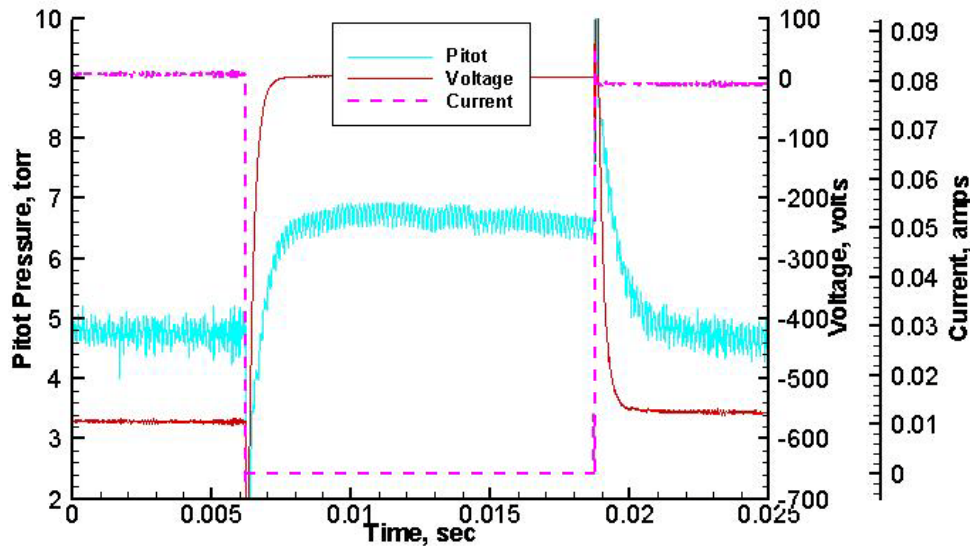


**Figure 84.  Averaged Pitot Probe Measurements in a Mach 5 Flow with an 80 mA Discharge that is Oscillated at 40 Hz**

At this time it is felt that the lack of a steady pitot probe measurement at a plasma pulse frequency of 160 Hz is because the response time of the pitot probe is approximately 3 ms. The averaged results shown in Figure 84 seem to point this out. Figure 84 shows one pulsing cycle for a 40 Hz pulsing rate. This plot shows the average of 40 measured cycles. This is a better way to eliminate noise in the measurement as opposed to performing a running average. This

84

averaging has reduced the observable noise in the pitot pressure, current, and voltage readings. Right at the time when the plasma goes from on to off and the point where the plasma goes from off to on, the response time of the pitot probe can be estimated to be about 3 ms. If the response time of the pitot probe is 3 ms, this effect would be noticeable in the average values shown at 80 Hz and somewhat evident at 40 Hz. At 40 Hz the plasma is off for 12.5 ms each cycle. For one quarter of this 12.5 ms the pitot probe is trying to alter itself from the lower plasma on pitot pressure to the higher plasma off pitot pressure. Thus one fourth of the measured pressures are lower than they should be. This lowers the average plasma off pressure shown in Table 3. This is the reason the 40 and 80 Hz plasma off values are lower than the 5 and 10 Hz values.

Another phenomenon made visible in Figure 84 is that when the plasma goes from the on to off state or from the off to on state, a large change in the pitot pressure is seen. This same phenomenon can be seen in Figures 80 through 83; however, it is more difficult to see because it is covered with the current and voltage curves. This has to be the pitot probe responding to electrical noise generated by the discharge. Rapid changes in the voltage or current in the discharge tend to produce electromagnetic radiation that interferes with the operation of the pressure transducer.

Notice that the plasma on portion of the cycle in Figure 80 has two current levels, 80 mA and 50 mA. For the portion of the plasma on part of the cycle where the discharge current is 80 mA, the current shows larger oscillations than the portion where the discharge current is at 50 mA. The 80 mA to 50 mA behavior seen in the 5 Hz results shown in Figure 80 is rather unusual, but it is the result of controlling the voltage on the power amplifier instead of the current. The time it takes for this current change from 80 mA to 50 mA is 20 ms. This is the reason the results in Figures 81, 82 and 83 do not show this current drop; the plasma is not on for 20 ms. This phenomenon is also seen when the plasma is pulsed at 10 Hz.

Similar to the results in Figure 84, averaged over 40 cycles for the 40 Hz plasma pulsing rate, the results for a 5 Hz pulsing frequency averaged over 5 cycles are shown in Figure 85. You cannot see the response time of the pitot probe to turning the plasma on and off in this figure because the time scale is too large. This response can be seen at a finer time scale as shown in Figure 86, and it does support the 3 ms response time for the pitot probe. What can be seen in Figure 85 is that the pitot probe senses a higher pitot pressure when the discharge is running at 50 mA, than when it is running at 80 mA. This is an expected response because more power is put into the air flow at 80 mA than at 50 mA. Notice the voltage level also drops when the discharge switches from 80 mA to 50 mA. What is unexpected is that the differences between the 80 mA and 50 mA measured pitot pressures is not larger.
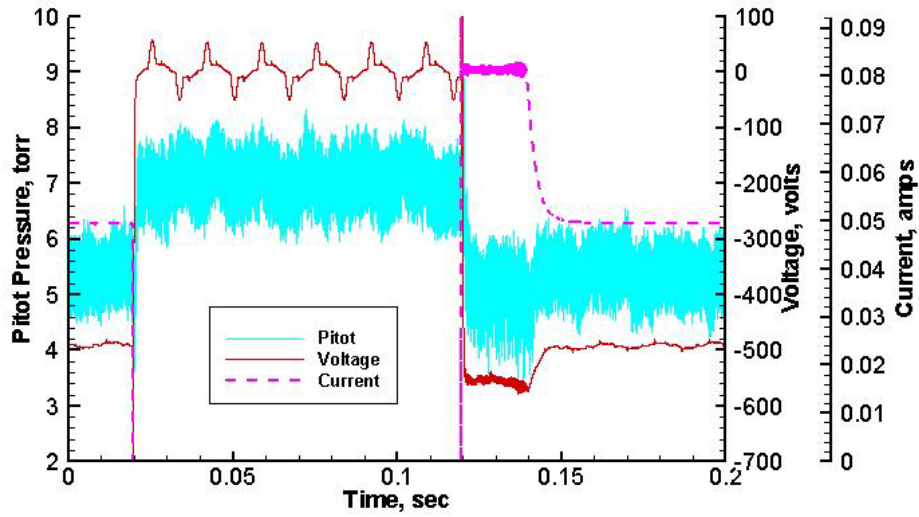
**Figure 85. Averaged Pitot Probe Measurements in a Mach 5 Flow with an 80 mA Discharge that is Oscillated at 5 Hz**
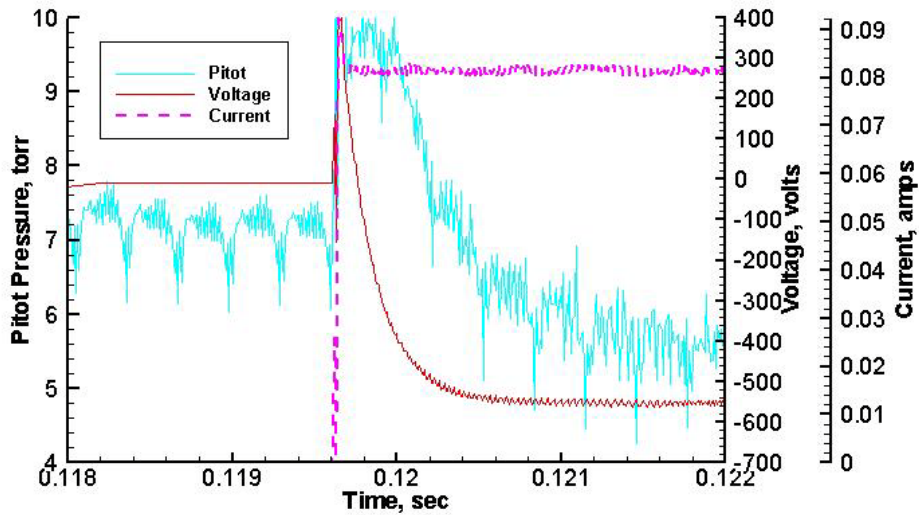


**Figure 86. Zoomed View of Data Shown in Figure 85**

The results in Figures 80 through 83 indicate that the flow field is responding to the applied discharge in less than 3 ms. In terms of thermal heating of the entire flat plate model, 3 ms is too fast of a time for this to be a factor for the change in pitot probe pressures. The location on the model which has the most potential to absorb heat quickly from the discharge and thus affect the pitot probe pressures in a 3 ms time interval is the copper cathode. The thermal conductivity of copper is high, 401 W/m-K, and the discharge deposits a large fraction of its energy in the cathode fall region right above the copper surface. On the other side of the argument the thermal capacitance of the copper cathode is 8.8 J/K, limiting the ability of the copper cathode to have any effect on the pitot probe measurements in 3 ms. For purposes of argument, assume the total power output of the discharge in the 80 mA operating mode, 45 watts, all goes into the cathode.

86

If this is the case the temperature of the cathode would not raise more than 0.02 $^{\circ}$C. This indicates there is no variation in the pitot probe results because of cathode or plate heating.

The same calculation as done in the previous paragraph can be done for the lowest plasma pulsing frequency tested. At 5 Hz the discharge is on for 0.1 seconds every cycle. Assuming all the power from the discharge goes into the copper cathode for this 0.1 second plasma on time, the cathode temperature will not increase more than 0.5 $^{\circ}$C. In looking at the results in Figures 80 through 83 it can also be deduced that the cathode is not heating over many cycles because the pitot probe results from cycle to cycle do not change significantly. This means that volumetric heating of the air flow over the plate is the mechanism for the flow changes indicated by the pitot probe measurements made with the discharge on and the discharge off. This means that the flat plate model is not adding heat or removing varying amounts of heat to or from the air flowing over it during the 1 second in which measurements are being taken for this work. Thus the changes seen in the flow have to be caused by volumetric heating, that is joule heating of the air flow above the model. In addition, volumetric heating causes changes to the air flow in a period less than approximately 3 ms. It is believed that the changes caused by volumetric heating are much faster than this, but the instrumentation utilized in this work is not capable of proving this.

While the model may not be adding heat to the air flow in the time frames being considered here, it does not mean that the model is not absorbing heat from the discharge in these time frames. The electrodes may be absorbing a noticeable amount of total electrical energy put into the discharge. Since the electrodes are not changing temperature to any noticeable amount, this effect would not show up as a change in the pitot pressure results shown here. In order for a change to be seen, the rate at which the electrodes absorb energy has to change. This rate will change if the temperature of the electrode changes. As the simple argument above points out, over the time frames considered in this work the electrode temperature is not changing to any important degree. This means that a power input of approximately 45 watts which causes a change in the pitot pressure of 27%, may be more power than is actually needed to cause this amount of change in the flow field.

One last observation on the results displayed in Figures 80 through 83. In Figures 80 and 81 the voltage is seen to go to large negative values when the discharge is on, and to values close to zero when the discharge current goes to zero. In Figure 83 this characteristic is not seen. The voltage appears to be out of phase with the current. In Figure 82 the voltage appears to be lagging the current. If capacitive and inductive effects are not present, the voltage should be close to zero when the discharge is off and the voltage should take on a large negative value when the discharge is on. The behavior of the voltage curves in Figures 82 and 83 is believed to be caused by capacitive effects of the discharge.

### 4.1.3.3  Magnetic Field Effects

For the tests where the magnetic field is applied to the test section of the wind tunnel the *x-y-z* translator mechanism had to be removed from the wind tunnel. Thus the pitot probe attached to the *x-y-z* translator cannot be used. For the magnetic field tests the pitot probe is attached to the model itself. The tap location of this pitot probe is located 8.4 cm downstream of the leading edge of the plate, 0.6 cm off the centerline in the spanwise direction, and 0.5 cm above the surface of the plate. The DC power supply with an electrically controlled switch is used to provide a square wave plasma current profile.

Some sample results of the effects of an applied magnetic field are shown in Figures 87 through 90. Figures 87 and 88 show the raw measured pitot pressures as a function of time for a negatively directed magnetic field and positively directed magnetic field respectively. The current and voltage profiles are also shown. A positively directed magnetic field applies a force on the electrons directed towards the plate surface as they travel from the cathode to the anode. A negative magnetic field applies a force away from the plate surface. Both of these figures show a great deal of noise in the measured results; the noise in the positively directed magnetic field is much greater than that for the negatively directed field case. The noise is present in the current, voltage, and pitot probe results. The magnitude of the noise oscillations is large relative to the average signal. If a more detailed look is made of the positively directed magnetic field results it can be seen that the current is actually zero most of the half cycle in which the discharge is suppose to be on. At a 4 Hz pulse rate the discharge does not have time to set up when a positively directed magnetic field is present. It is this rapid off and on behavior of the discharge which is generating the electrical noise being sensed by the data acquisition equipment.
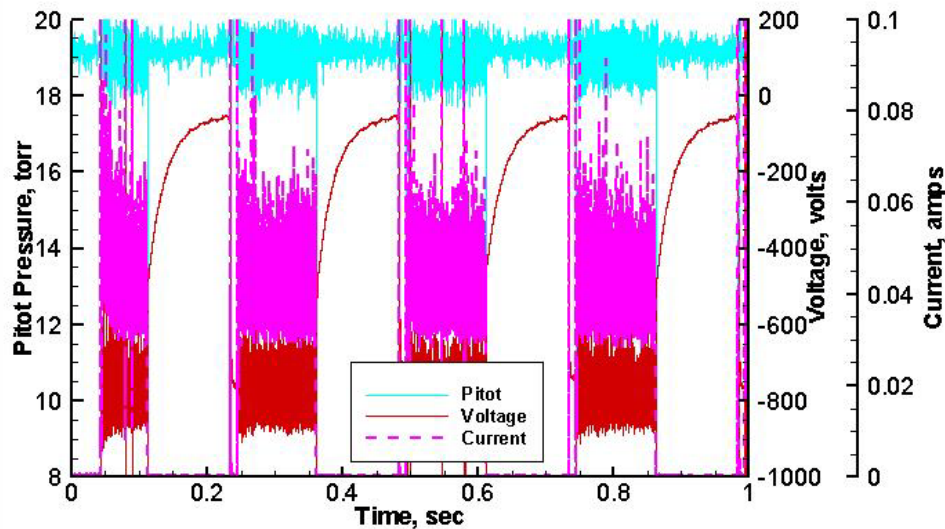


**Figure 87. Measured Results for a Mach 5 Flow with a 40 mA Discharge Pulsed at 4 Hz and a -0.2 Tesla Magnetic Field Applied**

Because of the large amount of electrical noise it is difficult to see if there are any changes in the pitot pressures as a result of applying a plasma and a magnetic field. This difficulty can be alleviated by smoothing the raw results. This smoothing process removes large quick spikes from the plots. The smoothed versions of the negative and positive magnetic fields are shown in Figures 89 and 90. In these figures it becomes obvious that the pitot pressures change with the application of a plasma and a magnetic field. The positively directed magnetic field shows bigger changes than the negatively directed magnetic field. This is surprising because the average current going into the discharge with a positively directed magnetic field is only 5 mA, whereas it is 40 mA for the discharge with a negatively directed magnetic field. The difference between the plasma/magnetic field on pitot pressure for the negatively directed magnetic field as compared to the plasma off portion of the cycle is 1.2%. For the positively directed magnetic field this percent change is 4.4%.
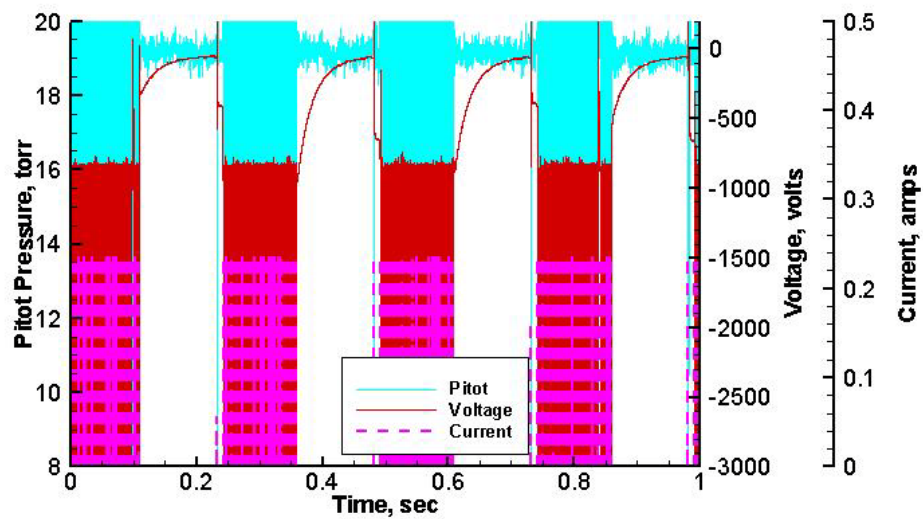
**Figure 88. Measured Results for a Mach 5 Flow with a 40 mA Discharge Pulsed at 4 Hz and a +0.2 Tesla Magnetic Field Applied**
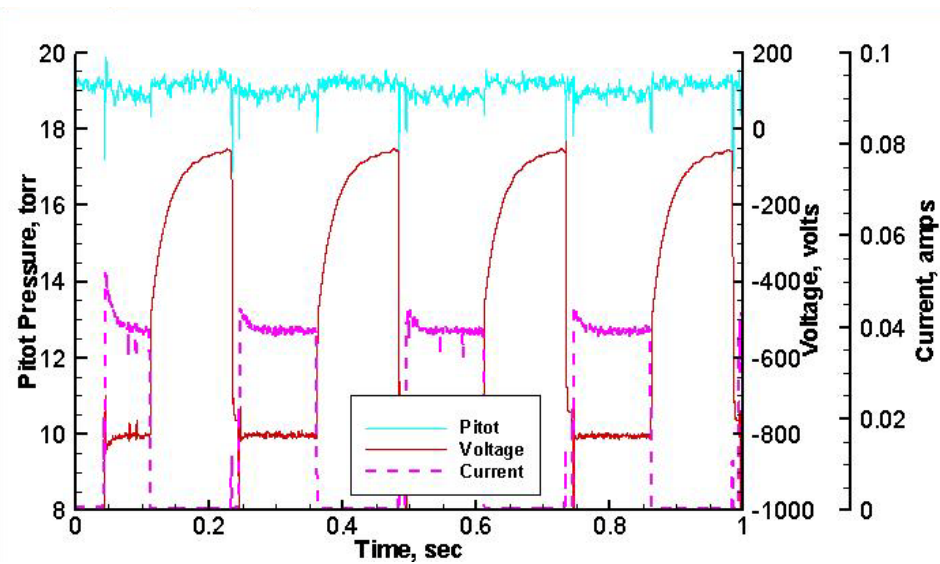


**Figure 89. Figure 87 Results That Have Been Smoothed**
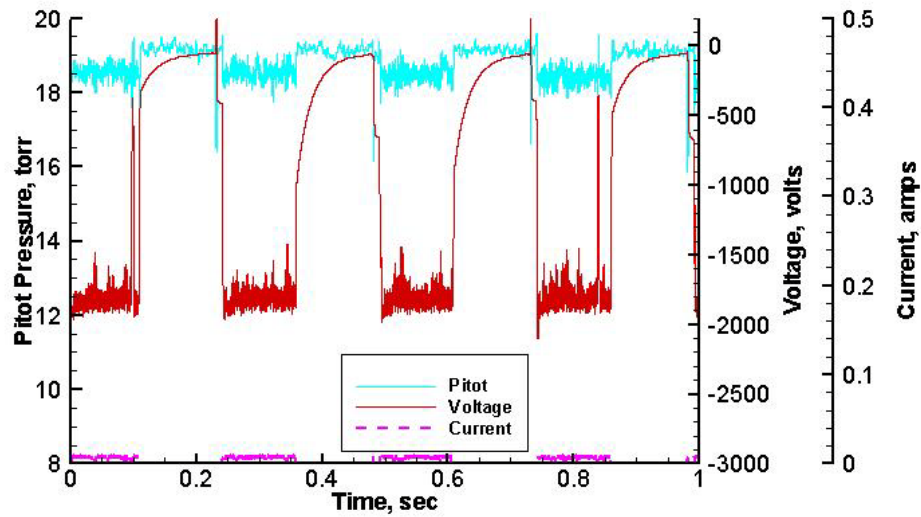
**Figure 90. Figure 88 Results That Have Been Smoothed**

Visual observation of the discharges to the applied magnetic fields indicates that the shape of the discharge is very different from the case when no magnetic field is applied. In addition, the discharge is a different shape when a positive or a negative directed magnetic field is applied. The fact that the relative change in the pitot probe pressures with the plasma on and the plasma off are different for the case where there is no magnetic field, the case where there is a negatively directed magnetic field, and the case where there is a positively directed magnetic field; and the fact that these discharges are all visually different indicates the indirect Lorentz force mechanism is in effect. No conclusions on the direct Lorentz force effect can be made from these results. In addition, no conclusions should be drawn from the changes between the negative and positive directed magnetic field results. These differences are small and the discharge is flickering on and off a great deal and it has not been determined which one is delivering more heating to the air flow.

### 4.1.4 Summary

This work has made pitot probe measurements which provide more information on the effect of a plasma and a magnetic field on a Mach 5 flow. An important aspect of this work is that a pitot probe with a response time of 3 ms was used. From the measurements performed it is determined that the heating of the air by the plate is not significant in approximately the first second that the discharge is applied. It will also be stated that the volumetric heating (Joule heating) of the air by the plasma discharge appears to occur at time scales less than 3 ms. It is believed that the volumetric heating effects are much faster than this, but the pitot probe used in these measurements is only capable of responding to changes slower than 3 ms. Because of the response time of the pitot probe, meaningful pitot probe results, can only be obtained up to plasma pulsed frequencies of about 40 to 80 Hz. Up to these frequencies there appears to be no change in the way the plasma discharge interacts with the high-speed flow. From voltage current measurements it appears there is some capacitive effects of the discharge showing at pulsing frequencies above 160 Hz.

The application of a magnetic field to the plasma discharge was seen to greatly increase the electrical noise generated by the discharge. This made measurement and data interpretation

90

difficult, but by using some smoothing techniques one can recognize a change in the pitot pressures with the application of a magnetic field and a plasma. The relative change of the pitot probe results between the plasma on case and the plasma off case is higher without the magnetic field than with it; however, it must be realized that when the magnetic field is applied the discharge is off more than when the magnetic field is not present. From the results presented in this paper it can reasonably be deduced that the indirect Lorentz force mechanism is at work, but nothing can be said about the direct Lorentz force mechanism.

## 4.2   Lift and Drag Force Measurements on a Flat Plate Measured by a Load Cell

### 4.2.1   Introduction

The work presented in this section of the report adds more evidence to the mounting amount of evidence that a plasma discharge does indeed affect a hypersonic flow; and that the addition of a magnetic field on top of the high-speed flow and the plasma discharge causes additional changes to the high-speed flow field. The difference between the work presented here and most of the other work in this area, of which the authors are familiar, is total lift and drag measurements are made. Investigators in the past have documented the effect of a plasma discharge alone and the effect of a plasma discharge and a magnetic field on the flow field by looking at the position of the shock (Kolesnichenko et al, 2004; Leonov et al. 2004; Borghi et al. 2004), surface pressure changes (Leonov et al., 2003; Kolesnichenko et al., 2004; Kimmel et al., 2004a; Menart et al. 2003b; Kimmel et al., 2004b), pitot pressure changes (Kimmel et al., 2004a; Bityurin et al., 2003; Kimmel et al., 2004b), spectroscopic temperature measurements (Takizawa et al., 2004), heat flux measurements (Bobashev et al., 2004), and density fluctuation intensity changes (Meyer et al., 2004). There appears to be a need for more measurements of the changes in total lift and drag caused by the application of a plasma discharge or the application of a plasma and a magnetic field to a high-speed flow.

Investigators who made measurements of the total drag on a body in an air flow with the application of a plasma are Leonov et al. (2003), Shang et al. (2002), Toro et al. (1999), Bracken et al. (2001), and Bityurin and Klimov (2005). Leonov et. al. (2003) measured the drag on a surface mounted body as a function of plasma input power. These investigators saw drag reductions of 90% at powers of 2500 watts. This is a large amount of power for a relatively small body. Shang et al. (2000) measured drag changes on a cylindrical model with a hemispherical nose. The plasma was injected into the Mach 6 flow in a counterflow fashion and seen to alter the drag on the body. Toro et al. (1999) used a directed plasma spike, like Shang et al. (2000), but used considerably more power, up to 127 kW, and used a pressure measurement to indicate a change in drag. Bracken et al. (2001) measured drag changes on a blunt body with a plasma arc of 13 kW or 30 kW generated upstream of the body. They show a small change in drag with rather large plasma powers. Bityurin and Klimov (2005) used a DC discharge and electron beam generated plasma between the wind tunnel nozzle and the model. The DC power was below 500 watts, but the electron beam was using 3 kW of power. These investigators saw large changes in the drag.

All the investigators in the investigations mentioned above used larger power inputs to their discharge than what is used in this work. In this work discharge power inputs of less than 300 watts are used. In addition, the investigators listed above focus on drag reduction while this work focuses on lift changes on a flat surface. The goal is to produce large changes in lift with small amounts of power input.

Measurements such as these are important because two uses for magnetohydrodynamics (MHD) in the hypersonic flow regime are to use a plasma discharge and a magnetic field to reduce drag on a high speed vehicle or change the lift so that a plasma and a plasma-magnetic field combination can be used to control an aircraft. This means that lift on different surfaces can be adjusted by a plasma or plasma and magnetic field. The work presented in this section presents measured data for both lift and drag. However, because of the location of the application of the plasma discharge, the main force that is studied in this paper is the lift force.

## 4.2.2   Experimental Facility

The wind tunnel used to carry out the work being presented in this section is the same as used in the previous section (see Figures 73 and 74). A brief description of this tunnel is given in Section 4.1.2 of this report. For the results presented in Section 4.2 the hypersonic wind tunnel is run at a stagnation pressure of 370 torr. This results in a static pressure of 0.6 torr at the test section.

The model used for the lift and drag measurements is different than that used for the high speed pitot probe measurements in the previous section; however, in general the models are similar. This model was specially built along with the load cell measurement device. For the load cell measurements a flat plate with a half wedge angle of $20^{o}$ at the leading edge is used as shown in Figures 91 and 92. The plate is constructed out of a machineable ceramic and has two rectangular shaped, copper electrodes that are flush with the upper surface of the model. For this work the cathode is always the upstream electrode and the anode is the downstream electrode. The distance between the electrodes is 3.8 cm and the cathode is 1.8 cm downstream of the leading edge. The thickness of the electrodes is small, 0.2 cm. The portion of the strut connecting the plate to the load cells that is exposed to the high-speed flow is 1.8 cm long in the spanwise direction and 1.8 cm wide in the flow direction. The frontal height of the strut is 0.2 cm.

The load cells used for measuring the lift and drag on the model are located in the phenolic disk shown behind the model in Figure 91. Located in this disk are four, 500 gram, subminiature Sensotec load cells that have stainless steel cases and are capable of measuring tensile and compressive forces. The accuracy of the load cells is ±0.5% of full scale. The four load cells are located in the phenolic disk such that two are used to measure the drag applied to the plate and two measure the lift applied to the plate. While theoretically only two load cells are required to make lift and drag measurements, using four load cells has an advantage. From experimental tests it has been recognized that the apparatus for transmitting the forces from the plate to the load cells has some sensitivity to temperature. The nice aspect of using four load cells is that the two load cells that measure drag and the two load cells that measure lift have an opposite sensitivity to temperature. In this paper the average drag and lift measured from the two load cells is presented. Taking the average of the two load cells tends to cancel any changes in the measured data caused by changes in temperature.
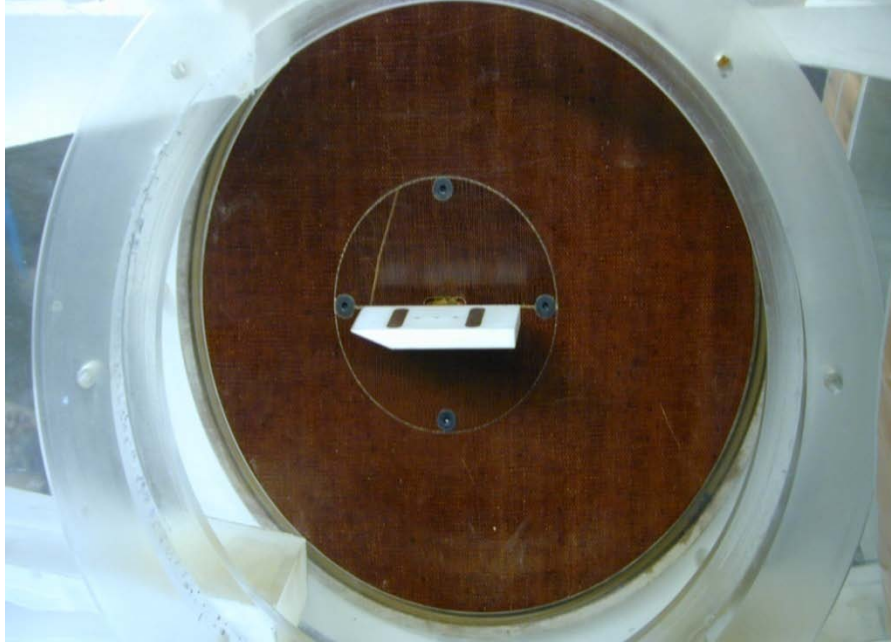
Figure 91.  Flat Plate Model Used for Load Cell Measurements Located in Mach 5 Wind Tunnel Test Section
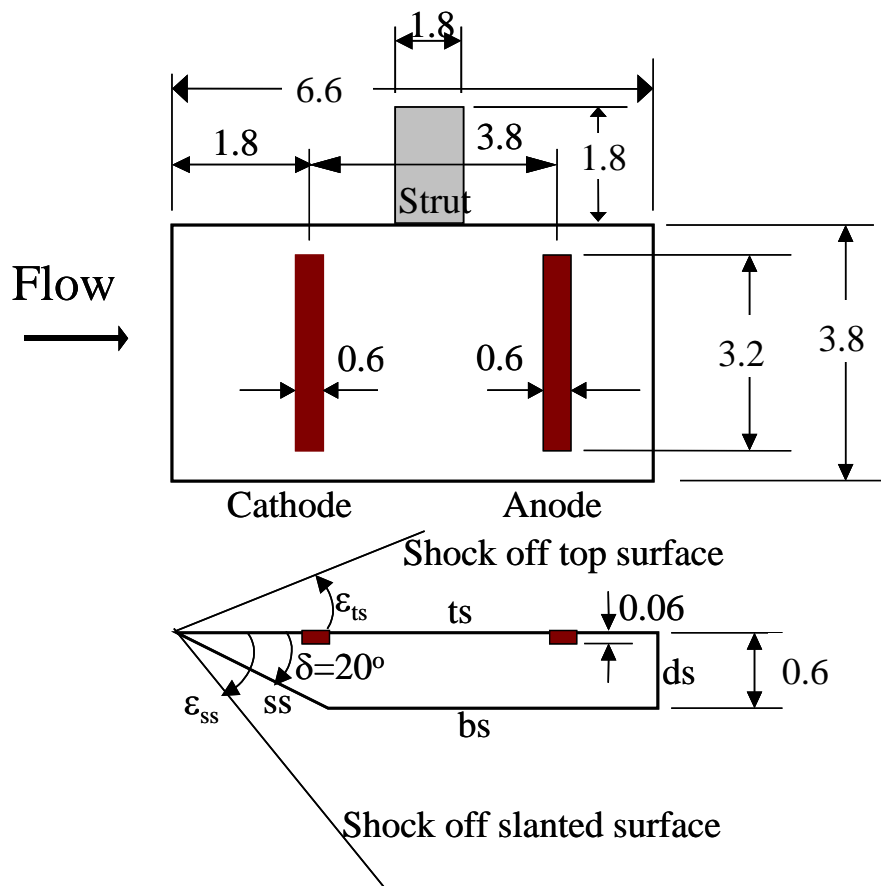


Figure 92.  Dimensioned Sketch of Flat Plate Model.  All Dimensions are in cm

The load cells are connected to the model using a small phenolic strut. The phenolic strut connects to a round phenolic disk under which lie the four load cells. The load cells are located under the disk in a diamond pattern. The phenolic strut comes out the side of the model and lies flush to the bottom surface. Running along the upstream edge of the strut is the electrical wire for the cathode and along the downstream edge is the electrical wire for the anode. These wires give the strut a rounded leading and trailing edge. The electrical lines to the airfoil are given slack so they do not affect the forces transmitted to the load cells.

An advantage to having the model, the connections to the model, and the load cells all placed in and connected to a solid phenolic disk that takes the place of one of the portal windows in the tunnel is that the model can be easily rotated to different angles of attack. This can simply be done by rotating the phenolic disk in the portal. This rotates the model, load cells, and all connections to the load cells relative to the Mach 5 flow direction. This means the drag forces measured and presented in this paper are always aligned along the long axis of the model. The lift forces are always perpendicular the upper and lower surfaces of the model. In the laboratory reference frame the direction of the drag and lift change, while in a reference frame attached to the model the directions of these forces do not change.

The output from the load cells is a voltage that is proportional to the force being applied to the load cells. This voltage signal is converted to a drag and lift force by calibrating the entire apparatus using standard masses. This is simply done by placing a known mass on the upper surface and reading the output from the load cells. This is done again by rotating the entire system $180^o$ and placing weights on the bottom surface of the model. By rotating the model $90^o$ each way from its normal orientation (see Figure 91), the leading edge of the model points straight down or the leading edge points straight up. In these two orientations the drag load cells can be calibrated. Each of the four load cells is calibrated separately and four calibration curves are obtained. The response of the load cells is linear. Calibrating the load cells along with the model and the connection equipment associated with the load cells includes all the moment arm effects on the load cells. This technique also allows for easy removal of the lift force caused by the weight of the model itself. Only the lift and drag caused by the flow is output from the load cells. The assumption made in this calibration process is that the center of lift and the center of drag act through the middle of the model. This probably is not exactly the case. This will introduce some error into the measurements.

To take data from the load cells a personnel computer and an HP3852a data acquisition unit is used. The software package used to write the program to control this data acquisition process is Lab Windows. In addition to reading the signals from the load cells, the software written also allows the user to zero the load cells when desired. This has advantages because it allows the operator to look for changes in drag or lift because of the application of the Mach 5 flow, or a plasma to a Mach 5 flow, or a plasma to a magnetic field and Mach 5 flow. This is what is done in this work. To determine the drag and lift caused by the Mach 5 flow, the load cells are zeroed with no flow in the tunnel. To determine the change in drag and lift caused by the application of a plasma discharge, the load cells are zeroed in the Mach 5 flow with no plasma. To determine the effect of the application of a magnetic field, the load cells are zeroed with the magnetic field set to the desired value with the flow on. A reading of lift and drag are taken when the plasma discharge is turned on. This gives the effect of the plasma on the flow passing through a magnetic field. It would have been better to zero the load cells in an environment with the flow and plasma on, but this could not be done because the magnetic field interacts with the stainless

steel casings of the load cells. Since this is a significant interaction, it had to be eliminated from the measurement by zeroing the load cells with the magnetic field on. The effects of the magnetic field are determined by comparing the flow-plasma-magnetic field measurement to the flow-plasma measurement. The zeroing of the load cells is done a few seconds before the actual measurement is made. This is advantageous from a temperature drift perspective, as well as detecting changes caused by the application of a plasma discharge. Since the load cells are zeroed a few seconds before the measurements are made, there is not time for temperatures to change a great deal.

The plasma discharge was generated using a Universal Voltronics, unipolar, DC electrical power supply capable of delivering 0.8 amps of current up to electrical potentials of 10,000 volts. The power supply was operated in the current control mode for all the data collected for this section of this report. In the current controlled mode the power supply automatically adjusts the voltage to deliver a set current. While this is a DC power supply, it has the capability of being controlled by a computer. This was done in this experiment. The power supply was remotely controlled to a constant current or a sinusoidal current that varied at 2, 4 or 16 Hz. While the power supply could be set to oscillate at a faster rate than 16 Hz, the maximum and minimum values of the current cannot be obtained by the power supply when this is done. This can even be seen to happen at 8 Hz. Since the power supply is unipolar, the current had to be oscillated so all currents were positive. This means the cathode position on the flat plate always remained upstream. If the control system sends a signal to the power supply to go negative, the power supply simply delivers zero current. This type of operation was utilized for some of the results presented in this paper.

### 4.2.3   Comparison to Analytical Results

To validate the lift and drag measurements from the load cell devices, the lift and drag results are compared to analytical results obtained from simple oblique shock and Prandtl-Meyer expansion expressions. The idea behind presenting these comparisons is to bolster confidence in the lift and drag measurement accuracy.

The main idea behind this simple analysis is to determine the pressure located on different surfaces of the plate. There are four surfaces for which the pressure needs to be determined: the top surface (*ts*), the bottom surface (*bs*), the slanted surface at the upstream portion of the plate (*ss*), and the downstream surface of the plate (*ds*) (see Figure 92). The slanted surface contributes to lift and drag while the top and bottom surfaces only contribute to lift. The downstream surface only contributes to drag. The pressures on the upper surface, the bottom surface, and the slanted surface are determined by using the relationships for jumping across an oblique shock wave and/or the relationships for jumping across a Prandtl-Meyer expansion. It is assumed that the pressure on the downstream surface is zero. The other assumptions made in this analysis are that viscous effects do not affect the shocks or expansion waves, the air is a perfect gas with a specific heat ratio of 1.4, spanwise flow effects are negligible, the effect of the strut holding the flat plate to the portal of the tunnel wall is ignored, and changes in the flow conditions in the streamwise direction only occur across the shocks and Prandtl-Meyer expansions.

The first item that needs to be determined is the shock angle off the top of the plate when the angle of attack is either zero or negative, and the shock angle off the slanted surface of the plate for all angles of attack considered in this work. This can be determined with (Zucrow and Hoffman, 1976)

$$tan\,\varepsilon = \frac{1}{tan\,\delta}\left\{\frac{(\gamma + 1)M_u^2}{2(M_u^2\,sin^2\,\varepsilon - 1)} - 1\right\}^{-1}.\tag{153}$$

After determining the shock angles, the static pressure downstream of the shock can be determined from the static pressure upstream of the shock with (Zucrow and Hoffman, 1976)

$$\frac{p_d}{p_u} = \frac{2\gamma}{\gamma + 1}M_u^2\,sin^2\,\varepsilon - \frac{\gamma - 1}{\gamma + 1}.\tag{154}$$

The static pressure upstream of the shock is connected to the stagnation pressure upstream of the shock, $p_{o,u}$, using

$$\frac{p_{o,u}}{p_u} = \left(1 - \frac{\gamma - 1}{2}M_u^2\right)^{\frac{\gamma}{\gamma - 1}}.\tag{155}$$

The static temperature downstream of the shock can be determined from the static temperature upstream of the shock with (Ames Research Staff, 1953)

$$\frac{T_d}{T_u} = \frac{\left[2\gamma M_u^2\,sin^2\,\varepsilon - (\gamma - 1)\right]\left[(\gamma - 1)M_u^2\,sin^2\,\varepsilon + 2\right]}{(\gamma + 1)^2\,M_u^2\,sin^2\,\varepsilon}.\tag{156}$$

The Mach number downstream of a shock can be determined using (Ames Research Staff, 1953)

$$M_d = \left\{\frac{(\gamma + 1)^2\,M_u^4\,sin^2\,\varepsilon - 4(M_u^2\,sin^2\,\varepsilon - 1)(\gamma M_u^2\,sin^2\,\varepsilon + 1)}{\left[2\gamma M_u^2\,sin^2\,\varepsilon - (\gamma - 1)\right]\left[(\gamma - 1)M_u^2\,sin^2\,\varepsilon + 2\right]}\right\}^{1/2}.\tag{157}$$

To jump across the expansion wave located at the intersection of the slanted surface and the bottom surface or the expansion wave off the top surface for negative angles of attack, the equation (Zucrow and Hoffman, 1976)

$$\delta = \left[-\left(\frac{\gamma + 1}{\gamma - 1}\right)tan^{-1}\left[\frac{(M_d^2 - 1)(\gamma - 1)}{\gamma + 1}\right]^{1/2} + tan^{-1}(M_d^2 - 1)^{1/2}\right]$$
$$+ \left[\left(\frac{\gamma + 1}{\gamma - 1}\right)tan^{-1}\left[\frac{(M_u^2 - 1)(\gamma - 1)}{\gamma + 1}\right]^{1/2} - tan^{-1}(M_d^2 - 1)^{1/2}\right]\tag{158}$$

is evaluated to find the downstream Mach number. In this equation a counterclockwise turning of the flow is taken as a positive angle and a clockwise turning is taken as a negative angle. Next the pressure on the bottom surface can be determined using

$$\frac{p_d}{p_u} = \left( \frac{1 - \frac{\gamma - 1}{2} M_u^2}{1 - \frac{\gamma - 1}{2} M_d^2} \right)^{\frac{\gamma}{\gamma - 1}} . \tag{159}$$

From the result of equation (159) the static temperature downstream of the expansion wave can be determined from

$$\frac{T_d}{T_u} = \left( \frac{p_d}{p_u} \right)^{\frac{\gamma - 1}{\gamma}} . \tag{160}$$

Using the properties determined downstream of the oblique shocks and Prandtl-Meyer expansions the shear stress on the surfaces of the model are determined from

$$\tau = c_f \frac{1}{2} \rho V^2 \tag{161}$$

where $c_f$ is the average friction coefficient, $\rho$ is the density and $V$ is the free stream velocity. Because the Reynolds number for the situation studied here is in the laminar flow regime the average friction coefficient is determined using (Incropera and DeWitt, 2002)

$$c_f = \frac{1.382}{\sqrt{Re}} . \tag{162}$$

To determine the viscosity, Sutherland's correlation is used.

Once all the required surface pressures and shear stresses are determined the lift is determined from

$$L = p_{ss} A_{ss} \cos \delta + p_{bs} A_{bs} - p_{ts} A_{ts} - \tau_{ss} A_{ss} \sin \delta , \tag{163}$$

where $p$ is the pressure along a given surface, $A$ is the area of that surface, $\tau_{ss}$ is the shear stress along the slanted surface, and the subscripts indicate the surface being considered. The drag is determined from

$$D = p_{ss} A_{ss} \sin \delta + \tau_{bs} A_{bs} + \tau_{ts} A_{ts} + \tau_{ss} A_{ss} \cos \delta . \tag{164}$$

The drag is taken as positive in the flow direction and the lift is taken as positive in the upward direction.

The computed values for the lift and drag, along with the measured values, are shown in Figure 93. The forces on this figure, as are all force values presented in this section, are given in grams. Grams are technically a mass unit, but the load cells used in these measurements are identified using grams for force, and the calibration of these devices was done by putting a certain number of grams on the model. Grams tend to be a convenient unit for the magnitude of the forces being considered here. To convert gram force to newtons multiply the gram force by 9.81 and divide by 1000. Figure 93 shows good comparisons between the simple theory put forth in the previous section and experimental measurements for lift values, but a rather poor comparison for drag values. For the assumptions made in the analytical model these comparisons are good. Note that the experimental values show a curvature in the lift as a function of angle of

attack. This same curvature is present in the computed lift values; but it is much smaller and difficult to see in Figure 93.

Note that two sets of experimentally obtained lift values and two sets of experimentally obtained drag values are presented in Figure 93. The two sets of data were taken on different days to verify that the lift and drag results could be reproduced. The two sets of experimental data compare very well. Note that one set of the data was taken over the range from $-10^o$ to $5^o$ and the other set was taken over the range from $-10^o$ to $10^o$.

For the lift values in Figure 93 the comparison between theory and experiment is better for negative angles of attack then positive angles of attack. It may be that viscous effects on the shock coming off the top of the plate are becoming more important for positive angles of attack. The deviation between the measured and calculated values of lift at an angle of attack of $-10^o$ is 4%, at $0^o$ it is 21%, and at $10^o$ it is 13%. These deviation percentages are calculated taking the experimental values as being the correct values.

For the drag values the differences between the measured values and the experimental values are more pronounced than the lift values. The differences vary from 10 to 12 grams. The most probable reason for these differences is the neglect of the strut in the calculations. Including the strut will increase the calculated drag values and bring them closer to the measured values. It is interesting to note that the effect of the wall shear stresses on the drag is about 5 grams.

Examples of the measured lift and drag values as a function of time are shown in Figures 94 and 95 respectively for an angle of attack of $0^o$. As can be seen there is scatter in the measurements, about the same amount for the lift and the drag. Each "x" in these figures represents a data point. The solid lines on the plots represent a least squares linear fit through the data. The slope of the fitted line through the experimental data points is practically zero. The slope should be zero because the lift and drag force measurements shown in Figures 94 and 95 are for steady state conditions; that is there is no physical phenomena occurring that should change the average value of these forces with respect to time. While there is nothing present in this run of the experiment that changes the average value of the lift and drag forces on the plate, there are forces present that change the instantaneous values. Most of the noise seen in the data in Figures 94 and 95 is from wind tunnel noise. There are some low frequency fluctuations in the Mach 5 flow field that are showing up in the lift and drag measurements. These fluctuations in the flow have been verified by high-speed pitot probe measurements as well. These were seen in the pitot probe results presented in Section 4.1 of this part of this report. In addition to the flow noise there is some electrical noise in the measured results. The electrical noise is smaller than the tunnel noise.
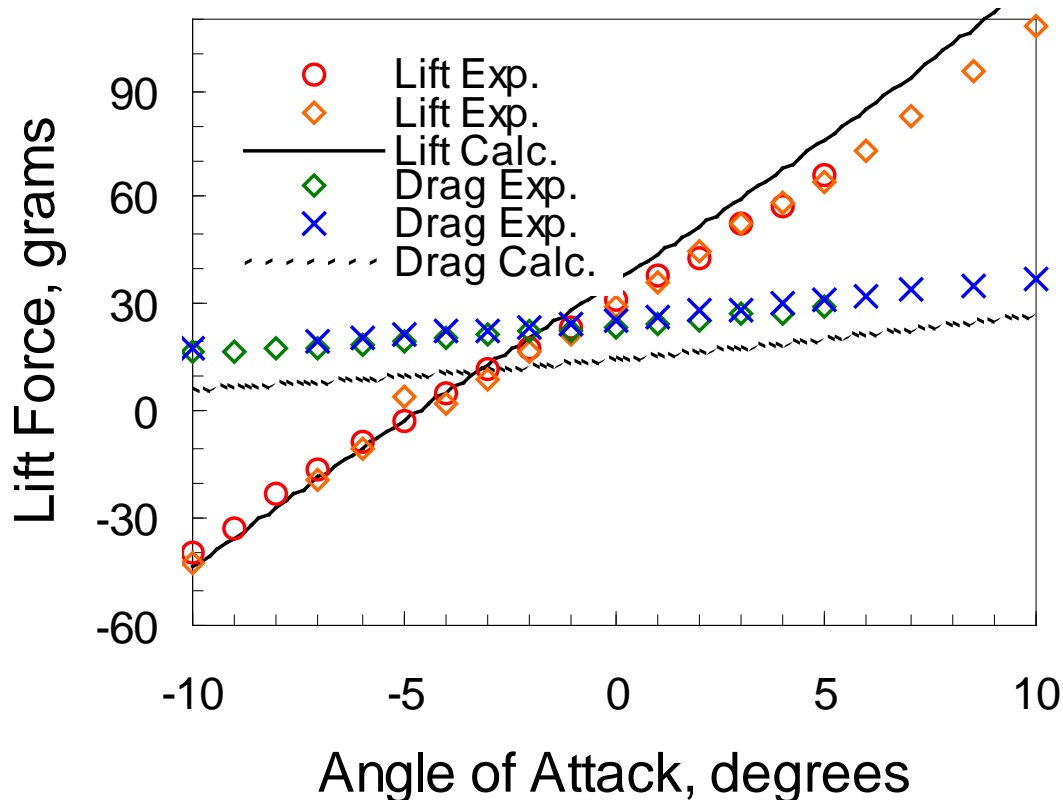
**Figure 93. Comparisons between Measured Lift and Drag and Calculated Lift and Drag on Flat Plate Model as a Function of Angle Of Attack**

To obtain each of the results in Figure 93 a least squares fit of a straight line, as shown in Figures 94 and 95, was put through the measured data as a function of time. The *y*-axis intercept was taken as the average value because the slopes of the lines are very small.

Figure 93 also points out that the lift tends to be larger than the drag. This is due to the larger surface area perpendicular to the direction of the lift pressure forces. Due to the shape of the model, form drag has much less surface area over which pressure forces can be exerted. Remember the lift is always taken perpendicular to the upper surface of the plate and the drag is taken along the length of the plate. The magnitude of the lift forces vary from –42 grams at a -10$^o$ angle of attack to 108 grams at a 10$^0$ angle of attack. At zero angle of attack the lift is 30 grams. It can also be seen that the lift goes to zero between -4$^o$ and -6$^o$ angle of attack. This zero point occurs at negative angles of attack for this flat plate model because of the half wedge frontal shape. The drag values show a continuous increase from a value of 18 grams at –10$^o$ to a value of 37 grams at 10$^o$.
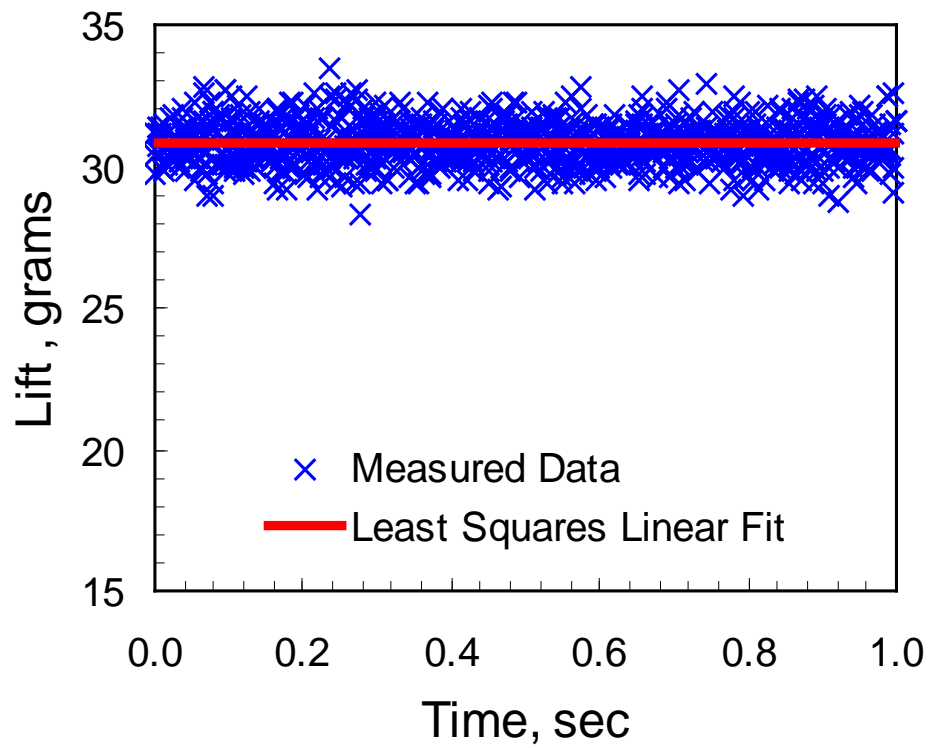
Figure 94.  Lift Measurements as a Function of Time for $0^o$ Angle Of Attack
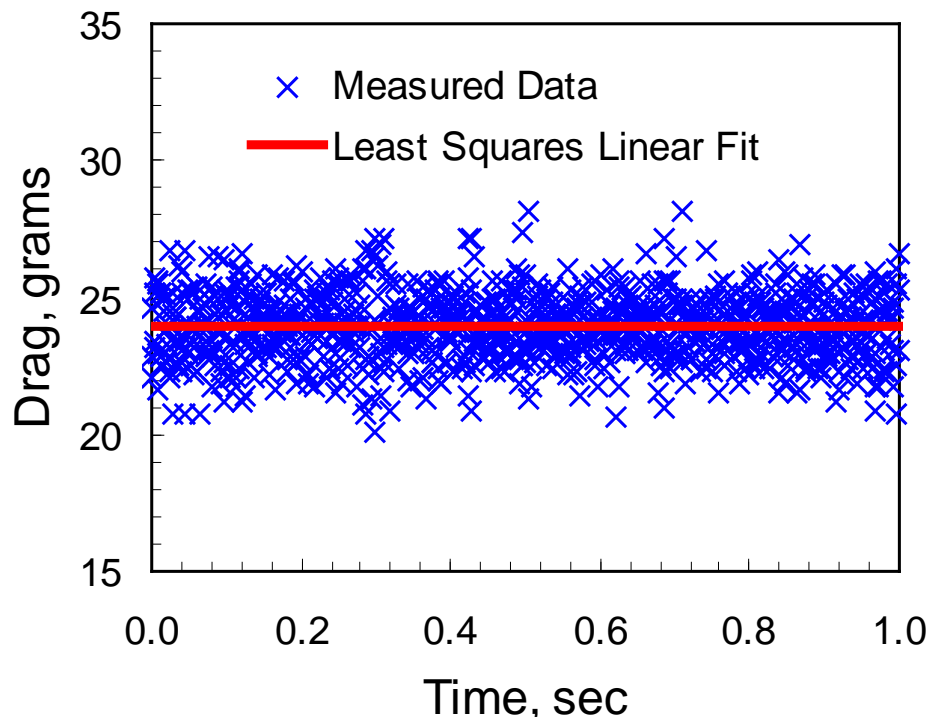


Figure 95.  Drag Measurements as a Function of Time for $0^o$ Angle Of Attack

### 4.2.4 Results

In this sub-subsection measured results of lift and drag for the case with the plasma discharge only and the case where the plasma discharge and the magnetic field are applied to the plate are presented. The plasma results are handled in the sub-subsection immediately below and the plasma and magnetic field results are presented in the sub-sub-subsection following the plasma results.

#### 4.2.4.1 Effect of Plasma Discharge

Because of the flow noise present in the lift and drag measurements, and because the changes caused by the plasma are 0 to 5 grams, the current of the plasma discharge was set to oscillate in a sinusoidal manner over a time frame of 1 second. The oscillation in the plasma discharge was done to mark lift and drag changes caused by the plasma discharge. The lift and drag measurements should oscillate at the same frequency that the plasma current is oscillating. If the same oscillatory behavior is seen in the lift and drag measurements, then lift changes can be attributed to the plasma discharge.

To prove that the lift measurements are oscillating at the same frequency as the plasma current Figures 96, 97 and 98 have been prepared. In these figures the power delivered to the plasma discharge and the lift measurements are shown as a function of time. Power should be read off the left vertical axis and lift should be read off the right vertical axis. In Figures 96 and 97 the measured data is shown without connecting the data points with a line. In Figure 98 the measured data points of the lift are connected with lines to help the reader see the shape of the measured lift results. The power delivered to the discharge is shown as opposed to the current because it has been found that changes in lift are a function of the power. The power and the current are in sync with one another; therefore if the lift measurements are in sync with the power, they are in sync with the current. The power of the discharge is proportional to the current, but it is also a function of the voltage. The power supply was driven with a sinusoidal pulse so that the current output of the power supply was a sinusoidal shape. For the results shown in Figures 96, 97 and 98 the current is varied from 0.005 to 0.100 amps. The power supply used in these experiments adjusts the voltage so that the specified current is delivered to the discharge. This means that the voltage does not have to be sinusoidal. It turns out that it is close to sinusoidal when the current is sinusoidal, but it is not exactly sinusoidal. Plots of the current and voltage associated with the power shown in Figure 97 are shown in Figure 99. Since the voltage signal is not exactly the same shape as the current signal, the power will not be exactly the same shape as the current signal. This cannot be seen from the plots, but it is seen when trying to fit the current, voltage, and power signals with a Fourier series with all frequencies higher than 6 Hz eliminated. The current signal fits nicely while the voltage and the power signals have some small deviations.
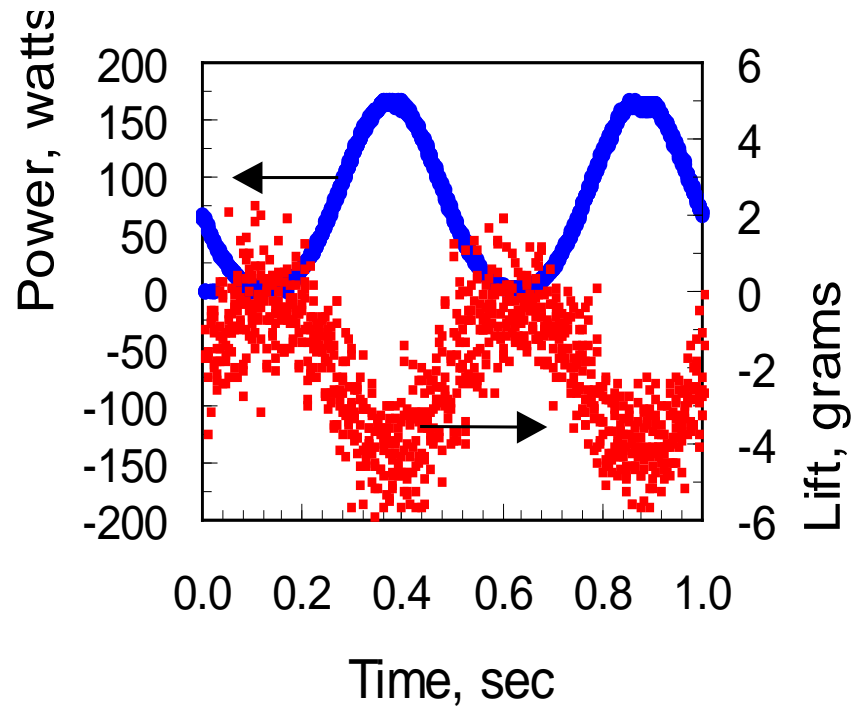
Figure 96. Power and Lift Results versus Time for an Input Current Oscillation of 2 Hz. These Results are for a 0° Angle Of Attack
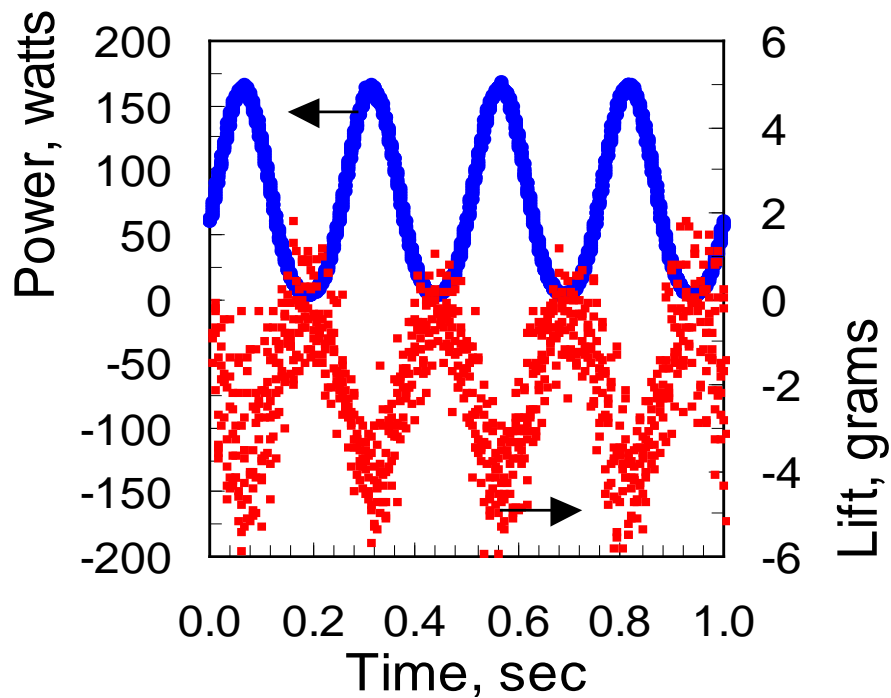


Figure 97. Power and Lift Results versus Time for an Input Current Oscillation of 4 Hz. These Results are for a 0° Angle Of Attack
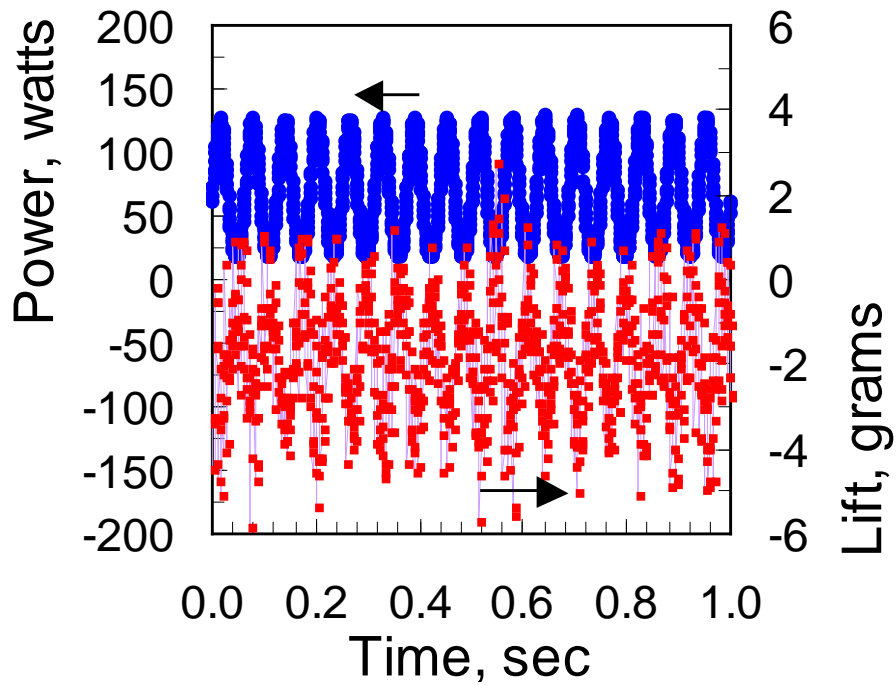
Figure 98. Power and Lift Results versus Time for an Input Current Oscillation of 16 Hz. These Results are for a 0$^o$ Angle Of Attack
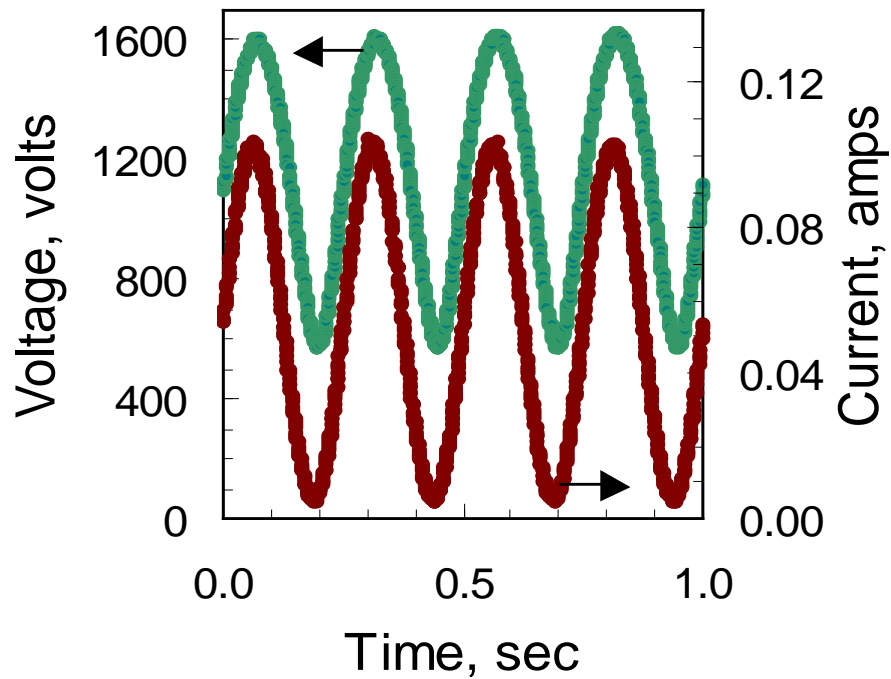


Figure 99. Current and Voltage as A Function of Time Corresponding To the Results Shown In Figure 97

From the plots in Figures 96, 97, and 98 it can be seen that the lift measurements are following the power input to the discharge. In each of these three cases the lift measurements have the same frequency as the power input. The phase between the power and lift is 180$^o$. When the power input is high the lift goes to large negative values and when the power input is low the lift goes to zero. Since the load cells are zeroed with no plasma it is reasonable to see the lift curves go to zero as the plasma input power approaches zero. These figures also show that greater changes in lift are seen with higher powers.

Figure 100 is a plot of drag force versus time corresponding to the lift force versus time plots in Figure 97. Unlike the lift measurements shown in Figure 97 the drag measurements do not show the same oscillatory pattern as the power. The drag force measurements just scatter themselves around a value of zero. A least squares linear fit of the drag measurements also indicates that the average drag is zero. This is reasonable because a plasma discharge applied on the top of the plate, back 1.8 cm from the leading edge, is not expected to have any effect on the pressure distribution on the slanted or back surfaces of the plate. While only two drag measurement plots are shown in this paper, see Figure 106 for the other plot, drag was looked at for all cases investigated, for all angles of attack, and all power settings. The results always indicated that the plasma discharge on top of the plate had no effect on drag within the precision of the measurement.
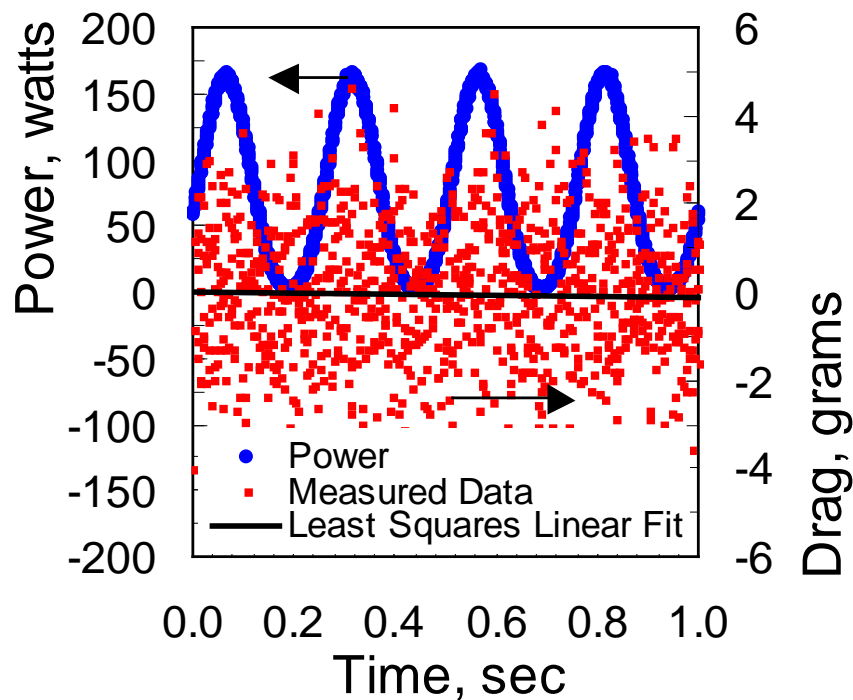


Figure 100. Power and Drag Results versus Time for an Input Current Oscillation of 4 Hz. These Results are for a 0$^o$ Angle Of Attack
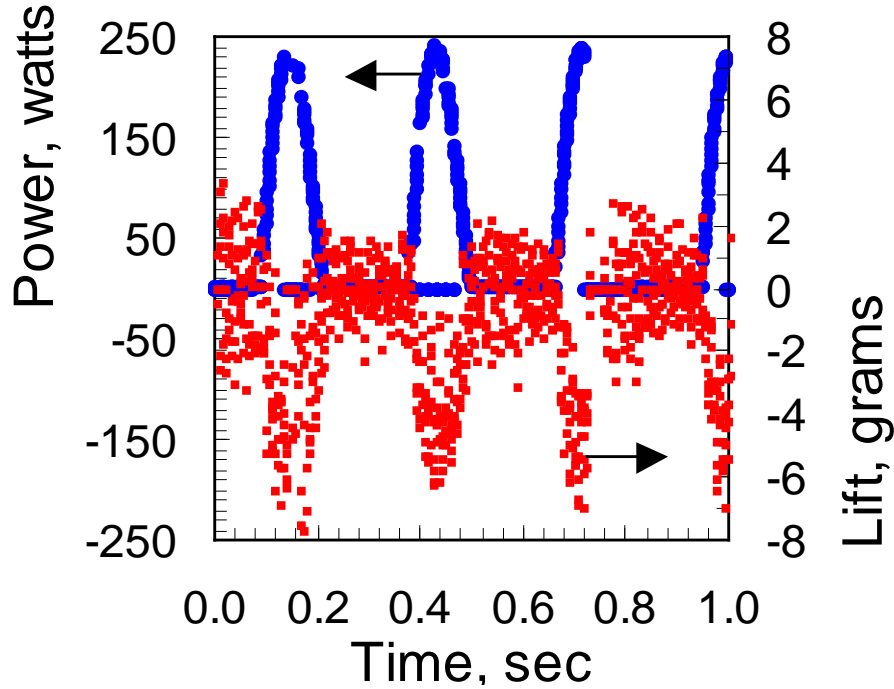
**Figure 101. Power and Lift Results versus Time for A Half Sine Wave Input Current Oscillation of 4 Hz. These Results are for a 0° Angle Of Attack**

One more shape of power input pulse is shown in Figure 101. This power input pulse can be described as a half sine wave. For half of the period the power input is close to the shape of the positive portion of a sine wave and for the other half of the wave the power is zero. The peak current obtained with this half sine wave profile is 0.17 amps. Just like the lift results shown in Figures 96, 97, and 98 the lift measurements in Figure 101 follow the power curve. Note that the discharge goes out for the downward portion of the wave located at 0.72 seconds. Also note that the discharge drops out on occasion for the portion of the pulse where it is suppose to be on. This higher current discharge is not as stable as the lower current ones used to obtain the results shown in Figures 96 through 98.

To get a better idea of how the lift force varies as a function of power the data shown in Figures 96, 97, and 98 are replotted in Figures 102, 103, and 104 with lift on the vertical axis and power on the horizontal axis. All of these plots clearly indicate that the lift increases with power. Because of the noise present in the results there is some room available to question whether the relationship between lift and power is linear; however, a linear relationship does seem reasonable. A linear, least squares fit was placed through the lift data in all three of these plots and the following equations were obtained for lift versus power:

for the data shown in Figure 102

$$L = -0.024P - 0.36 \quad grams, \tag{165}$$

for the data shown in Figure 103

$$L = -0.023P - 0.36 \quad grams, \tag{166}$$

and for the data shown in Figure 104,

$$L = -0.026P - 0.14 \quad grams. \tag{167}$$

The same procedure can be done for the data shown in Figure 101 and the following equation is obtained:

$$L = -0.021P - 0.34 \quad grams. \tag{168}$$

From these four equations an average valued equation can be written as

$$L = -0.024P - 0.30 \quad grams. \tag{169}$$

The slopes of equations (165) through (168) vary from that shown in equation (169) by no more than 13%. The fact that these three slopes are so close to one another is encouraging and indicates that there is repeatability in these measurements and that the noise present in the measured data is on top of a lift signal that is determined by the plasma power. The zero power intercept value in equation (169) is –0.3 grams. Reason dictates that the intercept values should be zero. Zero power is the situation at which the load cells are set to give a null reading. The fact that a nonzero value for the lift intercept is obtained is due to the inaccuracy of the load cells. The intercept value of 0.3 grams is an indication of how well the load cells can be zeroed. Other measurements made with this load cell system indicate that the load cell system cannot make accurate measurements below 0.3 grams.

Equations (165) through (168) were determined for powers up to 230 watts. This peak power was obtained from the data taken to obtain equation (168). Equation (167) had the shortest range of power to which a linear curve was fit. As can be seen in Figures 102, 103, and 104 or Figures 96, 97 and 98 the peak power decreases as the frequency at which the power supply is driven increases. Note also that the minimum powers increase as the frequency increases. The current amplitude range set for all three of these cases is the same value. The data in these figures just highlights the inability of the high voltage DC power supply used in these experiments to quickly change current values. The data for equation (168), which is shown in Figure 101, has higher peak powers than those in Figures 96, 97, and 98 because the peak currents were set to larger values.

Since equation (169) was obtained from Figures 102, 103, 104 and 101 it can be said that this equation is valid for powers up to approximately 230 watts. This equation is only valid for the specific experimental arrangement used in this work. This equation is not to be taken as a general relation between power and lift for plasma actuator applications. The peak lift change given by equation (169) for the peak power of 230 watts is 5.2 grams. The lift on the plate at zero angle of attack with no plasma is 29.8 grams. This means 230 watts causes an 18% change in the lift. According to equation (169) a 60 watt power input causes a 4% change in lift. Higher current inputs were tried than that used to obtain the peak power of 230 watts. The difficulty in obtaining higher currents is that the diffuse looking discharge starts to constrict into filaments. This even occurs at much lower power settings. When the diffuse discharge breaks down into filaments the voltage drops and the power input goes down. Other problems that occur are that more electrical noise is present in the measurements and the electrodes start to erode. The electrodes are not water-cooled and therefore cannot take the concentrated heat loads of a constricted discharge for any extended period of time.
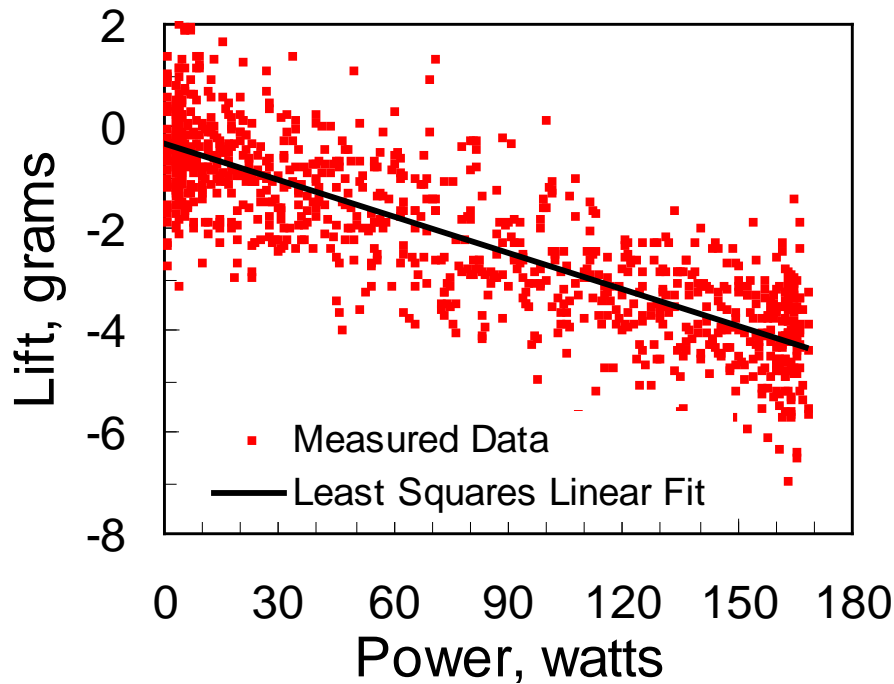
**Figure 102. Lift Versus Power for an Input Current Oscillation of 2 Hz. These Results Are For a 0° Angle Of Attack**

The change in lift versus power for different angles of attack is shown in Figure 105. The same type of plot for drag is shown in Figure 106. Raw data is not shown in these graphs only the least square linear curve fits of the raw data. These curve fits indicate that the affect of the plasma on the lift and the drag is not a strong function of the angle of attack. This is not surprising for drag results because the plasma tilts with the plate and is always located on the top of the plate. Thus there is no plasma near the surfaces that would change the form drag. The difference in the drag curves is mostly due to inaccuracies in zeroing the load cells. It was expected that the lift results would show more of a change then they do in Figure 105. Once again the difference in the zero power intercepts is due to inaccuracies in the measurements and in zeroing the load cells. Thus the line for a –1° angle of attack is separated from the group simply because of inaccuracies in determining the zero intercept. The intercept for all angles of attack should be zero. The changes that were expected in these curves is the slopes. If there is a trend to be obtained from the lift data, it is that there is slight decrease in the slope as the angle of attack deviates from 0°. All the data in Figures 105 and 106 were obtained with a 7 Hz oscillation of the current from a minimum value of 0.005 amps to a maximum value of 0.055 amps.
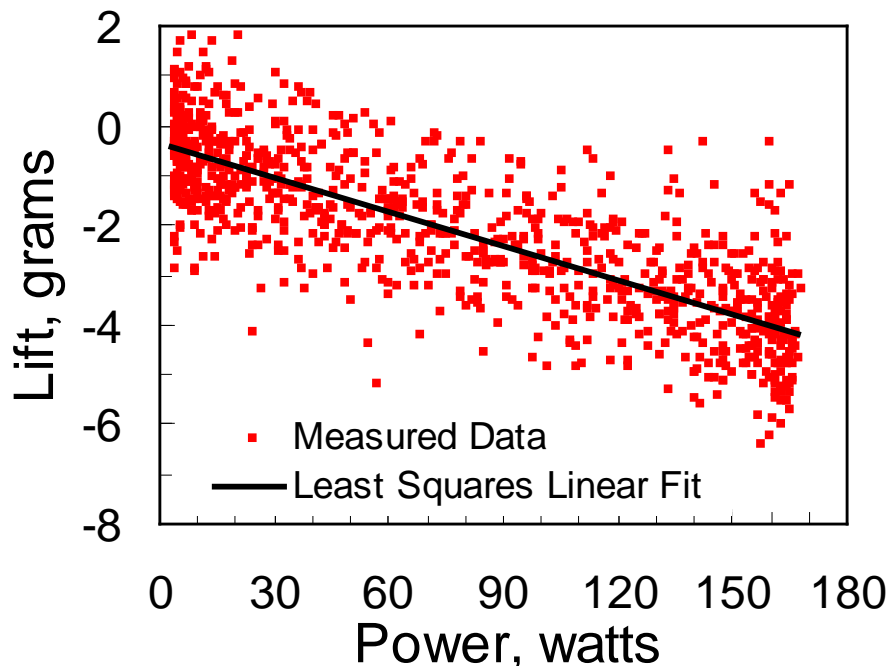
Figure 103. Lift Versus Power for an Input Current Oscillation of 4 Hz. These Results Are For a 0° Angle Of Attack
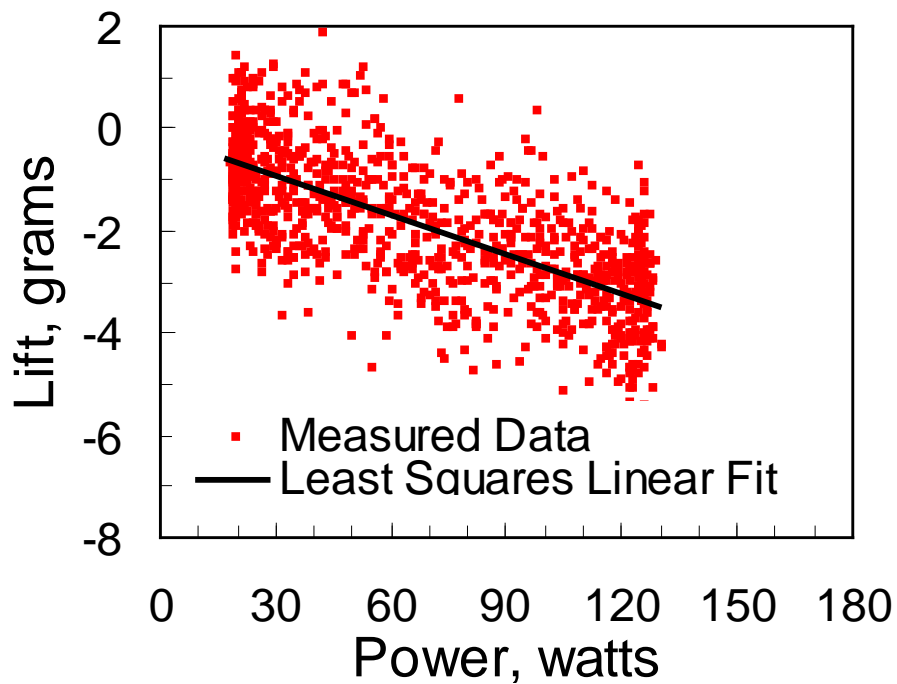


Figure 104. Lift Versus Power for an Input Current Oscillation of 16 Hz. These Results Are for a 0° Angle of Attack
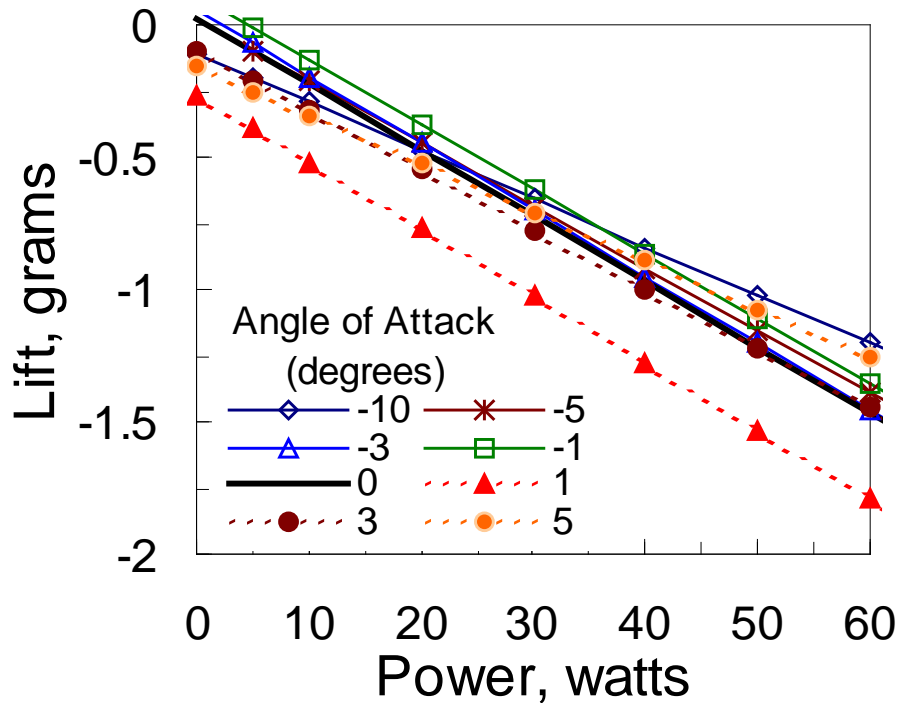
**Figure 105. Lift Versus Plasma Power for a Range of Angle of Attacks**

One last figure shown in this sub-sub-subsection is a voltage versus current plot corresponding to the voltage and current versus time graph in Figure 99. These results are shown in Figure 107. This is an interesting plot because it shows that the voltage undergoes a hysteresis with respect to the current. Except at the ends of the oval shape in Figure 107, all currents can be supported by two voltages. The low voltages on these curves correspond to the regions of the plot shown in Figure 99 where the current is going from a low value to a high value. The higher voltage at any current comes from the portion of the graph where the current is going from a high to a low value. The voltage values in this work are measured across the electrodes and the current values are determined by measuring the voltage across a resistor located next to the anode. The behavior in Figure 107 indicates that the plasma/electrical circuit has some low frequency capacitance associated with it.

### 4.2.4.2  Effect of Magnetic Field and Plasma Discharge

A few difficulties in obtaining accurate changes in lift and drag with the application of a magnetic field were encountered. The biggest difficulty was that the load cells are made of stainless steel and thus interacted with the applied magnetic field. With no flow over the model and no plasma present fairly large changes in the load cell readings were recognized as the magnetic field strength was increased. The means by which this problem was overcome was to zero the load cells with the flow and magnetic field on, and then look for a change when the plasma is turned on. Thus in order to see the effect of the magnetic field, the results taken with the magnetic field on have to be compared to a similar case with no magnetic field. This is done in this section.

An example of data taken with the magnetic field on is shown in Figure 108a. These results are for a magnetic field of -0.2 tesla and a discharge current that is varied from zero to 0.075 amps in a half sine fashion. Thus half of the cycle no current is delivered to the discharge. The power

profile for this case is also shown in Figure 108a. This power profile should be compared to that shown in Figure 108b, which was taken for a similar case as that shown in Figure 108a, except there is no magnetic field present. The major difference between these two power profiles is the peaks are a little smaller for the magnetic field case. The peaks for the no magnetic field case go up to 100 watts, while those for the magnetic field case only go up to 90 watts. For a given current input the voltage required to run the discharge with the magnetic field on decreases a small amount.
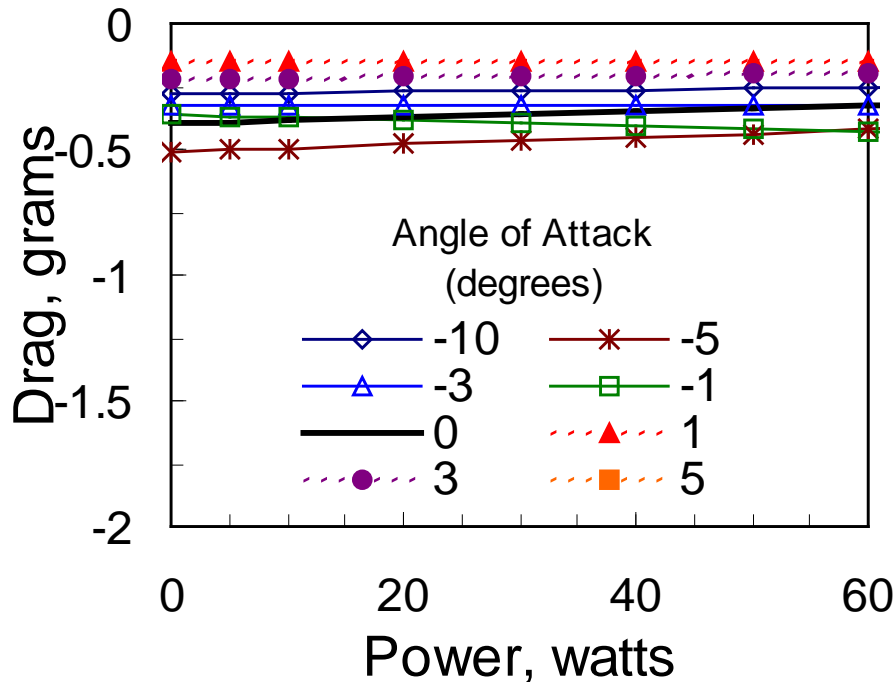


Figure 106. Drag Versus Plasma Power for a Range of Angles of Attack

The lift profiles taken for the -0.2 tesla magnetic field case and the no magnetic field case are also shown in Figures 108a and 108b respectively. For both cases it can be seen that the general trend of the lift signal follows the power input; however, it can also be seen that there is more noise in the data with the magnet on, than with the magnet off. This was the case for all magnetic field data taken. The discharge was less stable and the lift measurements had more noise associated with them. The noise is also more bothersome in the magnetic field case because the changes in lift with power are smaller than the case without a magnetic field. To help see the lift results caused by the power changes through the noise, the lift measurements were numerically filtered to eliminate all frequencies larger than 50 Hz. This is plotted on Figure 108a as a solid black line. This was also done for the no magnetic field lift data shown in Figure 108b. This filtering of the measured data brings out, in a clearer way, the response of the lift measurement to the power input. The low pass numerical filter was kept at 50 Hz instead of 5 Hz because filtering at 5 Hz did not match the measured power signal as well as filtering at 50 Hz. The 50 Hz filtered power signals are plotted in Figures 108a and 108b. They cannot be seen because they lie right under the unfiltered power data.

The lift results shown in Figures 108a and 108b show that there is an effect of the magnetic field on the lift. This is more clearly shown in Figure 109 where least squares fitted lift results are plotted as a function of power for a magnetic field of -0.2, -0.1, 0, 0.1, and 0.2 tesla. The lines

that are shown in Figure 109 come from plots such as that shown in Figure 102. Figure 109 clearly shows that the effect of the magnetic field is to reduce the lift change with the application of a plasma relative to the change seen with the application of a plasma with no magnetic field. It also appears as if positive magnetic fields reduce the lift more than negative directed fields. For the experimental results presented in this paper the cathode is located upstream and the anode is located downstream. A positive directed magnetic field tends to keep the discharge closer to the flat plate's surface relative to the no magnetic field case. The negatively directed magnetic field pulls the middle of the discharge further from the plate than the no magnetic field case, but the discharge at the cathode is suppressed. Figures 110, 111, and 112 show pictures of plasma discharges for magnetic fields of –0.1, 0, and 0.1 tesla respectively.

While the data shown in Figure 109 clearly shows and effect of the magnetic field, the question still remains unanswered as to what is the reason for this change. Is the primary reason for this change that the magnetic field is altering the means by which the plasma heats the flow and then this altered heating changes the measured lift? Or, is the primary reason for this change that the magnetic field is applying a Lorentz force to the plasma which is directly transmitted to the bulk of the flow? In the first case mentioned above there is a Lorentz force present, but the Lorentz force only acts to move the plasma so that it heats the high-speed air flow differently. In the second case mention the magnetic field uses the plasma to transmit a force to the bulk of the high-speed air-flow. In the work performed here it is known that the discharge moves when a magnetic field is applied. This is shown in Figures 110 through 112. This has also been seen in other documented experiments performed by the authors (Menart et al., 2003b). It is suspected that the movement of the heating location has a dominate effect on the measured changes in lift.

It should be noted that drag measurements were also made for the case of the magnetic field. Just like the case for a plasma discharge alone, no noticeable changes in the drag were seen when a magnetic field was applied. As mentioned before there was no expectation that there would be any change in the form drag caused by the plasma or the magnetic field. However, the results presented here also indicate that there is no significant change in the viscous drag.
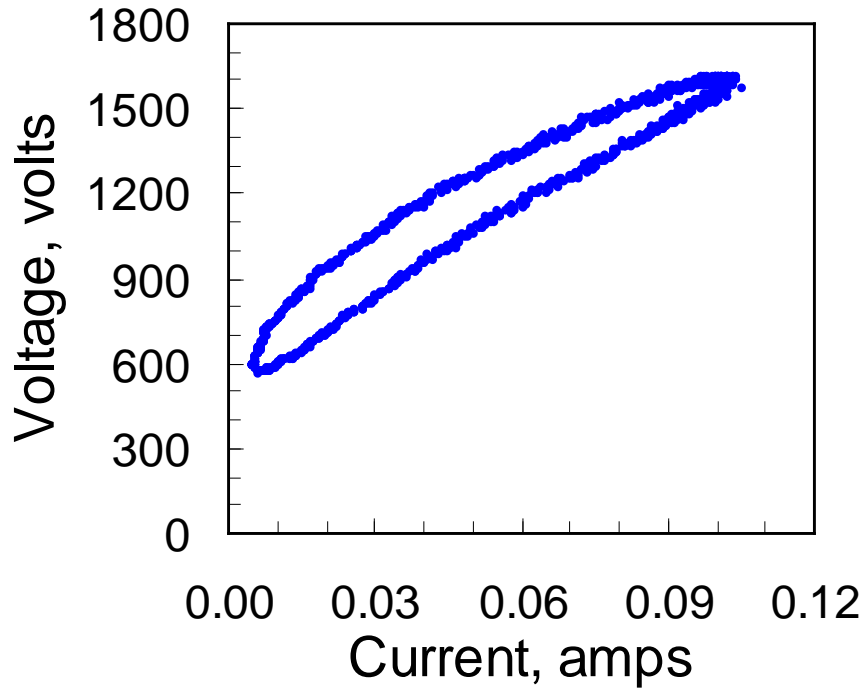
Figure 107. Voltage versus Current for the Case Shown In Figure 99



(a)                                    (b)
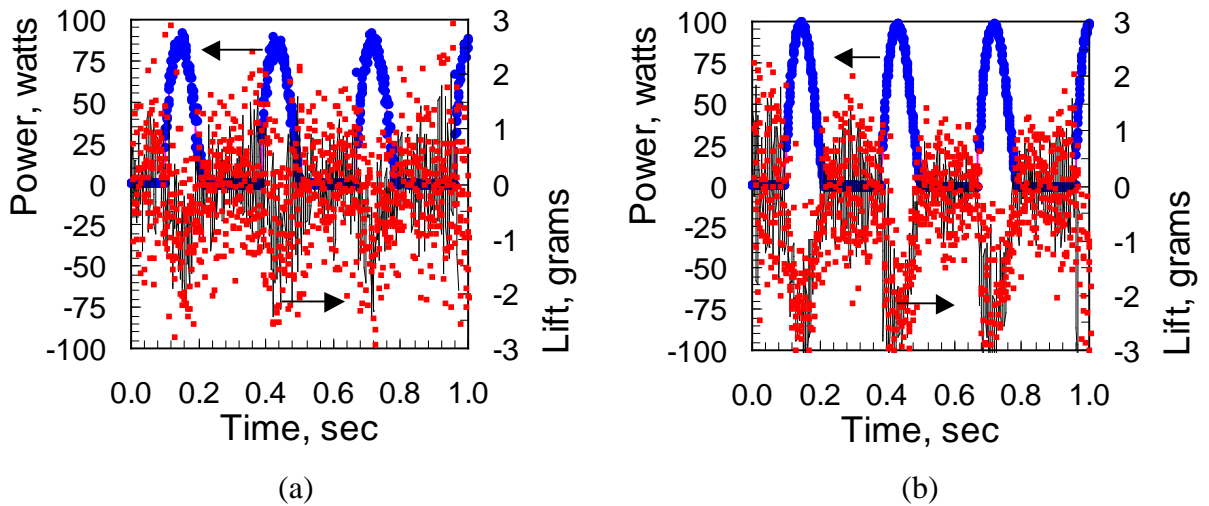
Figure 108. Power and Lift Results Versus Time For An Input Current Oscillation of 4 Hz for the Case of (a) -0.2 Tesla Magnetic Field and (b) the Same Case Without a Magnetic Field. These Results are for a $0^o$ Angle of Attack. The Raw Lift Data Is Shown as Points and the Fourier Series Fit of the Lift Data Utilizing Frequencies Below 50 Hz is Shown as a Solid Line.
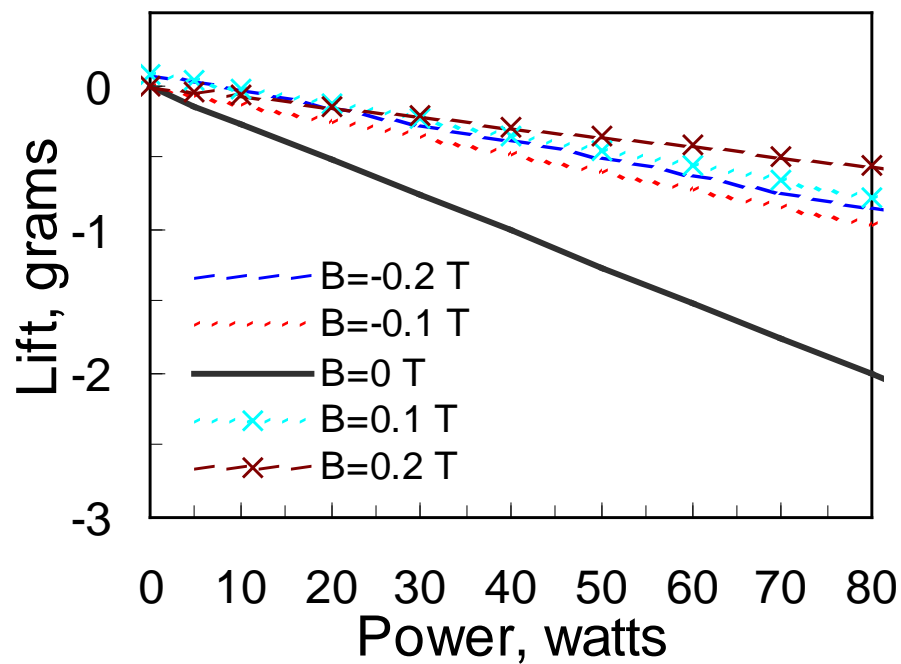
Figure 109. Lift Versus Power and Magnetic Field Strength for an Angle Of Attack of $0^o$



Figure 110. 0.05 Amp Plasma Discharge in a –0.1 Tesla Magnetic Field at $0^o$ Angle of Attack
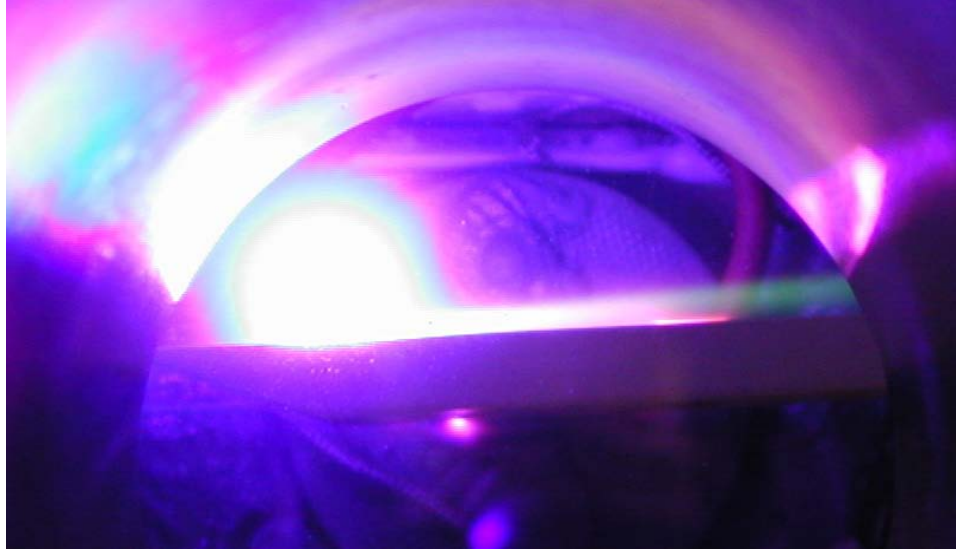
Figure 111. 0.05 Amp Plasma Discharge without a Magnetic Field Present at $0^o$ Angle of Attack
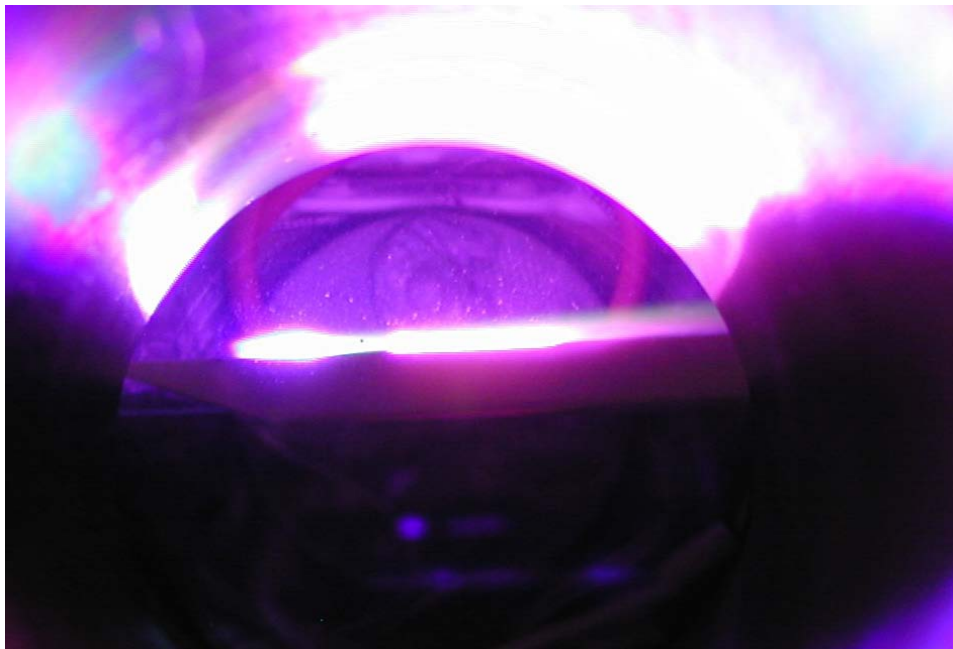


Figure 112. 0.05 Amp Plasma Discharge in a 0.1 Tesla Magnetic Field at $0^o$ Angle of Attack

### 4.2.5 Summary

This portion of the experimental work has investigated the effects of a plasma discharge and a magnetic field on the lift and drag acting on a flat plate with a half wedge leading edge, flat plate model located in a Mach 5 airflow. These measurements were done with a lift and drag measurement device designed and built specifically for these measurements by the authors. Comparisons of the measured results against some simple calculated results indicate that this lift and drag measurement device is working well.

In this work it was determined that a DC plasma discharge located on the upper surface of a flat plate model alters the lift, but has little effect on the drag. This is a reasonable result because the

114

discharge on the top of the plate does not affect the flow field in front of the plate and the viscous forces on the plate are small to start with. The data measured as part of this work indicates that the changes in lift caused by the discharge on top of the plate are negative and they are linearly proportional to the power applied. For the model and electrode configuration tested in this work an empirical equation describing this relationship is

$$L = -0.024P - 0.30 \quad grams \ .$$

It must be realized that this is not a general equation that can be used to determine the amount of lift change for any plasma actuator situation. This equation is specific to the configuration and conditions tested here. It is believed that the location where the heat is applied on the plate will be important in lift changes caused by a plasma discharge. The maximum change in lift seen is 18%. This was seen at the highest applied discharge power for a zero angle of attack. Measurements of lift and drag with a plasma discharge applied were taken at angles of attack between -10 and 5 degrees from the flow direction. It appears that the angle of attack does not make a significant difference in the manner in which the plasma discharge alters the lift on the plate for angles between $-10^o$ and $5^o$. It must be remembered that lift in this work is always measured perpendicular to the upper surface of the plate. At any of the angles of attack investigated, no significant change in drag was noticed because of applying a plasma discharge. In this work drag was always measured parallel to the surface of the plate.

The effect of the application of a magnetic field in addition to the discharge is to suppress the ability of the plasma discharge to alter the lift. The magnetic field does affect the shape and location of the plasma discharge because of Lorentz forces acting on the charged particles in the discharge. Thus a possible reason for the suppression of the lift change caused by the plasma discharge is that the location of the discharge heating has been altered. The discharge also tended to became unsteady because of the application of the magnetic field.

## 4.3   Study of Electrode Size and Position on a Flat Plate

### 4.3.1   Introduction

From the work done in Section 4.2 of this report the question arose if the electrode geometry and electrode position has an effect on the amount of power required per unit lift change obtained. This is what is studied in this subsection of this report. Both the cathode position and the cathode shape are altered and lift measurements made. The anode size and position are held constant. In general, the affect of the anode on lift changes relative to changes caused by the cathode seem to be small. This is a reasonable assumption because most of the energy from the DC discharges being used in this work is deposited in the hypersonic air stream over the cathode. Four different cathode sizes and four different cathode positions are considered. The cathode is always kept upstream of the anode on the surface of a flat plate model with a half-wedge leading edge.

In this subsection a new force measurement device is used. This force measurement device was developed to avoid the damage that happened to our previous device because of plasma arcing. There are advantages to both types of force measurement devices used in this work.

### 4.3.2 Experimental Facility

The wind tunnel used to carry out the work being presented in this section is the same as used in the previous section (see Figures 73 and 74). A brief description of this tunnel is given in Section 4.1.2 of this report. For the results presented in this subsection the hypersonic wind tunnel is run at a stagnation pressure of 370 torr. This results in a static pressure of 0.6 torr at the test section.

The model used for the lift measurements in this subsection (see Figures 113 and 114) is similar to the model used in the previously described lift and drag measurements (Section 4.2. There are some differences as can be seen by comparing Figures 91 and 92 with Figures 113 and 114. The model used in this work is made out of a circuit board. This is the reason the overall thickness of the model is only 0.2 cm; as compared to the 0.6 cm thick model shown in Figure 92, which is constructed out of a machineable ceramic. The baseline electrode configuration in the circuit board model can simply be etched out of the 0.03 mm thick copper layer on the upper surface of the circuit board. The electrodes in the model shown in Figure 92 are made of 0.6 mm thick copper straps. The overall length of the model has been shrunk from 6.6 cm shown in Figure 92 to 5.1 cm shown in Figure 114. One other difference between the two models is the model used in this subsection has two struts to connect it to the side wall of the tunnel and the one shown in Figure 91 only had one strut connecting it to four load cells on the side wall of the tunnel.

The work described in Section 4.2 of this report used the model shown in Figure 91 to make lift and drag measurements in the wind tunnel shown in Figure 74. Four load cells were utilized to perform this task. Two were used for making the lift measurements and two were used for making drag measurements. The load cells sensed the forces applied to the model as compressive or tensile stresses and extremely small deflections were involved. These compressive and tensile stresses can be calibrated to determine the lift and drag forces on the model. Since forces are being sensed with this system, with almost no movement of the model, the response time is very fast. A difficulty with this type of measurement is that the load cells sometime offer themselves as an alternative path for the plasma discharge. When this happens, the load cells are destroyed. This problem was one reason the lift measurement system used in this section was devised. Another reason is that a verification of the lift and drag results presented in Section 4.2 by a second measurement technique is desired. Comparisons of the results from these two measurement techniques will be given in this work.

For the work described in this section, a displacement technique for determining the lift on the model is utilized. A given lift force acting in the downward direction causes the plate to deflect down, and a given lift force in the upward direction causes the plate to deflect upward. This deflection is proportional to the lift force acting on the plate. The deflection of the plate is measured with a Keyence LK-G157 laser displacement sensor. This meter is rated to be able to measure deflections of 0.6 μm. A nice aspect of this measurement is that the displacement meter is located in the bottom of the wind tunnel test section, out of the high speed flow, 11.2 cm away from the plasma discharge located on the surface of the model. This greatly reduces the chances of the plasma passing through the laser displacement sensor instead of between the electrodes. The principle used by the laser displacement sensor is to measure the model deflection. The model deflection is determined by sending out a laser beam that reflects off the bottom of the model to a detector located in the laser displacement sensor. The strength of the reflected laser light from the bottom of the model is proportional to the distance between the laser displacement sensor and the bottom of the model. This detected light intensity is converted to a displacement

116

of the object being interrogated. A calibration curve of lift to deflection, or lift to voltage output from the laser displacement sensor, is linear. The sampling frequency of the Keyence LK-G157 laser displacement sensor is 50 kHz. The response time of the model is much slower than this. Because this technique requires the plate to be deflected on the order of tens of microns, the plate does not respond as quickly to changes as the load cell arrangement used in the previous section. A model with a slow response time tends to eliminate flow noise present in the Mach 5 wind tunnel from the measurement. The Mach 5 wind tunnel flow noise was sensed by the fast response of the load cell measurement technique used in Section 4.2 while it is not by the plate and laser displacement sensor used in this subsection. The natural frequency of the model used in this subsection is 50 Hz.



**Figure 113. Picture of the Flat Plate Model Used in Section 4.3 of this Work**

To take data from the laser displacement sensor a personnel computer, a national instruments M-series high speed data acquisition board, and an amplifier are used. All the data in this paper was sampled at a rate of 500 samples per second. In addition to the laser displacement sensor readings, the stagnation pressure, stagnation temperature, voltage across the discharge, and current to the discharge are monitored at 500 Hz. To determine the effect of the plasma on the lift, the laser displacement sensor is zeroed just before the plasma is ignited. This way the deflection of the model measured by the laser displacement sensor is only that caused by the plasma. All results presented in this paper show only the lift changes caused by the application of the plasma discharge.

The plasma discharges are generated using a Universal Voltronics, unipolar, DC electrical power supply capable of delivering 0.8 amps of current up to electrical potentials of 10,000 volts. This power supply is operated in the current control mode for all the data collected in this subsection of this report. The current output from the power supply is modulated into a 3 Hz square wave by a computer controlled switch that opens and closes at the selected frequency. In this work the square waves have a peak current of 9 or 24 mA. The minimum current in the square wave is zero since this corresponds to an open circuit condition. A low frequency discharge modulation is chosen in this work because of the response time of the model. To obtain a sine wave current profile, used for one set of results shown in the comparison section, the DC power supply is computer controlled to give this type of output.
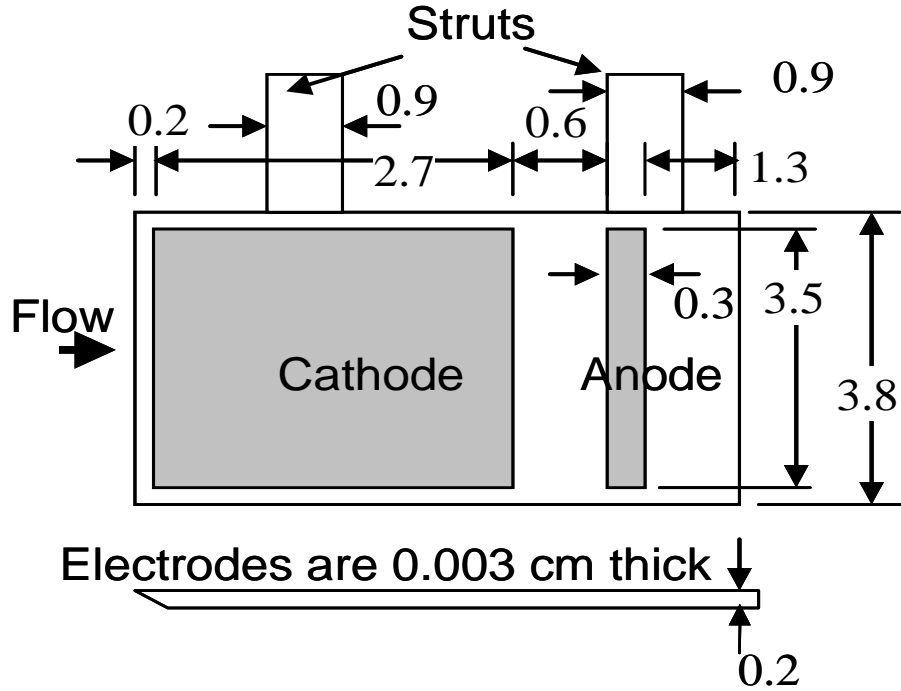
**Figure 114. Dimensioned Drawing of the Flat Plate Model Used in Section 4.3 Work**

### 4.3.3 Electrode Arrangements

As mentioned in the introduction the primary goal of the work presented in this subsection of this report is to check the effect of the lift generated per unit power input for different size cathodes and different locations of the cathode. In this sub-subsection drawings of all the electrode arrangements studied are presented. For some of the cathode arrangements pictures of the plasma generated are given also.

To study the effect of size of the cathode the electrode arrangements shown in Figures 115 and 116 are tested. The leading edge of the cathode in the Figure 115 arrangements are increasingly lengthened in the streamwise direction, but in each case the leading edge of the cathode coincides with the leading edge of the plate. Figure 116 cathodes are increasingly lengthened in the streamwise direction, but in this case the trailing edge of the electrode is held fixed. The electrode arrangements in Figure 116 never completely reach the leading edge. Even for the largest size electrode there is 0.4 cm of nonconducting surface upstream of the leading edge of the cathode. In both the Figure 115 electrode arrangements and the Figure 116 electrode arrangements the size of the cathode increases in 0.6 cm increments.

To study the effect of the cathode position the electrode arrangements shown in Figure 117 and Figure 118 are tested. The electrodes shown in Figure 117 are all the same size, 0.6 cm long in the flow direction and 3.5 cm wide in the spanwise direction. Four different positions of this electrode are shown in Figure 117. Note that the most upstream position is still 0.2 cm downstream of the leading edge of the plate. The cathode arrangement shown in Figure 118 is essentially the cathodes shown in Figure 117 rotated 90$^o$. It should be noted that the long dimension of the electrode was changed from 3.5 cm to 2.7 cm.

All the cathode arrangements shown in this paper were made from the electrode arrangement shown in Figure 115d. The cathode shown in Figure 115d simply has to be masked down to

obtain any of the arrangements shown in Figures 115 through 118. This masking process is done with boron nitride paint. This paint is easy to apply and easy to remove. Boron nitride is a good electrical insulator.

### 4.3.4  Results

### 4.3.4.1  Results from Displacement Meter Measurements

Before presenting the results showing the effect of cathode size and cathode position some of the fundamental measured values are presented so the reader can assess the accuracy of the results. A typical lift versus time plot for a 24 mA discharge is shown in Figure 119. This plot shows the results for a 10 second period using a 3 Hz square wave current. The 3 Hz square current wave gives rise to a 3 Hz square power wave. The power wave is also shown on this plot. The measured lift is the oscillating curve that gradually decreases up to a time of 4 seconds and then oscillates around a constant average value of -0.84 grams. The change in the average value of the lift from 0 to 4 seconds is due to the copper cathode heating to higher temperatures. This same trend occurs when the air flow is removed and the plasma power is oscillated in still air at 7 torr. In this case, however, the 3 Hz oscillations in the lift are not seen. The lift curve is just a smooth change to larger negative values until it levels off to a constant value. Since this average change in lift is seen with the air flow off, as well as with it on, it cannot be due to the plasma changing the aerodynamic lift forces on the model. The cause of this average change in the lift has to be due to the model heating and deflecting in the downward direction. At this time the authors believe it is due to expansion of the copper cathode relative to the circuit board upon which the copper is attached. It is thought that the expansion of the copper bends the model, which is sensed as a change in the position of the model. Every 20 µm displacement of the model corresponds to a 1 gram force. The key aspects of the lift curve that have to be noticed is that the 3 Hz oscillations continue throughout the 10 seconds, these oscillations follow the power input curve, and these oscillations essentially have the same peak-to-peak value for the entire 10 seconds. It is this peak-to-peak value of the lift curve that is the amount of aerodynamic lift caused by the plasma discharge. It is the average of this peak-to-peak value over the last four seconds of the data acquisition period that is presented as the aerodynamic lift caused by the plasma. An enlarged view of the 8 to 10 second results shown in Figure 119 is given in Figure 120. In this figure, as well as Figure 119, there appears to be noise on top of the 3 Hz lift signal. The rapid oscillations seen in the lift results are the model vibrating at its natural frequency of 50 Hz.
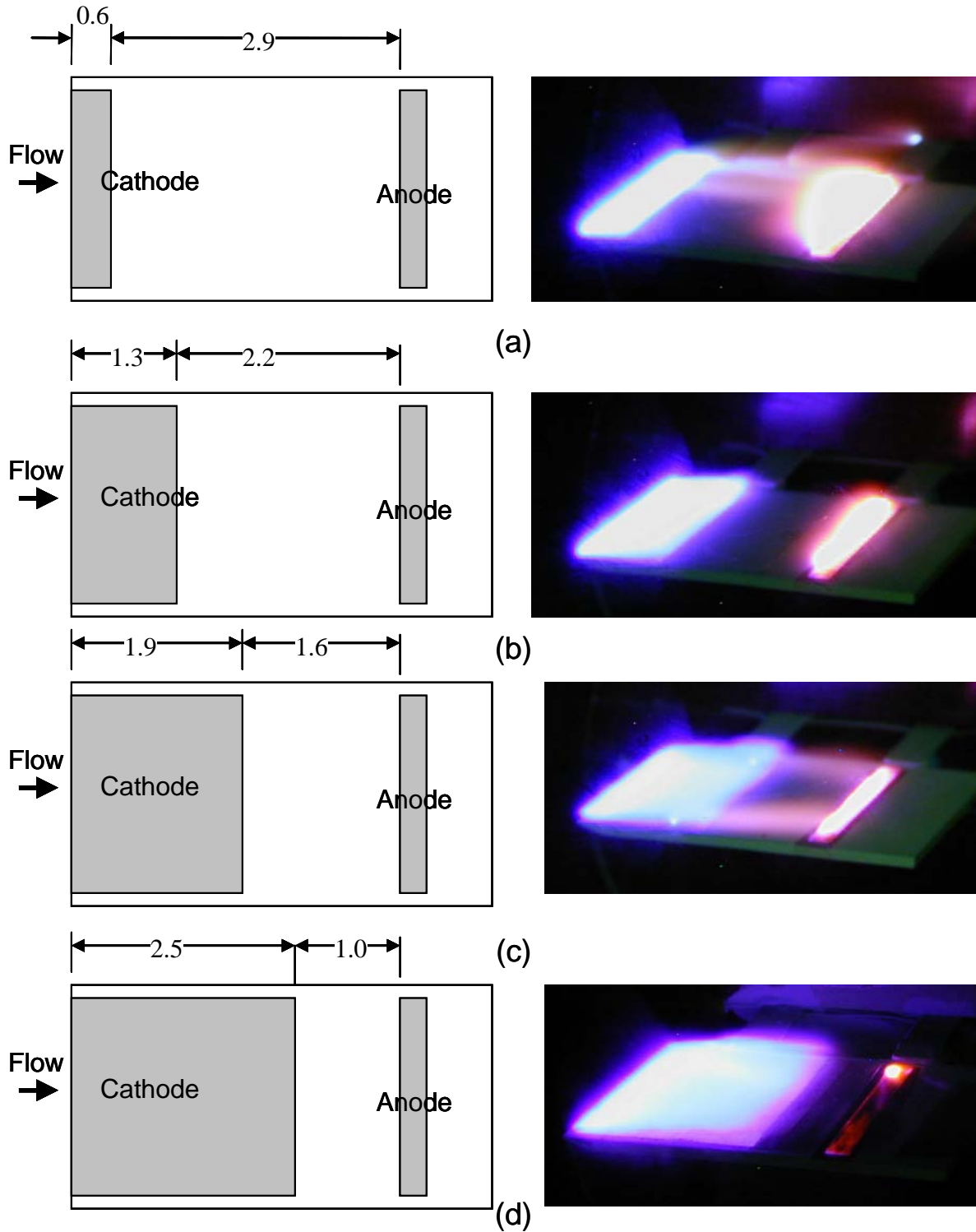
Figure 115. Drawings and Discharge Pictures of Different Size Electrodes Where the Cathode Becomes Larger In the Streamwise Direction Starting From the Leading Edge of the Model

Flow  Cathode  Anode

2.3  0.6  0.6

Flow  Cathode  Anode

2.0  0.6  0.9

(a)

1.6  1.3  0.6

Flow  Cathode  Anode

1.4  0.6  1.5

Flow  Cathode  Anode

(b)

1.0  1.9  0.6

Flow  Cathode  Anode

0.8  0.6  2.1

Flow  Cathode  Anode

(c)

0.4  2.5  0.6

Flow  Cathode  Anode

0.2  0.6  2.7

Flow  Cathode  Anode
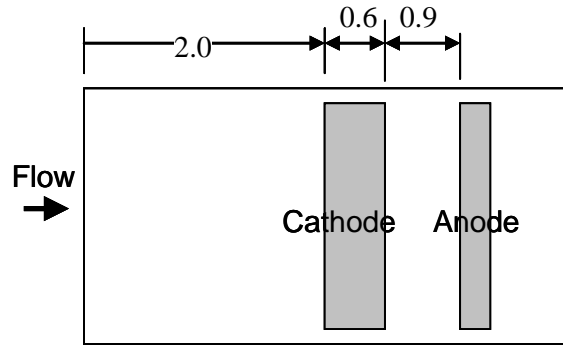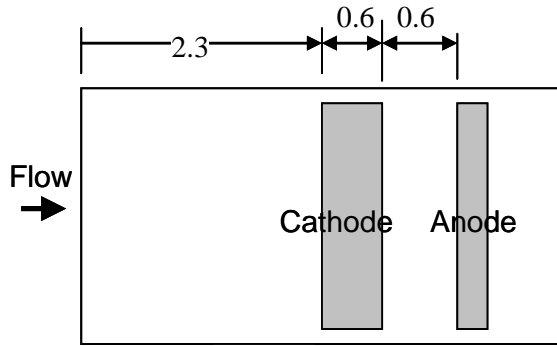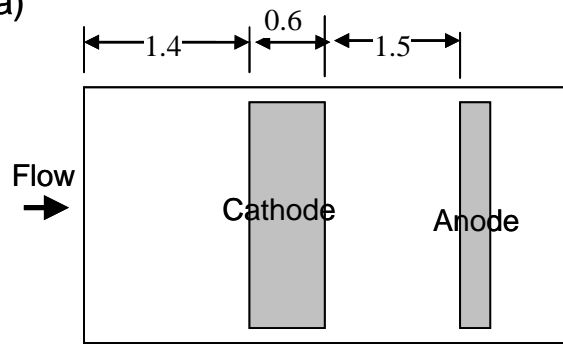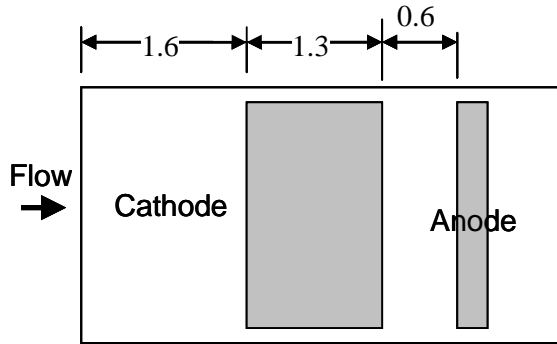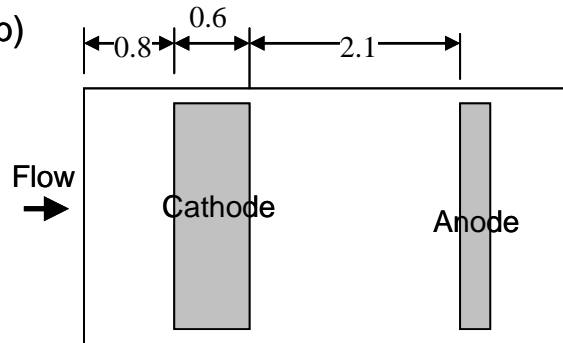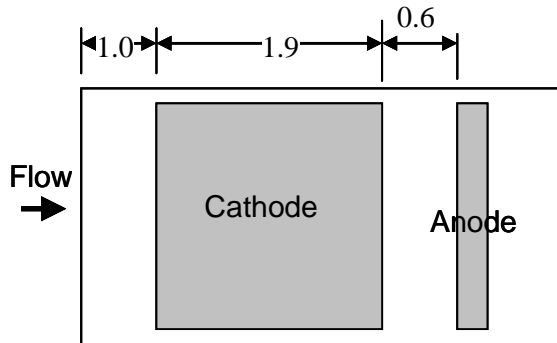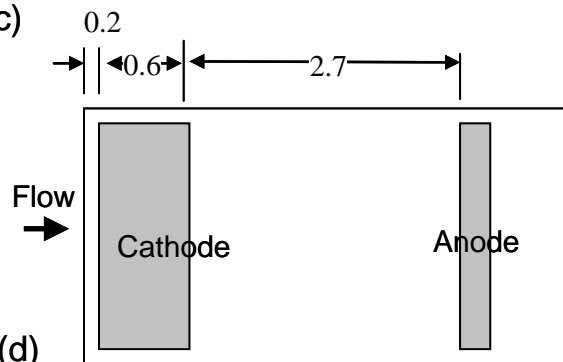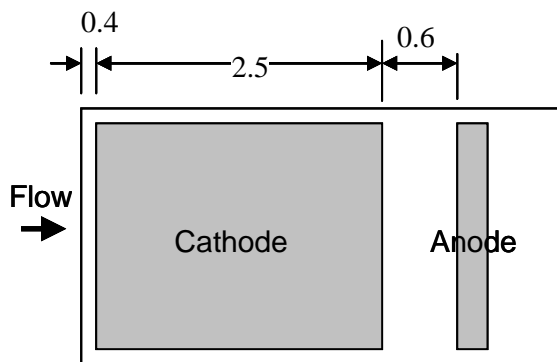
(d)

Figure 116. Drawings of Different Size Electrodes Where the Cathode Becomes Larger Starting from the Middle of the Model Getting Larger in the Upstream Direction

Figure 117. Drawings of Different Electrode Positions

121
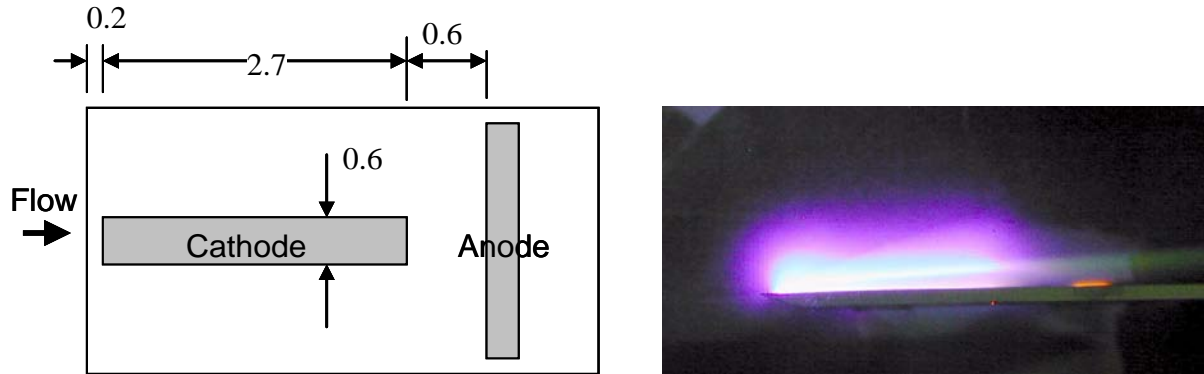
**Figure 118.  Drawing and Discharge Picture of Streamwise Cathode**

The lift and power curves for a modulated 9 mA discharge are shown in Figure 121. For a 9 mA discharge the lift changes become smaller making it more difficult to extract the aerodynamic lift change caused by the plasma. It can still be done, but the results have a little more uncertainty in them. More scatter will be seen in the 9 mA results then in the 24 mA results.
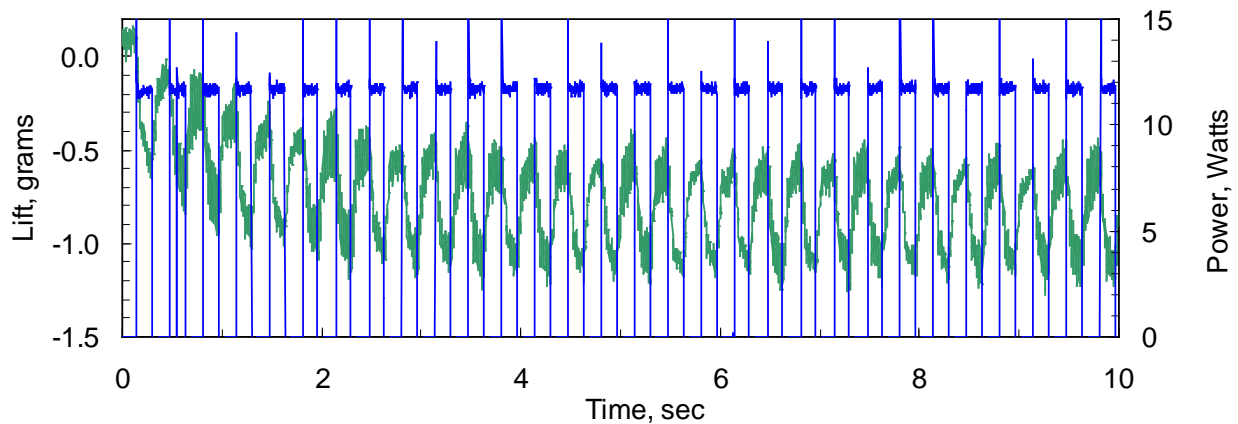


**Figure 119.  Lift and Power versus Time for a 24 mA Discharge Over 10 Seconds.  The Power Is the Square Wave**
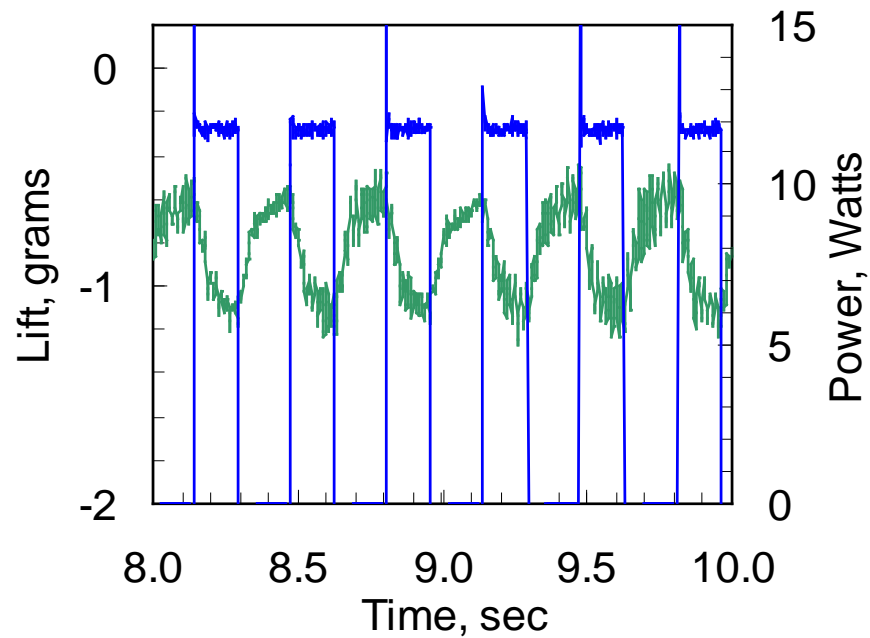
Figure 120.  Lift and Power versus Time for a 24 mA Discharge Over 2 Seconds.  The Power Is the Square Wave
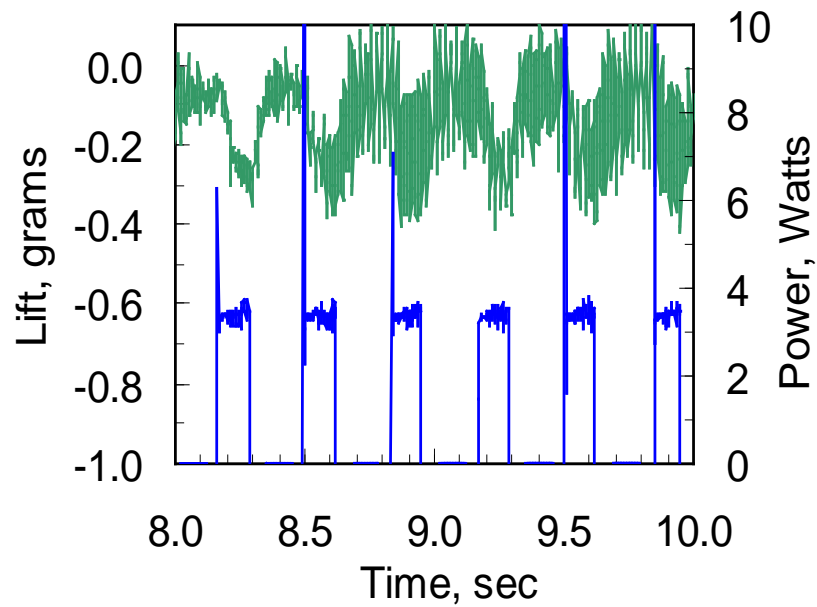


Figure 121.  Lift and Power versus Time for a 9 mA Discharge Over 2 Seconds.  The Power Is the Square Wave

Another aspect that should be realized about this technique for making lift measurements is that it is sensitive to the location on the plate where the lift is applied. The calibration between model displacement and lift was done at the center of the model. In the streamwise direction a detected lift value can change by as much as 10% depending on where the lift is applied in the streamwise direction. This is an important issue in the results that will be presented. Since the deflection of the plate is a function of the bending moment around a line parallel to the flow direction, any movement of the center of lift in the spanwise direction causes substantial changes in the measured lift. If the center of lift moves from one side of the plate to the other side of the plate in the spanwise direction, the measured lift can vary by ±44%. Since all the discharges studied in this work have symmetry around the flow direction axis of the model this should not be a problem.
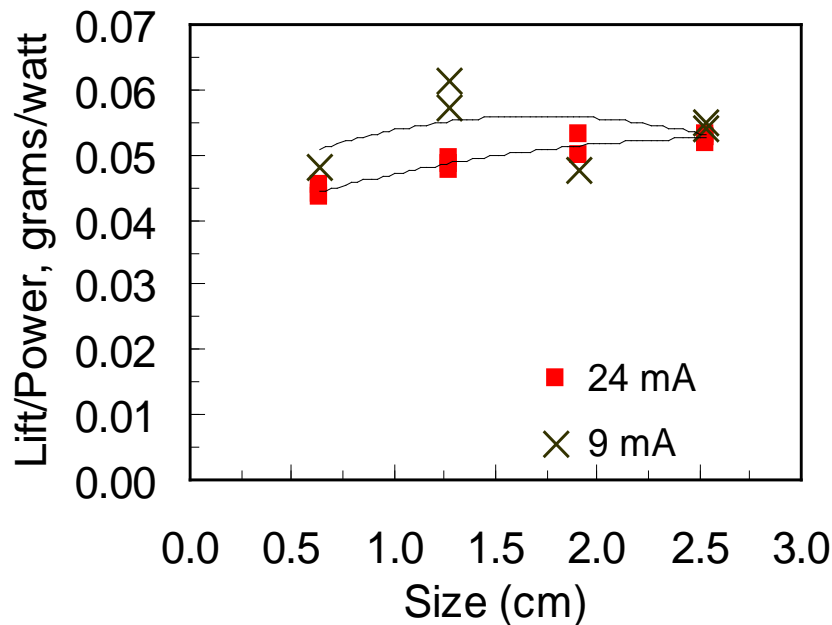


**Figure 122.  Lift Per Unit Power versus Cathode Size Where the Size of the Cathode is Increasing from the Leading Edge of the Model Downstream.  Figure 115 Electrode Arrangement is Used**

The effect of the electrode size can be seen in Figures 122 and 123 for a 9 mA discharge and a 24 mA discharge. The results in Figure 122 are for the cathode sizes shown in Figure 115 where the cathode increases in size in the downstream direction. The results shown in Figure 123 are for the cathode sizes shown in Figure 116 where the cathode increases in size towards the upstream direction. Both of these plots show the lift per unit power increasing as the cathode size increases. This is emphasized by the $2^{nd}$ order polynomial trend lines placed through the data points. This increasing trend is very clear in the 24 mA results and the 9 mA results in Figure 123. The trend is not quite as clear in the 9 mA results shown in Figure 122. These results have scatter for the reasons mentioned above. Even with the 9 mA data scatter, these results show that the lift per unit power for the 9 mA cases is higher than those for the 24 mA cases. It appears that the lift per unit power input is a weak function of the discharge current. This is a rather surprising result. At this time the authors are speculating that this is due to the discharge having slightly different shapes at different currents. The different shapes give rise to heating at different

locations. Since the plasma essentially alters the flow field by heating it, it is reasonable that heating at different locations will affect the flow field differently.
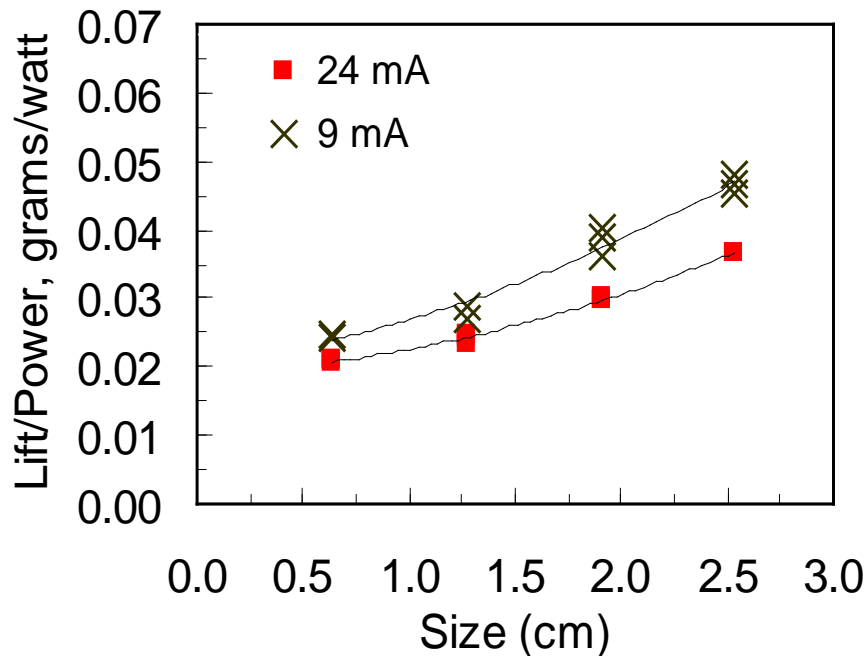


**Figure 123. Lift Per Unit Power versus Cathode Size Where the Size of the Cathode Is Increasing From a Location 2.9 cm Downstream of the Leading Edge Towards the Leading Edge. Figure 116 Electrode Arrangement Is Used**

The effect of the cathode position can be seen in Figure 124. These results are for the cathode arrangements shown in Figure 117. The cathode size remains the same for all the positions shown in Figure 117, only the location changes. The data points, with the $2^{nd}$ order polynomial trend line, clearly show the lift per unit power decreasing as the cathode position moves away from the leading edge. A possible reason for this is that the shock is much closer to the surface of the model at the leading edge than distances downstream. In addition, the boundary layer is thinner at this location. It may be that a given amount of heat causes larger perturbations in the boundary layer thickness when the boundary layer is thin. Hayes and Probstein (1959) show that pressure changes along the surface of a plate are related to changes in the boundary layer thickness.

The conclusion that larger changes in the flow field for a given power input are realized at cathode locations closer to the leading edge can be determined from the results in Figures 122 and 123. Notice that the lift per unit power results in Figure 122 are larger than those in Figure 123 for the same size cathode. The cathodes in Figure 122 are located upstream of their counterparts in Figure 123. For the 2.5 cm long cathodes, the two values are starting to converge. The large electrode Figure 123 value is still a little smaller because this cathode is 0.4 cm downstream of the 2.5 cm cathode in Figure 122. This can be seen in Figure 116d and Figure 115d.

Besides the cathode positions of Figure 117, the cathode arrangement shown in Figure 118 is also plotted in Figure 124. The 24 mA results are plotted at a cathode location of 2.2 cm and the

9 mA results are plotted at a cathode location of 2.4 cm. For this electrode arrangement the cathode position has no meaning, these were just convenient locations to place these results so that they could be compared to the other cathode positions. From these results it might be deduced that placing a cathode with its longest dimension in the spanwise flow direction is better than placing the longest dimension in the flow direction, at least if the spanwise cathode is located close to the leading edge.
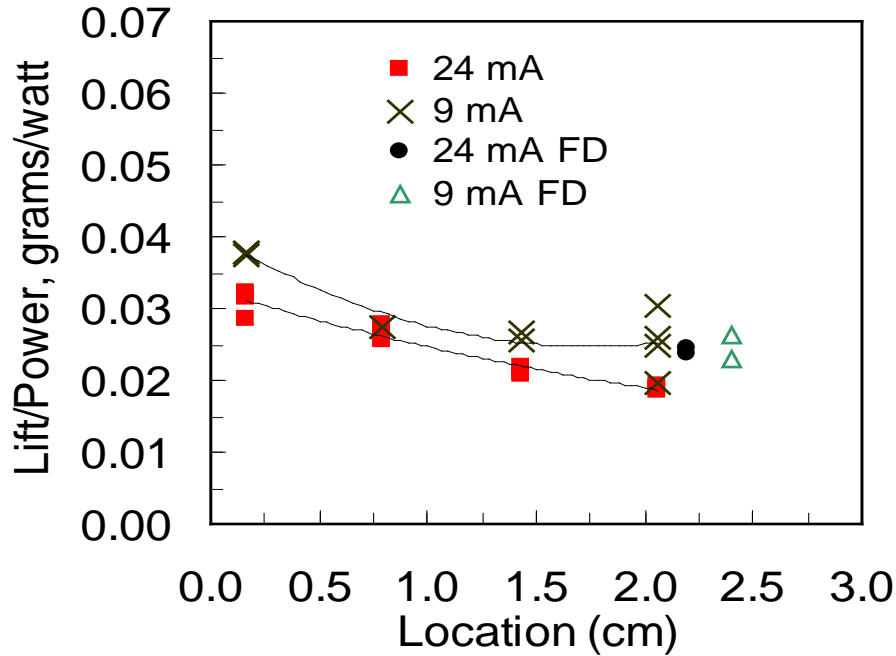


**Figure 124. Lift Per Unit Power versus Cathode Position for Figure 117 Electrode Arrangement. FD In the Plot Means Flow Direction Cathode Orientation and These Points Use the Figure 118 Electrode Arrangement**

Another observation made from the measurements made as part of this experimental work is that the discharges are changing when the electrode size or position changes. This can be seen from the discharge voltage plots in Figure 125. Figure 125 results are for varying cathode sizes and show that the discharge voltage decreases as the electrode size increases. Increasing voltage with decreasing cathode surface area is an indicator that the discharges being used in this work are not in the normal glow regime. To the eye and from the pictures shown in Figures 115 and 118 the discharges look diffuse, and they are fairly stable. However, from the voltage versus cathode surface area characteristics these discharges appear to be operating in the abnormal glow mode. Note that both Figure 125 and Figure 126 show that more voltage is required when a 24 mA discharge is used as compared to a 9 mA discharge. This also indicates this is not a normal glow discharge.
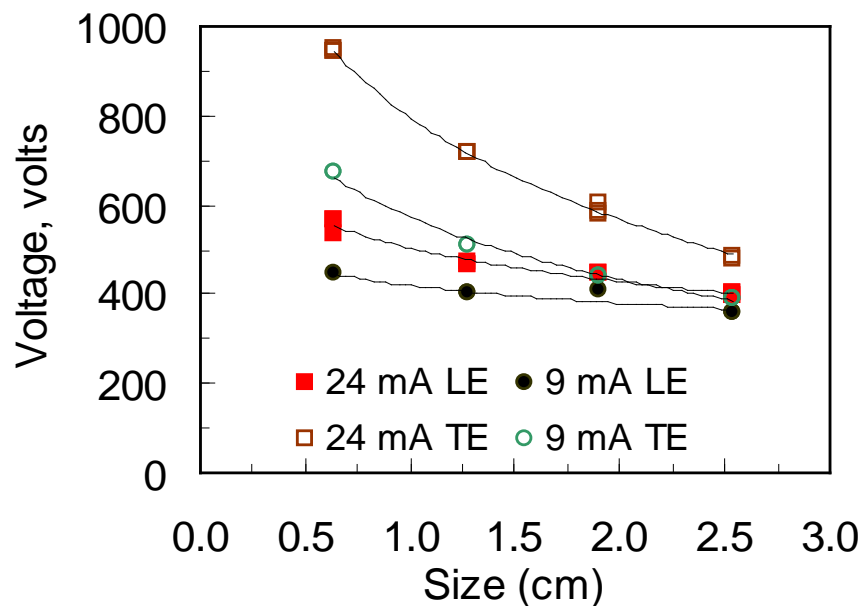
Figure 125. Discharge Voltage versus Cathode Size Where the Size of the Cathode is Increasing from the Leading Edge of the Model Downstream, LE (see Figure 115), and from a Downstream Location Upstream, TE (see Figure 116)
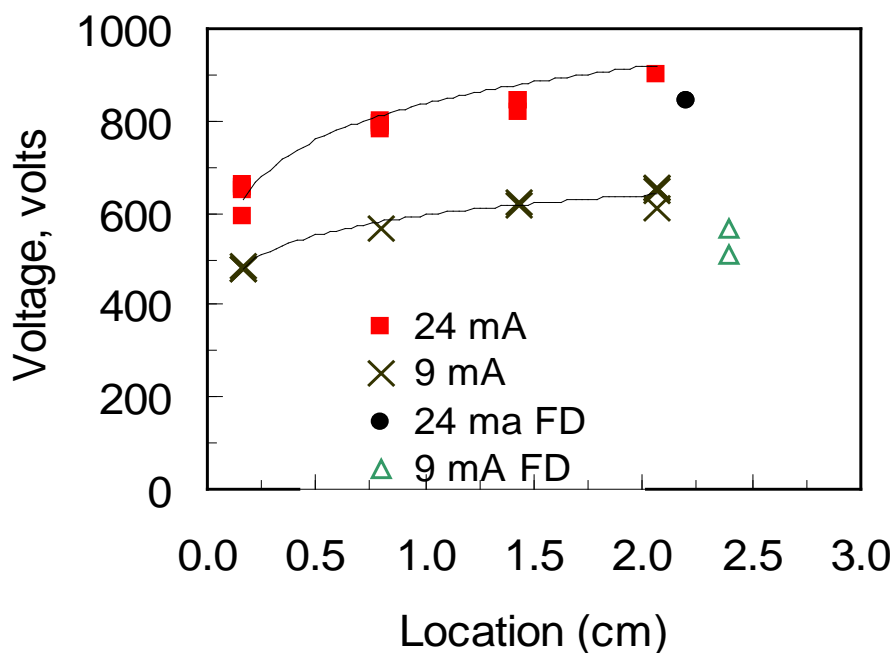


Figure 126. Discharge Voltage versus Cathode Position for Figure 117 Electrode Arrangements. FD in the Plot Means Flow Direction and these Points use the Figure 118 Electrode Arrangement

### 4.3.4.2 Comparisons to Load Cell Measurements

In this section comparisons to the lift results of Section 4.2 are made. This is done to verify the results presented in this subsection utilizing a deflection measurement technique and to verify the results obtained in Section 4.2 utilizing a load cell measurement technique. To do this comparison the linear curve fits of the lift versus power results from Section 4.2 and from this section are compared. The equation presented in the previous section for the configuration shown in Figure 92 is equation (169). This equation was presented as a good average curve fit for all the lift measurements presented. Four of these equations that are slightly different from one another were presented.

Lift versus power curves using the displacement measurement device are shown in Figures 127 and 128. The results in Figure 127 are for the electrode arrangement shown in Figure 114. The results shown in Figure 128 use the electrode arrangement shown in Figure 117b. The results in Figure 127 use a sine wave current pulse to run the discharge and those in Figure 128 use a square wave. This is the reason for the small number of data points. The lift versus power equations obtained from these electrode configurations are

$$L = -0.026P - 0.041 \quad grams \tag{170}$$

for the results in plotted in Figure 127 and

$$L = -0.021P - 0.014 \quad grams \tag{171}$$

for the results plotted in Figure 128.
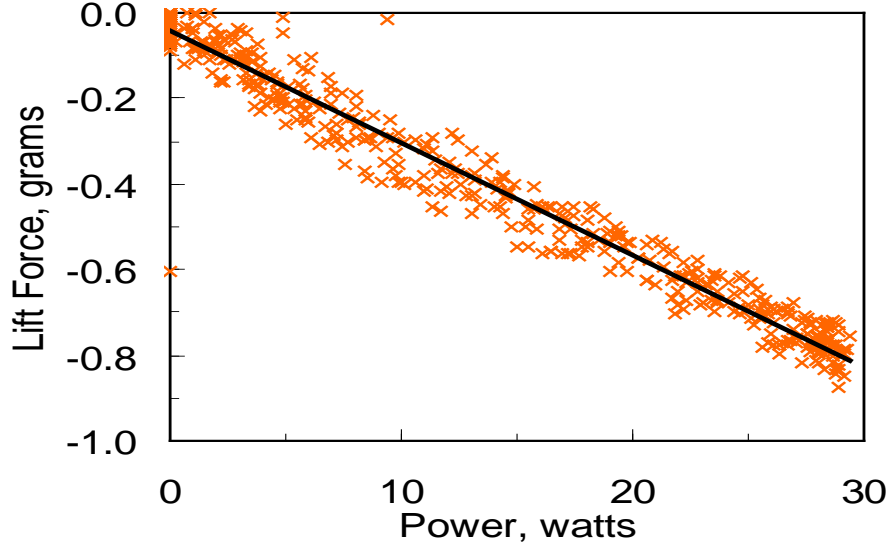


**Figure 127.  Lift Versus Power Using the Electrode Arrangement Shown in Figure 114 and Using a Sine Wave Current Input**

The slopes in equations (170) and (171) are different from one another because the electrode geometries are different in these two cases. Both of these slopes are slightly different than the one shown in equation (169), but they are within 13%. This indicates that the displacement measurement technique and the force measurement technique used in Section 4.2 both give reasonable results. These results also verify what was presented in this subsection of this report; the electrode geometry does affect the lift to power ratio. The closest electrode arrangement used

in this work to that used in Section 4.2 is that shown in Figure 117b. This electrode arrangement is not exactly like that shown in Figure 92, but it is close. The differences include the spacing between the cathode and anode, the length of the anode in the flow direction, and the width of the cathode and anode in the spanwise direction. The biggest difference between the electrode arrangement shown in Figure 117b and that shown in Figure 92 is the spacing between the cathode and anode. The spacing between the cathode and anode used in this work is less than half that used in Figure 92. The length of the anode in the flow direction in this work is also half that used in Figure 92. In all the experimental work that we have done using these types of models, there has never been any indication that anode size or anode shape is important. This is reasonable from an air heating perspective because the discharge does most of its heating above the cathode, and a relatively small amount of heating above the anode. The important difference between these two electrode arrangements is probably the distance between the cathode and the anode.
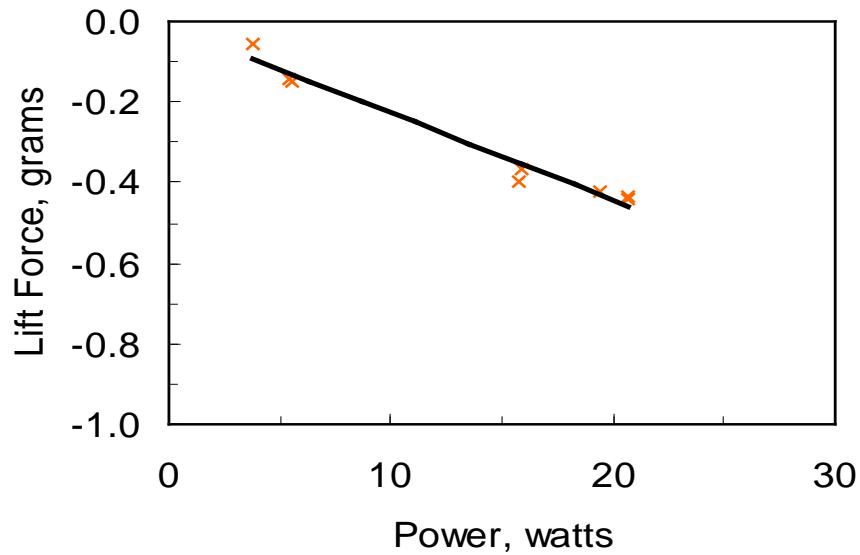


**Figure 128.  Lift Versus Power for the Electrode Arrangement Shown in Figure 117b and a Square Wave Current Input**

In comparing equations (170) and (171) to equation (169) it should be noticed that the intercept terms in the linear equations are different. If the measurement devices used in this work and the work of the Section 4.2 were perfectly accurate, then the intercept value in all three of these equations should be zero. With no discharge there should be no change in lift. The reason these intercepts occur is because 0.3 grams for the load cell measurement device and 0.04 grams for the displacement meter are within the measurement accuracy of these devices. Note that the Section 4.2 measured lifts are for much higher input powers, up to 230 watts, while the highest power looked at in this subsection is 30 watts. A 0.3 g offset is important for the results presented in this subsection and not so significant for the results presented in Section 4.2.

The important comparison to be made here is the slopes. The slopes from equations (170) and (171) obtained using the displacement measurement technique differ by no more than 13% from the slope shown in equation (169), obtained with the load cell measurement technique. This is a very good comparison and indicates that good results were obtained with both force

measurement techniques. The 13% difference can easily be explained by the differences in the electrodes.

### 4.3.5 Summary

This work has shown that electrode size and position do affect the lift change caused per unit power delivered by the plasma to the air flow. In general, it seems that the most lift per watt of input power is obtained when the discharge is located close to the leading edge of the flat plate. Changing the location of the cathode changes the location of the heating and it is believed that lift changes on the plate are a function of the location where the heat is applied. The experimental results presented here also indicate that larger electrodes provide a better lift to power ratio. For the most part the changes seen by altering the electrode configuration are within a factor of two. In addition to doing an electrode size and position study, a comparison of the results obtained here with a displacement measurement technique, to those obtained in Section 4.2 with a load cell measurement technique is made. The comparisons indicate that both measurement techniques detect the lift change caused by the plasma discharge well. Both of these lift measurement techniques have their advantages, and both of these techniques have their disadvantages.

## 4.4 Magneto-Fluid-Dynamic Compression in a Square Inlet

### 4.4.1 Introduction

In an air-breathing propulsive system, the inlet ingests ambient air from the oncoming stream and compresses it to a higher temperature and pressure for the combustor. The optimal performance for a high-speed inlet is reached when the Mach number at its exit is near sonic and attains the highest pressure/temperature with a minimum loss of stagnation pressure (Oates, 1997; Kurth, 2002). In high-speed flight, the propulsive power need varies greatly from take-off to cruise and finally landing; a fixed inlet configuration is unable to meet all these requirements. The desired performance is often obtained by a variable configuration inlet through a combination of compression ramps, unparallel sidewalls, and mass removing slots. In order to reduce the loss of stagnation pressure through shockwaves, the flow path also involves a multiple shock wave system to minimize the undesirable entropy jump through a single shock. The ideal isentropic compression is however unattainable. All these mechanical flow control devices lead to significant weight penalty, and when operating beyond their design conditions become parasitic (Kurth, 2002). Therefore an alternative to these mechanical devices, such as a non-intrusive, rapid response flow control mechanism, should be appealing.

A unique approach for integrating electromagnetic perturbations and viscous-inviscid interactions for hypersonic flow control has proven to be effective by a series of numerical simulations and experimental measurements (Shang and Surzhikov, 2005; Shang et al., 2005b; Menart et al., 2004a; Kimmel et al., 2004a). The basic premise is built on the pressure interaction theory of Hayes and Probstein (1959) that describes the viscous-inviscid interaction near the sharp leading edge of a solid surface. In supersonic flows, the slope of the displacement thickness of a shear layer, $\partial\delta^*/\partial x$, deflects the oncoming stream away from the solid surface, induces a series of compression waves, and coalesces into an oblique shock. The induced surface pressure beneath the oblique shock can be calculated easily by the tangent-wedge approximation. A key parameter of the pressure interaction is defined as $\chi=(C/Re)^{1/2}M_\infty^3$. Depending on the combination of the free stream Mach number and Reynolds number, based on the running distance from the leading edge, the pressure interaction is further classified as strong or weak

according to whether the value of $\chi$ is either greater or less than 3. The major difference is that for the strong pressure interaction the growth rate of the shear layer is altered by a strong favorable pressure gradient, $\nabla p \leq 0$, and grows proportional to $x^{3/4}$, instead of $x^{1/2}$ for laminar flows. The basic idea of the present approach is that an aerodynamic force of flow control can be derived from an electromagnetic surface perturbation that increases the slope of the shear-layer displacement for the viscous-inviscid interaction. This chain of events in turn produces a higher surface pressure for flow control (Shang and Surzhikov, 2005; Shang et al., 2005c).

This concept has fully demonstrated its viability as a magneto-fluid-dynamic (MFD) flow control mechanism in side-by-side experimental and computational investigations (Shang and Surzhikov, 2005; Shang et al., 2005c; Menart et al., 2004a; Kimmel et al., 2004a). Following this idea; the present effort applies the amplified viscous-inviscid interaction near the leading edge of a rectangular inlet to act as a MFD compressor. For the present experimental investigation, a direct current discharge (DCD) is adopted as the plasma actuator. The electrodes of the DCD are embedded in the sidewalls of a constant cross-section area inlet; this arrangement is non-intrusive when deactivated. Once the discharge is actuated the combined volumetric Joule and conductive surface heating thickens the local displacement thickness. The increased slope of the displacement thickness through a viscous-inviscid interaction generates a series of compression waves which coalesce into an oblique shock. The compression is directly controlled by the power input to the plasma generation of the electromagnetic perturbation. A high compression is automatically generated by the pressure interaction near the leading edge which is a strong function of the free stream Mach number.

For present purposes the electromagnetic perturbation via a DCD is imposed on the shear layer, and the combined volumetric Joule and convective electrode heating is the principal mechanism of disturbance. The DCD plasma actuator could be replaced by a dielectric barrier discharge (DBD) or microwave radiation (Shang, 2005a; Boeuf and Pitchford, 2005; Kolesnichenko, 2005). In the presence of an externally applied magnetic field, additional forces such as the Lorentz accelerations can play an enhancing role. Oscillatory perturbations are also not a critical concern as long as the time scales of the perturbation are much shorter than the characteristic time frame of the fluid motion (Shang, 2005a; Boeuf, 2005).

To demonstrate the viability of this concept of MFD compression, a side-by-side experimental and computational investigation becomes necessary. The experiments are conducted in a plasma channel with a nominal Mach number of 5.15, and the computational results are obtained by solving the three-dimensional, compressible Navier-Stokes and magneto-fluid-dynamic equations with a weakly ionized air model. The major emphasis of the present effort is focused on experimental observation which is the start of validating a database for future research and development.

### 4.4.2 Experimental Facility

The wind tunnel used to carry out the work being presented in this section is the same as used in the previous sections (see Figures 73 and 74). A brief description of this tunnel is given in Section 4.1.2 of this report. To ensure a stable inflow environment, tests are conducted at two stagnation pressures of 370 and 580 torr. The incoming air stream has a static pressure of 0.59 or 0.92 torr, and density of $6.4 \times 10^{-3}$ or $10.03 \times 10^{-3}$ kg/m$^3$ according to the different stagnation pressures. These conditions produce two Reynolds numbers based on the model length of

$1.64 \times 10^5$ and $2.57 \times 10^5$ respectively. At this hypersonic Mach number and relatively low Reynolds number, the flow field is considered to be laminar.

Because of the size of the Mach 5 wind tunnel, the rectangular inlet model is limited to a dimension of $10.16 \times 3.81 \times 3.11$ cm. The four sidewalls of the model have sharp leading edges with an outside bevel angle of 20 degrees. The electrodes are embedded in the phenolic, the vertical sidewalls are made of copper, and the horizontal sidewalls are constructed of Plexiglas. A sketch of the tested model and the installation of the model in the hypersonic MHD channel are presented in Figures 129 and 130.
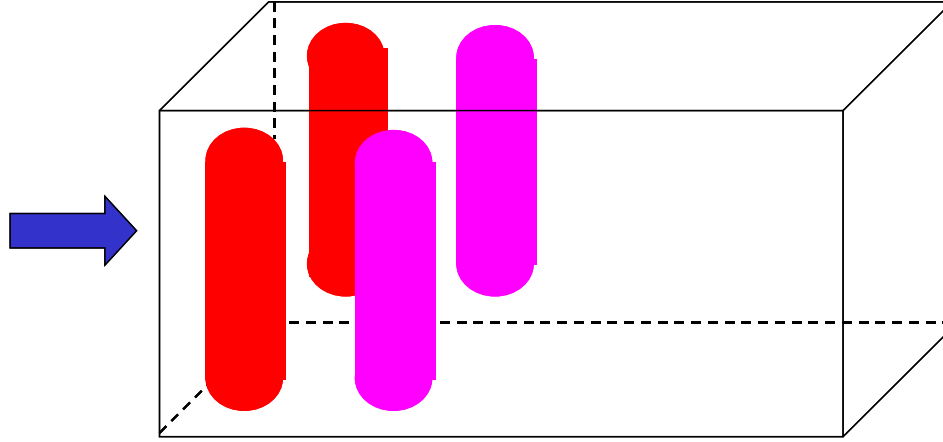


**Figure 129. Sketch of Inlet Model with Cathodes and Anodes ($3.175 \times 0.64$ cm)**

In the preliminary study, the copper cathode and anode are embedded in opposite sidewalls parallel to the $z$-coordinate. Therefore the gap distance between the electrodes is 3.11 cm. A direct current discharge is sustained by an electric potential strength up to 800 V for electrical currents of 40 and 80 mA. The electrodes are placed a short distance of 0.64 cm downstream of the leading edge of the inlet to enhance the pressure interaction. The anode has half the width of the cathode in the streamwise direction (1.74 cm). In addition to this electrode arrangement, the second electrode configuration had an anode and a cathode on each side of the sidewalls. The discharges are now parallel to the surfaces. Most of the experimental data are collected for this configuration, where all electrodes have the identical dimensions of $3.175 \times 0.64 \times 0.16$ cm, (length×width×depth). The cathodes are placed a short distance of 0.79 cm downstream from the leading edge of the inlet, and the distance between the centerline of the cathode and anode is 2.22 cm. In order to make comparisons between the diffusive discharges, the electric potential strength and current in the circuit remain nearly identical for the two different electrode arrangements (Menart et al., 2003b; Kimmel et al., 2004a). The electrical current density on the anode of the cross channel discharge is 25.16 mA/cm$^2$ and the value is 21.27 mA/cm$^2$ for the discharge along the sidewalls.
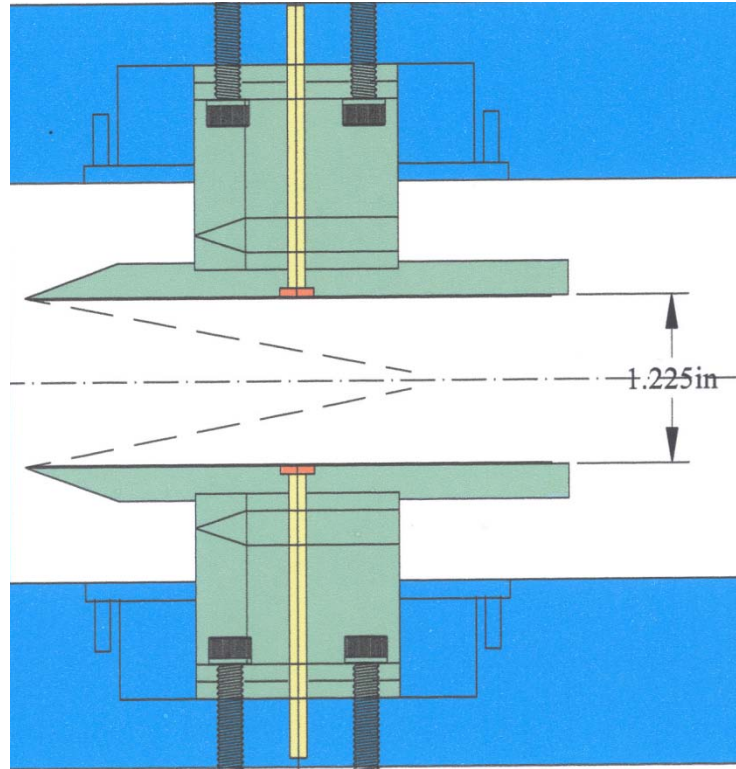
Figure 130.  Model Installation

The direct current discharge (DCD) is powered by a Universal Voltronics BRC-10-1000R-STD-3PH-208V reversible polarity switching power supply. The maximum output is rated at 8 kW with a 10 kV output voltage at a signal impedance of 10 kohm. At the breakdown voltage of 800 V, a diffusive discharge is achievable for plasma currents as high as 120 mA. For the two-pair electrode placement on parallel sidewalls, the total discharge area is 7.72 cm$^2$ representing only 5.48% of the total sidewall surface area.
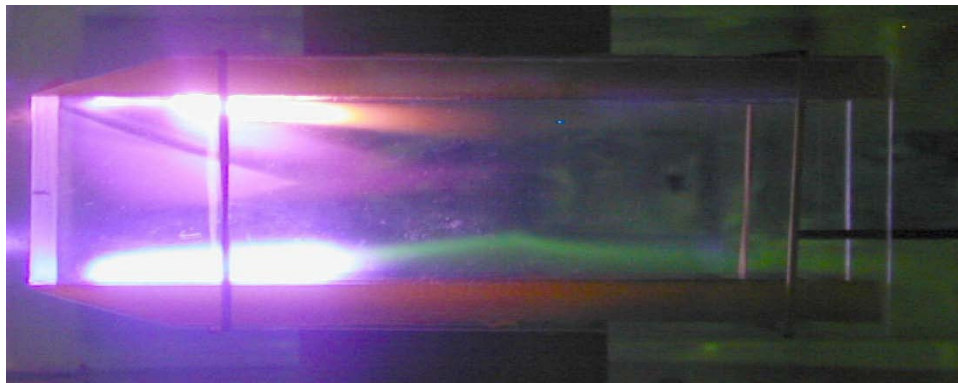

Figure 131.  Discharge across Inlet Sidewalls, E=650V, I=40 mA

133
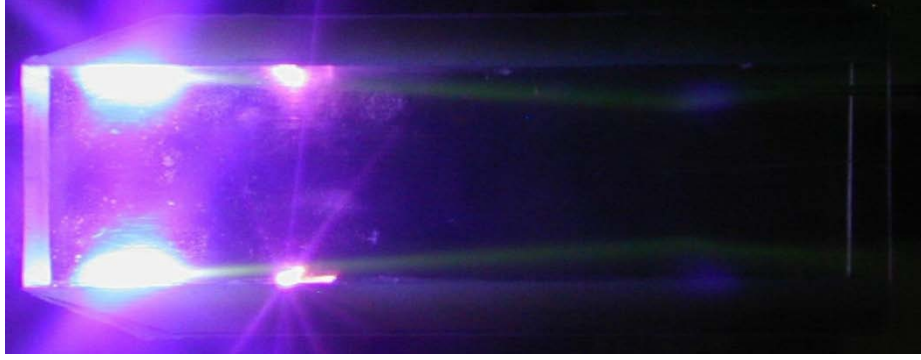
**Figure 132. Discharge along Inlet Sidewalls, E=650V, I=40 mA**

The discharging patterns of both electrode arrangements are given in Figures 131 and 132. Figure 131 presents the photographic top view of the flow field within the inlet with the actuating DCD across the sidewalls. Similarly, Figure 132 depicts the DCD along the sidewalls. Both discharges are generated by an electric potential from 600 to 800 V and an electric current from 40 to 80 mA. Since the electric field is introduced into the flow field as a small perturbation, the basic flow structure is unaltered. The only changes are reflected by the stronger oblique shock waves. This modification is detectable by the steeper shock angle originating from the leading edges of the inlet. As a consequence, the shock intersection points move upstream, and most importantly the static pressure at the exit plane of the inlet is higher than when the DCD is deactivated.

Menart et al. (2003a) and Kimmel et al. (2003) have thoroughly surveyed the weakly ionized air plasma in the Mach 5 wind tunnel using emission spectroscopy, microwave absorption, and a double Langmuir probe. For a normal glow DCD over a wide range of electrode arrangements, with discharge currents up to 400 mA, the rotational and vibrational temperatures of the air plasma are scattered around 150 K and 5000 K. The maximum ion number density is also determined to be $8\times10^{11}/cm^3$, and the electrical conductivity is less than 1 mho/m near the electrode. At the lower stagnation pressure condition, the air number density is $1.33\times10^{17}/cm^3$; thus the mass fraction of the charged particles is less than $10^{-5}$. At the higher stagnation pressure condition, the ionization fraction is even lower.

A three-dimensional traverse mechanism has been developed for this facility for flow field surveys (Shang et al., 2005a). This device has freedom of movement to cover the entire domain of the test section. The placement of the traverse is controllable within a distance of 0.25 mm. In the present effort, the collected data includes only the pitot pressure measurements and optical observations. A stainless steel pitot probe has outer and inner diameters of 1.59 and 1.27 mm respectively. All pressure measurements were collected by a HP 385A data acquisition and control system. A single pressure transducer was used to collect all data. The Baratron MKS model 722A-23320 absolute pressure gauge has a calibrated accuracy of 0.1% of the 100 torr full range.

The typical data collection is shown in Figure 133. The MHD channel is operated in a continuous and steady flow condition at a preset stagnation condition. The DCD is then ignited and the discharge is maintained at a constant current. The initial phase of the pressure response is on a second time scale, then the conductive electrode heating effect appears (Menart et al., 2003a; Kimmel et al., 2004a; Menart et al., 2003b, Kimmel et al., 2003). The surface discharge electric current exhibits a random, low-amplitude ($\pm0.2\%$), and continuous fluctuation (for the

present tests, the measured spectrum is limited to 1.5 kHz). Therefore, the collected data are time-averaged over the sampling period. The pitot pressure data is monitored for the entire data collection period of twenty seconds and continuously recorded. This data collecting procedure is standardized for the entire experimental effort.
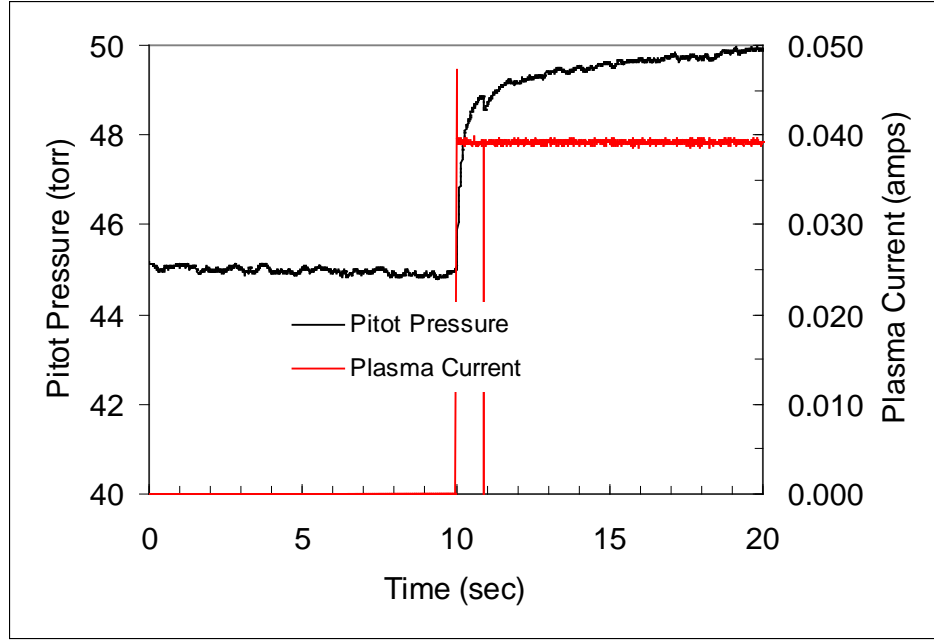


**Figure 133. Typical Data Collecting Process**

### 4.4.3 Numerical Procedure

The magnetic Reynolds number, $R_m$, based on the experimental conditions is $8.48\times10^{-6}$. Under this circumstance, the low magnetic Reynolds approximation prevails. The governing equations for this simulation are described in Section 3.3.2 of this report. For the present purpose, the only required information for the numerical simulation are the transport properties of the weakly ionized gas to describe the applied electrical field intensity, $E$, and electrical current density, $J$, in the basic formulation.

All numerical simulations are generated on two mesh systems: $(85\times81\times45)$ and $(105\times101\times57)$. The minimum grid spacing immediately adjacent to the sidewall is one hundredth of the laminar boundary thickness at the inlet exit. The grid spacing is stretched from the inlet sidewalls toward the centerline by a geometric constant of 1.05. Clustered mesh spacing is also implemented at the leading edge of the inlet; four streamwise cross-section planes are set upstream of the leading edge to describe the unperturbed free stream. The streamwise grid spacing is then stretched from the leading edge downstream. For the present analysis, the iterative convergence is accelerated through a multi-grid technique using a three-level mesh sequencing (Thomas et al., 2003). The data processing rate on a 400 MHz, SGI Octane2 workstation is $61.6\times10^{-6}$ seconds per number of cells per iteration. The convergence criterion of the present analysis is preset at a value of $3.0\times10^{-7}$ of the normalized global residual. A coarse grid solution attains its steady state asymptote after 300 iterations requiring 5400 seconds.

135

### 4.4.4 Flow Field Structure

The flow field structure of the simple rectangular inlet is surprisingly complex. Four equal strength oblique shocks emanate from the mutually perpendicular sharp leading edges. These shocks are the result of the weak pressure interaction near the hypersonic leading edges. The peak pressure at the leading edge is as high as 4.2 times the free-stream value, and expands downstream. The coalesced shocks from the entrance of the inlet have a deflection angle of 11.7 degrees. The four shocks do not intercept each other at the same streamwise location, because the width of the inlet is smaller than the height; thus the oblique shocks over the vertical sidewalls intercept each other at x/L=0.50. The intersection of the oblique shocks over the horizontal sidewalls is located at x/L=0.54. At these locations, shock-on-shock interactions also take place. The shock wave structure is clearly discernable from the computed density contours shown in Figure 134 which duplicates the experimental conditions. Downstream of the intersections, all shocks continuously propagate, reflect from the sidewalls, and eventually exit the inlet.



XY Plane



XZ Plane
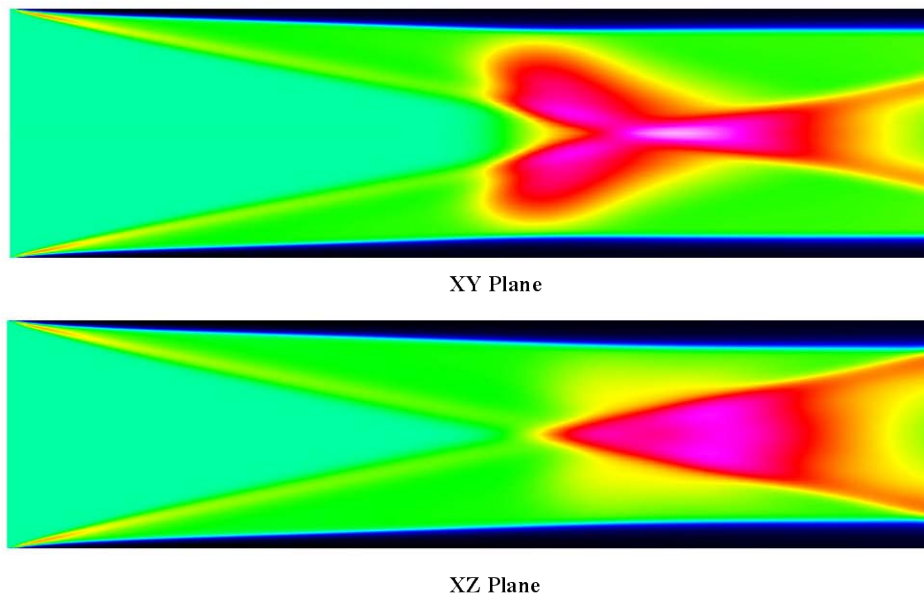
**Figure 134. Density Contours in *x-y* and *x-z* Central Planes**

Upstream of the shock intersections, connecting shock waves must exist between the two perpendicular families of shocks parallel to the *y* and *z*-coordinates in order that the continuity condition is satisfied (Shang and Hankey, 1977). Therefore, there are a total of eight triplet points in the shock wave formation in each cross-sectional plane. In Figure 135, the Mach number contours at the streamwise location of *x/L*=0.25 from the inlet leading edge are depicted. Although all oblique shocks are relatively weak, the numerical solution captures this peculiar shock structure. The multiple shock compressions in the corner regions are clearly reflected through the thinning of the viscous layer as it enters these domains.
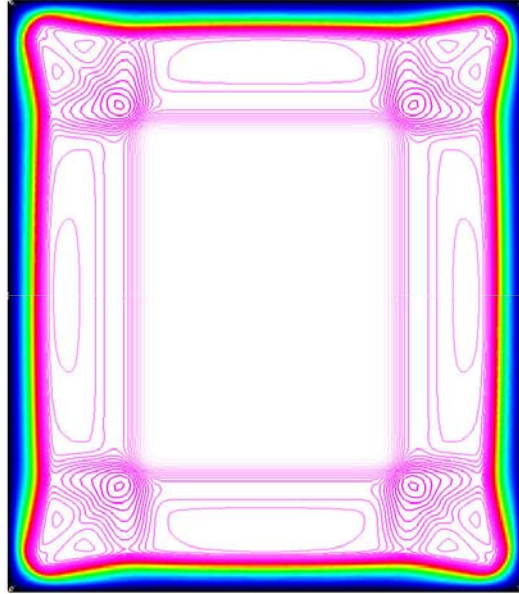
**Figure 135.  Triple-Point Shock Formations in Cross-Flow Plane at** *x/L*=0.25

### 4.4.5   Discharge Across Sidewalls

In the early phase of the experimental effort, the DCD was applied across the vertical walls of the inlet. The discharging column has a height identical to the width of the inlet, 3.11 cm. After the initial breakdown, the DCD is maintained at an electrical field intensity of no more than 820 V for an external circuit current up to 80 mA. Both of the electrodes are placed a short distance of 0.64 cm downstream of the leading edge to enhance the pressure interaction. The copper cathode has a dimension of 2.54×2.54×0.16 cm (length×width×depth), thus a discharging surface area of 6.45 cm$^2$. The anode has half the width of the cathode in the streamwise direction (1.74 cm). Although the discharging pattern is fully understood (Surzhikov and Shang, 2004), the difference in electrode surface areas and electrical field intensity due to the cathode fall leads to an asymmetrical electromagnetic perturbation. For this reason, a limited number of tests were conducted for this particular electrode arrangement.

Figure 136 presents the measured pitot pressure contours at a stagnation pressure of 370 torr. At the streamwise location of *x/L*=0.75, the shocks originating from the sidewalls have already intercepted each other upstream and are propagating on a divergent path. Thus the shocks over the horizontal sidewalls are moving away from each other. The surface discharge is sustained at 650 V and 40 mA; the total power input for plasma generation is 26 watts. Since the DCD is introduced as a small perturbation to alter the flow field structure, the basic shock formation in pitot pressure contours, with and without the discharge, is similar to what was anticipated. The most significant difference between the two test conditions is that when the DCD is activated the vertical shocks are closer to each other because of the steeper oblique shock angle. Meanwhile, the value of the pitot pressure at the shock front is elevated when the DCD is actuated. The pitot pressure data are collected by a probe with a finite external diameter, and therefore are limited in how close they can be positioned relative to the sidewalls.
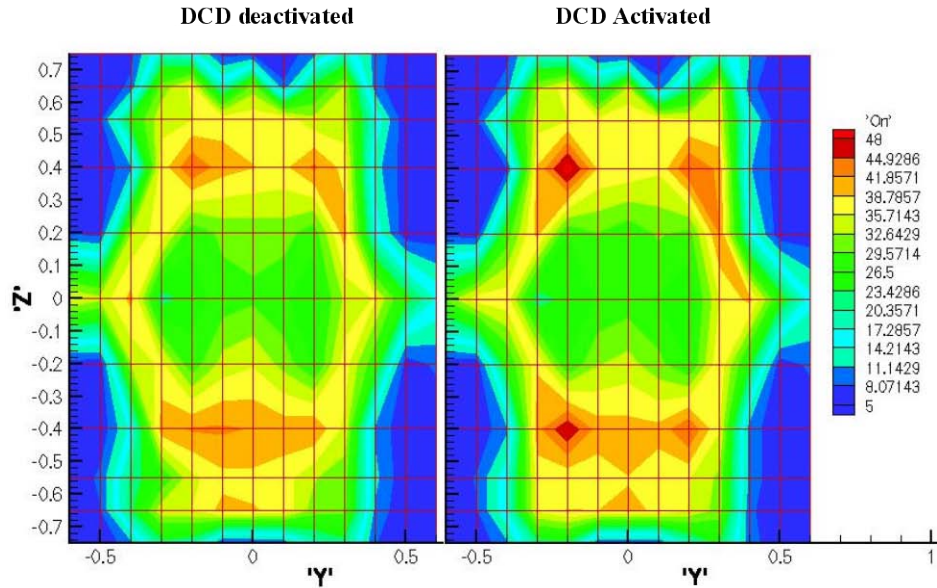
**Figure 136. Comparison of Pitot Probe Pressure Contours With/Without A DCD**
**($E$=800V and $I$=40 mA)**

The effect of an electromagnetic perturbation on the pitot pressure distribution is better described by the numerical simulation than the experimental results under identical conditions, because of the much higher data point density (11514 versus 143). A composite drawing of the computed pitot pressure contours in Figure 137 clearly highlights the interaction and agrees with the experimental observation. At the lower stagnation pressure tested, 370 torr, the pitot pressure of the unperturbed stream registers a value of 20.42 torr, and this is confirmed by measurements and computations. Based on this reference value the inviscid core still exists in the middle section of the inlet. From the experimental data and computational results this complex flow field structure within the inlet becomes traceable.

Figure 138 depicts the experimental and computed results of pitot pressures along the centerline of the rectangular inlet when the DCD is either actuated or deactivated. At the higher tested stagnation pressure of 580 torr, the experimental and computational results reveal the consequence of interacting oblique shocks within the inlet. The DCD is maintained in the hypersonic inlet by an applied electric potential of 820 V between the electrodes. When the DCD is actuated, the induced oblique shock becomes steeper, and advances the shock intersection upstream. The reduced Mach number behind the strengthened shock, and a higher local static pressure, produce a higher pitot pressure value. The actuated DCD produces a higher static pressure than the deactivated counterpart. The computed results indicate an interacting pressure rise further downstream than the experimental observations. The probable causes of this discrepancy are tentatively identified to be the slightly blunt leading edge of the inlet model and a higher inlet Mach number due to the model blockage. The computations underpredict the peak pitot pressure by 4% and overpredict the uniform entrance condition by 4.2%. This discrepancy in magnitude is directly attributable to the uncertain Mach number at the entrance of the inlet. Nevertheless, the agreement between the experimental data and computations is reasonable.
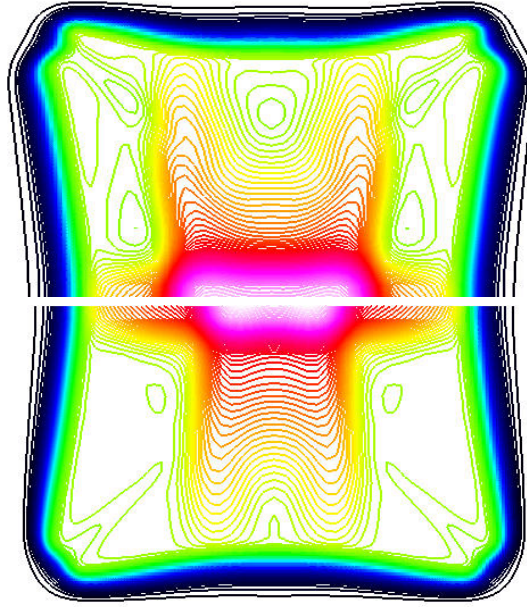
**Figure 137.  Computed Pitot Pressure Contours With/Without DCD**
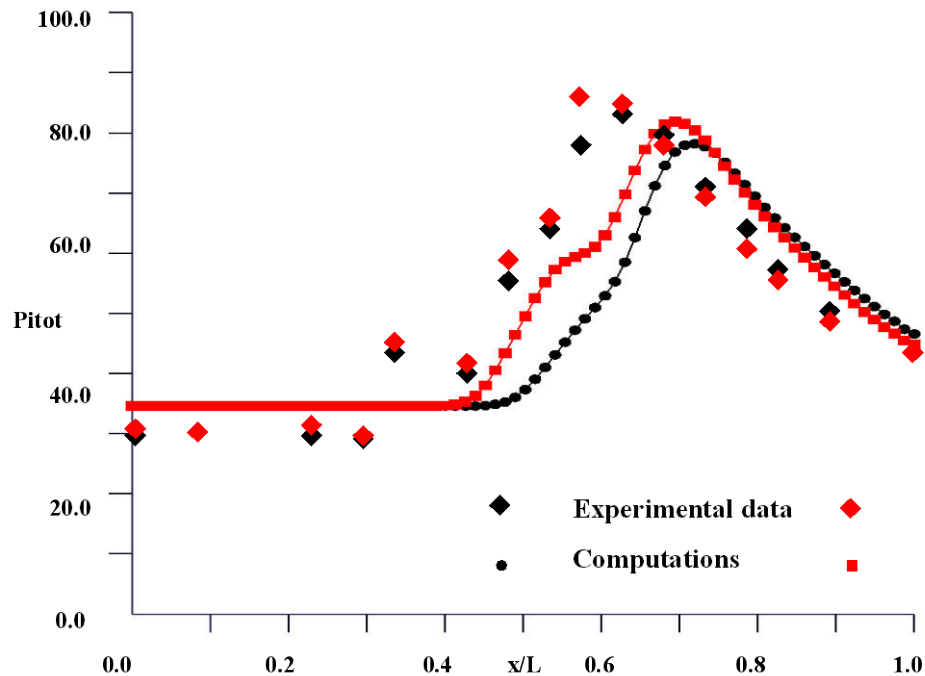


**Figure 138.  Comparison of Pitot Pressures from Experimental Measurements and Computations at the Inlet Centerline.  Red Points Are for the Activated DCD and Black Points are for the Deactivated DCD**

Since all experimental data are limited to pitot pressure measurements, the compression produced by the combined effect of a plasma perturbation and viscous-inviscid interaction can only be evaluated by computational simulation. The static and stagnation pressure distributions are deduced from the numerical results. It is found that the static pressure at the exit plane of the inlet is greater when the DCD is deactivated and the loss in stagnation pressure due to the

stronger oblique shock is negligible. This result is the first demonstration that magneto-fluid-dynamic compression can be achieved in a rectangular constant cross-section inlet.

### 4.4.6   Discharge Along Sidewalls

A major portion of the experimental data is collected for the DCD along the parallel vertical sidewalls. A part of the reasons is that this electrode arrangement alleviates the possibility of an unsymmetrical electromagnetic perturbation and allows more power input to the plasma for a diffusive discharge. This electrode arrangement was successfully used for hypersonic flow control over a wedge model (Shang et al., 2005c; Menart et al., 2003b; Kimmel et al., 2004a). In those series of investigations, the plasma-induced surface pressure is equal to the compression of an oblique shock generated by a deflection angle of five degrees or more in a free-stream with a Mach number of 5.15. The compression beneath the oblique shock is 1.41 times the freestream value and the value increases to 2.23 at a Mach number of 10.

A comparison of the streamwise pitot pressure distributions under three different discharge conditions along the centerline of the rectangular inlet is given in Figure 139. When the DCD is deactivated, the measurements reveal a repeatability pattern upstream of the MFD interaction ($x/L < 0.3$). In this region, the pitot pressure data essentially duplicate one another. The time-averaged data however exhibit a scattering band in the shock-shock and shock-shear-layer interacting zone to reveal an unsteady interaction behavior. At a data sampling rate of two hundred points per second, a maximum time-average data scatter of 6.3% occurs at the streamwise location $x/L$=0.55. In fact, the maximum difference in pitot pressure measurements is of the same order of magnitude when the DCD is actuated either across or along the sidewalls of the inlet. In any event, the pitot pressure data is consistently higher when the DCD is actuated than deactivated. For the DCD across the inlet sidewall, the discharge is sustained by an averaged applied electric potential of 820 V and at an electric current of 81 mA. The corresponding input to the side-by-side DCD is 745 V and 82.1 mA. In this regards, the power input for plasma generation has a small difference from 61.16 to 66.42 W. The pitot pressure distributions under the two different electric perturbations are essentially identical within the data scattering band.

The pressure rise induced by the electromagnetic perturbation is a function of the power input for plasma generation. This control mechanism is demonstrated by reducing the power input from 61.16 W (745 V and 82.1 mA) to 24 W (600 V and 40 mA). In Figure 140, the effectiveness of this control mechanism is depicted in the streamwise pitot pressure distributions. The flow conditions are identical, except the difference in the DCD power input. The difference between the flows is the applied electric potential that leads to different electric current densities; 21.6 mA/cm$^2$ versus 12.7 mA/cm$^2$. For the Joule heating dominant MFD interaction, the term $\mathbf{E \cdot J}$ reduces by a factor of 2.11, resulting in a proportional but smaller 9.6% decrease in the maximum pitot pressure rise. A higher power input for surface plasma generation of 120 mA at 940 V was also investigated. The experimental data exhibit a more drastic change, both in discharge characteristics and flow structure that requires repeatable measurements and further study.
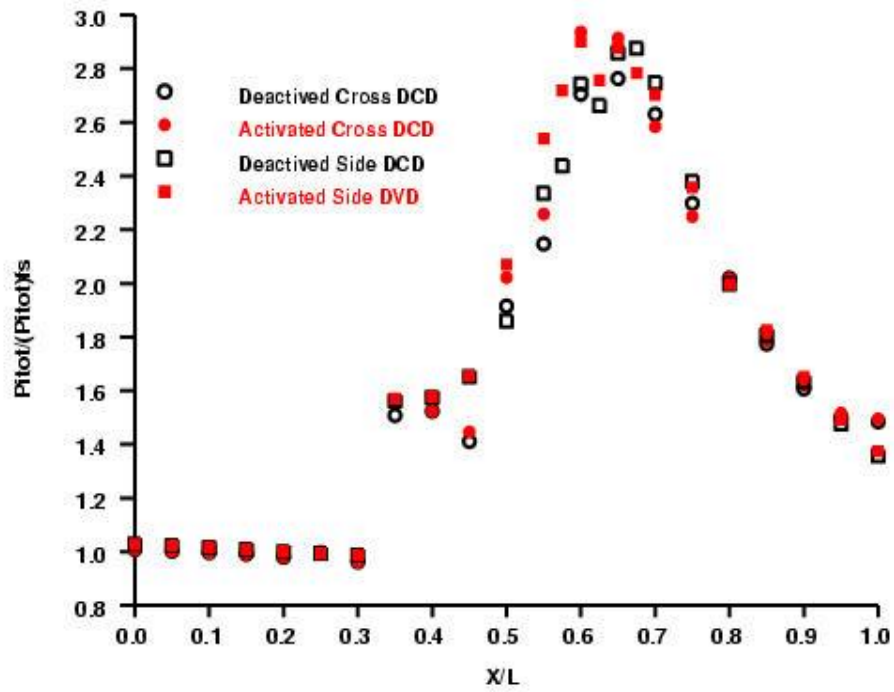
Figure 139. Comparison of DCDs Cross and Along Sidewalls
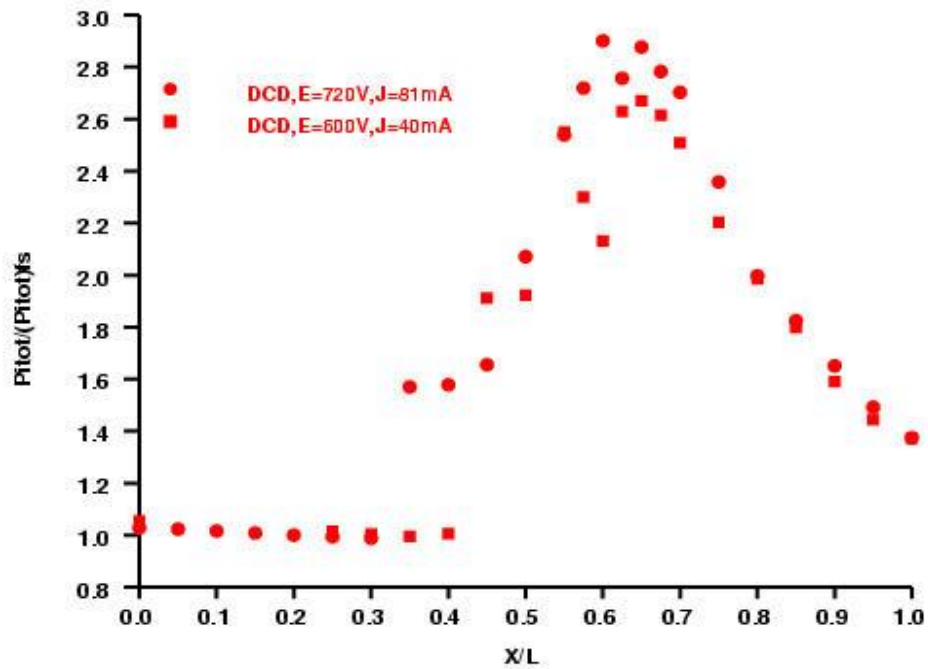


Figure 140. Effect of Power Input to MFD Interaction

141

The magneto-fluid-dynamic interaction is best described by the cross flow formation that is induced by a plasma perturbation and subsequently amplified by a viscous–inviscid interaction. A much clearer pictorial description can be provided by numerical simulations, which describe the changes with smaller data scatter. In Figure 141, the computed pitot pressure distributions across the *y*-coordinate near the inlet exit plane (*x/L*=0.95) are presented. The pressure distributions along the centerline (*z/L*=0.0) and close to the upper discharging surface (*z/L*=0.8), with and without an actuated DCD, are depicted in this figure. The computed results indeed show that the electromagnetic perturbation produces a small perturbation to the shock wave structure at a relatively low hypersonic Mach number. The change of the flow field structure is most accentuated at the shock front and is fully substantiated by the experimental observation shown in Figure 136.
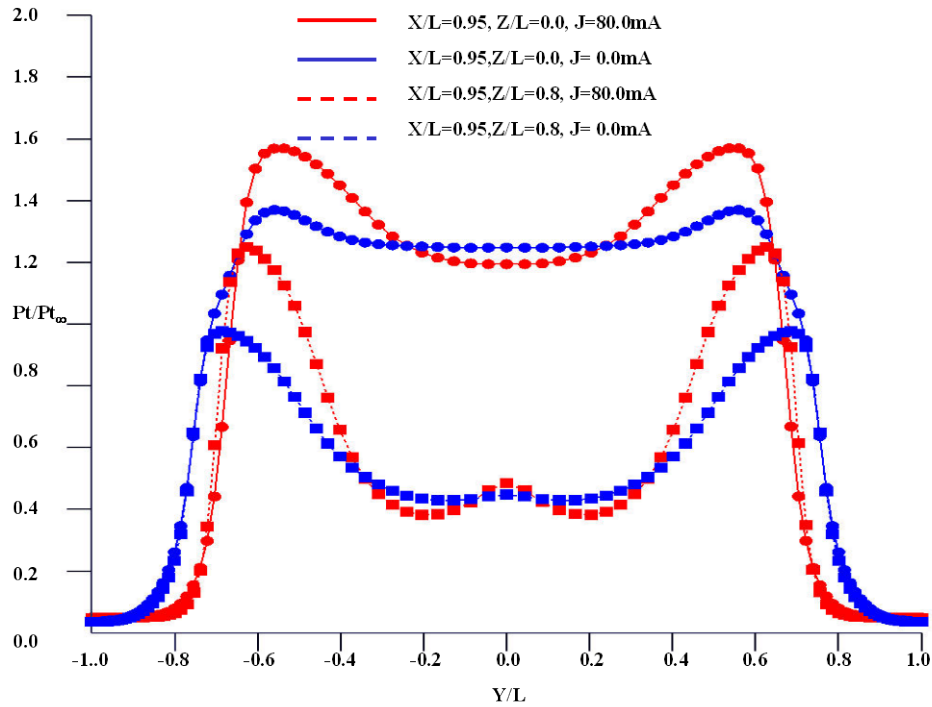


**Figure 141. Computed Pitot Pressure Distributions With/Without DCD, *x/L*=0.95**

The measured pitot pressure data at the identical streamwise location are presented in Figure 142. The surface discharge when actuated is sustained with an applied electric potential of 745±10 V and the electrical current at is 80±2 mA. The data are collected at the streamwise location of *x/L*=0.95. A total of four sets of data are shown across the width between the electrodes embedded in the sidewalls. Two sets of data are recorded at the same location on the *y*-coordinate, but with an actuated and deactivated DCD. The data recording position does not always coincide with the location where the maximum difference occurs. The pitot pressure data cross each other at different spanwise locations (see numerical results in Figure 141). Even with the measurement scatter, the data show a consistently higher value when the DCD is actuated.
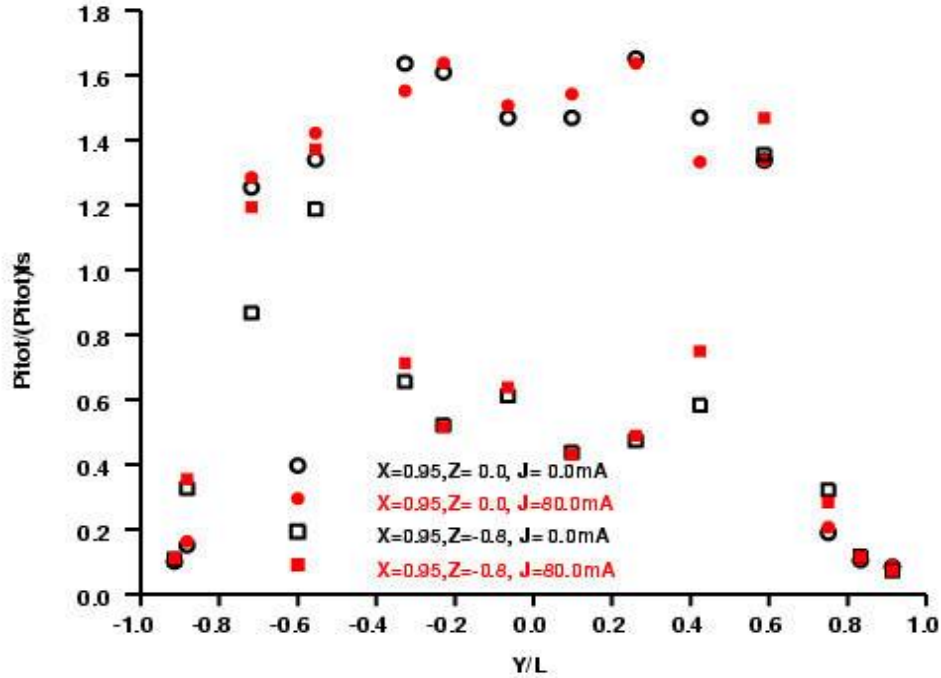
**Figure 142. Pitot Pressure Profiles In Cross-Flow Plane a _x/L_=0.95**

This similar behavior is also noted in the upstream pitot pressure survey at _x/L_=0.5, shown in Figure 143. At the central plane of the inlet, the oblique shocks originating from the horizontal sidewalls begin to intersect each other, and the shock-shock interaction produces a high pitot pressure plateau near the centerline. The pitot pressure profile off the centerline, _z/L_=0.5, captures the pressure plateau of the intersecting compression waves originating from the electrodes embedded in the sidewalls. The pressure with the actuated surface discharge is persistently higher than its deactivated counterpart. This pattern of pitot pressure measurements is consistent over all experimental observations. The appearance of a random data scatter is in part due to the complex and weak shock-shock and shock-boundary-layer interactions. A better definition of the profile may be acquired by data collection at different locations for an actuated and deactivated surface discharge or simply with a greater data density.

A quantitative assessment of the static pressure recovery from the plasma-compression within the inlet must rely on numerical simulation. The computed result employs a plasma model which must first be calibrated against the experimental data. The comparison of the computed pitot profiles near the inlet exit plane at _x/L_=0.95 is depicted in Figure 144. The numerical results not only duplicate the flow condition of the MHD channel, but also the placement of the cathode and anode. Only an additional input of the electrode temperature for the numerical simulation is required. This temperature is assigned a value of 460 K in an attempt to mimic the experimental condition (Menart et al., 2003b; Kimmel et al, 2004a). The computed pitot pressure distributions under-predict the peak values near the centerline, but are in excellent agreement with data in the middle span.
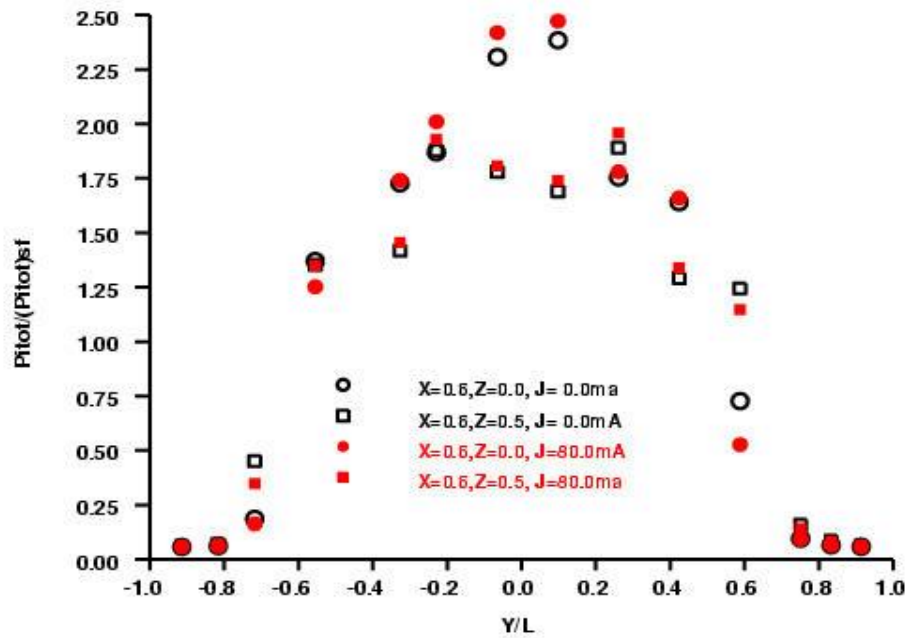
Figure 143.  Pitot Pressure Profiles of Cross-Flow Plane *x/L*=0.5
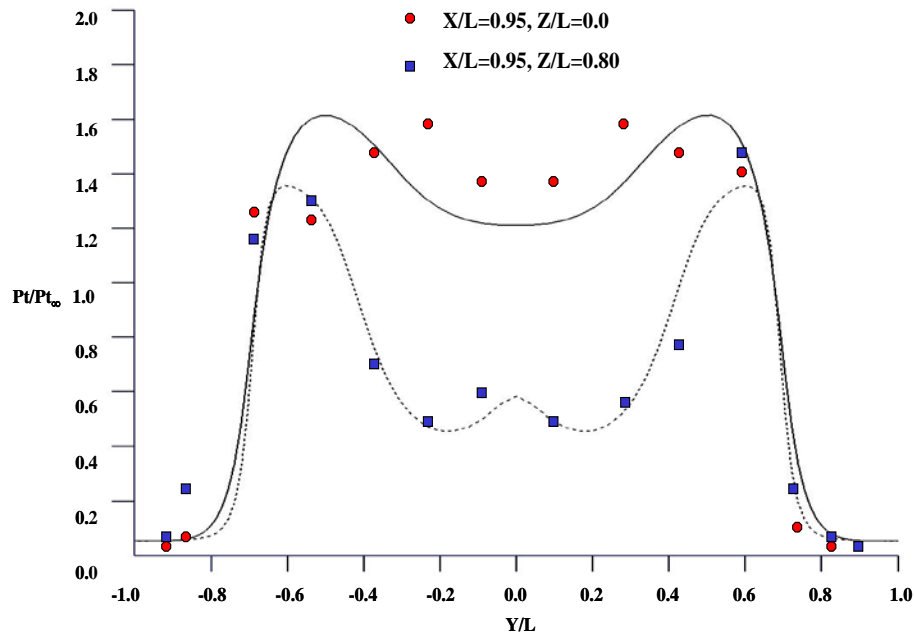


Figure 144.  Computed Pitot Pressures (Solid Lines) Calibrated Against Experimental Data (Data Points)

The computed static pressure distributions with and without a DCD across the half *z*-span of the inlet central plane are presented in Figure 145. The basic static pressure distribution is similar to the pitot pressure, but without the accentuation of the Mach number variations. The characteristic of a strengthened shock-on-shock and shock-boundary interaction is clearly revealed. The static pressure in the shear layer is uniformly higher and with a greater weak shock compression away from the center of the inlet than the flow without the DCD. Integrating the computed static

144

pressure distributions over the entire exit plane of the inlet with and without an activated surface discharge shows a net gain in plasma compression of 11.6 %. This additional compression within a rectangular and constant cross-section area inlet is generated by a small power input for the surface plasma generation of 61.2 W, and at an entrance Mach number of 5.15. At an electrode length of 3.175 cm, the scaled power input is 19.21 W/cm based on the electrode length. These values of the required power for plasma generation and the gained compression are also nearly identical to earlier hypersonic flow control simulations (Shang and Surzhikov, 2005; Shang et al., 2005c; Menart et al, 2003b; Kimmel et al., 2004a).
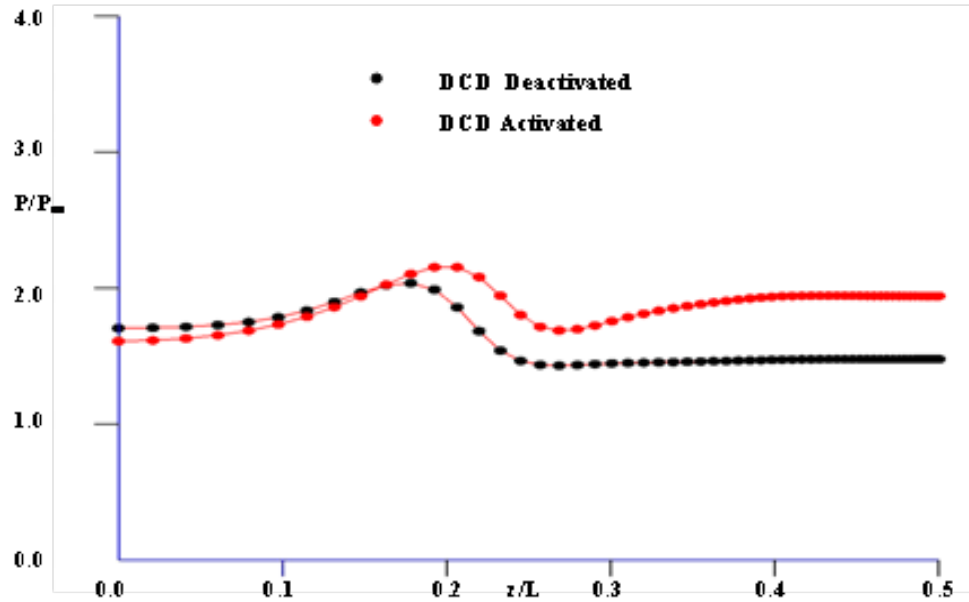


**Figure 145. Static Pressure Distributions With/Without DCD, x/L=0.95**

## 4.4.7 Summary

The magneto-fluid-dynamics interaction within a rectangular, constant cross-section area inlet achieves 11.6% greater pressure compression for the inlet with an entrance Mach number of 5.15 when the surface discharge is actuated. According to classic hypersonic pressure interaction theory, the compression will increase proportional to the cubic power of the entrance Mach number. Therefore, it has a viable application in hypersonic flows.

The electromagnetic force is introduced into the magneto-fluid-dynamics interaction as a small perturbation and amplified by the viscous-inviscid interaction. This chain-of-events is further substantiated by the two entirely different electrode arrangements. The net compressions are nearly identical; independent of whether the discharge is across or along the two inlet sidewalls

The reported magneto-fluid-dynamic interaction is characterized by low-amplitude and high frequency fluctuations. The source of the unsteady motion is linked to the oscillatory surface discharge behavior. The fluctuating electromagnetic perturbation generates a maximum time-averaged data scatter of 6.3%.

## 4.5 Magneto-Fluid-Dynamic Compression in a Round Inlet

### 4.5.1 Introduction

In the prior section a rectangular inlet was studied from an experimental and computational perspective. In this section a cylindrical inlet will be investigated. Most of the results presented will be experimental; however, some computational results will be presented as well.

The concept of amplifying a small electromagnetic perturbation via a viscous-inviscid interaction is straightforward (Shang and Surzhikov, 2005). For hypersonic flows, the pressure interaction near the leading edge is well-known. It is the classic viscous-inviscid interaction that involves the Mach waves, flow deflection angle, and surface pressure (Hayes and Probstein, 1959). The MFD (magneto-fluid-dynamic) interaction is initiated by a surface DCD (direct-current-discharge). The chain of events is triggered by an electromagnetic perturbation through Joule and electrode heating near the leading edge that thickens the local displacement of the boundary layer. The outward displacement induces compression waves which coalesce into an oblique shock. A significant surface compression over the immovable surface is generated by the MFD interaction which performs as a virtual compression ramp. In earlier investigations, the induced higher surface pressure over the fixed control surface has been demonstrated to perform as a virtual leading strake, as if the immobile control surface had executed a pitching movement (Shang et al., 2005b; Surzhikov and Shang, 2003a; Menart et al., 2003b; Shang and Surzhikov, 2004; Kimmel et al., 2004a; Kimmel et al., 2004b).

The application of this plasma actuator has been expanded to create a magneto-compression of a constant cross-section, square inlet in the prior section. When the plasma actuator is placed at the entrance region of a rectangular, constant cross-sectional inlet, the MFD interaction performs as a variable geometry cowl. The results obtained are encouraging. The repeatable phenomena have been successfully duplicated by computing simulations and verified by experimental observations (Shang et al., 2006b). From the side-by-side experimental and computational efforts, flow control is found to be governed by the magnitude of the plasma-flow interaction and the actuation is operable in milliseconds. According to the pressure interaction theory of Hayes and Probstein (1959) the MFD compression increases greatly with increasing free-stream Mach number.

The basic MFD phenomenon over a range of Mach numbers, however, is very complex, because the viscous-inviscid interaction is non-linear and dependent on the on-coming flow conditions. Prior research results also exhibit a dependence on the electrode placement; this observation is fully supported by the pressure interaction theory. The MFD interaction can substantially alter the growth rate of the displacement thickness and may lead to a laminar-turbulent transition by-pass (Reshotko, 2006). To fully validate the concept of the virtual variable geometry cowl, the present investigation applies this implementation to a cylindrical inlet.

### 4.5.2 Experimental Facility

The wind tunnel used to carry out the work being presented in this section is the same as used in the previous sections (see Figures 73 and 74). A brief description of this tunnel is given in Section 4.1.2 of this report. For the round duct experimental measurements the stagnation pressure is set to 560 torr (74.7 kPa). This provides a free-stream velocity and density in the test section of 675.5 m/s and 0.0096 kg/m$^3$ respectively. Under these conditions, the unit Reynolds number in the test section is $2.44 \times 10^6$ per meter.

The test section has the dimensions of 17.8×22.9×7.3 cm (L×H×W), which limits the cylindrical inlet model to a relatively small outer diameter of 3.76 cm and a length of 10.2 cm. The cylindrical inlet model has a nominally sharp leading edge with an outward 20-degree bevel made of phenolic. Due to the manufacturing techniques used, the leading edge of the model has a radius of curvature of 0.127 mm. The cathode ring is embedded flush to the inlet internal surface with a diameter of 3.49 cm and a width of 1.43 cm in the flow direction. The anode ring has a width of 0.64 cm and is also embedded and located downstream of the cathode separated by a phenolic spacer which is 1.59 cm wide. The assembled model is presented in Figure 146.
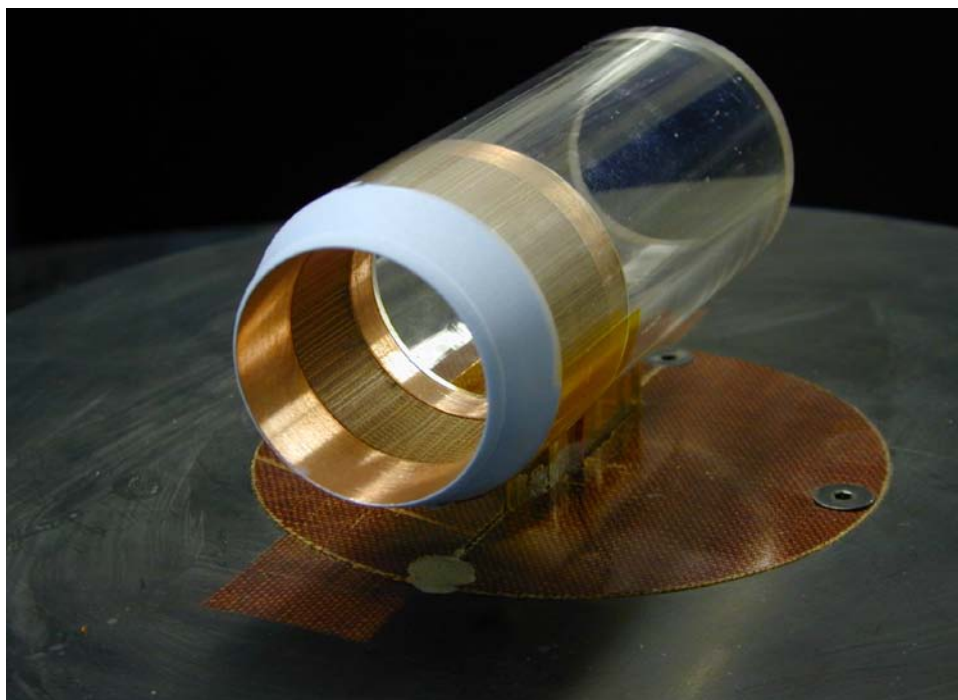


Figure 146. Cylindrical Inlet Model

The relatively small inlet model imposes a rather severe limit on the data collection technique. For the present purpose, only pitot pressure data were collected at several locations using a manually driven traversing mechanism. The pitot probe is constructed of a stainless steel tube with outer and inner diameters of 1.59 and 1.27 mm respectively. All pressure measurements were collected by a National Instruments 6259 M series data acquisition card and PC computer. A Baratron MKS model 722A-23320 absolute pressure gauge with a calibrated accuracy of 0.1% at the full range of 100 torr was used to collect all data. The maximum data sampling rate of the data acquisition system is one million per second; however, due to the long tube connections between the pitot probe and the pressure transducer, the temporal resolution of the measurements is on the order of 0.1 second.

The surface discharge is generated between the two ring electrodes within the cylindrical inlet model. The power supply to the direct current discharge is provided by a Universal Voltronics (BRC-10-1000R-STD-3PH-208V) reversible polarity unit. In a typical operation, the DC discharge is maintained by a voltage up to 480 V and a constant electric current of either 50 or 150 mA. Based on the calculations of a two-component weakly ionized gas model (Surzhikov and Shang, 2004), less than 17% of the total power is dissipated into Joule heating. This value

has not been verified by any specific measurement, but is in general agreement with classic theory (Raizer, 1991; Howatson, 1975).

The cylindrical inlet model is installed along the centerline of the plasma channel and the alignment is checked within one-tenth of one degree. The model is mounted on a knife-edge strut through one of the side port windows as shown in Figure 147. Therefore, all the data is collected for the hypersonic inlet at zero angle of attack and yaw. The leading edge of the inlet model is placed in the exit plane of the nozzle to minimize the axial gradient of the channel. The location of the pitot pressure probe is controlled by a three-dimensional traverse mechanism that has the freedom of movement to cover the entire domain of the test section. The placement of the traverse is controllable within a distance of 0.25 mm. The installation of the model in the plasma channel and the pitot probe attachment to the traverse mechanism is depicted in Figure 147.
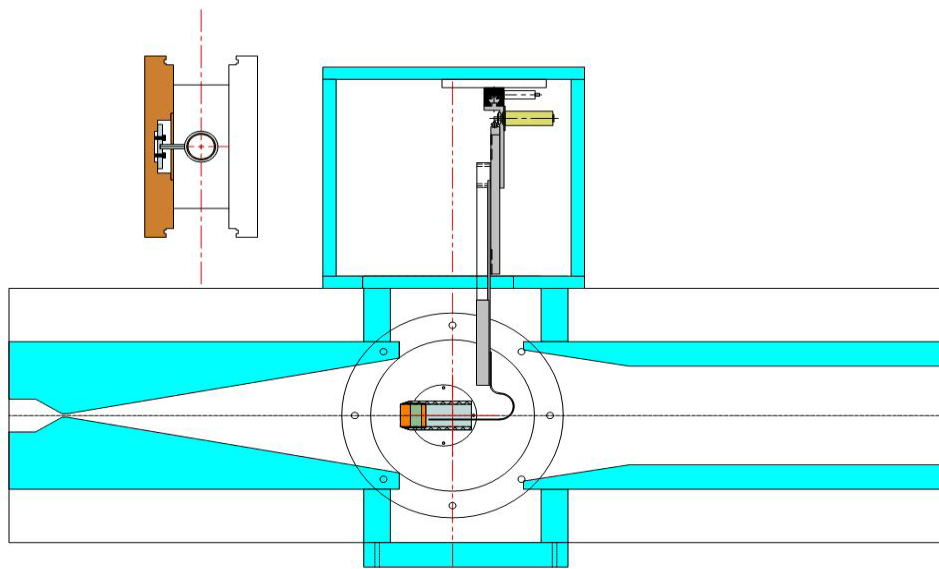


**Figure 147. Model and Probe Traverse Installation**

### 4.5.3 Testing Procedure

The observed basic flow structure within a cylindrical inlet is much simpler than that of the rectangular inlet (Shang et al., 2006a, Shang et al., 2006b). In the absence of mutually perpendicular sidewalls, the triplet-point shock structure is replaced by a continuous conical shock. The induced oblique shock surface from the leading edge is an inverted cone which originates from the inlet leading edge and converges to an apex or a focus on the axis of symmetry downstream. The shock formation is similar to the result of a shaped charge, but whether the detailed flow structure at the shock focus is a regular or Mach reflection is presently uncertain (Homung, 1986; Ivanov et al., 1997). Downstream of the shock intersection, the reflected shock propagates toward the inlet exit and impinges on the boundary layer of the inlet sidewall. Figure 148 depicts the computed density contour within the cylindrical inlet under identical conditions to those used in the experiment: $P_o = 560$ torr, $T_o = 270$ K, and $M_\infty = 5.15$. The preliminary numerical result is obtained by an axisymmetric formulation to identify the flow field structure and to guide the data collecting process. The detailed shock structure at the apex of the conical shock will be investigated in the following computational simulation. For the

present purpose, the quantification of the MFD compression within the cylindrical inlet model is the foremost objective.
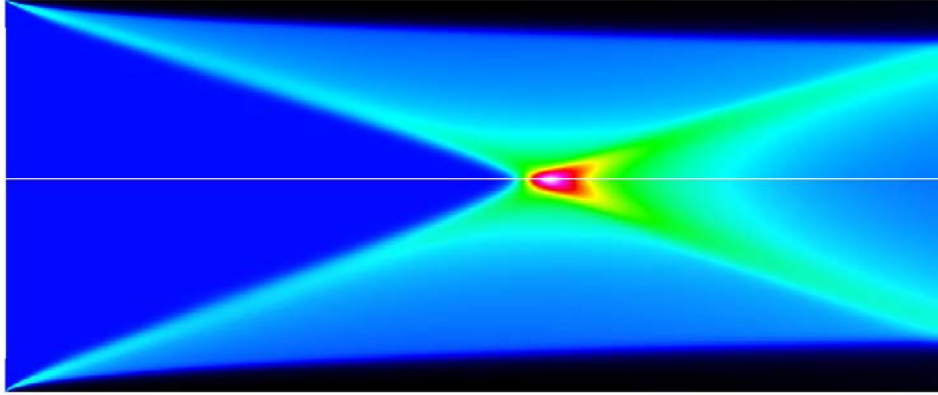


**Figure 148. Density Contour of Cylindrical Inlet, $M_\infty$=5.15, $Re_y$=2.58×10⁵**

The induced shock from the leading edge is strongly influenced by the minuscule radius of curvature of the leading edge (0.127 mm) and the slope of the boundary-layer displacement thickness, $\partial\delta^*/\partial x$. The latter depends on the Reynolds number based on the free-stream conditions and the electromagnetic perturbation. The surface pressure can be computed easily by the tangent-cone approximation (Hayes and Probstein, 1959). When the plasma actuator is ignited, the slope of the boundary-layer displacement is expected to increase and to induce a stronger oblique conical shock. As a consequence, the shock intersection moves upstream and the shock impingement on the sidewall boundary layer shifts upstream. The net result of the actuated plasma control is as anticipated; the plasma produces a greater compression to act as a virtual compression ramp of the constant cross-section inlet. To substantiate this anticipation, the flow field structure is investigated by experimental measurements up- and down-stream of the leading-edge induced shock focal point. To measure the performance of the MFD compression, multiple data samplings are collected near the exit plane of the inlet model.

Figure 149 presents a photograph of the ignited DC discharge (DCD) in the cylindrical inlet. The discharge is sustained by an applied electric potential of 400 V and a current of 50 mA. The DC discharge is viewed from the inlet exit at an oblique angle from the axis. The dominant visual feature of the discharge is the glow over the electrodes and the reflections on the model sidewalls. Under this testing condition, the discharge current density on the anode is 6.78 mA/cm². This value is three times lower than that of the rectangular inlet with a different electrode arrangement (see Section 4.4). For this reason, the DC discharge pattern of the cylindrical inlet is essentially fluctuation free. This behavior persists even when the current density reaches a value of 20.34 mA/cm² with the increased circuit current of 150 mA. As a consequence, the present experimental measurements from this configuration have substantially reduced data scatter from the previous results for a rectangular inlet (see Section 4.4).
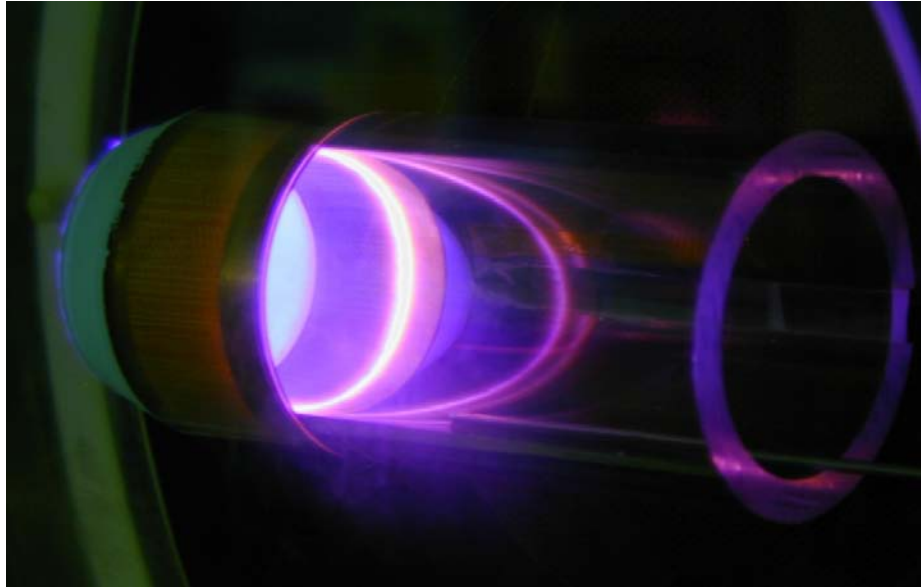
Figure 149. DC Discharge at Leading Edge of the Cylindrical Inlet
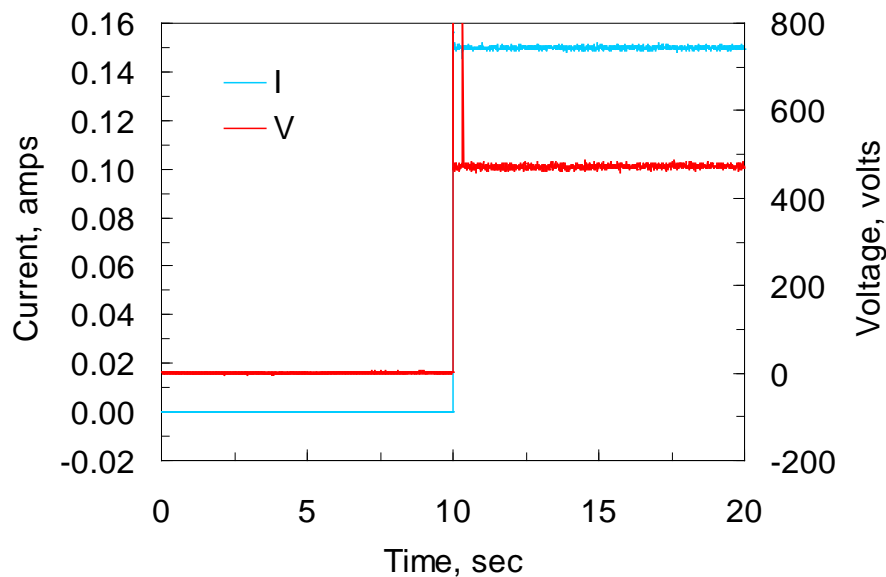


Figure 150. Trace of Discharge Current and Voltage

In a continuous and steady flow condition, the typical data collecting procedure is standardized for the entire experimental study. The pitot probe is placed in a preset location of the channel in a steady running condition and the data recording starts for a 10 second period with the DCD deactivated. Then the DCD is ignited at a constant current for 10 seconds. A typical electric current and voltage record is given in Figure 150. In this test case, an electric current of 150 milli-amperes is maintained by an electrical potential of 480 volts during the data sampling period. Thus the collected data are the time-averaged value over the sampling period of 10 seconds for the activated and deactivated DCD conditions. The pitot pressure surveys were conducted in cross-flow planes upstream of the shock focal point and near the inlet exit, together with measurements parallel to the axis of symmetry at different radial locations.

150

### 4.5.4 Measurement Accuracy

The overall flow field structure can be reconstructed by the pitot pressure surveys at two streamwise locations within the inlet and in an orthogonal orientation along the radius. Upstream of the apex of the induced conical shock, the inviscid core exists over a major portion of the inlet cross-section. A continuous compression toward the sidewall is generated by the inverted conical shock. Two pitot pressure profiles at the streamwise location of $x/L = 0.325$ are presented in Figure 151. One of the profiles is measured along the vertical radius and the other is recorded along the horizontal radius. Data were collected at stagnation pressures ranging from 556 to 560 torr and a stagnation temperature of 270 K. The theoretical pitot pressure in the freestream, upstream of the shock, is 30.69 torr (4.09 kPa), which agrees very well with the averaged experimental data of 30.57 torr. All the presented pitot pressure data are normalized by this reference value. A slight asymmetry of the data distributions is observed for the pitot pressure surveys along the horizontal and vertical radii (see Figure 151). Differences between the data are attributed to a maximum difference in vacuum sphere back pressure of 1.2 torr between the two tests. Attempts were made to maintain the back pressure of the channel at a nominal value of 8 torr from run to run. For a relatively large blockage area of the model, the effect of the back pressure on the nozzle performance is significant. This rather large discrepancy in measured data occurred because of the abnormally high back pressure which was closely monitored during the entire investigation. In addition, the alignment of the model with the Mach 5 wind tunnel channel has been checked. These steps have helped to minimize data scatter.
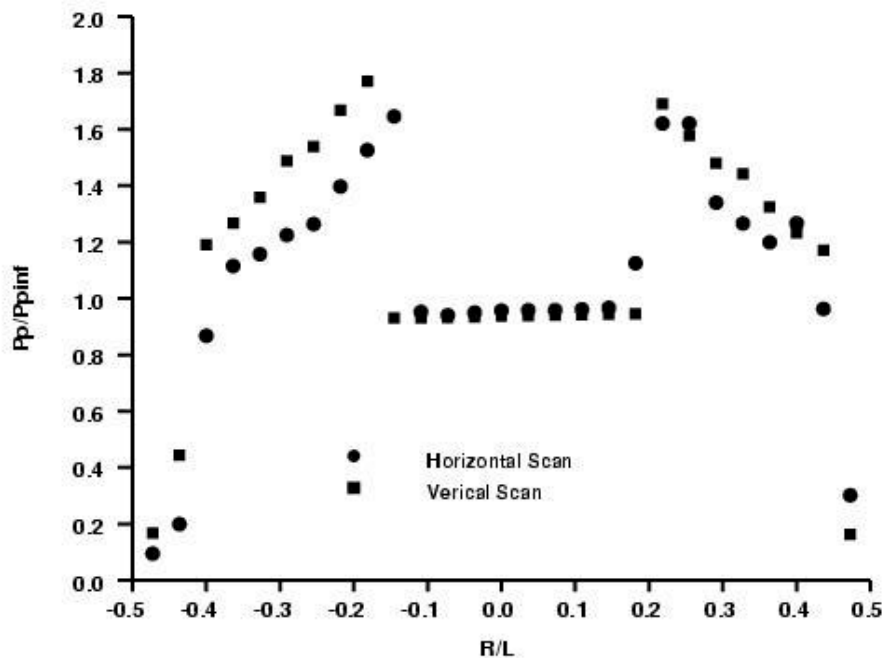


Figure 151.  Pitot Pressure Surveys at $M_\infty$=5.15 and $x/L$=1.3

Figure 152 shows the comparison of the pitot pressure distributions at the streamwise location $x/L$=0.95, which is located near the exit plane of the inlet model. Again, the data were obtained by two pitot probe surveys, one along the vertical axis and one along the horizontal axis. Except for a large anomaly of the data for the horizontal survey near the axis, the average data discrepancy is confined within 5.5% of the full data range. The unusually high pitot pressure data

immediately adjacent to the axis of symmetry, associated with the horizontal survey, may be associated with the transition between regular and Mach reflection of the shockwave (Homung, 1986; Ivanov et al., 1997). The shock structure is extremely complex at the focus of the conical shock and the domain of influence is extremely compact. For this reason, this behavior might not be captured if the vertical survey has a slight misalignment. Near the singular shock wave focal point, it is not certain whether an oblique shock jump condition will hold. In any event, a rapidly changing Mach number occurs at the shock focal point, which is not necessarily located right on the axis of the model. The pitot pressure measurements near this location are also an average value over the inner diameter of the probe; therefore it is unable to pinpoint this location. This anomaly will be investigated by the accompanying computational study.
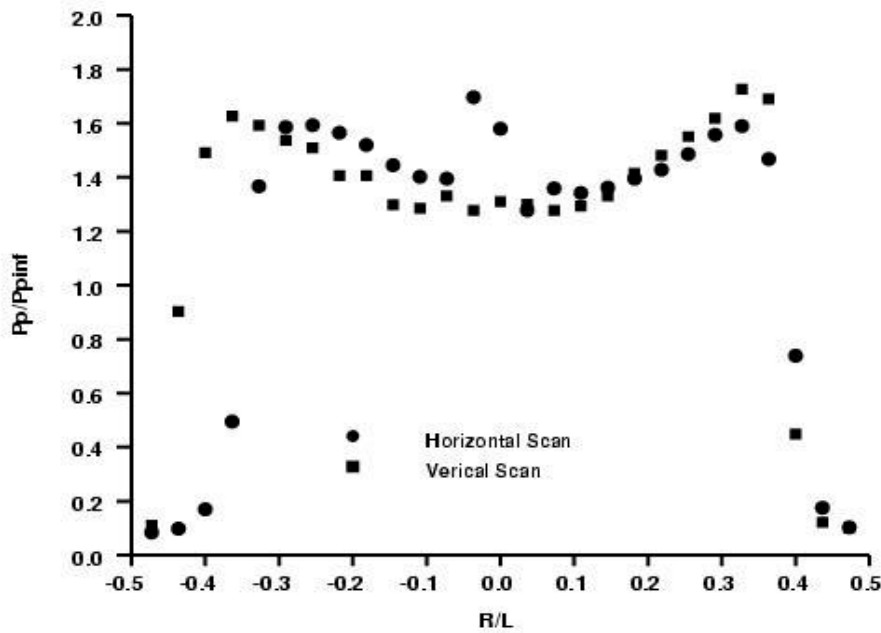


**Figure 152. Pitot Pressure Survey at M$_\infty$ =5.15 and *x/L*=0.95**

The horizontal pitot pressure profiles near the exit plane, *x/L*=0.95, for different plasma power settings are depicted in Figure 153. One of the activated DCDs is powered by 20.1 watts (402 V and 50 mA) and the other is generated by 69.0 watts (460 V and 150 mA). Even at the higher power discharge condition, the current density of the cathode has a small value of 9.02 mA/cm$^2$. The data clearly reflect the fact that the DCD is a small perturbation to the flow field. There are small differences in the pitot profiles. For the higher power input condition the induced oblique, conical shock exhibits a stronger compression at the shock and is followed by a rapid expansion toward the model centerline. Near the centerline both surveys in the horizontal plane show a sharp pitot pressure rise that is considered to be associated with the shock focal point; this behavior has been mentioned previously. The redundant measurements at this location yield a data range of 2.74%, which is greater than either the scatter in stagnation conditions or discharge voltages at a constant electric current.
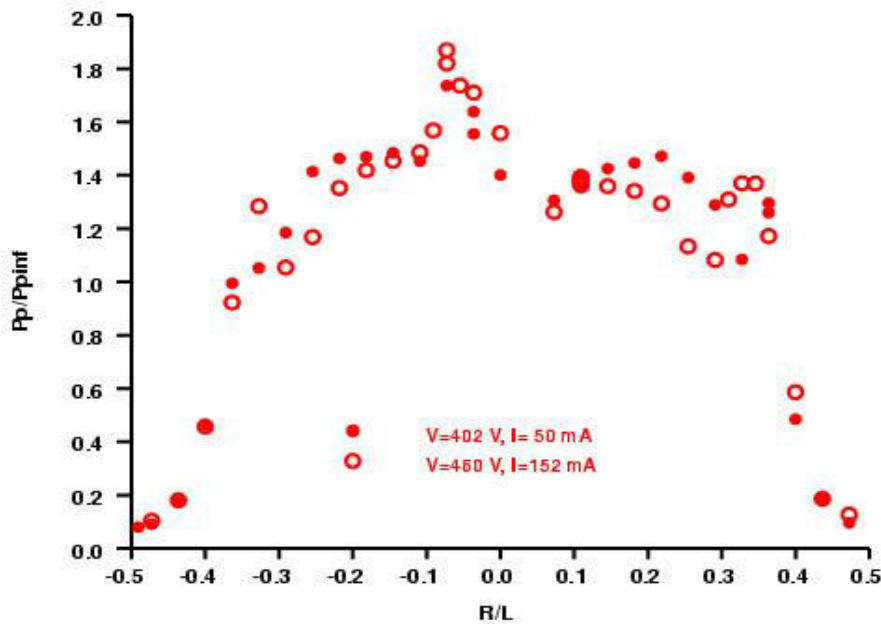
**Figure 153. Pitot Pressure Distributions with Different Surface Plasma Powers**

### 4.5.5 Plasma Interactions

All the following data for the MFD interaction are collected for the constant electric current of 150 mA. This current is maintained by 460±2.5 volts, thus the total power to the electromagnetic perturbation is limited to a maximum of 69.4 watts. To best describe the overall MFD compression induced within the inlet model, the data surveys include streamwise pitot pressure distributions along a fixed radial location and cross-flow pitot pressure profiles at two streamwise locations.

Figure 154 presents the pitot pressure measurements along the model centerline with and without the activated DCD. It is observed that the MFD interaction strengthens the conical shock by steepening the oblique shock angle and moving the shock focus upstream. From an experimental observation the conical shock is seen to have a half-cone angle of 11.8 degrees. The pitot pressure near the shock focal point attains a value of 3.57 times the freestream value. The peak pitot pressure of the activated DCD is also slightly elevated in comparison with the deactivated DCD data. The most noticeable behavior of the pitot pressure distributions is the irregular higher pressure distribution in the exit regions of the inlet model. The pressure plateau first appears at the streamwise location where the reflected shock impinges on the boundary layer. Due to the shallower conical shock associated with the deactivated DCD flow structure, the pressure plateau is farther downstream compared to the activated DCD counterpart. The onset of the exit pressure plateau is dependent on the model leading edge nose radius and the rate of growth of the displacement thickness or the freestream Reynolds number.
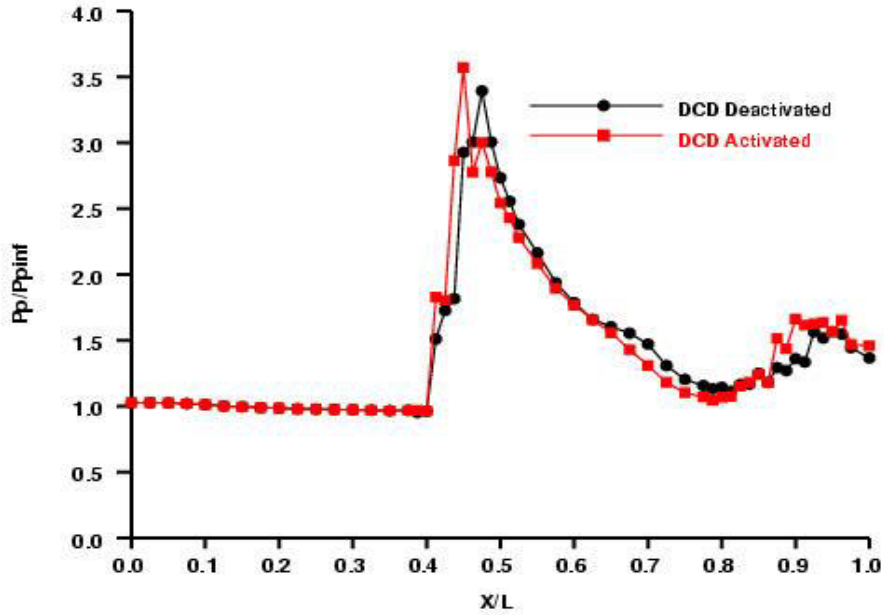
**Figure 154. Streamwise Pitot Pressure Distribution, *r/R* = 0.0**

The streamwise pitot pressure distribution along a constant radial position, *r/R*=0.44, or *r*=0.76 cm from the centerline is given in Figure 155. In this figure, the strengthened conical shock by the MFD interaction is much more pronounced. The pitot pressure distribution with the activated DCD executes a constant shift upstream because of the steepened conical shock wave. The first pitot pressure peak indicates the passage of the induced conical shock originating from the model's leading edge, and the second reveals the presence of the reflected wave downstream of the shock focal point. The maximum pitot pressure is recorded at the reflected shock wave and has a normalized peak value of 2.21.

Figure 156 depicts the streamwise pitot pressure distribution along a constant radial distance *r/R*=0.87, or *r*=1.52 cm from the model centerline. This radial distance is only 0.22 cm away from the model sidewall. Therefore the pitot probe is deeply immersed within the boundary layer toward the exit region of the model and the measured pitot pressure is approaching the static pressure value. Again the first pressure rise in the distribution reveals the intersection of the original conical shock wave and the second pressure rise indicates the impingement of the reflected wave on the boundary layer. The induced compression by the MFD interaction is consistently indicated in the exit region of the model. The additional pressure increment by the MFD compression is 13.9% produced by a power input to the surface plasma of 69 watts.

Detailed cross-flow surveys were conducted at two selected streamwise locations from the model leading edge, these were done at *x/L*=0.325 (*x*=3.3 cm) and *x/L*=0.950 (*x*=9.5 cm). The first cross-flow survey station is upstream of the focal point of the conical shock. The pitot pressure profiles were collected along the horizontal and vertical axes. It was found that the flow field in the model is not perfectly axisymmetric; the deviation in the measured profiles is around 0.127 cm. Since the alignment of the model centerline to the open jet is controlled within one-one tenth of one degree, the miss-alignment is most likely caused by the protrusion of the electrodes embedded in the model studied. For a small model, this was not avoidable because of the different materials used for the electrodes and spacer which gives rise to different thermal expansion effects.

154
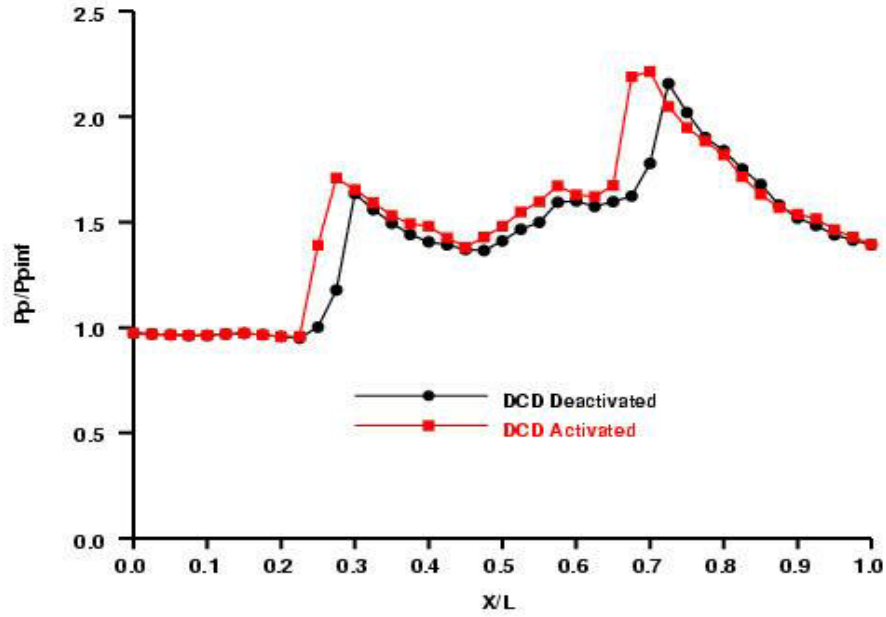
Figure 155. Streamwise Pitot Pressure Distribution at $r/R = 0.44$
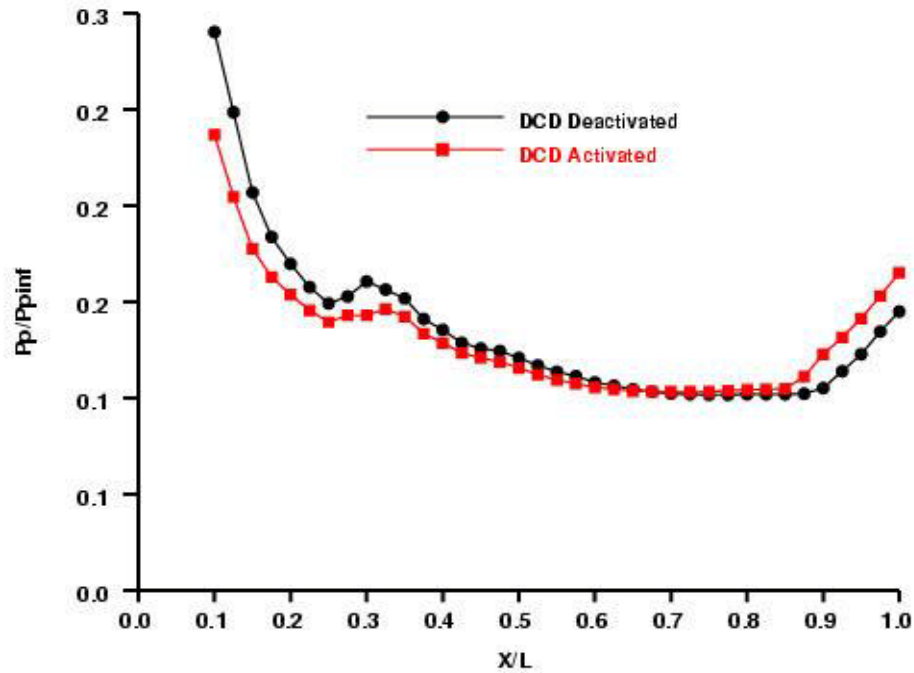


Figure 156. Streamwise Pitot Pressure Distribution, $r/R = 0.87$

The horizontal pitot pressure profiles at $x/L$=0.325 along the axis of the model are presented in Figure 157. Two sets of data are presented together, one of the data sets is collected with the activated DCD and the other is recorded with the deactivated DCD under identical flow stagnation conditions. When the surface plasma is ignited, the weakly ionized gas is generated by a voltage of 478.5±1.1 V and at a constant current of 152 mA. At the upstream flow station, the

difference in measurements between the activated and deactivated DCD conditions is relatively small, as expected, because the surface discharge is a small electromagnetic perturbation and the viscous-inviscid amplification is just beginning. The pitot data reveal that the boundary-layer thickness at this streamwise location is less than 0.34 cm, and the conical shock attains a compression ratio of 1.80 times the freestream value. The inviscid core at the deactivated DCD condition has a radius of 0.61 cm. The electromagnetic perturbation reduces the inviscid core by a small amount, about 0.064 cm. The basic characteristic of the pitot pressure profile along the vertical axis is similar to the measurement along the horizontal axis; therefore it is not included here.
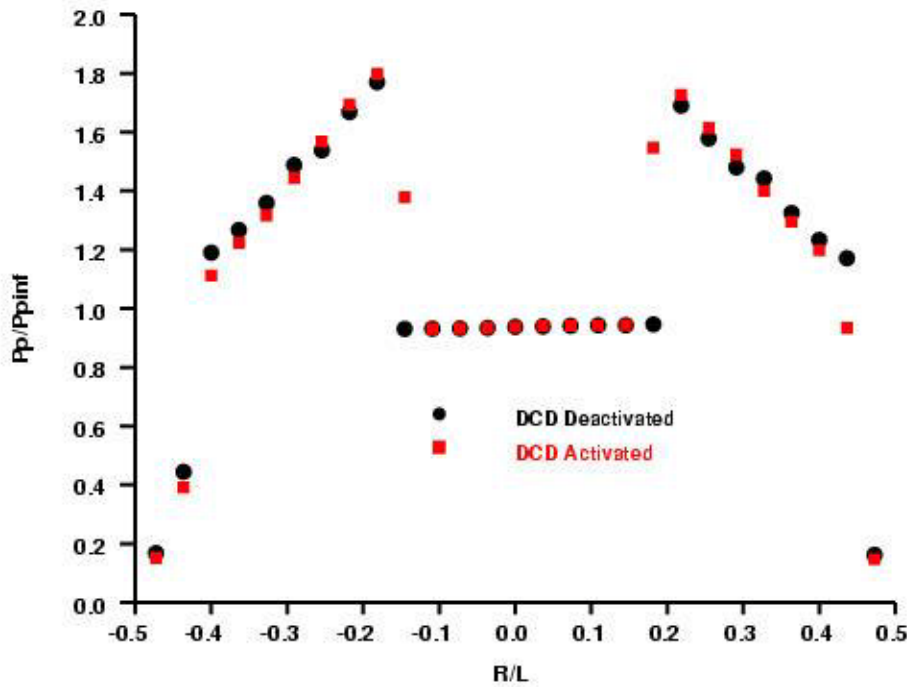


**Figure 157. Comparison of Horizontal Scan Pitot Pressure Profiles With/Without Activated DCD, $x/L = 0.325$**

The comparison of the pitot pressure measurement near the model exit plane, $x/L$=0.95, with and without the MFD interaction is given in Figure 158. These sets of data are collected along the horizontal axis of the model and the DCD is generated by a power supply of 73.0 watts (480±1.4 V and 150 mA). At this streamwise location, the boundary-layer thickness has grown to a value of 0.61 cm under the mild adverse pressure gradient condition downstream of the weak impinging shock. The compression gain through the MFD interaction appears to be modest. The pitot pressure spike near the centerline of the model stands out for both flow conditions, with and without the activated DCD. The magnitude of the pressure spike appears too large to be induced by any small protuberance from the embedded electrode and dielectric spacer rings.
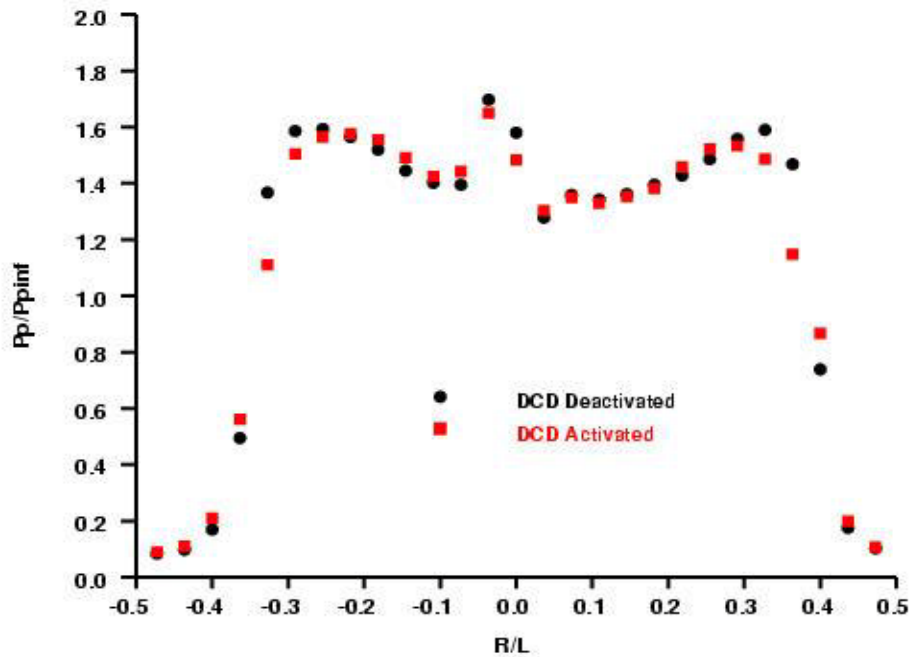
**Figure 158. Comparison of Horizontal Scan Pitot Pressure Data With/Without Activated DCD at *x/L* = 0.95**

Two pitot pressure surveys along the vertical axis of the model are presented next. The first test was conducted at stagnation pressure of 546 torr and stagnation temperature of 270 K. The DCD is maintained at 480±1.2V for an electric current of 152 mA. The total power supply for the surface plasma generation is 73.0 watts. The comparison of the measured pitot pressure profiles is presented in Figure 159. The overall pattern in comparing the data is very similar to the data collected along the horizontal axis, except with the absence of the anomalous pressure spike. Again, the compression gain from the MFD interaction is relatively modest in contrast to the rectangular model due to the relatively lower current density on the electrodes.

The second comparison of pitot pressure data with and without the MFD interaction at *x/L*=0.95 along a vertical axis reveals a different pattern than the data obtained in Figures 157 through 159. This comparison is presented in Figure 160 under nearly identical flow conditions ($P_o$=560 torr, $T_o$=270 K) and surface plasma discharge conditions (460±2.5V, 152 mA, 70.0 watts) as the prior surveys. By integrating the total area under the measured curves, the MFD interaction produced an additional compression of 8.7% as compared to the DCD off case.

157
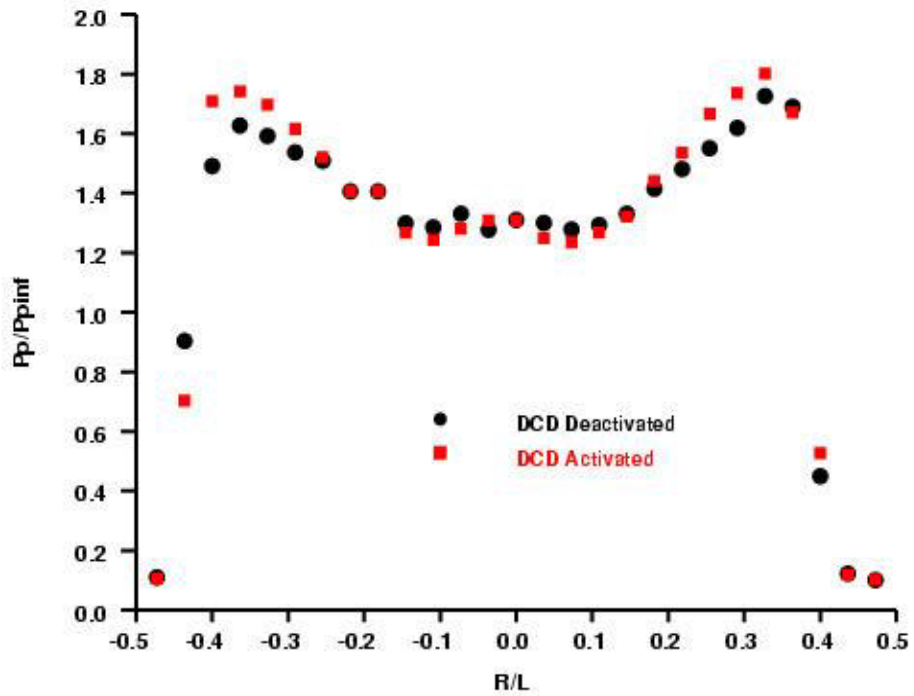
Figure 159. Comparison of Vertical Scan Pitot Pressure Data With/Without Activated DCD at $x/L = 0.95$ (72.96 Watts)
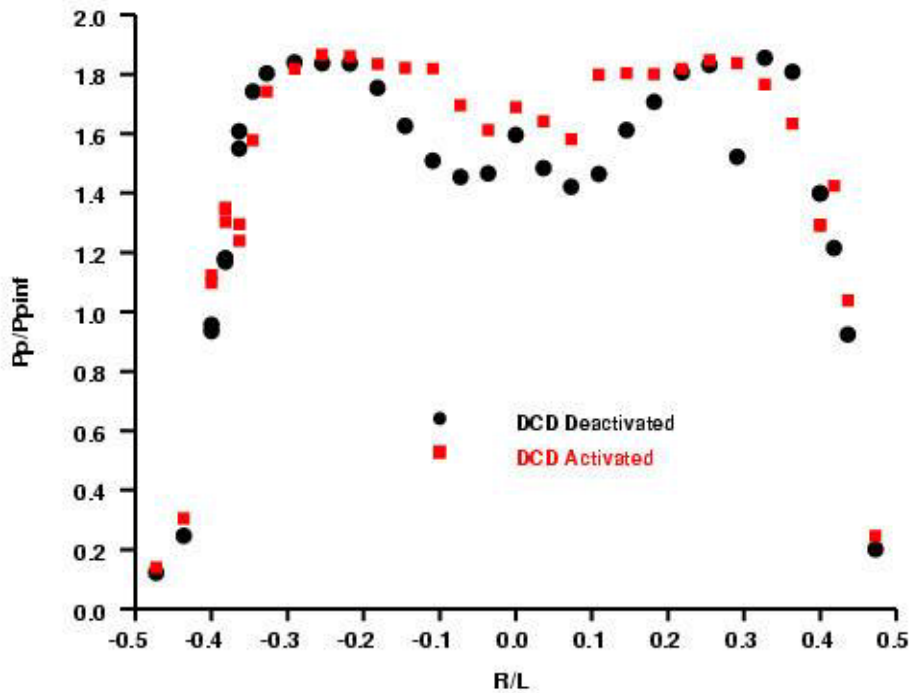


Figure 160. Comparison of Vertical Scan Pitot Pressure Data With/Without Activated DCD at $x/L = 0.95$ (69.92 Watts)

The differences between the presented cross-flow pitot pressure profiles highlights the shock wave boundary layer interaction at the model exit. Meanwhile the impingement of the reflected shock wave can induce separated flow locally. A possible incipient flow separation has been observed to affect the pitot pressure distribution near the model exit plane. Partial evidence has been brought out to support this claim by the pitot pressure distribution along the streamwise direction of the model depicted in Figure 154. From time to time a substantial difference in pitot pressure measurements at the model exit region is seen. This also seems to substantiate this conjecture. The domain of flow separation may be very limited by the mild adverse pressure gradient condition produced by shock impingement, but a slowly varying unsteady flow field can be created by upstream feeding through the subsonic portion of the boundary layer. Unfortunately, the present experimental setup is not designed for investigating the slowly varying unsteady flow.

### 4.5.6  Summary

The concept of utilizing the magneto-fluid-dynamic interaction to generate additional compression within an inlet has been experimentally investigated for a cylindrical model. The electromagnetic perturbation is introduced at the leading edge of the cylindrical inlet model by a surface plasma discharge. The total energy for a weakly ionized gas is limited to less than 73 watts with a current density over the electrode area of 6.33 mA/cm$^2$. The maximum compression gain over an unperturbed constant area cylindrical inlet model has a modest value of 8.7%. This induced compression is less than that achieved in a rectangular inlet of the same cross-sectional area due to the amount of current density used in each case. In principle, the magneto-fluid-dynamic compression can be increased by either a greater electromagnetic perturbation or by operating the virtual inlet cowl at a higher freestream Mach number.

During this research process, it was found that the flow field is much more complex than anticipated for this simple configuration. From the measurements, a wide range of variations were noted. However, the time-dependent behavior has a characteristic low frequency rather than a fluctuating motion. A peculiar fluid dynamic phenomenon was also detected at the apex of the conical shock that originated from the pressure interaction at the leading edge. The basic issue may rest on the possible transition between a regular and a Mach reflection at the focal point of the conical shock.

## 5.0 PLASMA DBD EXPERIMENTAL WORK

In Section 5 of this report asymmetric surface mode dielectric barrier discharges (ASDBD) are studied. ASDBDs are flow control devices that through momentum coupling are capable of altering the gas flow around them (Enloe et al., 2004b). It has been shown that ASDBDs are capable of controlling the boundary layer, suppressing flow separation, reducing drag and controlling the wake of a circular cylinder (Roth et al., 1998; Huang et al., 2006; Post and Corke, 2004; Wilkison, 2003; McLaughlin et al. 2004). There has also been experimental and theoretical research on understanding the fundamental mechanisms of the ASDBD (Enloe et al., 2004b; Enloe et al., 2006; Enloe et al, 2004b) along with computational research (Font, 2006; Boeuf and Pitchford, 2005). The work presented in Section 5 of this report adds to the fundamental understand of ASDBDs.

The characterization of dielectric barrier discharges (DBDs) by means of emission spectroscopy has been carried out for gas mixtures other than air (Chiper et al., 2004; Luque et al., 2003). Chipper et al. (2004) conducted spectroscopic studies for DBDs operating in He/Air and He/$N_2$ gas mixtures. They used emission spectroscopy to determine the rotational temperature at one location within the discharge as a function of the flow rate of $N_2$. Luque et al. (2003), investigated DBDs operating in $CH_4$/$CO_2$ gas mixtures and studied both the rotational and vibrational temperature at a single location within the discharge. The rotational and vibrational temperatures were determined by looking at the $A^2\Delta - X^2\Pi$ band of CH. The emphasis of both investigations was towards the application of surface treatment.

In Section 5 of this report emission spectroscopy, which is a non-intrusive technique, is used to map the rotational and vibrational temperatures and the relative concentrations of the $N_2(C^3\pi_u)$ and $N_2^+(B^2\Sigma_u^+)$ states for the discharge region of an ASDBD in atmospheric air. Section 5.1 of this report discusses rotational and vibration temperatures averaged over the entire voltage cycle. In Section 5.2 rotational temperatures, vibrational temperatures, and relative concentrations are obtained over the negative and positive halves of the voltage cycle. Thus increased temporal resolution is displayed in Section 5.2. The work in Section 5.2 also uses a different experimental apparatus than that in Section 5.1. Both of these experimental facilities are described below.

### 5.1 Full Cycle Rotational and Vibrational Temperatures

### 5.1.1 Introduction

In this section of this report rotational and vibrational temperatures averaged over the entire voltage cycle are presented. Rotational temperatures are obtained by comparing the measured spectrum of the nitrogen second positive 0-2, 1-3 and 2-4 transitions to different theoretical spectra calculated for different rotational temperatures. This method has been used successfully in the past to determine the thermal boundary layer of a DC glow discharge on top of a flat plate in a Mach 5 flow (Stanfield et al., 2005). The vibrational temperature is obtained by the Boltzmann plot method. The translational temperature is assumed to be equal to the rotational temperature. This is a valid assumption at the temperatures and pressure involved in this work, because the rotational energy levels are closely spaced and allow for rapid energy transfer between the two energy storage modes (Biberman, 1987).

Given below is a detailed description of the experimental facility, the experimental procedure, and the data reduction technique used to obtain rotational and vibrational temperatures averaged over the entire voltage cycle. Rotational and vibrational temperatures are presented at spatial

locations throughout the discharge region of an ASDBD generated with a sinusoidal voltage input that has a peak to peak voltage of 11,700 volts and a frequency of 5000 Hz. Two optical lines of sight are utilized providing spatial resolution in the spanwise and flow directions. Because the ASDBD is very thin, no attempt was made to resolve the temperatures in a direction normal to the electrodes.

## 5.1.2  Experimental Facility

### 5.1.2.1  Asymmetric Surface Dielectric Barrier Discharge

The ASDBD used in this work is shown in Figure 161 and consists of two electrodes; one exposed and one buried beneath a dielectric material. The electrode material is copper and the dielectric material is 1 mm thick glass. As can be seen from Figure 161 there is a 2 mm overlap between the exposed and buried electrode. This was done to reduce the chances of arcing. The width of the buried electrode is 10.7 mm and the width of the exposed electrode is 4.4 mm. The region where the electrodes overlap in the spanwise direction is rather short, 38.1 mm.
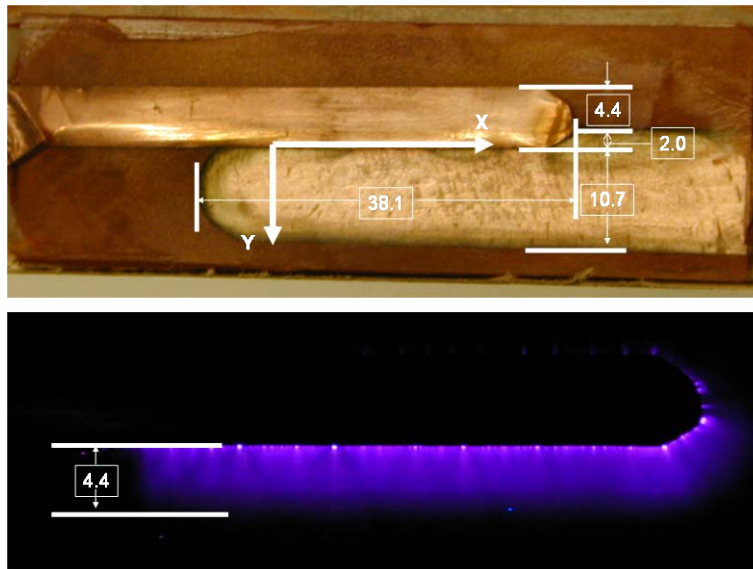


**Figure 161.  Electrodes used in this work shown without an ASDBD and with an ASDBD. All Dimensions are in mm**

A discharge is established over the buried electrode by placing an oscillating voltage between the two electrodes. In this work the applied voltage is an 11,700 volt, peak-to-peak sinusoidal function with a frequency of 5000 Hz and the buried electrode is grounded. The oscillating electric field is the means by which the discharge is created and sustained. For the most part electrons pick up energy from the electric field and then transfer some of this energy to the heavy particles, nitrogen and oxygen molecules and atoms, via excitation and ionization collisions. The excitation collisions are what give rise to the spectra being studied in this work. The ionization collisions produce the free electrons that are required to maintain the discharge. The magnitude of the electric field has to be continually altered to sustain the discharge because of the dielectric surface used. A DC current would not produce a discharge when a dielectric surface is used. This oscillatory process also helps to maintain a diffuse discharge at atmospheric pressure (Enloe et al., 2006). A DC discharge at atmospheric pressure between two exposed, metal electrodes would quickly degrade to an arc.

### 5.1.2.2 Collection Optics and Spectroscopic System

Figure 162 shows the optical collection system which channels the emitted radiation from the ASDBD to the spectrometer. The emitted radiation from the ASDBD is collected and collimated by a Newport KBX250 bi-convex lens with an effective focal length of 250 mm. The collimated radiation is focused with a Newport KBX1000 bi-convex lens with an effective focal length of 1000 mm onto a Roper Scientific LG-455-020-1 fiber optic bundle. The magnification of the system at location A in Figure 162 is four and is given by

$$M = \frac{f_2}{f_1} ,$$
(172)

where $f_1$ is the focal length of the front lens and $f_2$ is the focal length of the back lens. The magnification at location B is given as

$$M_B = -\frac{f_1 f_2}{f_1(f_1 - L) + L(g - f_2)} ,$$
(173)

where $L$ is the thickness of the discharge and $g$ is the spacing between the two lenses. Equation (173) can be approximated by equation (172) so long as $L$ is small, which is the case in this work. The spatial resolution of the measurement depends on the magnification, the diameter of the opening of the fiber optic cable, $d$, and the angle $\theta$ given as

$$\theta = \tan^{-1}\left(\frac{D_{eff}}{2f_1}\right) ,$$
(174)

where $D_{eff}$ is the effective diameter of the front lens. The spot size of the collection volume at point A and B, shown in Figure 163, are

$$Spot\ Size(A) = \frac{d}{M}$$
(175)

and

$$Spot\ Size(B) = Spot\ Size(A) + 2L\tan(\theta) .$$
(176)

The fiber optic bundle channels the collected radiation into an Acton 2756 spectrometer where it is diffracted and focused onto an Andor DU 440-BU CCD camera. The fiber has a round ferrule on the collection end and a slit pattern on the exit end which is designed to match the entrance slit of the spectrometer. The spectrometer has a spectral resolution of 0.05 nm at 435.8 nm using a 1200 groove per mm grating. The spectral response of the system was calibrated using a Newport 63976 tungsten halogen lamp. The slit height and width for all measurements presented are 4 mm and 15 μm respectively.
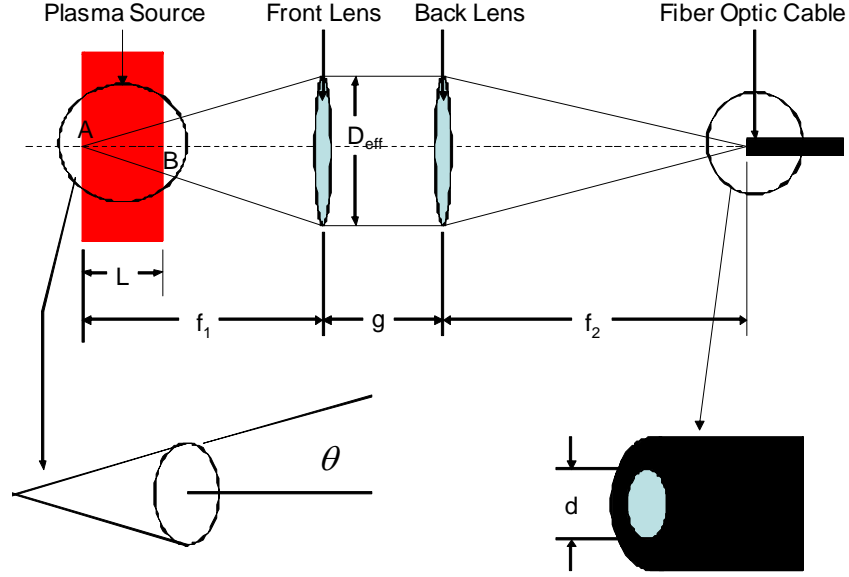
**Figure 162. Optical Collection System**
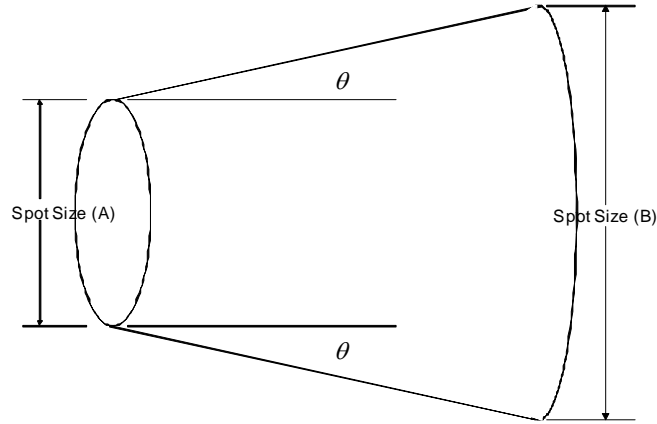


**Figure 163. Collection Volume of Optical System**

The spectral response of the system was calibrated using a Newport 63976 tungsten halogen lamp. This is a crucial step for properly measuring the relative intensity of the different rotational and vibrational transitions. This is necessary for obtaining accurate temperature measurements. The portion of the radiant energy detected due to stray light inside the spectrometer, caused from imperfections in the mirrors and other internal optical components, is accounted for using a Newport 10LWF-400-B filter that blocks the wavelength range being calibrated. The calibration curve is given by

$$Calibration\ Curve(\lambda) = \frac{Tungsten\ Lamp\ Spectra(\lambda) - Stray\ Light\ Spectra(\lambda)}{Theoretical\ Tungsten\ Lamp\ Spectra(\lambda)} . \quad (177)$$

The calibrated data is given by

$$Calibrated\ Data(\lambda) = \frac{Raw\ Data(\lambda)}{Calibration\ Curve(\lambda)} . \quad (178)$$

Optical components are mounted onto a rail positioned perpendicular to the ASDBD. This rail is mounted onto another rail perpendicular to it so that the optics can move parallel to the spanwise direction of the ASDBD. The optical rails are mounted on a steel elevating table. Figure 164 shows the table along with the optics and how they are oriented with the ASDBD. Alignment of the table with respect to the model was done using a large square. A level was used to adjust the table and model so that these surfaces are parallel.
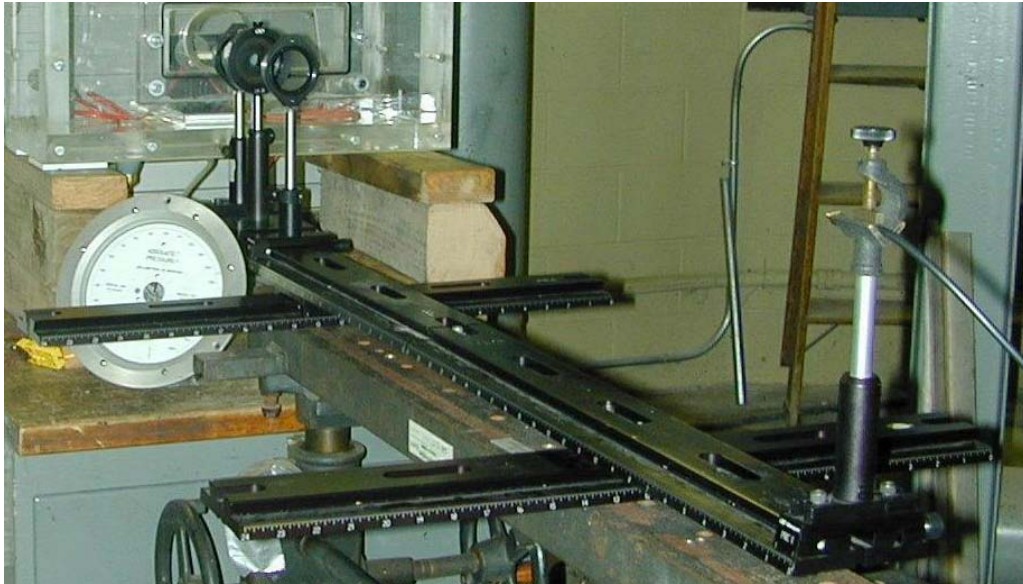


Figure 164.  Optics Arrangement on Optical Rails and Elevating Table

## 5.1.2.3   Voltage and Current Measurement Technique

The voltage and current of the discharge is obtained from the circuit shown in Figure 165. The measurement is made with an oscilloscope. The average dissipated power of the ASDBD can be obtained by multiplying the instantaneous voltage and current and integrating the resultant power curve over one or two voltage cycles. The average is then obtained by dividing this energy by the time period of integration. A number of difficulties arise in making a measurement such as this. The first is interference from the noise caused by the high frequency voltage signal being delivered to the ASDBD. Some shielding was done to reduce this problem. Another issue to be dealt with is unwanted capacitance or inductance in the portion of the circuit used to make the measurement. These were kept as small as possible.

For the ASDBD operating condition used in this work the voltage and current characteristics over two cycles are shown in Figure 166 . The peak voltage is 11,700 volts and the peak current is 1.2 mA. The voltage and current curves shown in Figure 166 were obtained by averaging 512 waveforms. If the instantaneous values are used, the peak currents are much larger. When the plasma is actively delivering current to the electrodes, the shapes of the curves are very spiked. The spikes can still be seen in Figure 166 , but their magnitudes are greatly reduced from their actual values. The power determined by integrating under the curve of the product of the instantaneous voltage and current is approximately 2.0 watts.
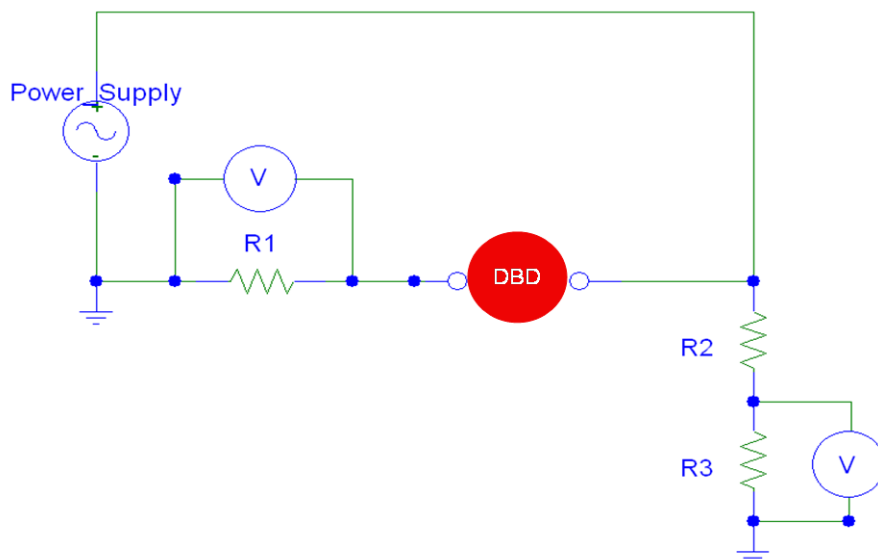
**Figure 165. Electric Circuit Used To Measure Current and Voltage of the ASDBD**
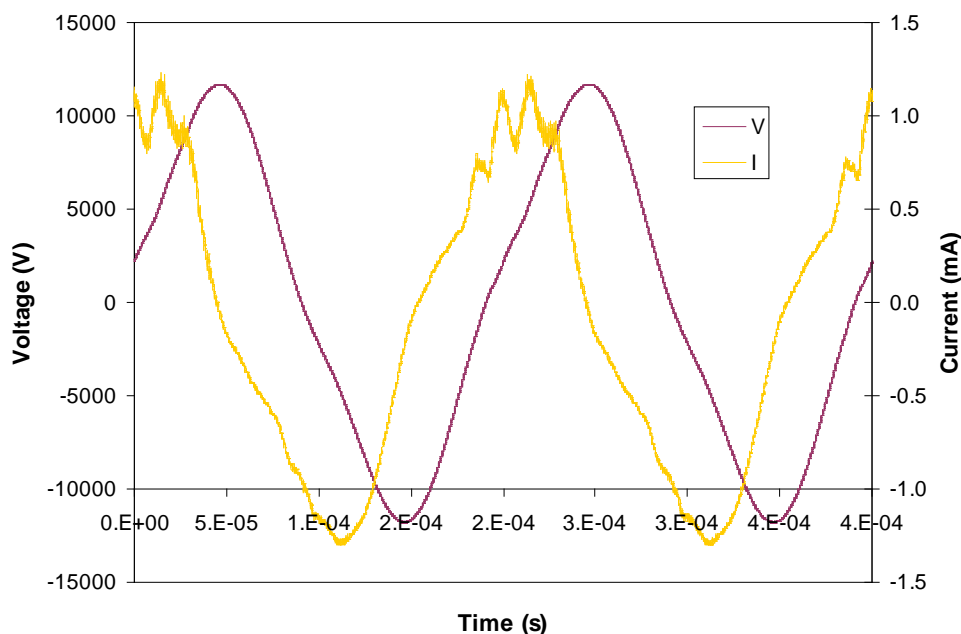


**Figure 166. Voltage and Current Characteristics of the ASDBD**

### 5.1.3 Rotational Temperature Measurement Technique

The rotational temperature is obtained by comparing the measured spectrum of the nitrogen second positive 0-2, 1-3, 2-4 and 3-5 transitions to different theoretical spectra calculated for different rotational temperatures (Williamson and DeJospeh, 2003; Stanfield et al. 2003). The rotational temperature obtained corresponds to the calculated spectrum that best matches the experimental spectrum. This iterative procedure is performed by a program called N2SPECFIT (Williamson and DeJoseph, 2003). The details of the theoretical equations used by N2SPECFIT are given below.

The intensity of a vibration-rotation line for an optically thin molecular gas is given as

$$I_{v',J'}^{v'',J''} = N_{v',J'} A_{v',J'}^{v'',J''} \frac{hc}{\lambda_{v',J'}^{v'',J''}}$$
(179)

where $v'$ is the upper vibrational quantum number, $v''$ is the lower vibrational quantum number, $J'$ is the upper rotational quantum number, $J''$ is the lower rotational quantum number, $I_{v',J'}^{v'',J''}$ is the line intensity, $N_{v',J'}$ is the number of upper-state molecules in the $v'$ vibrational level and $J'$ rotational level, $A_{v',J'}^{v'',J''}$ is the Einstein coefficient, $\lambda_{v',J'}^{v'',J''}$ is the wavelength of the transition and $hc$ is Planck's constant times the speed of light (Herzberg, 1950). Assuming the rotational energy levels are in equilibrium, the distribution of molecules in the different energy levels is described by the Boltzmann distribution,

$$N_{v',J'} = \frac{N_{v'}}{Q_r} g_{J'} e^{-F_J/kT}$$
(180)

where $N_{v'}$ is the number of molecules in the upper vibrational level $v'$, $Q_r$ is the rotational partition function, $g_{J'}$ is the degeneracy of the $J'$ upper rotational energy level, $F_j$ is the rotational energy of the $J'$ upper rotational energy level, and $kT$ is the Boltzmann constant times the rotational temperature. The Einstein coefficient of the vibration-rotation transition can be related to the Einstein coefficient of the vibrational transition through

$$A_{v',J'}^{v'',J''} = A_{v'}^{v''} \frac{S_{J'}^{J''}}{g_{J'}}$$
(181)

where $A_{v'}^{v''}$ is the Einstein coefficient for the vibrational transition and $S_{J'}^{J''}$ is the rotational line strength (Kovacs, 1969). Substituting equations (180) and (181) into equation (179) gives the intensity of a vibration-rotation line as

$$I_{v'J'}^{v''J''} = \frac{N_{v'} A_{v'}^{v''}}{Q_r} S_J^{J''} e^{-F_{J'}/kT_{rot}} \frac{hc}{\lambda_{v'J'}^{v''J''}}.$$
(182)

The intensity predicted in equation (182) is for a line without any width; however, a measured transition is spread over a small frequency band caused by various broadening mechanisms such as Doppler, pressure, and natural line broadening (Griem, 1997). To account for the line shape the line intensity is multiplied by the correct line shape function,

$$L_{v',J'}^{v'',J''} = I_{v',J'}^{v'',J''} \Phi\left(\lambda, \lambda_{v',J'}^{v'',J''}\right).$$
(183)

In equation (183), $L_{v',J'}^{v'',J''}$ is the spectral line and $\Phi\left(\lambda, \lambda_{v',J'}^{v'',J''}\right)$ is the line shape function. The line shape function is a normalized Voigt distribution and it is the convolution of the various broadening mechanisms listed above. Equation (183) gives the spectral line for a single rotational transition within a vibrational transition, but there are many rotational transitions within a single vibrational transition. Therefore all the rotational transitions within a single vibrational transition can be obtained by summing over all possible rotational quantum numbers. This is given as

166

$$L_{v'}^{v''} = \sum_{J',J''} L_{v',J'}^{v'',J''},$$

(184)

where $L_{v'}^{v''}$ is the intensity of the vibrational transition.

Equation (184) gives the spectral lines for a perfect measuring device; real spectrometers, however, have error which causes the spectral line predicted in equation (184) to broaden even more. The error of the spectrometer is given by the instrumental line shape and the measured spectral line is obtained numerically by convolving equation (184) with the instrumental line shape. This is given as

$$W_{v'}^{v''}(\lambda) = \int_0^\infty L_{v'}^{v''}(\lambda')P(\lambda,\lambda')d\lambda'$$

(185)

where $W_{v'}^{v''}(\lambda)$ is the spectral line and $P(\lambda,\lambda')$ is the instrumental line shape. Substituting equation (183) into equation (185) gives

$$W_{v'}^{v''}(\lambda) = \sum_{J',J''} I_{v',J'}^{v'',J''} \int_0^\infty \Phi(\lambda', \lambda_{v',j'}^{v'',j''})P(\lambda,\lambda')d\lambda'.$$

(186)

The different broadening mechanisms of the measured spectrum produce half-widths that are at least an order of magnitude smaller than the half-width of the instrumental line function in the environment being investigated. Therefore the half-widths of the different broadening mechanisms present in the measured spectrum can be approximated by a Dirac delta function with minimal error resulting in

$$W_{v'}^{v''} = \sum I_{v',J'}^{v'',J''} P(\lambda, \lambda_{v',J'}^{v'',J''}).$$

(187)

The final equation for the spectral line is obtained by substituting equation (182) into equation (187)

$$W_{v'}^{v''}(\lambda) = \frac{N_{v'}A_{v'}^{v''}}{Q_r} hc \sum_{J'J''} S_{J'}^{J''} e^{-F_{J'}/kT_{rot}} \frac{P(\lambda, \lambda_{v'J'}^{v''J''})}{\lambda_{v'J'}^{v''J''}}.$$

(188)

The program N2SPECFIT uses equation (188) to calculate the numerical spectrum for a particular rotational temperature which is supplied as an initial guess and then iteratively changed until the measured spectrum matches the numerical. Figure 167 shows the agreement with one of the measured spectra in this work and the corresponding calculated spectrum. The spectroscopic constants used in equation (188) by N2SPECFIT are those tabulated by Gilmore et al. (1992) and Laher and Gilmore (1991).

The instrumental line shape function was obtained by measuring and curve fitting the spectra of a mercury discharge tube at 435.833 nm. This value, when convolved, may not broaden the calculated spectra enough to match the measured due to representing the line shape function as a Dirac delta function. The reduced chi square of the calculated spectrum with respect to the

167

measured spectrum can be minimized by modifying the instrumental line function obtained. It should also be noted that the temperature obtained is the average temperature throughout the collection volume sampled (Stanfield, 2005; Herzberg, 1950).
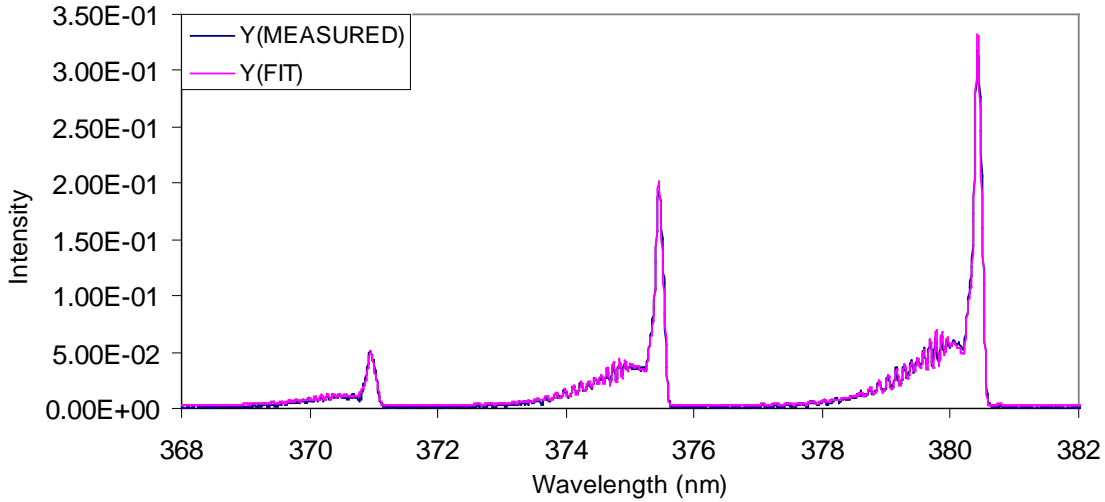


**Figure 167. Example of a Measured Spectrum Overlaid with the Fitted Spectrum Generated by N2SPECFIT**

### 5.1.4 Vibrational Temperature Measurement Technique

The vibrational temperature is obtained from the Boltzmann plot method described in Marr (1968), which is outlined below. The relative intensity measured by the spectrometer is given as

$$I_{v'v''} = DN_{v'}\overline{v}_{v'v''}^4 S_{v'v''} ,$$

(189)

where $I_{v'v''}$ is the measured intensity, $D$ is a constant dependent on the geometry of the experimental set up, $N_{v'}$ is the population of the upper state, $\overline{v}_{v'v''}$ is the wave number of the transition, and $S_{v'v''}$ is the band strength of the transition. The band strength of the transition is

$$S_{v'v''} = R_e^2(\overline{r}_{v'v''})q_{v'v''} ,$$

(190)

where $R_e^2(\overline{r}_{v'v''})$ is the sum of the squared electronic-vibrational transition moment and $q_{v'v''}$ is the Franck-Condon factor. The spectroscopic constants used are again tabulated by Gilmore et al. (1992) and Laher and Gilmore (1991). The Boltzmann distribution is given as

$$N_{v'} = \frac{N}{Q_v(T)} \exp\left[\frac{-G(v')hc}{kT}\right],$$

(191)

where $Q_v(T)$ is the vibrational partition function, $N$ is the total molecular species population in a given electronic state, $h$ is Planck's constant, $c$ is the speed of light, $k$ is the Boltzmann constant and $G(v')$ is given as

$$G(v') = \left(v' + \frac{1}{2}\right)\omega_e' - \left(v' + \frac{1}{2}\right)^2 \chi_e'\omega_e' + \left(v' + \frac{1}{2}\right)^3 y_e'\omega_e'........$$

(192)

168

where the terms $\omega_e'$, $\chi_e'\omega_e'$ and $y_e'\omega_e'$ are tabulated spectroscopic constants. The vibrational intensity is obtained by combining equations (189), (190) and (191),

$$I_{v'v''} = \frac{DN}{Q_v(T)} \bar{v}_{v'v''}^4 R_e^2(\bar{r}_{v'v''})q_{v'v''} \exp\left[\frac{-G(v')hc}{kT_{vib}}\right].$$ (193)

The intensity calibration is relative, which means that the above intensity needs to be relative to another vibrational transition in the band system. In general this is done with the 0-0 band, but for this work the 0-2 band was used. The intensity of the 0-2 band from equation (193) is

$$I_{0,2} = \frac{DN}{Q_v(T)} \bar{v}_{0,2}^4 R_e^2(\bar{r}_{0,2})q_{0,2} \exp\left[\frac{-G(0)hc}{kT_{vib}}\right].$$ (194)

Dividing equation (193) by equation (194) gives

$$\frac{I_{v'v''}\bar{v}_{0,2}^4 R_e^2(\bar{r}_{0,2})q_{0,2}}{I_{0,2}\bar{v}_{v'v''}^4 R_e^2(\bar{r}_{v'v''})q_{v'v''}} = \exp\left[\frac{hc}{kT_{vib}}\left(G(0)-G(v')\right)\right].$$ (195)

Taking the logarithm of equation (195) gives

$$\ln\left(\frac{I_{v'v''}\bar{v}_{0,2}^4 R_e^2(\bar{r}_{0,2})q_{0,2}}{I_{0,2}\bar{v}_{v'v''}^4 R_e^2(\bar{r}_{v'v''})q_{v'v''}}\right) = \frac{hc}{kT_{vib}}\left(G(0)-G(v')\right)$$ (196)

which is equivalent to an equation of a line given as $y = mx + b$ where $y$ is

$\ln\left(\frac{I_{v'v''}\bar{v}_{0,2}^4 R_e^2(\bar{r}_{0,2})q_{0,2}}{I_{0,2}\bar{v}_{v'v''}^4 R_e^2(\bar{r}_{v'v''})q_{v'v''}}\right)$, $x$ is $\left(G(0)-G(v')\right)\frac{hc}{k}$, the slope $m$ is given by $\frac{1}{T_{vib}}$, and the $y$-offset $b$ is

0. The vibrational temperature is obtained by plotting the above quantities for the measured spectra and fitting it with a straight line. It should also be mentioned that the vibrational intensity is obtained by determining the area under all the rotational lines within a single vibrational transition. This integration is done numerically.

## 5.1.5 Results

The first results presented are for an optical line-of-sight that provides spanwise resolution while averaging in the flow direction and over the depth of the discharge. The optical line-of-sight is shown in the top of Figure 168. This drawing depicts the edges of the electrodes. The location of each of the 14 measurements is marked with a dot. Scan locations 1, 2, 12, 13 and 14 have edge effects in the measurement; whereas, the other sampled points are for the interior of the ASDBD. The collection volume (spatial resolution) in this orientation has a spot size at location A (Figure 163) of 0.25 mm and a spot size at location B (Figure 163) of 0.7 mm. The measurements were taken after the ASDBD ran for 30 minutes in order to reach a quasi-steady operational state.
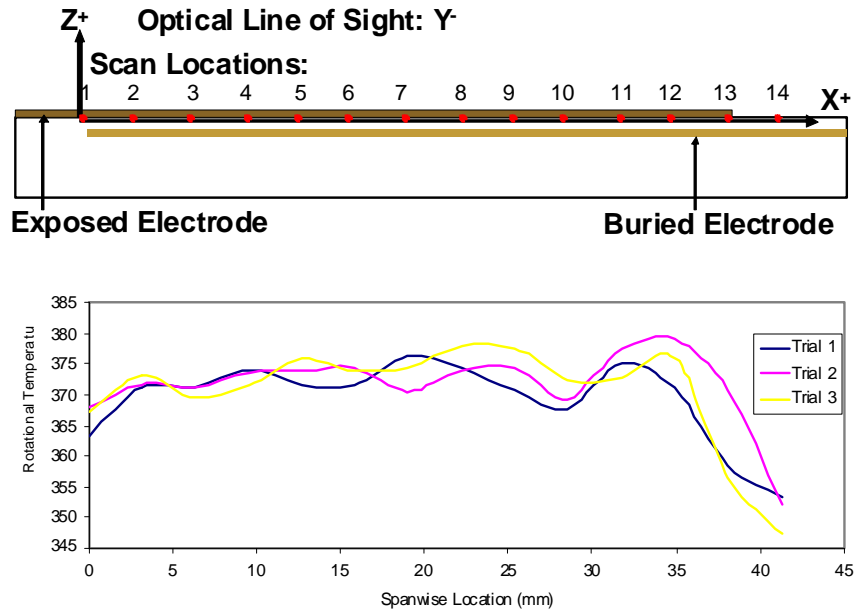
**Figure 168. Rotational Measurements as a Function of Spanwise Location where the Line-of-sight of the Spectrometer is in the Flow Direction. The Top Image Shows the Orientation of the Optical Line-Of-Sight with Respect to the ASDBD Along with the Sampled Spatial Points**

The rotational temperature results in Figure 168 indicate the temperature profile of the interior of the device appears to have a periodic behavior. When these oscillatory temperature profiles are compared to the bright attachment points, shown in a picture of the ASDBD (see Figure 161), the peaks in the temperature profile line up reasonably well with the bright spots in the picture. It is felt that these localized hot spots are due to small cathode jets that form in the ASDBD discharge. Note that these localized hot spots are only 5 K for this line-of-sight, but later on it will be shown from a different line-of-sight, one which averages over less contribution from colder regions of the discharge, that they are on the order of 40 to 60 K. While it is not the focus of this work, it appears that these jets affect the flow structure as well. Figure 161 shows what appears to be fan shaped structures coming out of the bright spots. These bright areas are the brightest at the very edge of the exposed electrode and diminish in brightness from this point in a fan shape. It is believed that these bright spots are localized arc jets with higher electron number density then the rest of the discharge. While the rotational measurements indicate that these spots have higher temperatures, the measured intensity indicates that these spots have a higher localized ion density (Enloe et al. 2004a). The higher ion density is probably associated with a higher electron density.

The small cathode jets may possibly affect the flow induced by the discharge. PIV measurements displayed in Figure 169 show spanwise periodic regions of higher and lower velocity (Kimmel et al., 2006). The data presented were obtained for a 2000 Hz square wave, but were also evident for a 5000 Hz sine wave. A correlation between the bright plasma spots and the flow streaks has not been definitively shown, however.

Vel (m/s):  0  0.1 0.2 0.3 0.4 0.5 0.6 0.7
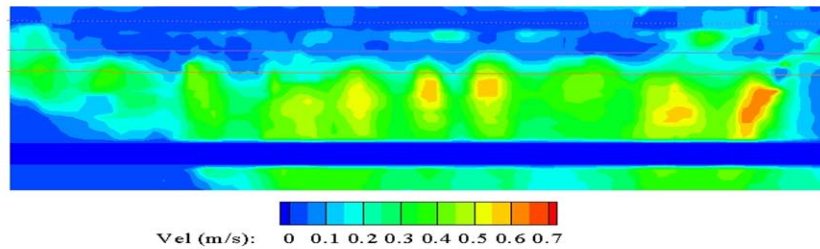
**Figure 169.  Velocity Contour Plot Obtained from PIV Measurements for A Square Wave (Kimmel et al. 2006)**

Figure 170 shows the vibrational temperature profile corresponding to the rotational temperature profile shown in Figure 168. Also included in this figure is the Boltzmann plot for one of the data points. It is immediately apparent from the Boltzmann plot that the population of the vibrational levels strays from the Boltzmann distribution. Thus the temperature plot is a best Boltzmann fit to vibrationally excited states that are not exactly Boltzmann. The vibrational temperatures range from 2840 K at the peak of an oscillation to 2700 K. These are high temperatures which indicate that a substantial amount of the input energy to the ASDBD is tied up in the vibrational states. Comparison of  Figures 171 and 168 shows that changes in the vibrational temperature correspond to changes in the rotational temperature. The same type of oscillatory behavior is seen in the vibrational temperatures. This is consistent with the presence of high electron density jets in the ASDBD discharge. These changes in vibrational temperature also indicate that the densities of dissociated species vary locally.

The second arrangement of the optical line-of-sight is perpendicular to the electrodes. This direction of measurement allows measurements to be made in the flow direction and the spanwise direction. This means that temperature profiles over the entire face of the dielectric covered electrode can be made. Since the line-of-sight is perpendicular to the discharge, the temperatures are averaged over the depth of the discharge. The depth of the discharge is very small, but there still has to be temperature gradients in this direction. The spot size at location A (see Figure 163) is again 0.25 mm, but the spot size at location B (see Figure 163) is 0.45 mm. The results for the rotational measurements over the dielectric covered electrode are shown in Figure 171 along with a picture of the discharge. The results show that the rotational temperature is greatest in the gap between the exposed and buried electrode, 465 K, and then decreases to 345 K as you go across the buried electrode away from the gap. These results also show a periodic behavior in the spanwise direction, like the measurements in Figures 168 and 170. Because it is difficult to see this periodic behavior in the contour plot, a line plot has been produced (see Figure 172). In this figure the rotational temperatures are seen to vary in a periodic manner in the spanwise direction with the magnitudes of the variations being strongest in the gap and decreasing until they are undetectable at the edge of the discharge. Remember that the measurements shown in Figure 168 are averaged over the flow direction. The measurements in Figures 171 and 172 provide resolution in the flow direction. The data clearly shows the oscillations being damped in the flow direction. This is what you would expect from cathode jets. It is also apparent from Figure 172 that the oscillations from six different scans line up at a

location of 20 mm, whereas four scans do not match up. It is believed that this is caused by the cathode jets changing location. From visual observation the bright attachment points tended to change back and forth between other points, but these changes happen slowly and occur between the same locations.
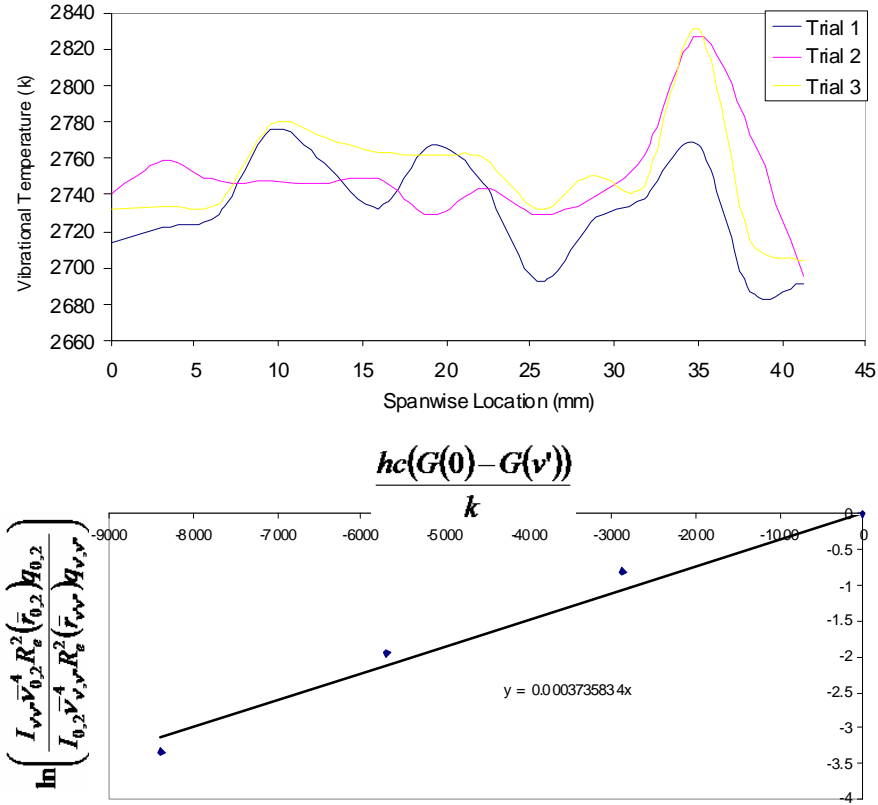


**Figure 170. Three Independent Vibrational Temperature Profiles for the Configuration Indicated in Figure 168 Along With the Boltzmann Plot**

Figure 173 gives the vibrational temperature plot corresponding to the rotational temperature plot in Figure 171. The maximum vibrational temperature of 3030 K is located close to the edge of the exposed electrode and is located in the same place as the maximum rotational temperature. The vibrational temperature decreases down to around 2600 K at the edge of the discharge. It is believed that the vibrational states are long lived which is the reason the vibrational temperatures do not drop to room temperature at the edge of the discharge.
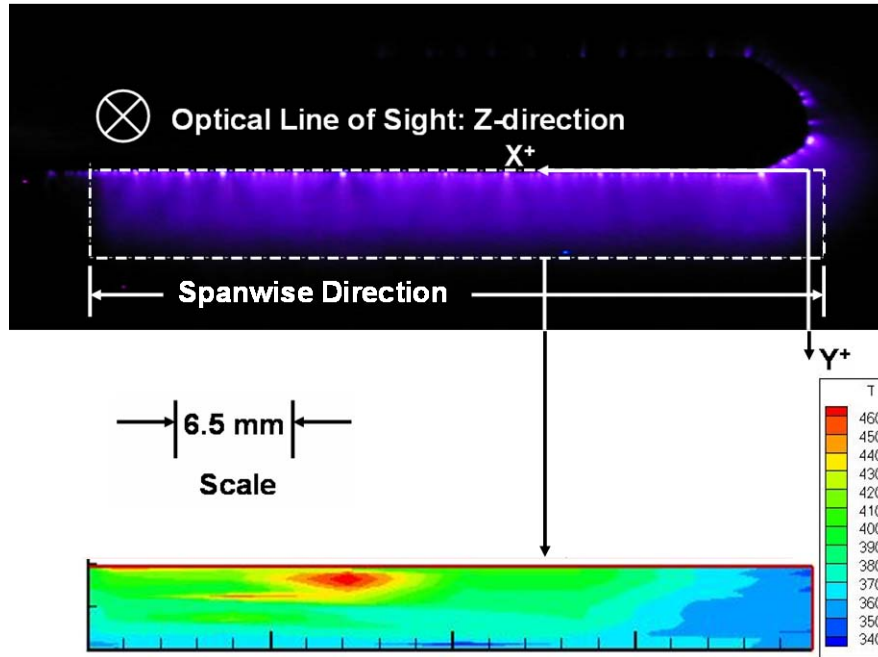
**Figure 171. The Rotational Temperature Profile for the Dashed Box as Indicated with The White Dashed Line in the ASDBD Picture Above. The Line-Of-Sight of the Measurements Is Perpendicular to the Electrodes**

## 5.1.6 Summary

The rotational and vibrational temperature profiles averaged over an entire voltage cycle for the discharge region of a dielectric barrier discharge have been obtained. The rotational temperatures have a periodic variation in the spanwise direction of the ASDBD, which we believe matches up with the bright spots of the discharge. These spots move, thus it is difficult to make a one-to-one correlation. This along with PIV results indicate the presence of localized cathode jets originating at the edge of the exposed electrode at various locations. These jets would explain the higher rotational and vibrational temperatures seen in the regions of these spots. The fluctuations of the vibrational temperatures corresponded directly to the fluctuations of the rotational temperature. The maximum rotational temperatures are located at the edge between the exposed and buried electrode and have a value around 400 K and decrease with distance from this edge to a value of 310 K. The maximum vibrational temperatures occur in the same location and have values ranging from 6000-6200 K with the minimum vibrational temperature being 5700 K. The population of the vibrational energy levels deviates somewhat from a Boltzmann distribution.
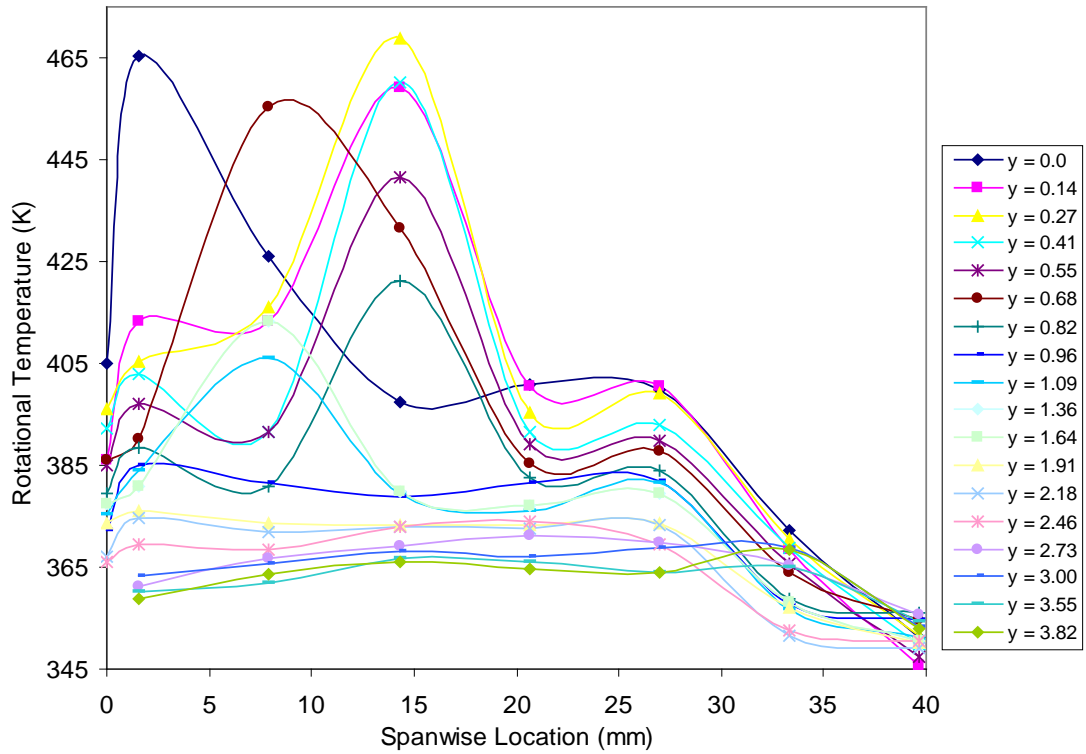
**Figure 172. Line Plots of the Rotational Temperatures as a Function of Spanwise and Flow Direction**
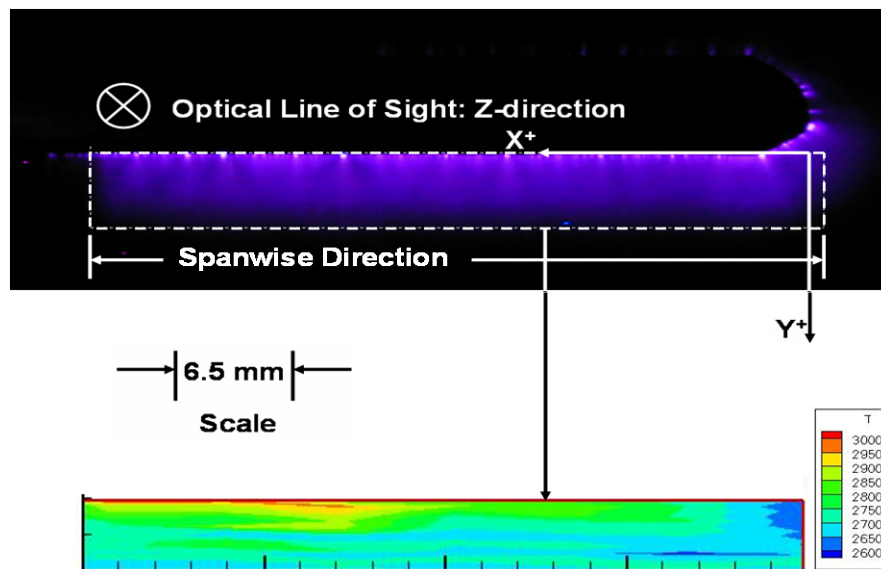


**Figure 173. The Vibrational Temperature Profile Corresponding To the Rotational Temperature Profiles in Figure 171**

## 5.2 Half Cycle Rotational Temperatures, Vibrational Temperatures, and Relative Concentrations of $N_2(C^3\pi_u)$ and $N_2^+(B^2\Sigma_u^+)$

### 5.2.1 Introduction

In this section, spatially resolved rotational and vibrational temperatures and relative concentrations of the $N_2(C^3\pi_u)$ and $N_2^+(B^2\Sigma_u^+)$ states for the negative voltage half-cycle (the exposed electrode is the cathode) and positive voltage half-cycle (the exposed electrode is the anode) for a sinusoidal voltage waveform are presented. The results presented are of higher temporal resolution than those presented in Section 5.1. Thus more detailed information is provided by these measurements than those in Section 5.1. This also means that additional understanding of the ASDBD can be obtained. In this work peak-to-peak voltages of 8,900, 11,700, 12,300, and 14,100 volts and a frequency of 3000 Hz are used. A smaller frequency is used in Section 5.2 than Section 5.1 because of limitations on the speed of the optical chopper used.

### 5.2.2 Experimental Facility

#### 5.2.2.1 Asymmetric Surface Dielectric Barrier Discharge

The ASDBD used in this work is the same as that used in the full cycle work of Section 5.1. This ASDBD is shown in Figure 161. A discharge is established over the encapsulated electrode by placing an oscillating voltage between the two electrodes. In this work four different peak-to-peak voltages of a sinusoidal form with a frequency of 3000 Hz are used. These are different settings than those used for the measurements in Section 5.1.

#### 5.2.2.2 Collection Optics and Spectroscopic System

The collection optics used in this section is different than that used in Section 5.1. Figure 174 shows this optical collection system which channels the emitted radiation from the ASDBD to the spectrometer. The emitted radiation from the ASDBD is collected by a fused silica bi-convex lens with an effective focal length of 35 mm. The collected radiation is focused onto a fiber optic bundle. An aperture is adjusted at the focal plane so that the diameter of the collected signal is smaller than the slits of the chopper blade. The aperture diameter was set at 2.0 mm. The purpose of the optical chopper is to block radiation from one half of the voltage cycle, only allowing radiation from the other voltage half-cycle to reach the spectrometer.

The fiber optic bundle, Acton 2756 spectrometer, and Andor DU 440-BU CCD camera are the same as described in Section 5.1. The calibration of the spectral system is also described in Section 5.1.

The experimental set-up is shown in Figure 175. The model is mounted vertically on a *xy*-translating stage. The translating stage consists of two Newport M-443 series linear stages connected together with a Newport 360-90 bracket. The desired positioning is obtained in both directions by adjusting a Newport SM-50 micrometer which has a maximum travel of 50.8 mm. The experiment is housed within a ventilated box lined with black flocked paper to reduce the signal contribution from background lighting.

The spatial resolution (i.e. the dimensions of the emitting volume collected by the optics) was obtained by shining an expanded laser beam through the backside of the optical fiber. The collection volume, shown in Figure 174, has dimensions of A $\approx$ 1.0 mm and B $\approx$ 1.7 mm. The

dimensions of the collection volume are essential for understanding the measured results because each measurement represents the averaged value of the measured quantity over the emitting region within the collection volume.
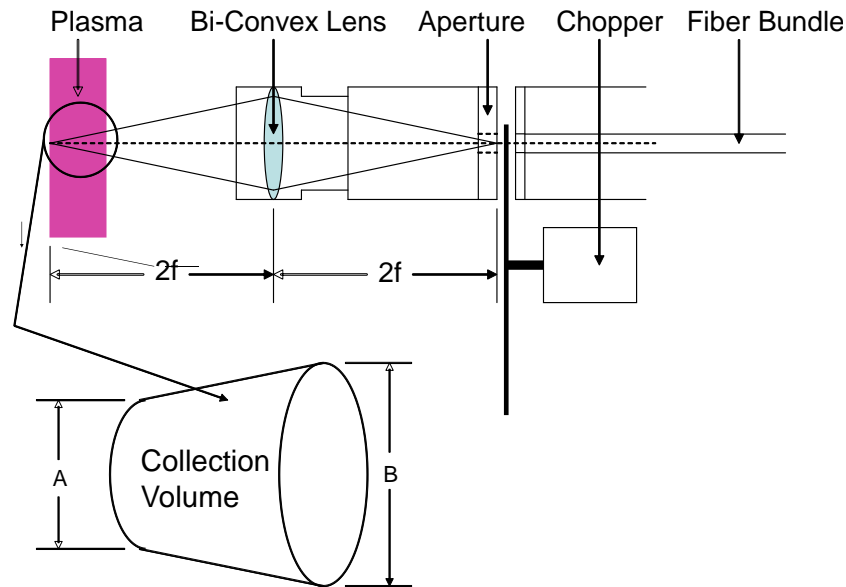


**Figure 174. Optical Collection System**
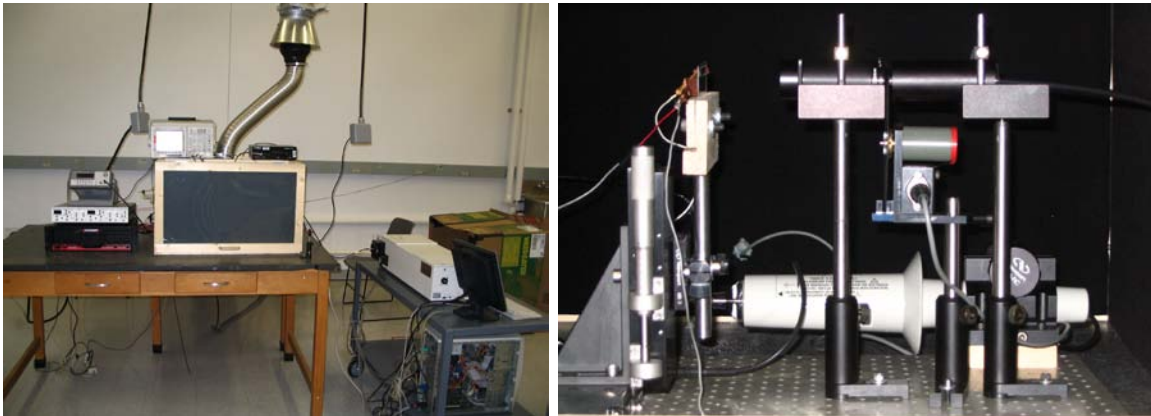


**Figure 175. The Left Figure Shows the Overall Experimental Set-Up. The Right Figure Shows the Optics and Other Components Housed Within the Box**

### 5.2.2.3 Voltage and Current Measurement Technique

The voltage output from an SI model 300 CD optical chopper is used to trigger an Agilent 33220A function generator. The voltage waveform from the function generator is sent to a Crown CE1000 power supply via a BNC connection. The voltage output from the power supply is further amplified with a Corona Magnetics Inc CMI-5012 step-up transformer. The transformer is directly attached to the ASDBD and is capable of delivering up to 20kV at 5 kHz. The voltage waveform is measured using a Tektronix P6015A high voltage probe and is connected to a Tektronix TDS 3034B oscilloscope with a BNC cable. The high voltage probe is capable of measuring peak-to-peak voltages up to 20kV and has a bandwidth of 75 MHz. The discharge current is obtained by measuring the voltage drop across a 100 Ohm resister with a

Tektronix P6139A probe. Both probes are designed for the oscilloscope and have been properly compensated. Example voltage and current profiles are given in Figures 176 and 177.
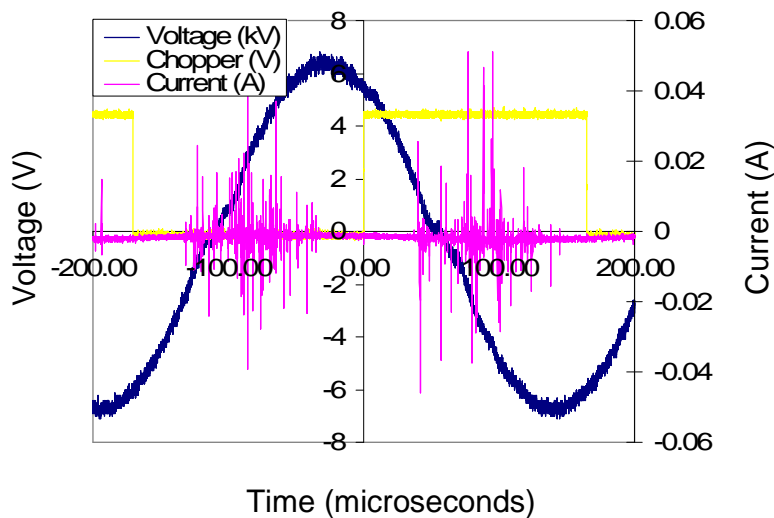


**Figure 176. Voltage and Current Characteristics of the ASDBD. Chopper is Blocking the Positive Half-Cycle**
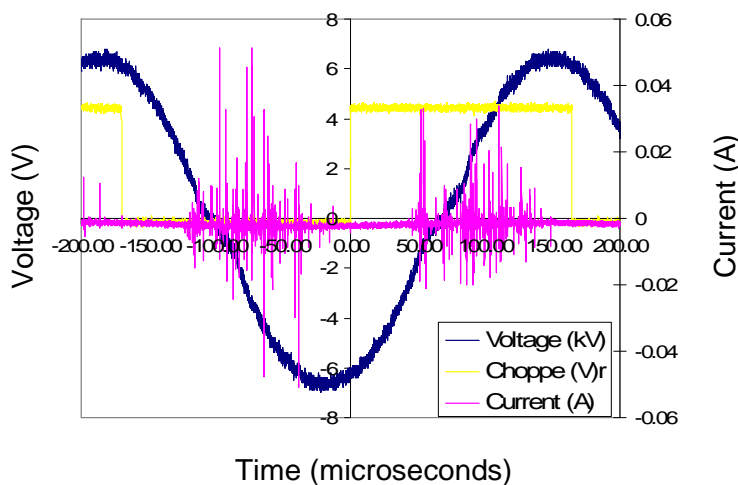


**Figure 177. Voltage and Current Characteristics of the ASDBD. Chopper is Blocking the Negative Half-Cycle**

### 5.2.3 Data Reduction Technique

A line-by-line code called N2SPECFIT (Williamson and DeJoseph, 2003) was used to fit the measured spectra. The fitting parameters determined by the code are the number density of the upper vibrational state for each band and the rotational temperature of each electronic band system (Williamson and DeJoseph, 2003; Stanfield et al., 2005). The code assumes the rotational energy levels of each separate electronic band system are described with a Boltzmann distribution; however, no assumption about the vibrational distribution is made. The vibrational upper state number densities and rotational temperatures are obtained from a two temperature non-linear least squares fit of the measured 0-3, 1-4, 2-5, 3-6 and 4-7 vibrational transitions of

$N_2(C^3\pi_u \to B^3\pi_g)$ and the 0-0 and 1-1 vibrational transitions of $N_2^+(B^2\Sigma_u^+ \to X^2\Sigma_u^+)$. The upper state number density of the excited electronic level is obtained by summing up the populated upper state vibrational number densities. Figure 178a shows the fit to spectra measured from the negative half-cycle and Figure 178b shows the fit for spectra measured from the positive half-cycle. The uncertainty of the measured relative vibrational upper state number densities is determined from the statistical parameter called reduced chi squared, which is a measure of how well the measured spectra were fit. The uncertainty ranges from 5 to 10% for all data presented in this subsection of this report.
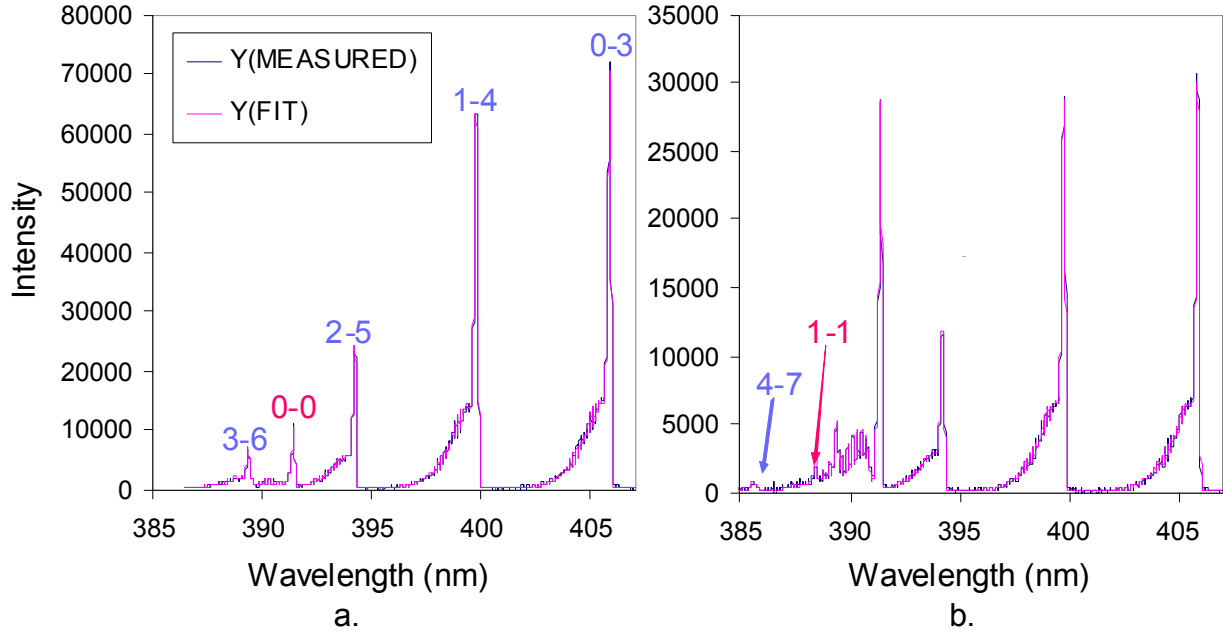


**Figure 178. Figure 178a Shows the Measured and Fit Spectra for the Negative Half-Cycle and Figure 178b Shows the Measured and Fit Spectra for the Positive Half-Cycle. Vibrational Transitions Marked with Red Numbers Indicate Vibrational Bands for the $N_2^+$ $\left(B^2\Sigma_u^+ \to X^2\Sigma_g^+\right)$ Electronic Band System and Vibrational Transitions Marked with Blue Numbers Indicate Vibrational Bands for the $N_2(C^3\Pi_u - B^3\Pi_g)$ Band System**

The Boltzmann plot method was applied to the 0-3, 1-4 and 2-5 vibrational transitions of the $C^3\Pi_u - B^3\Pi_g$ electronic band system of $N_2$ to obtain the vibrational temperatures. The Boltzmann distribution for the vibrational energy levels is given as

$$\frac{N_{v'}}{N} = \frac{\exp\left(-\frac{G(v')hc}{kT_{vib}}\right)}{Q_v}$$

(197)

where $N$ is the number density, $v'$ is the upper vibrational state quantum number, $h$ is Plank's constant, $k$ is Boltzmann's constant, $c$ is the speed of light, $Q_v$ is the vibrational partition function, $T_{vib}$ is the vibrational temperature, and $G(v')$ is the energy of the upper vibrational state and is given by equation (192).

The spectral response of the spectroscopic system has been accounted for with a relative calibration which means that the measured spectral transitions need to be taken relative to another measured transition. In this work, the population distribution is relative to the $v'=0$ energy level. The fraction of $N_{v'=0}$ is given as

$$\frac{N_{v'=0}}{N} = \frac{\exp\left(-\dfrac{G(v'=0)hc}{kT_{vib}}\right)}{Q_v}.$$

(198)

Dividing equation (197) by equation (198) gives

$$\frac{N_{v'}}{N_{v'=0}} = \exp\left[(G(v'=0)-G(v'))\frac{hc}{kT_{vib}}\right].$$

(199)

Taking the natural logarithm of both sides of equation (199) results in an equation of a line in the form $y = mx$,

$$\ln\left(\frac{N_{v'}}{N_{v'=0}}\right) = \frac{1}{T_{vib}}\frac{(G(v'=0)-G(v'))hc}{k}.$$

(200)

The vibrational temperature is determined by plotting $\ln\left(\dfrac{N_{v'}}{N_{v'=0}}\right)$ versus $\dfrac{(G(v'=0)-G(v'))hc}{k}$ and

setting the slope equal to $\dfrac{1}{T_{vib}}$. The error in measuring the vibrational temperature is determined by summing the contribution to the error from the uncertainty of the measured concentrations and the uncertainty of the slope obtained from a least squares fit of the data. The uncertainty associated with measuring the upper state number density ($N_{v'}$) was determined by tracking the sensitivity of this quantity within equation (200) using an uncertainty analysis. The smallest and largest error in vibrational temperatures for all the data presented in this section is ±240 and ±366 K, respectively.

Note that the vibrational temperature determination given in this portion of the report is equivalent to that shown in Section 5.1. This section provides a slightly simpler perspective of this calculation.

### 5.2.4   Results

For the measurements shown in this subsection of this report the ASDBD was run for 20 minutes for each voltage setting before any data was taken to ensure a quasi-steady operational state. Data was taken with respect to the coordinate system defined in Figure 161. The region of interest within the ASDBD was limited to the interior region to eliminate end effects. The optical line of sight for all measurements was in the $z$-direction of Figure 161 (going into the page). Error bars are left off all figures to improve visual clarity, but are reported in the description of each figure.

Figure 179 gives the rotational temperatures obtained from the $N_2(C^3\Pi_u \to B^3\Pi_g)$ electronic band system along the gap at $y = 0.0$ for both voltage half-cycles and peak-to-peak voltages of 12,300 and 14,100 volts. The maximum temperature obtained is approximately 350 K and corresponds

179

to the negative half-cycle at 14,100 volts. Error bars for all rotational temperatures reported for the $N_2$($C^3\Pi_u \rightarrow B^3\Pi_g$) electronic band system have a range of $\pm$ 7-15 K. It is therefore noted that the rotational temperature of the neutrals for both half-cycles and both voltages are the same within experimental accuracy.
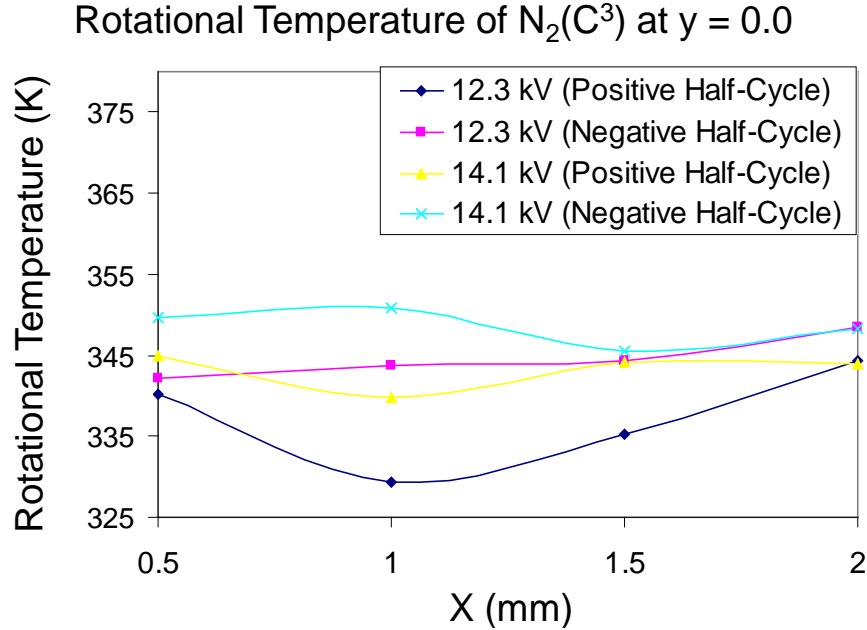


**Figure 179. Rotational Temperatures Obtained from the $N_2$($C^3\Pi_u \rightarrow B^3\Pi_g$) Transition Along the Gap Between the Electrodes**

Figure 180 gives the rotational temperatures obtained from the $N_2^+$($B^2\Sigma_u^+ \rightarrow X^2\Sigma_g^+$) electronic band system along the gap at $y = 0.0$ for both voltage half-cycles and peak-to-peak voltages of 12,300 and 14,100 volts. It is immediately noted that the rotational temperature of the excited ion is around 200 K greater for the negative half-cycle than the positive half-cycle. It also noted that the rotational temperature of the excited ions is around 250 K greater than the rotational temperature of the excited neutrals for the negative half-cycle and 70 K greater for the positive half-cycle. The good agreement of the fits for both electronic band systems (see Figure 178) indicates that the rotational energy levels of both band systems are well described by their own separate Boltzmann distributions. Error bars for all rotational temperatures obtained for the $N_2^+$ ($B^2\Sigma_u^+ \rightarrow X^2\Sigma_g^+$) electronic band system reported have a range of $\pm$ 15-25 K.
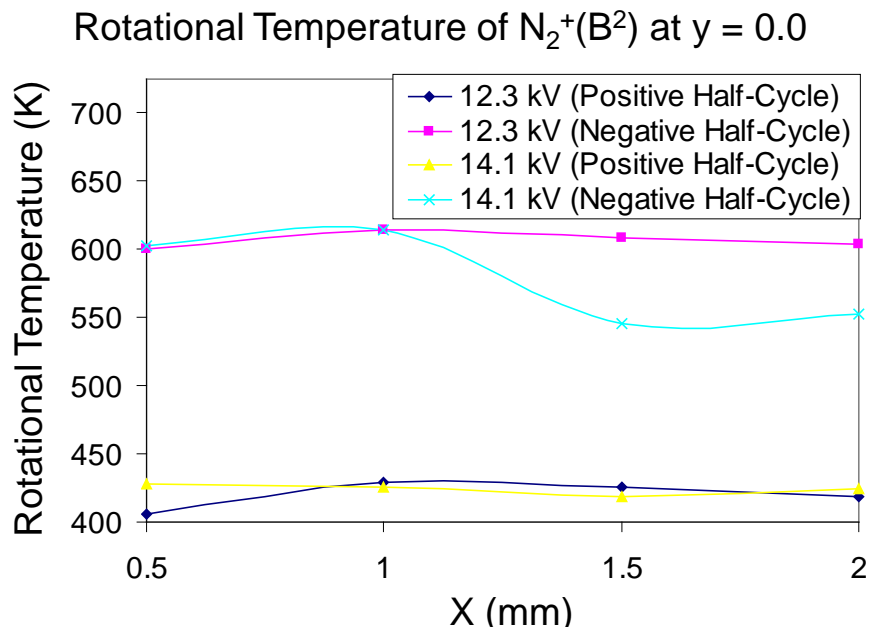
Figure 180. Rotational Temperatures Obtained from the $N_2^+\left(B^2\Sigma_u^+ \rightarrow X^2\Sigma_g^+\right)$ Transition Along the Gap Between the Electrodes
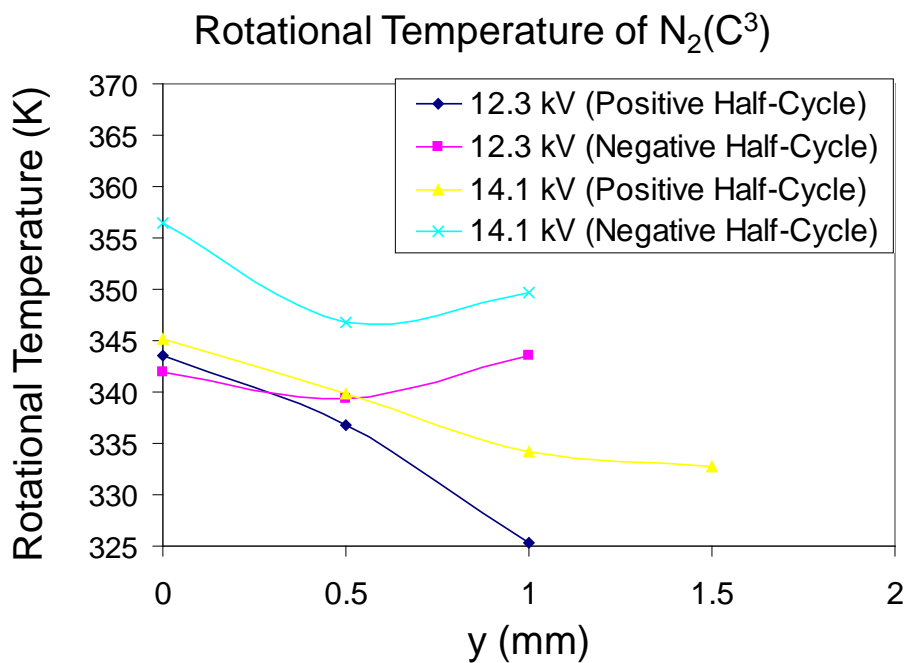


Figure 181. Rotational Temperatures Obtained from the $N_2(C^3\Pi_u \rightarrow B^3\Pi_g)$ Transition in the $y$-Direction

In Figure 181, rotational temperatures for the excited neutrals are obtained for both voltage half-cycles and peak-to-peak voltages of 12,300 and 14,100 volts. The rotational temperatures are at a maximum in the gap at $y = 0.0$ and are observed to decrease in the $y$-direction for the positive half-cycle. During the negative half-cycle, the temperature decreases in the $y$-direction until $y \approx$ 0.5 mm and then increases.

181

Figure 182 shows the rotational temperatures for the excited ions decreasing rapidly in the $y$-direction for the negative half-cycle, but remaining relatively constant during the positive half-cycle. It is also noted that it appears the ion temperature of the negative half-cycle decreases below the ion temperature of the positive half-cycle at $y \approx 1.0$ mm. Data points at greater $y$-coordinates could not be obtained because of signal drop off.

## Rotational Temperature of $N_2^+(B^2)$
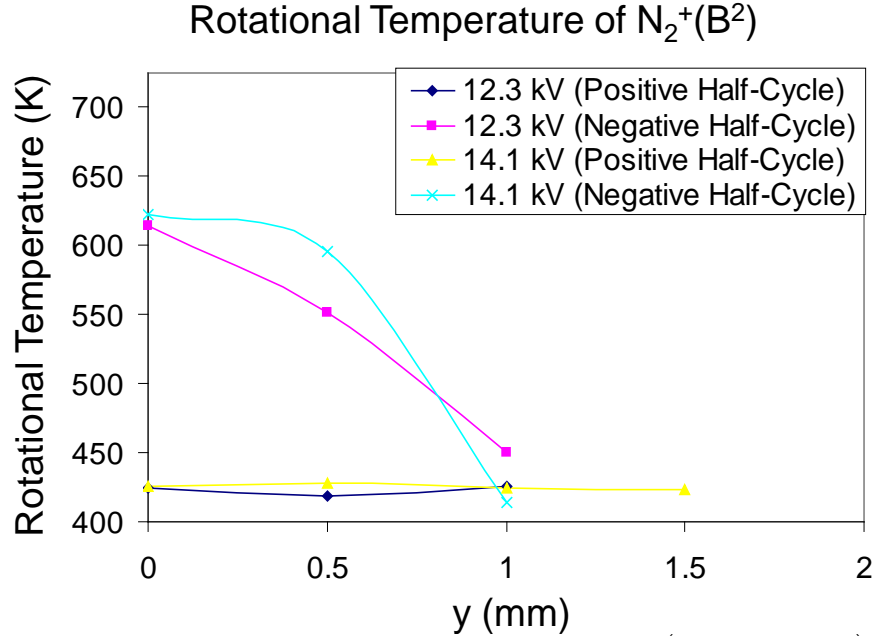


**Figure 182. Rotational Temperatures Obtained from the $N_2^+\left(B^2\Sigma_u^+ \rightarrow X^2\Sigma_g^+\right)$ Transition in the $y$-Direction**

The rotational temperatures presented in Figures 179 through 182 show observable differences in the rotational temperatures during the negative and positive voltage half-cycles. It is believed that the mechanisms responsible for the rotational temperature during the negative half-cycle are different than those occurring during the positive half-cycle. In particular, the difference in rotational temperature obtained from the two electronic transitions during the negative voltage half-cycle appear to result from the preferential production of $N_2^+(B^2\Sigma_u^+)$ within the inner electrode gap (where the exposed and encapsulated electrode meet) whereas $N_2(C^3\pi_u)$ was produced throughout the entire discharge. The gas temperature of the inner electrode gap, which is assumed to be in equilibrium with the rotational temperature, was determined to be elevated due to the presence of cathode spots. The rotational temperature of $N_2^+(B^2\Sigma_u^+)$, which was around 600 K, represents the region within the discharge containing the cathode spots, whereas the rotational temperature of $N_2(C^3\pi_u)$, which was around 340 K, represented the bulk gas temperature of the discharge. Detailed concentration measurements presented later in this section will provide further evidence of the plausibility of this explanation. During the positive voltage half-cycle, the temperature difference can be explained in terms of the dynamics and structure of the discharge. An overview of the structure and dynamics of the cathode-directed streamers occurring during the positive voltage half-cycle can be found in Pancheshnyi et al. (2000, 2001, 2003, 2005). In summary, cathode-directed streamers propagate very rapidly in the form of an ionization wave on the order of $10^6$-$10^7$ m/s by the process of photoionization. It is composed of a streamer head, where most of the voltage is dropped, and a streamer channel. The streamer

head has a positive net charge and is characterized by a highly nonuniform local electric field. Results obtained using cross-correlation spectroscopy have shown that the emission of the $N_2^+(B^2\Sigma_u^+ \to X^2\Sigma_u^+)$ electronic band system from a cathode-directed streamer occurs first with emission from the $N_2(C^3\pi_u \to B^3\pi_g)$ electronic band system lagging behind by ~0.3 ns (Kozlov et al., 2001; Shcherbakov and Sigmond, 2007). Emission of the $N_2^+(B^2\Sigma_u^+ \to X^2\Sigma_u^+)$ electronic band system therefore occurs somewhere near the front of the streamer head; whereas the emission of the $N_2(C^3\pi_u \to B^3\pi_g)$ electronic band system, given the speed of the streamer head and the lag in emission, occurs on the order of 0.3-3 mm behind the streamer head. Based on this information, the proposed mechanism for the deviation in rotational temperature of the ion and neutral during the positive voltage half-cycle is caused by the presence of a large temperature gradient that stretches from the front of the streamer head to 0.3-3 mm behind the streamer head. Emission of the $N_2^+(B^2\Sigma_u^+ \to X^2\Sigma_u^+)$ electronic band system occurs where the gas temperature is elevated (near the front of the streamer head); whereas emission of the $N_2(C^3\pi_u \to B^3\pi_g)$ electronic band system occurs where the gas temperature is lower. The mechanisms for why the temperature is large at the streamer head are not completely understood. A possible mechanism includes energy deposition in the positive space charge in the streamer head. It is also not entirely understood why emission from the $N_2^+(B^2\Sigma_u^+ \to X^2\Sigma_u^+)$ electronic band system lags behind emission from the $N_2(C^3\pi_u \to B^3\pi_g)$ electronic band system given that the production channels are the same and the energy requirement to produce $N_2^+(B^2\Sigma_u^+)$ is much greater than that needed to produce $N_2(C^3\pi_u)$.

For the vibrational temperature results shown in this section the ASDBD was run for 20 minutes at a voltage setting 11,800 V before any data was taken to ensure a quasi-steady operational state. The region of interest within the ASDBD was limited to the interior region to eliminate end effects. The optical line of sight for all measurements was in the z-direction of Figure 161 (going into the page). The data points of each profile were taken as a single set and each set was taken twenty times. The data displayed is the average over the twenty points within the sample. The error bars displayed on all the figures are the precision uncertainty of the sample with a 95% confidence interval.

Figure 183 shows the measured distribution of the $N_2(C^3\pi_u)$ vibrational manifold versus the linear least squares fit for the positive and negative voltage half-cycles. The distributions for both voltage half-cycles deviate approximately the same amount from a Boltzmann distribution; however, the deviation is small and the vibrational manifold of $N_2(C^3\pi_u)$ can be approximated by a Boltzmann distribution enabling the use of a vibrational temperature.
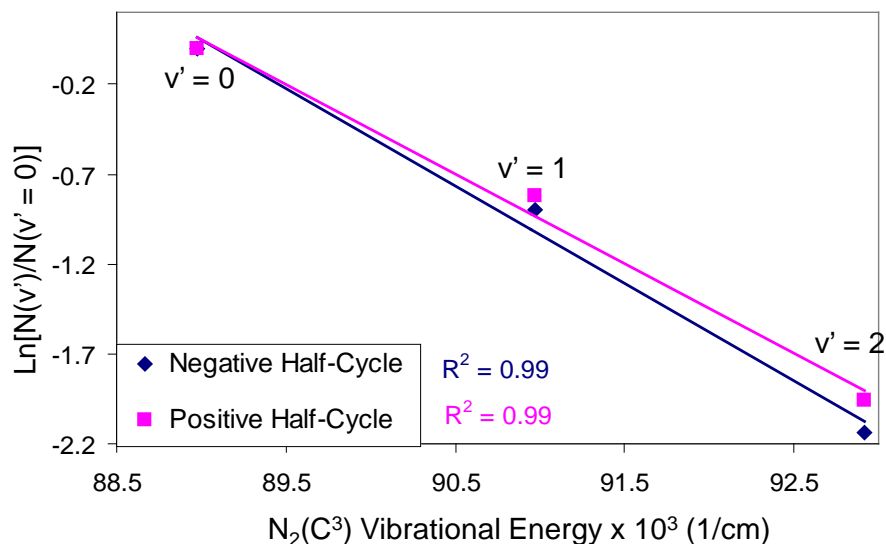
Figure 183. The Best-Fit Boltzmann Distribution of the Measured Vibrational Manifold of the $N_2(C^3\pi_u)$ Vibrational Energy Levels for the Positive and Negative Voltage Half-Cycles. The Vibrational Quantum Number is Indicated above the Measured Point
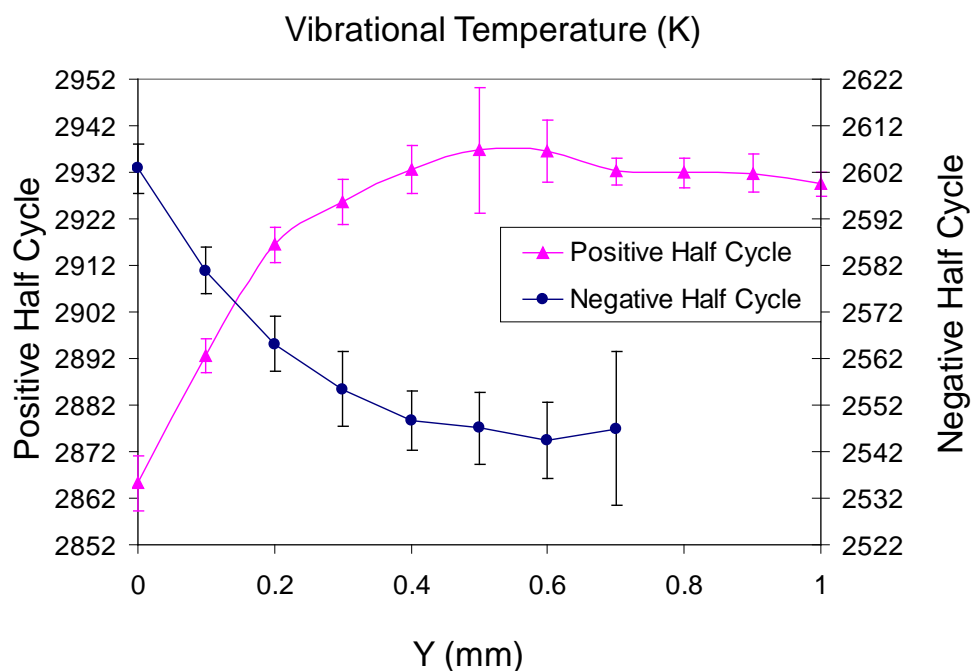


Figure 184. Vibrational Temperature Profiles for the Positive and Negative Voltage Half-Cycles versus Y-Direction for a Peak-To-Peak Voltage of 11,800 Volts

The vibrational temperature profiles for the negative and positive voltage half-cycles versus y-coordinate (induced flow direction) at a voltage of 11,800 volts are shown in Figure 184. Results show that during the negative voltage half-cycle the vibrational temperature starts out at a maximum at 2600 K within the inner electrode gap and then decreases to a minimum of 2530 K in the y-direction. This gives some indication to how the electron energy distribution function (EEDF) behaves as a function of the y-coordinate. The vibrational temperature during the positive voltage half-cycle has a minimum value of 2860 K at the inner electrode gap, then

increases to a maximum of 2930 K at $y \sim 0.5$ and finally remains constant. Note that the behavior of the vibrational temperature during the two voltage half-cycles is inversely related.

For the concentration results shown in this section the ASDBD was run for 20 minutes for each voltage setting (8,900 V and 11,800 V) before any data was taken to ensure a quasi-steady operational state. The largest electronic upper state number density measured was used to normalize all the concentration data. This included the concentrations measured for both voltage settings and both electronic band systems. The region of interest within the ASDBD was limited to the interior region to eliminate end effects. The optical line of sight for all measurements was in the $z$-direction of Figure 161 (going into the page). The data points of each profile were taken as a single set and each set was taken twenty times. The data displayed is the average over the twenty points within the sample. The error bars displayed on all the figures are the precision uncertainty of the sample with a 95% confidence interval.

The relative concentrations of $N_2(C^3\pi_u)$ and $N_2^+(B^2\Sigma_u^+)$ versus $y$-coordinate for the positive voltage half-cycle are shown in Figure 185 for voltages of 8,900 and 11,800 volts. In Figure 185b, the relative concentration of $N_2(C^3\pi_u)$ is on the left axis and $N_2^+(B^2\Sigma_u^+)$ is on the right axis. The relative concentrations of the measured excited states are at a maximum at the inner electrode gap and then decrease in the $y$-direction. The profiles for $N_2(C^3\pi_u)$ and $N_2^+(B^2\Sigma_u^+)$ at 11,800 volts vary from one another, however, they are very similar for the 8,900 volt case. In particular, for the higher voltage case, the figure indicates that the relative concentration of $N_2(C^3\pi_u)$ decreases much slower than $N_2^+(B^2\Sigma_u^+)$. This is because of the difference in excitation energies of the two states. This provides some verification to the mechanism given for why the rotational temperature of $N_2^+(B^2\Sigma_u^+)$ is greater than $N_2(C^3\pi_u)$. Essentially, the emission characteristics of the ion during the negative voltage half-cycle are dominated by the ions in the inner electrode gap where the local gas temperature is elevated due to the presence of cathode spots; whereas the emission characteristics of the neutral are determined over a larger region of influence resulting in the average temperature of the neutral within the collection volume to appear smaller. Note that the characteristic dimension of the collection volume is ~1 mm which is large enough for this to occur.

Another important feature of Figure 185b is the difference in the profiles for $N_2^+(B^2\Sigma_u^+)$ at 8,900 volts versus 11,800 volts. From the figure it can be seen that the relative concentration at 11,800 volts is substantially higher, and more importantly the dependence in the $y$-direction is different near the inner electrode gap. The cause of this difference is as follows: strong cathode spots are present during the 11,800 volt case whereas weak cathode spots occur during the 8,900 volt case. The presence of strong cathode spots during the 11,800 volt case results in an elevated production of electrons via ion bombardment of the electrode. Equations

$$N_2\left(X^1\Sigma_g^+\right) + e \rightarrow N_2\left(C^3\Pi_u\right) + e \qquad E_{ex} = 11.2 \text{ eV} \tag{201}$$

and

$$N_2\left(X^1\Sigma_g^+\right) + e \rightarrow N_2^+\left(B^2\Sigma_u^+\right) + 2e \qquad E_{ex} = 18.6 \text{ eV} \tag{202}$$
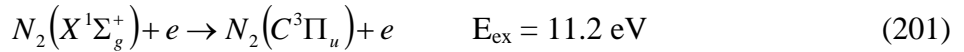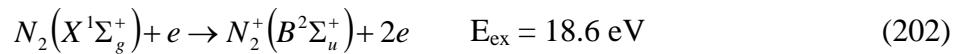
are statements of the production mechanisms for the $N_2(C^3\pi_u)$ and $N_2^+(B^2\Sigma_u^+)$ states. Extra electrons due to cathode spots will result in more $N_2(C^3\pi_u)$ and $N_2^+(B^2\Sigma_u^+)$. This alternative

185

production mechanism of electrons could have a profound effect on the cathode directed streamers produced during the positive voltage half-cycle because, at high frequencies, electrons produced during the negative voltage half-cycle will not have enough time to recombine resulting in some fraction of produced electrons left near the dielectric surface during the positive voltage half-cycle (Likhanskii et al., 2007). The dependence of streamer radius and propagation velocity of cathode-directed streamers on the number of seed electrons have been demonstrated by Pancheshnyi et al. (2001).

The effect on the discharge produced by the presence of strong and weak cathode spots can also be seen in Figure 186 which shows the ratio of the relative concentration of $N_2^+(B^2\Sigma_u^+)$ to $N_2(C^3\pi_u)$ for the negative voltage half-cycle. For the 8,900 volt case, the weak cathode spots result in the ratio decreasing linearly. The ratio for the 11,800 volt case takes on a much different functional dependence on the $y$-coordinate near the inner electrode gap. Given that the only production mechanisms of the excited states are those listed in equations (201) and (202), indicates that the EEDF must change rapidly with respect to the y-coordinate. In particular, the presence of the positive sheath which makes up the cathode spot, appears to produce a locally nonuniform electric field. The properties of the EEDF in the presence of a nonuniform electric field are given in Moratz et al. (1987). The results from Moratz et al. needed in this discussion are the following: in the presence of a nonuniform electric field, electrons within the high energy tail of the EEDF are most affected and can be increased by as much as an order of magnitude. This relationship is easily seen considering the electrons corresponding to the most probable energy of the EEDF are those which travel one mean free path between collisions. The electrons which make up the high energy tail of the EEDF travel more than one mean free path between collisions. It is these electrons which are affected the most by a nonuniform field because they have a longer distance to accelerate unhindered by collisions and thus reach greater velocities (higher energies). The result of an increase in the population of high energy electrons results in an increase in production of excited states, as is evident from our results.

The relative concentrations of $N_2(C^3\pi_u)$ and $N_2^+(B^2\Sigma_u^+)$ versus $y$-coordinate for the positive voltage half-cycle are shown in Figure 187 for voltages of 8,900 and 11,800 volts. Figure 187a shows the relative concentrations of both species on the same axis whereas Figure 187b shows the relative concentration of $N_2(C^3\pi_u)$ on the left vertical axis and $N_2^+(B^2\Sigma_u^+)$ on the right vertical axis. The concentration of each excited state, excluding $N_2(C^3\pi_u)$ at 11,800 volts, increases to a maximum and then decreases linearly in the positive y-direction.

The relationship of the ratio of the relative concentrations of $N_2^+(B^2\Sigma_u^+)$ with $N_2(C^3\pi_u)$ for the positive voltage half-cycle is given in Figure 188. The figure shows a larger concentration of $N_2(C^3\pi_u)$ compared to $N_2^+(B^2\Sigma_u^+)$ for 11.8 kV occurs within the inner electrode gap and then decreases in the positive $y$-direction.
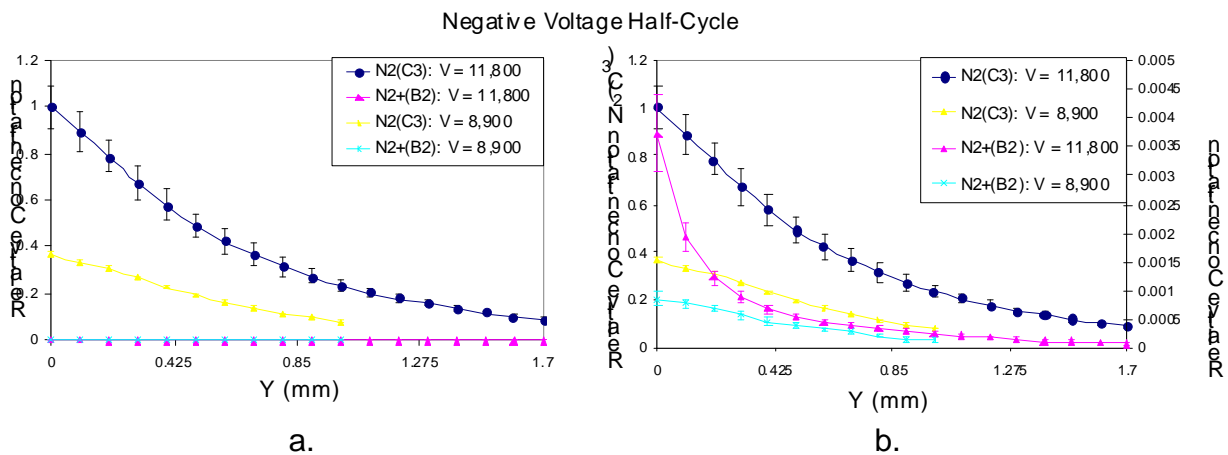
**Figure 185. Relative Concentration of $N_2^+(B^2\Sigma_u^+)$ and $N_2(C^3\pi_u)$ versus *y*-Coordinate (Induced Flow Direction) for the Negative Voltage Half-Cycle. In Figure 185a, the Relative Concentrations of Both Excited Species are on the Same Axis, whereas in Figure 185b, the Relative Concentration of $N_2(C^3\pi_u)$ is on the Left Vertical Axis and $N_2^+(B^2\Sigma_u^+)$ is on the Right Vertical Axis**
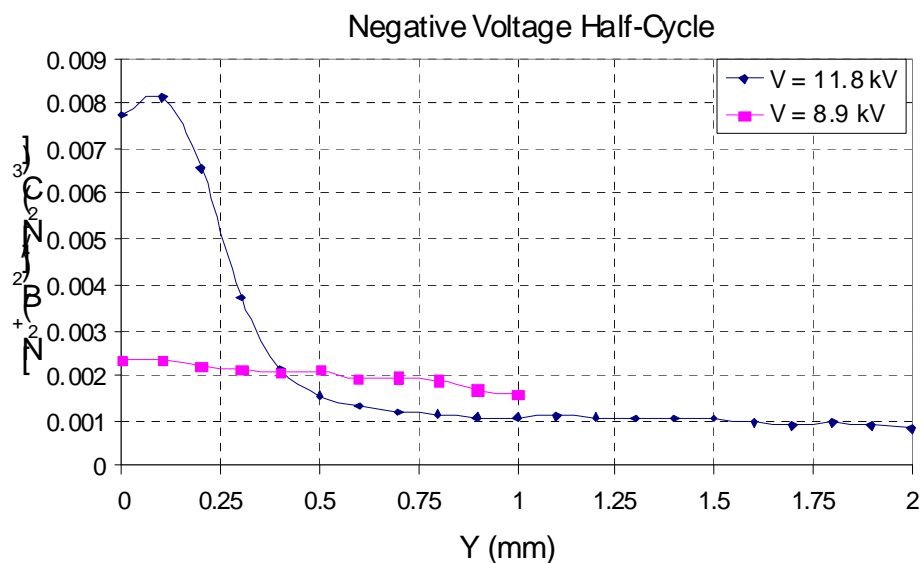


**Figure 186. Ratio of the Concentration of $N_2^+(B^2\Sigma_u^+)$ to $N_2(C^3\pi_u)$ versus *y*-Coordinate during the Negative Voltage Half-Cycle For Both Voltages**
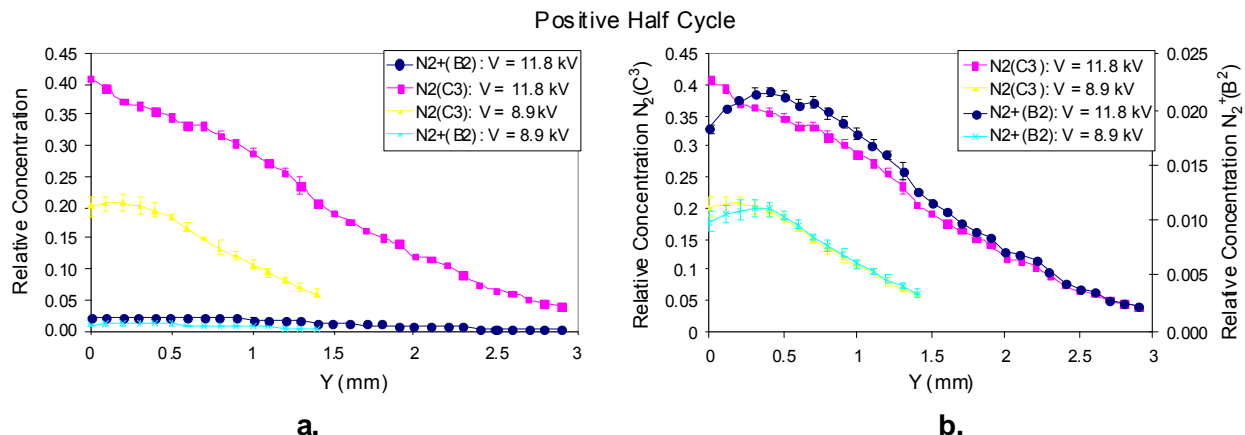
**Figure 187.  Concentrations of N₂(C³πᵤ) and N₂⁺( B²Σᵤ⁺ ) versus *y*-Coordinate (Induced Flow Direction) for the Positive Voltage Half-Cycle.  In Figure 187a, the Relative Concentrations of Both Excited Species are on the Same Axis, whereas in Figure 187b the Relative Concentration of N₂(C³πᵤ) is on the Left Vertical Axis and N₂⁺( B²Σᵤ⁺ ) is on the Right Vertical Axis**



**Figure 188.  Ratio of the Concentration of N₂⁺(B²Σᵤ⁺ ) to N₂(C³πᵤ) versus *y*-Coordinate during the Positive Voltage Half-Cycle for Both Voltages**

The relative concentrations of $N_2(C^3\pi_u)$ are shown for both voltage half-cycles and voltages in Figure 189. The figure shows that the relative concentration in the inner electrode gap is greater during the negative voltage half-cycle than the positive voltage half-cycle for both voltages. This changes downstream because the relative concentration drops off much more rapidly during the negative voltage half-cycle. The location at which the change occurs appears to be dependent on voltage. In particular, at 8,900 volts the change occurs at 0.6 mm and at 11,800 volts at 0.8 mm. The difference in the concentration profiles for the two voltage half-cycles is a direct consequence of the difference in the structure of the discharge during the two voltage half-cycles. Finally, the extent of the discharge in the *y*-direction is greater during the positive voltage half-cycle than the negative voltage half-cycle. The ratio of the relative concentrations of

$N_2(C^3\pi_u)$ during the negative voltage half-cycle and positive voltage half-cycle as a function of $y$-coordinate for both voltages is shown in Figure 190. The figure shows the greatest difference in relative concentration of $N_2(C^3\pi_u)$ occurs within the inner electrode gap and is greater during the negative half-cycle as opposed to the positive half-cycle.
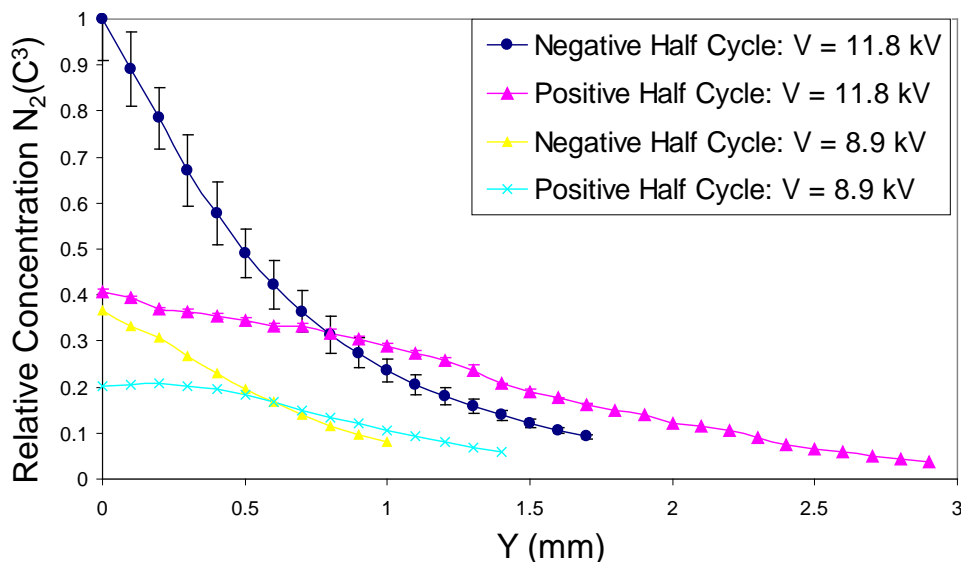


**Figure 189. Relative Concentration of $N_2(C^3\pi_u)$ versus $y$-Coordinate for Both Positive and Negative Voltage Half-Cycles**
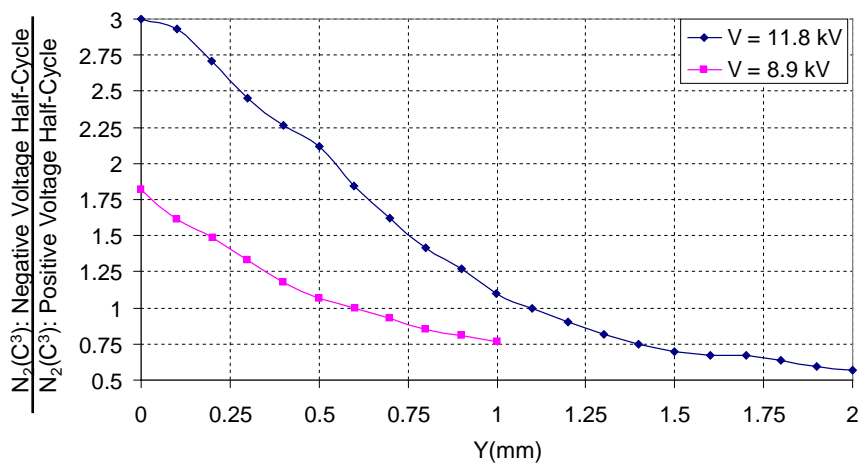


**Figure 190. Ratio of the Relative Concentration of $N_2(C^3\pi_u)$ during the Negative Voltage Half-Cycle to $N_2(C^3\pi_u)$ during the Positive Voltage Half-Cycle as a Function of $y$-Coordinate for 8,900 and 11,800 Volts**

The relative concentration of $N_2^+(B^2\Sigma_u^+)$ is shown for both voltage half-cycles and voltages in Figure 191. In Figure 191b the relative concentration during the positive voltage half-cycle is on the left vertical axis and the concentration during the negative voltage half-cycle is on the right vertical axis. During the positive voltage half-cycle, the relative concentration increases to a maximum and then decreases linearly whereas during the negative voltage half-cycle it appears to decrease exponentially in the presence of a strong cathode spot and linearly in the presence of

a weak cathode spot. The ratio of the relative concentration of $N_2^+(B^2\Sigma_u^+)$ during the positive voltage half-cycle and negative voltage half-cycle as a function of $y$-coordinate for both voltages is shown in Figure 192. The figure shows that there is more $N_2^+(B^2\Sigma_u^+)$ during the positive voltage half-cycle than during the negative half-cycle. The amount more is seen to increase from 1.6 at the inner electrode gap to ~100 at $y = 1.7$ mm for the 11,800 volt case and from ~15 at the inner electrode gap to ~48 for the 8900 volt case. The presence of cathode spots is seen to drive the ratio from 15 (weak cathode spots) down to 1.7 (strong cathode spots) at the inner electrode gap.

## 5.2.5 Summary

The rotational and vibrational temperatures along with the relative concentrations of $N_2^+(B^2\Sigma_u^+)$ and $N_2(C^3\pi_u)$ have been spatially resolved for the positive and negative voltage half-cycles for an asymmetric surface mode dielectric barrier discharge operating in air with a sinusoidal voltage at a frequency of 3000 Hz and varying peak-to-peak voltages.

Rotational temperatures were measured for peak-to-peak voltages of 12,300 and 14,100 volts. The rotational temperature of $N_2$ within the inner electrode gap is around 350 K for both half-cycles and both voltages. Variations with peak-to-peak voltage are within the experimental accuracy. The rotational temperature of $N_2^+$ during the negative half-cycle is approximately 200 K greater than during the positive half-cycle. The rotational temperature of $N_2$ during the negative half-cycle decreases in the induced flow direction and then increases. There may be some small effect of peak-to-peak voltages, but it is deemed to be unimportant. The rotational temperature of $N_2^+$ does the exact opposite; it increases up to the same inflection point as the neutral and then decreases. This might indicate energy transfer between the two species. For every location within the discharge during all voltage half-cycles the rotational temperature of $N_2^+$ was found to be significantly higher than the rotational temperature of $N_2$. It was noted that the spectra fits of the measured electronic band systems indicate the rotational energy levels of both systems are described with a Boltzmann distribution.

Measured vibrational temperatures are reported for peak-to-peak voltages of 11,800 volts. The vibrational temperature started at a maximum of 2600 K at the inner electrode gap and then decreased in the induced flow direction during the negative voltage half-cycle. The opposite behavior was observed during the positive voltage half-cycle. In particular, the vibrational temperature started at a minimum of 2800 K at the inner electrode gap and increased in the induced flow direction to a maximum of 3000 K.

During the negative voltage half-cycle, the relative concentration profiles of $N_2^+(B^2\Sigma_u^+)$ and $N_2(C^3\pi_u)$ were at a maximum at the inner electrode gap and then decreased exponentially for the 11,800 volt case and linearly for the 8,900 volt case. In addition, the relative concentrations of $N_2^+(B^2\Sigma_u^+)$ and $N_2(C^3\pi_u)$ increased by a factor of 6 and 1.8 from the 8,900 volt case to the 11,800 volt case within the inner electrode gap, respectively. The difference in the concentration profiles and the preferential increase in production of $N_2^+(B^2\Sigma_u^+)$ for the two different voltages was explained in terms of the presence of strong cathode spots during the 11,800 volt case and the presence of weak cathode spots during the 8,900 volt case.
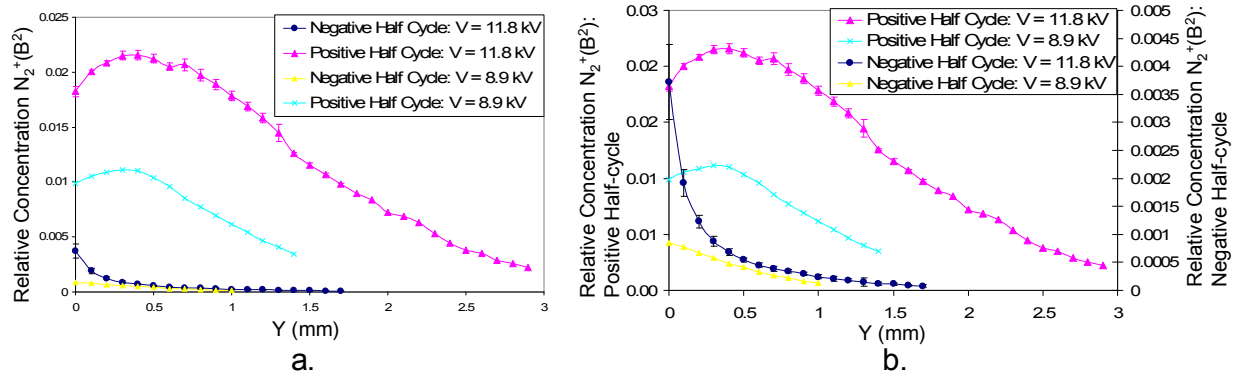
Figure 191. Relative Concentration of $N_2^+(B^2\Sigma_u^+)$ versus *y*-Coordinate for Both Positive and Negative Voltage Half-Cycles. In Figure 191a the Relative Concentrations of Both Voltage Half-Cycles Are on the Same Axis, Whereas in Figure 191b Relative Concentrations during the Positive Voltage Half-Cycle are on the Left Vertical Axis and the Relative Concentrations during the Negative Voltage Half-Cycle are on the Right Vertical Axis.
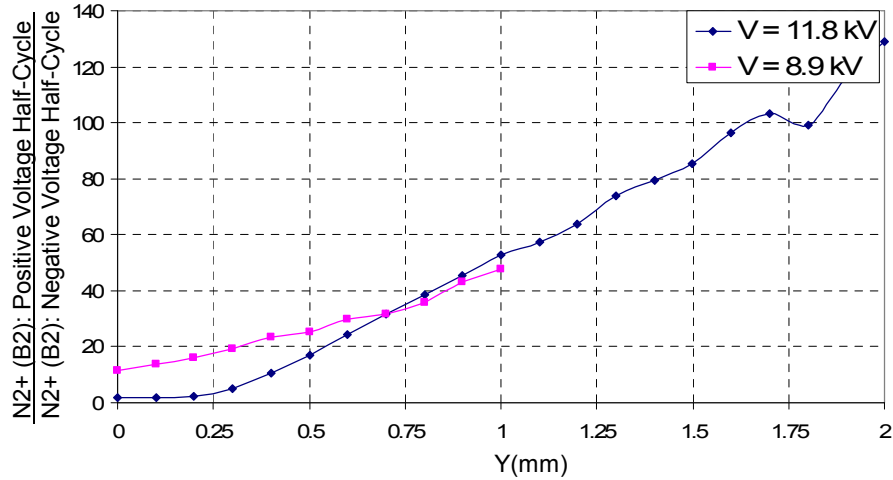


Figure 192. Ratio of the Relative Concentration of $N_2^+(B^2\Sigma_u^+)$ during the Positive Voltage Half-Cycle over $N_2^+(B^2\Sigma_u^+)$ during the Negative Voltage Half-Cycle as a Function of *y*-Coordinate for 8,900 and 11,800 Volts

During the positive voltage half-cycle, the relative concentration profiles of $N_2^+(B^2\Sigma_u^+)$ during both voltage cases and $N_2(C^3\pi_u)$ during the 8,900 volt case increased to a maximum at a location downstream of the inner electrode gap and then decreased linearly. The relative concentration profile of $N_2(C^3\pi_u)$ was at a maximum at the inner electrode gap and then decreased linearly during the 11,800 volt case.

Finally, the production of $N_2^+(B^2\Sigma_u^+)$ during the positive voltage half-cycle was on average 50 times greater than during the negative voltage half-cycle. The difference increased from 1.8 at the inner electrode gap to 130 downstream. The apparent increase in production in the induced flow direction is because the extent of the discharge is significantly greater during the positive voltage half-cycle than during the negative voltage half-cycle (on the order of 100% greater).

191

This is a direct consequence of the difference in discharge structure of the two voltage half-cycles.

## 6.0 SUPERSONIC FLOW CONTROL BY HEAT ADDITION

Section 6 of this report summarizes all the work performed under the contract Supersonic Flow Control by Heat Addition. The work is comprised of two main sections. The first study investigates the effect of energy deposition on pressure and thermal loads generated by an Edney IV interaction. This complex supersonic jet impingement problem is formed by the intersection of an oblique shock generated by a $15^o$ wedge with a Mach 3.45 bow shock in front of a 0.0254 m diameter sphere. The full three-dimensional Reynolds-Averaged Navier-Stokes equations are solved with the k-$\omega$ turbulence model. Mesh resolved simulations show that surface pressure without energy addition is in good agreement with experiments. The peak value is 1.8 times the observed value without the impinging shock. Results from a grid resolution study confirm that the surface pressure is less sensitive than the heat flux. For flow control, a spherical energy pulse with a volume of 3 mm$^3$ and energy of 283 mJ is deposited upstream of the primary triple point. The unsteady interaction of the energy spot and its induced blast wave with the oblique shock, the distorted bow shock and the impinging supersonic jet, is elucidated in the context of the "lensing" phenomenon. The simulations indicate significant impact of the energy deposition on the surface pressure and heat flux. The instantaneous surface pressure and heat flux rise when the blast wave and high energy spot hit the surface, and fall when the expansion waves reach the surface. However, the overall integrated stress and thermal loads are reduced, mainly due to the effect of the expansion waves.

The second part of Section 6 of this report investigates the flow instability induced by the thermal perturbation in a Mach 1.5 flat plate boundary layer. A high-resolution upwind-biased Roe method is used with the compressive Van Leer harmonic limiter on a suitably refined mesh. The dependence of flow stability characteristics on variation of the geometry of the thermal bump (shape and dimension) and the pulsing properties (the disturbance amplitude and frequency of the forcing) is assessed. The thermal bump generates two pairs of counter-rotating streamwise vortices. For a constant amplitude pulse, this disturbance decays downstream. When the boundary layer is expected to be unstable, pulsing causes vortex shedding to be observed and the streamwise vortices grow with downstream distance. Analysis of the integrated disturbance energy indicates that the streamwise kinetic disturbance energy dominates over those associated with the other two velocity and thermal components. Immediately downstream of the bump, the dominant frequency corresponds to that of the imposed excitation, while higher harmonic components are observed farther downstream. A preliminary analysis of the parametric variation of shape and dimensions indicate that a finite bump span is important to obtain three dimensionality and that the rectangular shape results in faster disturbance growth than the circular one. This study concludes that disturbance growth is non-linear with bump temperature.

### 6.1 Control of Shock Structures by Heat Addition

### 6.1.1 Introduction

Shock-on-shock interactions occurring in the vicinity of surfaces are of significant interest in the development of high-speed vehicles because of their profound impact on thermo-mechanical loading. For example, forebody shocks are designed to impinge on cowl lips to optimize mass capture in inlets, and often lead to catastrophic failure because of the shock-on-cowl lip interactions.

When an incident oblique shock impinges on a bow shock, one of six different interference patterns is possible according to the strength of the impinging shock and the location of the intersection point relative to the bow shock. Edney (1968) showed that the interference increases heating, which can result from one or more of the following mechanisms: shock/boundary-layer interaction, free shear layer attachment, and supersonic jet impingement. Of these patterns, the Edney IV interaction (see Figure 193) is one of the most striking: a supersonic jet is formed by the interaction of an incident oblique shock with a bow shock, resulting in a significant increase of heat fluxes and pressure in a concentrated region on the surface. The peak heat transfer can be several orders of magnitude higher than the ordinary stagnation heat transfer of an isolated body. Control of the formation and development of the supersonic jet can alleviate the heat transfer rate.
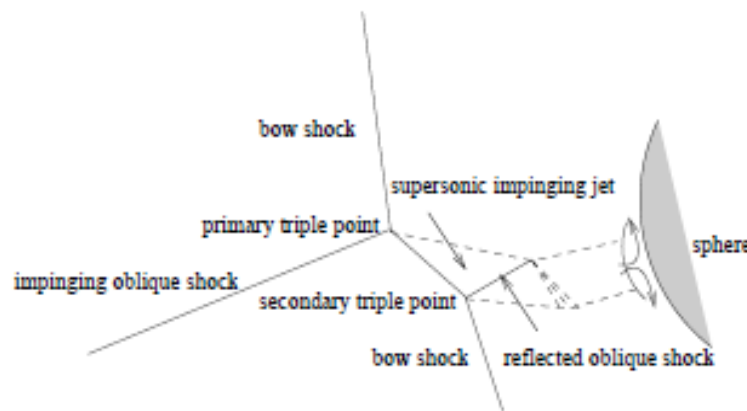


**Figure 193. Edney IV Interaction**

Several efforts by Adelgren et al. (2005), Kandala and Candler (2004), Kogan and Starodubtsev (2003), Gaitonde and Miller (2003), Trumble and Candler (2006), Wieting and Holden (1989), Yan and Gaitonde (2006) and Zhong (1994), have explored the structure and control of the Edney IV interaction by means of energy deposition and magnetogasdynamic force (MGD). Adelgren et al. (2005) performed a series of experiments, in which a single laser pulse was introduced upstream of a 3-D Edney IV interaction. The experiments demonstrated the effectiveness of laser-based energy deposition in the reduction of surface pressure: the instantaneous peak value was reduced by 30% compared to the value observed without energy deposition. Kandala and Candler (2004) performed a three dimensional simulation, wherein the Navier-Stokes equations incorporated with a plasma formation model and a chemical kinetics model were utilized to simulate a pulsed laser spot interacting with the Edney IV structures. The flow conditions were chosen to simulate the experiments performed by Adelgren et al. (2005). The peak surface pressure and heat transfer rate were reduced due to the change of shock structures caused by the interaction of the energy spot with the incident shock and blunt body shock. No quantitative comparison was made with the experiments by Adelgren et al. (2005). Kogan and Starodubtsev (2003) examined the effect of a continuous heat source which was added upstream of the interaction in a 2-D flow. The results indicated that the energy addition effectively reduced the instantaneous peak pressure and heat fluxes with only a very small fraction of the heat resulting in an increase in the integral heat fluxes. Gaitonde and Miller (2003) used electromagnetic forces to reduce heat loads on the surface by altering the structural form of the interaction and reducing the strength of the impinging supersonic jet under both

electrodeless and electrode-based conditions. Trumble and Candler (2006) conducted a simulation to understand the effect of laser energy deposition on an Edney IV interaction over a swept fin. The results showed that the laser energy deposition did not mitigate the localized heat flux in this configuration. Wieting and Holden (1989) conducted an experimental study of two-dimensional shock-wave interference heating on a cylindrical leading edge at Mach numbers of 6.3, 6.5 and 8.0. This study provided detailed pressure and heat flux distributions. Yan and Gaitonde (2006) performed a three dimensional simulation to reproduce the experimental results by Adelgren et al. (2005). The results on a relatively coarse grid indicated that the integrated pressure load was alleviated due to the impingement of the expansion wave onto the surface. Zhong (1994) conducted a two-dimensional numerical study on the Edney IV interaction at a Mach number of 8.0. The pressure and heat flux showed good agreement with the experiment by Wieting and Holden (1989). The inherent unsteadiness of the Edney IV interaction was demonstrated.

The objective of this research is to employ high-fidelity numerical simulations to reproduce recently obtained experimental observations and to elucidate the physics of the unsteady evolution of the flow field and surface loads due to pulsed energy deposition.

## 6.1.2 Experimental Conditions

Experimental efforts conducted in the Rutgers University Mach 3.45 supersonic wind tunnel have been detailed in Adelgren et al. (2005). The operating stagnation temperature and pressure are 290 K and $1.4 \times 10^6$ Pa, respectively. The Reynolds number based on the sphere diameter (0.0254 m) is $1.863 \times 10^6$. An Edney IV interaction is generated in the test section by the intersection of an oblique shock generated by a $15^o$ wedge mounted on the test section ceiling. The energy spot with a focal volume of 3 mm$^3$ and energy of 283 mJ is generated by focusing a pulsed Nd:YAG laser through a 250 mm focal length lens. The Nd:YAG laser is frequency doubled to a wavelength of 532 nm with a temporal pulse width of about 10 ns and a repetition rate of 10 Hz.

## 6.1.3 Numerical Methodology

The three-dimensional Reynolds-averaged Navier-Stokes equations are used to represent the flow field. The flow solver GASPex is used, wherein the third-order accurate Roe scheme with Harten correction (Roe, 1981) along with the Min-Mod limiter is employed in each direction for inviscid fluxes to suppress the "carbuncle" phenomenon and central second order differences are used for viscous terms. The fourth order Runge-Kutta scheme is used for the time integration. The effects of fine-scale turbulence are described by the k-ω turbulence model (Wilcox, 1998). The k-ω model predicts free shear flows well. In contrast to the k-ε models, the k-ω models solve the laminar subregion of the turbulent boundary layer without the introduction of additional new low Reynolds number terms or the use of a wall function.

The numerical model reproduces the experiment to the extent possible. A Mach 3.45 incoming flow forms a bow shock in front of a sphere with a diameter of 0.0254 m. The Reynolds number and the freestream stagnation values are extracted from the experiment (Adelgren et al., 2005) as described earlier. An incident oblique shock is generated by imposing jump conditions, this impinges onto the bow shock with a flow deflection angle of $15^o$. The Mach number behind the impinging shock is 2.57. The resulting interaction between the impinging and bow shocks results in the distortion of the bow shock and the formation of triple points.

The energy deposition region is in the shape of a narrowband, stretched in the laser incident direction (Kandala and Candler, 2004). However, this hot spot is highly distorted by the impinging shock before it reaches the interaction region as presented in the following section. Meanwhile, based on our previous study (Yan et al., 2003; Yan et. al. 2007c) the blast wave becomes spherical 5-10 μs after the pulse. Therefore, the initial energy pulse is assumed to be a sphere in the simulation. The spherical energy pulse with the same properties as the experiments (Adelgren et al., 2005) is added instantaneously upstream of the primary triple point with its center located in the z=0 plane, 1 sphere diameter upstream of the sphere, and 0.45 diameters above the x=0 plane. Because the pulse width of the laser is 10 ns, which is much smaller than the characteristic flow time scale ($D/U_\infty = 40$ μs), the energy deposited into the flow can be considered an instantaneous event. The inviscid perfect gas model assumes an initial Gaussian distribution for the static temperature in the spherical focal region of the laser pulse,

$$T = T_i + \Delta T_o \, e^{-r^2/r_o^2}$$
(203)

where $T_i$ is the temperature at the beginning of the energy deposition. The peak temperature rise $\Delta T_o$ is related to the total energy of the laser pulse $Q_T$ by

$$\Delta T_o = \frac{\epsilon_Q Q_T}{\pi^{3/2} r_o^3 \rho_i c_v}$$
(204)

where $r_o$ is chosen to be one-half of the radius $R_o$ of the focal volume $V_o = \frac{4}{3}\pi R_o^3$, $c_v$ is assumed constant, and $\rho_i$ is the density at the beginning of the energy deposition. The coefficient $\varepsilon_Q$ must be determined by comparison with experiment, and is expected to be a function of the laser energy pulse $Q_T$ and ambient conditions in the region of the energy deposition. The initial density in the focal region is assumed to be constant at the instant of energy deposition.

At the inflow boundaries, the flow vector is specified, which satisfies the Rankine-Hugoniot conditions appropriate to the impinging shock. The wall is assumed to be no-slip and isothermal at $T_w = 209$ K, which is lower than the recovery temperature. By convention, positive heat flux denotes the surface heating process, while negative values indicate surface cooling. At outflow boundaries, first-order extrapolation is applied because the flow is supersonic except very near the wall.

### 6.1.4  Comparison with Experiment

### 6.1.4.1  Grid Refinement

A well-defined and refined grid is required to accurately predict the surface pressure, heat flux, details of the shear layer instabilities, and shock-shock interaction structures near the surface. For an ideal non-reacting gas, several studies have been performed (Yan and Gaitonde, 2006) to establish resolution requirements to ensure that shear layer instability and surface loads are resolved. The structure of the grid employed is shown in Figure 194. Mesh clustering is enhanced in the region where high gradients are encountered, such as between the surface and the bow shock, and around the energy pulse.

**Figure 194. Grid Configuration**
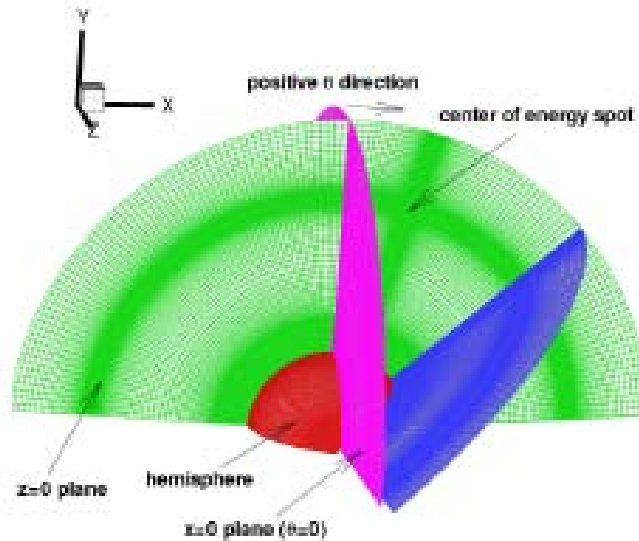
Since no theoretical or experimental data of peak heat flux in Edney IV interactions is available, the flow past a sphere is employed to determine the grid resolution within the shock stand-off distance. Van Driest's formula (Van Driest, 1956) for the heat flux at the stagnation point of a sphere is

$$q_{van} = 0.763 Pr^{-0.6} \sqrt{\rho_{02}\mu_{02}} \sqrt{\frac{2}{D}} [\frac{2(p_{02} - p_\infty)}{\rho_{02}}]^{1/4} c_p (T_{01} - T_w)$$

(205)

The subscripts 1 and 2 indicate the conditions before and after the normal shock, respectively, and $Pr = 0.72$. The Van Driest heat flux $q_{van}$ is 8.95x $10^4$ W/m$^2$ for the Mach 3.45 sphere case. For the steady state condition, the shock stand-off distance is obtained from the correlation by Billig (1967),

$$\Delta = 0.0715 D\, e^{3.24/M_\infty^2}$$

(206)

The peak surface pressure is the stagnation pressure behind the bow shock, which can be obtained through the Rayleigh supersonic pitot formula and is 2.53x$10^5$ Pa. The grid resolution is measured by the number of grid points within the shock stand-off distance ($\Delta$) and the ratio of the first grid spacing away from the surface and the diameter of the sphere ($\Delta r_1/D$) in the normal-wall direction. The number of grid points in the other two directions is fixed. Table 4 shows the properties of four different meshes and the comparison of the peak surface pressure and stagnation heat flux with the theoretical value. The spacing is varied by an order of magnitude. The pressure and heat flux are non-dimensionalized by the stagnation pressure and the Van Driest heat flux $q_{van}$ on the surface of the sphere, respectively. The study shows that the surface pressure is less sensitive to the grid resolution than the heat flux. The former is virtually unchanged with mesh resolution, while the latter varies from extremely low values to the expected value on the finer meshes. Both grid 3 and grid 4 show good comparison with the Van Driest heat flux with errors restricted to 10% and 7% of the theoretical value, respectively. Based on these studies, to reduce the computational expense, resolution constraints of grid 3 are

197

employed for the fine mesh, while the coarse grid employed in the Edney IV interaction case for exploratory studies is similar to that in grid 1. The coarse and fine grids have a total of 6 million and 17 million cells, respectively. Results will focus on those obtained on the fine grid.

### Table 4. Grid Refinement for a Sphere

| Grid | Grid points within $\Delta$ | $\frac{\Delta r_1}{D}$ | Peak surface pressure | Stagnation heat flux |
|---|---|---|---|---|
| 1 | 32 | $2.603 \times 10^{-3}$ | 0.99 | 0.040 |
| 2 | 94 | $4.850 \times 10^{-4}$ | 1.00 | 0.780 |
| 3 | 114 | $3.235 \times 10^{-4}$ | 1.00 | 0.90 |
| 4 | 154 | $1.617 \times 10^{-4}$ | 1.00 | 0.93 |

### 6.1.4.2 Baseline Edney IV Interaction

The baseline simulations are described first. In the following, the plotted temperature is normalized by the theoretical adiabatic wall temperature, and the pressure and density are normalized by the theoretical stagnation values behind a Mach 3.45 bow shock. Furthermore, in all three-dimensional contour plots, the temperature and Mach number contours on the hemisphere are shown on the first grid plane away from the surface, while other variables are shown on the surface. Figure 193 displays the basic structures of the Edney IV interaction shock pattern. Two three-shock $\lambda$-patterns are observed at their corresponding triple point. The first $\lambda$-pattern is generated by the interaction of an impinging oblique shock with a bow shock. A strong vortex sheet emanates from the primary triple point. A second $\lambda$-pattern is observed at the intersection between the reflected shock and the continuation of the strong bow shock. An additional oblique wave is reflected upwards at the secondary triple point and a second vortex sheet is produced. A supersonic jet embedded in the surrounding subsonic shock layer is bounded by two vortex sheets that entrain the subsonic flow into it; the jet impinges onto the sphere and is balanced by a terminating shock in front of the sphere.

Figures 195 and 196 show the pressure and temperature contours. As expected, the pressure behind the distorted bow shock is not symmetric about the x = 0 plane as in the isolated sphere. The pressure and temperature on each side of the jet immediately behind the distorted bow shock (zone 1 and zone 2) can be estimated as the values behind two normal shocks. One has the freestream Mach number of 3.45 and another has the impinging Mach number of 2.57 before the normal shock. This estimation gives a pressure and temperature rise ratio of 1.8 and 1.0 across the jet, respectively, which is consistent with the observation in Figures 195 and 196. The stagnation pressure ratio between zone 2 and zone 1 is about 2, causing the jet to turn to the left towards the lower stagnation pressure zone (zone 1). The temperature in the impinging jet area is lower than that behind the distorted bow shock because the temperature rise is smaller through a series of oblique shocks in the jet as compared to that across a nearly normal shock.
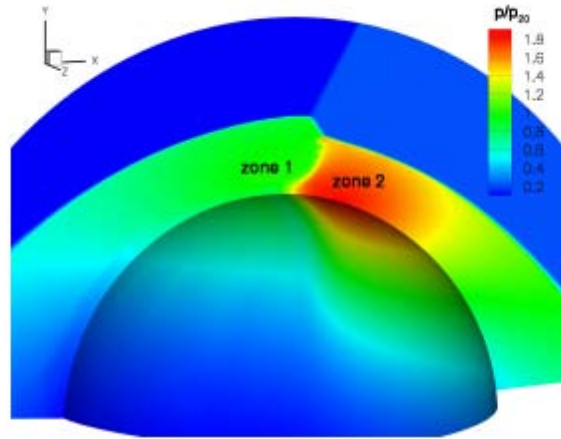
**Figure 195. Static Pressure Contours**
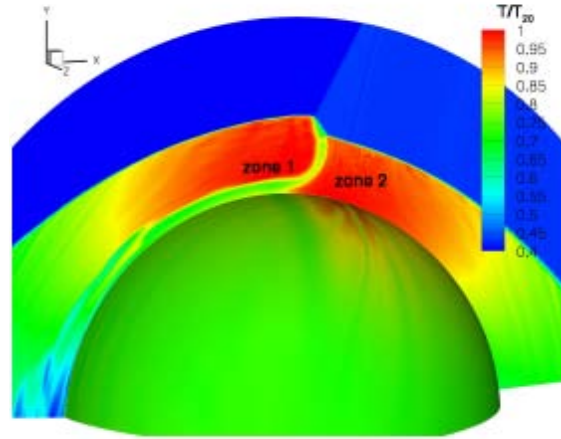


**Figure 196. Static Temperature Contours**

Figure 197 compares the predicted surface pressure in the $z = 0$ plane to the experimental data taken from Adelgren et al. (2005). The angle $\theta$ is the polar angle in the $x$-$y$ plane and is measured clockwise from the $y$-axis as shown in Figure 194. The surface pressure is in good agreement with the experiment. Relative to the flow past a sphere, the peak surface pressure is shifted to the right, where the enveloping shock becomes oblique. The peak pressure is increased to about 1.8 times as much as for flow over the sphere, because for the same flow condition before the shock, the stagnation pressure behind an oblique shock is greater than that behind a normal shock. Surface loads are generally lower than that in the 2D simulation because of the relief effect associated with the 3D configuration. Due to a lack of experimental data for the surface heat flux, only the numerically predicted result is presented in Figure 198. The surface heat flux is nondimensionalized by the predicted stagnation heat flux ($0.90q_{van}$) for the sphere, which is obtained from the fine grid simulation (grid 3) shown in Table 4. Following the same trend as surface pressure, the peak surface heat flux is shifted to the right. The magnitude increases by a factor of 1.61 compared to the sphere. As indicated by equation (205) the increase in stagnation heat flux is correlated to the rise in stagnation pressure and density.

199
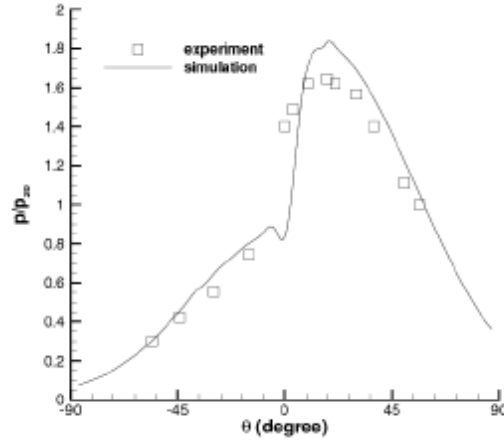
Figure 197.  Surface Pressure for Baseline Case
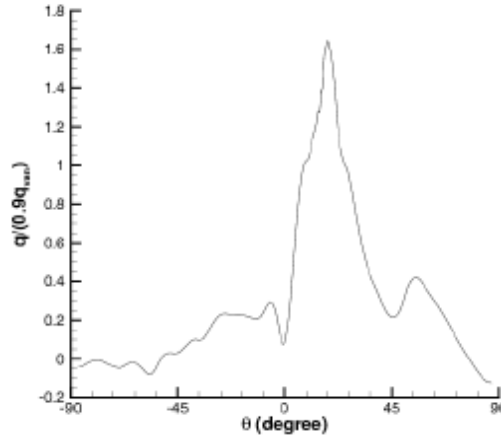


Figure 198.  Heat Flux for Baseline Case

### 6.1.5  Edney IV Interaction with Energy Deposition

After the simulation has reached a relatively stable state, a 3 mm$^3$ spherical spot of 283 mJ is deposited in the freestream upstream of the primary triple point. In the simulation, the deposited energy is assumed to be completely absorbed by air with $\varepsilon_Q = 1.0$, while in the experiment, only partial energy is absorbed by the plasma and the rest is used to ionize the gas and is radiated off. Although real gas effects are excited, because the initial peak temperature inside the energy spot reaches $1.1 \times 10^6$ K, which is obtained from the perfect gas model in equation (203), previous studies on the energy deposition in quiescent air (Yan et al., 2003) have shown that after the initial transient, ($< 10$ μs) the pressure, temperature and velocity distributions along the radius predicted by the perfect gas model were in good agreement with experiment. In addition, this study is focused on the fluid dynamics effect of an energy pulse. Therefore, the plasma formation and chemical reactions are not considered here.

The choice of $\varepsilon_Q$ is determined by matching the position of the blast wave induced by a single laser pulse in the uniform ambient condition in the simulation with the experimental data. The simulation adopts a separate numerical procedure with the assumption of a spherical laser pulse.

200

The details are presented by Yan et al. (2003). However, in the current case, the energy spot and its induced blast wave are highly distorted by the impinging oblique shock, which makes it impossible to calibrate $\varepsilon_Q$. In addition, the choice of $\varepsilon_Q$ does not affect the fluid dynamics effect of an energy pulse characterized by an increase in local temperature and pressure, therefore, $\varepsilon_Q$ is set to 1.

As described in Adelgren et al. (2005), three major events in the energy deposition process play an important role in establishing the effect of the energy deposition on the Edney IV interaction. The first event is when the high energy spot induces a blast wave that interacts with the bow shock and the subsequent wave structures reach the surface, causing a rise in surface pressure and heat flux. The second event is when the high energy spot interacts with the complex shock structures in the vicinity of the surface, resulting in the upstream movement of the bow shock and subsequently, the decrease in surface pressure and heat flux. The third event is when the high energy spot hits the surface, leading to the rise in surface pressure and heat flux. Each of these experimentally observed phenomena is captured by the numerical simulation.

Figures 199 and 200 show the contours of predicted surface pressure and heat flux of the $z = 0$ plane in a $\theta$ - $t$ plane, where the energy pulse is instantaneously deposited into the flow field at $t = 0\,\mu\text{s}$. The contours in these two figures exhibit complex flow structures generated by the interaction of the energy spot and the expansion and blast waves with the sphere. The surface pressure and heat flux display a correlated pattern. Basically in these two figures, three distinct regions divided in the time axis are characterized by the increased ($20 < t < 30\,\mu s$), decreased ($30 < t < 80\,\mu s$), and increased ($80 < t < 150\,\mu s$) surface pressure and heat flux, respectively. They correspond to the effect of the blast wave, expansion waves, and high energy spot hitting the surface, respectively. This indicates that the effect of the high energy spot on both surface pressure and heat flux last longer than that of the blast wave. It is seen that the peak surface pressure in Figure 199 during $20 < t < 30\,\mu s$ is about two times that during $80 < t < 150\,\mu s$, while the peak heat flux in Figure 200 during $80 < t < 150\,\mu s$ is about three times that during $20 < t < 30\,\mu s$. Thus the effect of the high energy spot is much greater on heat flux than on surface pressure, while the effect of the blast wave is greater on surface pressure than on heat flux. During the time when the expansion waves hit the surface, both surface pressure and heat flux at the surface decrease, even briefly cooling portions of the surface as shown by the negative heat flux in Figure 200.
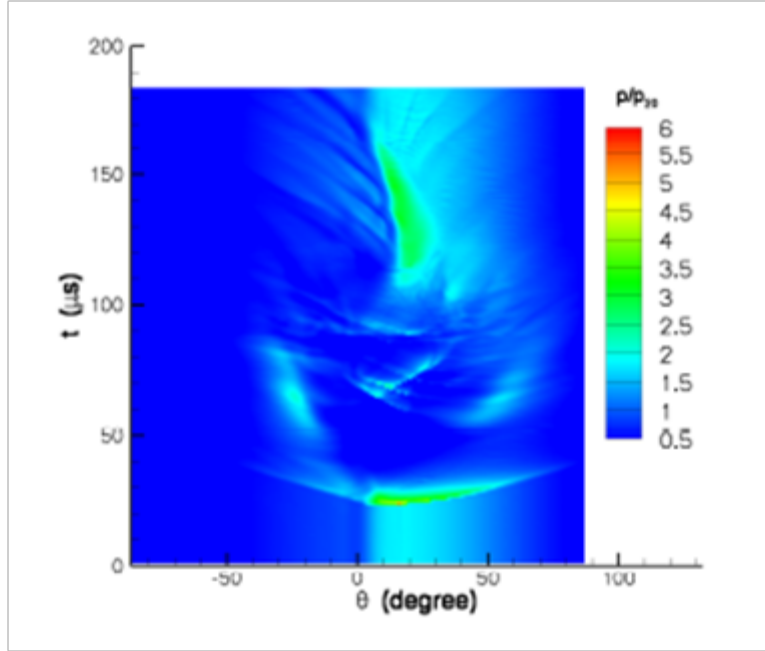
Figure 199.  Surface Pressure Contours on $\theta - t$ Plane
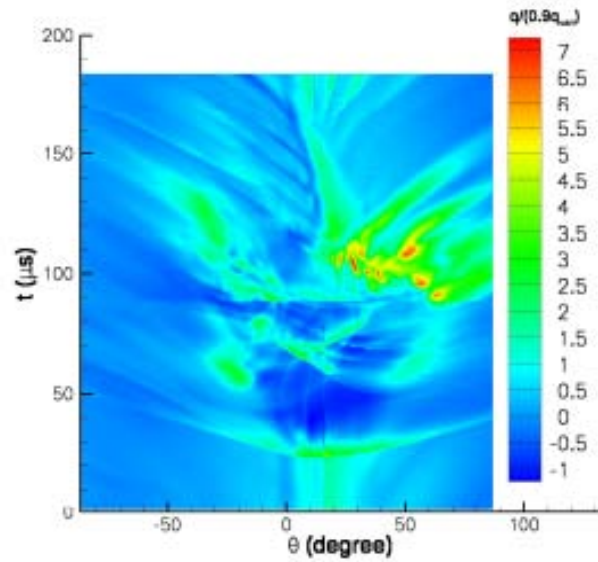


Figure 200.  Heat Flux Contours on $\theta - t$ Plane

The detailed flow structure is now described to more clearly elucidate the physics of these phenomena. A series of snap shots at several time instants are shown in Figures 201 through 203 to illustrate the main flow features. An energy pulse creates a low Mach number (Figure 201) and density region (Figure 202) in the freestream. The spot propagates radially while convecting with the local flow, as clearly shown by the instantaneous streamlines in Figure 202. The effect of an energy pulse on the flow field in the quiescent air is characterized by a blast wave and a high-temperature core. The blast wave weakens rapidly until it propagates at the local speed of sound. As the energy spot encounters the oblique shock, it becomes elongated and stretched along the incident shock direction, causing the oblique shock to distort.

202
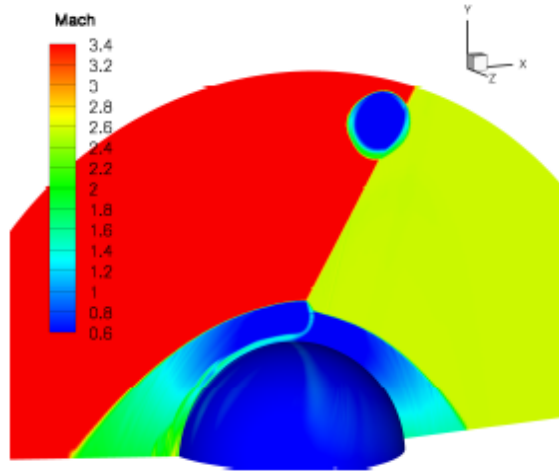
**Figure 201. Mach Number Contours at $t$=1 μs**
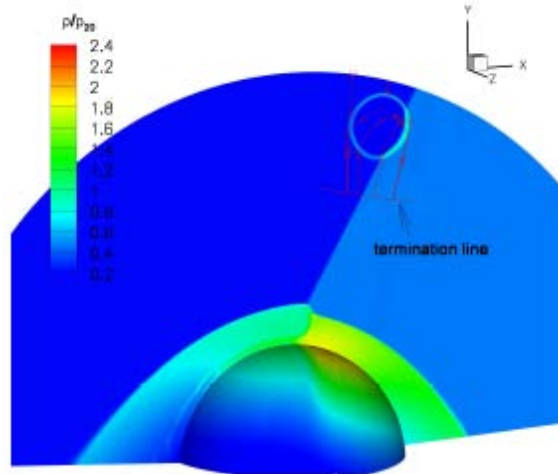


**Figure 202. Density Contours at $t$=1 μs**

Figures 203(a) through 203(e) show a series of snap shots of the predicted pressure contours in the $z = 0$ plane. The experimental Schlieren images are shown in Figures 204(a) through 204(c) for comparison. Once the energy is deposited, the local pressure rises rapidly due to the propagating blast wave. The pressure rise behind the oblique shock is higher than that in the free stream as shown in Figure 203(a) because the local pressure behind the oblique shock is higher than that in the free stream, leading to a stronger compression of the blast wave. During the $20 < t < 30$ μs period the blast wave induced by the energy spot initiates a perturbation to the Edney IV interaction location. Figure 203(b) demonstrates some of the main features during this time duration. The blast wave convects downstream at the local flow speed, and distorts the incident shock and impinging jet. The blast wave is partly reflected off of the sphere surface and partly transmitted around the sphere. The surface pressure increases significantly when the blast wave hits the surface as shown in Figure 203(b), which is also observed in the Schlieren image as a bright spot in the vicinity of the surface in Figure 204(a). By the time that the blast wave transports around the sphere, the high energy spot begins to interact with the shock structures. The interaction creates a more complex flow structure as shown in Figures 203(b) and 203(c) at $t$

$=50\,\mu$s. The bow shock moves away from the surface while the expansion waves move towards it, resulting in the reduction in surface pressure and heat flux observed in Figure 200. Adelgren (2002) described this interaction by using a one-dimensional analysis of a shock-wave interaction with a temperature discontinuity. This phenomenon is termed "lensing effect" by Georgievski and Levin (1993). Subsequently, the distorted high energy spot along with the downstream portion of the blast wave convects onto the surface, yielding the rise in surface pressure and heat flux as shown in Figure 203(d) and Figure 200 at $t = 94\,\mu$s. This observation is consistent with that in the experiment shown in Figure 204(c). Finally, the bow shock resumes its steady state shape as shown in Figure 203(e). Although the solution has not yet reached the initial no-control state, the simulation does not indicate hysteresis.

From the standpoint of effectiveness, in addition to localized transient peaks, integrated values of pressure (drag) and heat transfer are also of interest. Figure 205 shows the variation of the surface-integrated pressure and heat flux with time. The observed variations can be correlated to the phenomena described above. The surface pressure and heat flux show an initial increase caused by the energy pulse induced blast wave, followed by a reduction when the series of expansion waves dominate the surface interaction. When the high energy spot, together with the weakened blast wave, convect towards the surface and interact with the distorted shock structures in the vicinity of the surface, the surface pressure and heat flux increase again. However, the second rise due to the energy pulse not being large enough for the surface pressure to reach above the initial value. Overall, the pressure load is alleviated during the energy deposition process due to the effect of the expansion waves; except during a very short period of time (10 μs) when the blast wave first hits the surface. For heat flux, the second rise is larger than the first. In addition, because the energy spot results in a broader gradual increase than the blast wave, the high energy spot becomes a major contributor to the amplification of the heat flux.

Figure 206 shows the time-averaged surface pressure and heat flux in the $z = 0$ plane. Comparison with Figure 205 suggests that the peak surface pressure and heat flux decrease from 1.8 to 1.5 and 1.6 to 1.0, about 17% and 30% compared to that without energy deposition, respectively. The surface-time-integrated surface pressure and heat flux are decreased by 11% and 4%, respectively. The total heating on the surface over a period of 184 μs is 0.25 mJ, only 0.1% of the total deposited energy. Most of the energy in the spot is effectively convected downstream as a consequence of the altered flow structures.
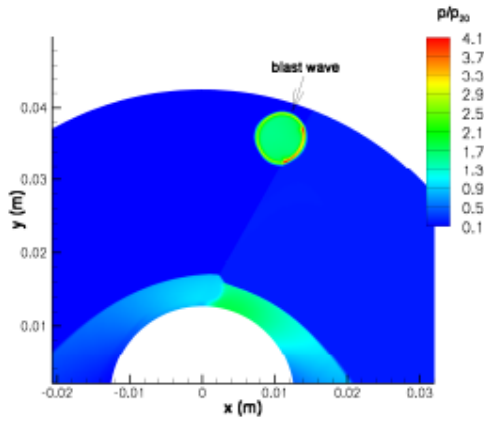
(a) $t = 1\mu s$
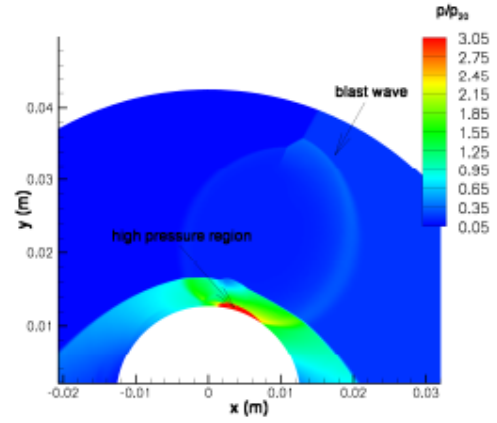
(b) at $t = 26\mu s$
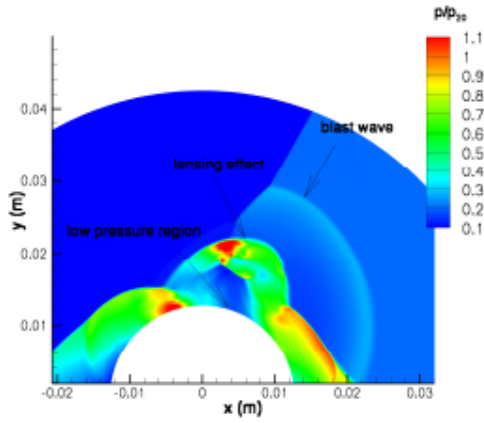
(c) at $t = 50\mu s$
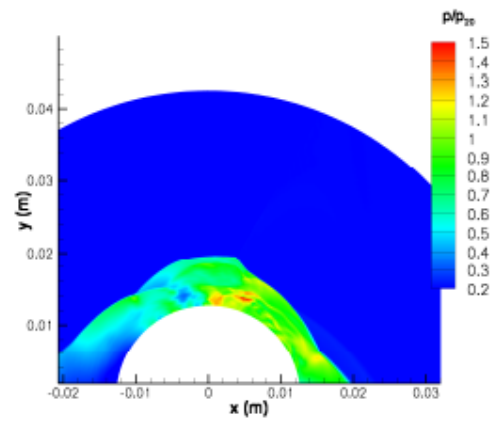
(d) at $t = 94\mu s$
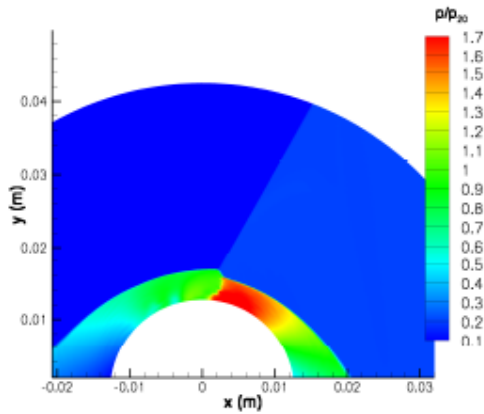
(e) at $t = 184\mu s$

Figure 203. Simulated Pressure Contours at Different Times

205
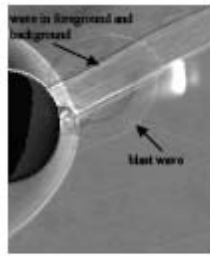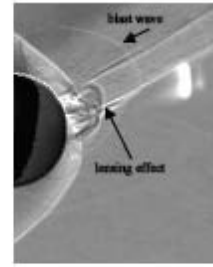
(a) at $t = 30\mu s$       (b) at $t = 50\mu s$
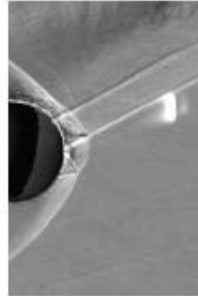
(c) at $t = 90\mu s$

Figure 204.  Schlieren Images at Different Times
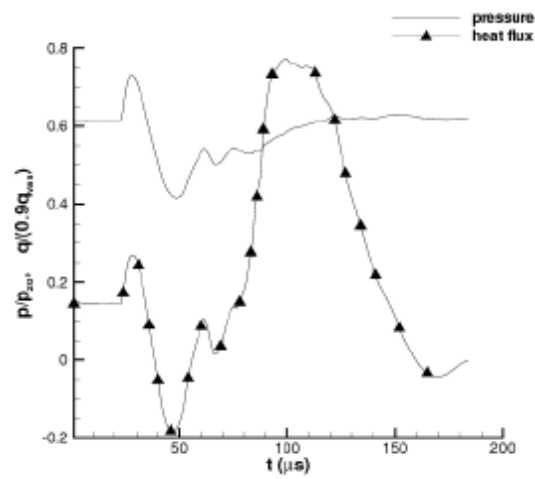


Figure 205.  Surface-Integrated Pressure and Heat Flux versus Time
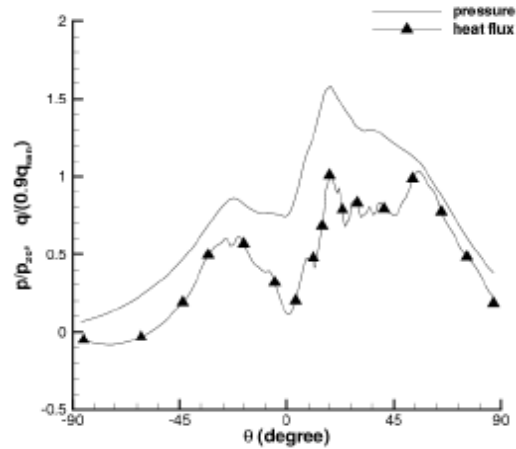
**Figure 206. Time-Averaged Pressure and Heat Flux on $z = 0$ Plane**

### 6.1.6 Summary

Energy deposition is explored as a local flow control technique to achieve a transient modification to heat and pressure loads in a three-dimensional Edney IV interaction. The simulation successfully captures the main physics in the Edney IV interaction and the effect of energy deposition on this flow structure. First, the predicted surface pressure without the energy deposition is in good agreement with the experiment. Second, after the energy pulse is deposited, the instantaneous surface pressure and heat flux experience a rise, a subsequent decrease, followed by a second rise in time; mainly due to the impingement of the blast wave, expansion waves, and high energy spot onto the surface, respectively. These predictions are consistent with experimental observation and with the lensing phenomenon. A detailed study shows that the surface-time-integrated surface pressure and heat flux values are reduced by 11% and 4%, respectively. Therefore, in the current case, the total stress and thermal load are alleviated to some extent. However, instantaneous peaks are larger and must be factored into the overall effectiveness. This study also shows that high energy spot impingement is the main source of surface heating, while this has little effect on surface pressure.

### 6.2 Control of Flow Instability with Thermal Perturbation

### 6.2.1 Introduction

In recent years, there has been considerable interest in the study of methods to modulate the stability of boundary layers (Breuer and Haritonidis, 1990; Breuer and Landahl, 1990; Gaster et al., 1994; Joslin and Grosch, 1995; Worner et al., 2003; White and Ergin, 2003; Fischer and Choudhari, 2004; Tumin and Reshotko, 2005; Rizzetta and Visbal, 2006). These studies are mostly focused on the incompressible regime and have revealed several interesting aspects of bump modulated flows. Surface roughness can influence the location of laminar-turbulent transition by two prominent mechanisms. First, they can convert external large-scale disturbances into small-scale boundary layer perturbations, and become possible sources of receptivity. Second, they may generate new disturbances to stabilize or destabilize the boundary layer. Breuer and Haritonidis (1990) and Breuer and Landahl (1990) performed numerical and experimental simulations to study the transient growth of localized weak and strong disturbances in a laminar boundary layer. They demonstrated that the three-dimensionality in the evolution of localized disturbances may be seen at any stage of the transition process, not confined to the

nonlinear development of the flow. For weak disturbances, the initial evolution of the disturbances resulted in the rapid formation of an inclined shear layer, which was in good agreement with an inviscid calculation. For strong disturbances, however, transient growth gives rise to distinct nonlinear effects, and the resulting perturbation depends primarily on the initial distribution of vertical velocity. Gaster et al. (1994) reported measurements on the velocity field created by a shallow oscillating bump in a boundary layer. They found that the disturbance was entirely confined to the boundary layer, and the spanwise profile of the disturbance field in the near-field region of the bump differed dramatically from that far downstream. Joslin et al. (1995) performed a Direct Numerical Simulation (DNS) to duplicate the experimental results by Gaster et al. (1994). In the far field, the bump generated a pair of counter-rotating streamwise vortices just above the wall and on either side of the bump location, which significantly affected the near-wall flow structures. Worner et al. (2003) numerically studied the effect of a localized hump on Tollmien-Schlichting waves traveling across it in a two-dimensional laminar boundary layer. They observed that the destabilization by a localized hump was much stronger when its height was increased as opposed to its width. Further, a rounded shape was less destabilizing than a rectangular shape.

Researchers have also studied the effect of surface roughness on transient growth. White and Ergin (2003) described experiments to explore the receptivity of transient disturbances to surface roughness. The initial disturbances were generated by a spanwise-periodic array of roughness elements. The results indicated that the streamwise flow was decelerated near the protuberances, but that farther downstream the streamwise flow included both accelerated and decelerated regions. Some of the disturbances produced by the spanwise roughness array underwent a period of transient growth. Fischer and Choudhari (2004) presented a numerical study to examine the roughness-induced transient growth in a laminar boundary layer. The results showed that the ratio of roughness size relative to the array spacing was a primary control variable in roughness-induced transient growth. Tumin and Reshotko (2005) solved the receptivity of boundary layer flow to a three dimensional hump with the help of an expansion of the linearized solution of the Navier-Stokes equations into the bi-orthogonal eigenfunction system. They observed that two counter-rotating streamwise vortices behind the hump entrained the high-speed fluid towards the surface boundary layer. Rizzetta and Visbal (2006) used DNS to study the effect of an array of spanwise periodic cylindrical roughness elements on flow instability. A pair of co-rotating horseshoe vortices was observed, which did not influence the transition process, while the breakdown of an unstable shear layer formed above the element surface played a strong role in the initiation of transition.

Although the effect of physical bumps on flow instabilities has been studied extensively, far fewer studies have explored the impact of thermal bumps. A thermal bump is particularly effective at supersonic and hypersonic speeds. One approach to introduce the bump is through an electromagnetic discharge in which motion is induced by collisional momentum transfer from charged to neutral particles through the action of a Lorentz force (Adelgren et al., 2005; Roth et al., 2000; Leonov et al., 2001; Shang, 2002a; Enloe et al., 2004a; Shang et al, 2005b). Joule heating is a natural outcome of such interactions, and is assumed to be the primary influence of the electric discharge plasma employed here to influence flow stability.

For supersonic and hypersonic flows, heat injection for control can be implemented in a number of ways, including DC discharges (Shang et al, 2005b), microwave discharges (Leonov et al., 2001) and lasers (Adelgren et al., 2005). Recently however, Samimy et al. (2006) have employed

Localized Arc Filament Plasma Actuators (LAFPA) in a fundamentally unsteady manner to influence flow stability. The mechanism is to utilize an arc filament initiated between electrodes embedded on the surface to generate rapid (on the time scale of a few microseconds) local heating. Samimy et al. (2006) employed this method in the control of high speed and high Reynolds number jets. The results showed that forcing the jet with m = ±1 mode at the preferred column mode frequency provided the maximum mixing enhancement, while significantly reducing the jet potential core length and increasing the jet centerline velocity decay rate beyond the end of the potential core.

Yan et al. (2007a, 2007b) studied the steady heating effect on a Mach 1.5 laminar boundary layer. Far downstream of the heating, a pair of counter-rotating streamwise vortices were observed above the wall and on the each side of the heating element in the spanwise direction. The finding was generally consistent with the DNS results of physical bumps by Joslin and Grosch (1995). This implies that the main mechanism of the thermal bump displays characteristics similar to the physical bump. These recent studies introduce the possibility of using thermal bumps, which can be realized by a localized electric discharge. Advantages of thermal bumps over physical ones include the ability to switch them on and off on-demand, but also in principle, to pulse at any desired frequency combination.

This research is aimed at further understanding the surface thermal perturbation. The effect of the disturbance amplitude and frequency of the forcing, and the shape and spanwise width of the thermal bump is examined and compared with both the no-heating and constant heating cases. A detailed description is provided for the vorticity evolution, as well as disturbance energy growth.

### 6.2.2 Flow Configuration

A Mach 1.5 flat plate flow is considered with the total temperature and pressure of 325 K and $3.7 \times 10^5$ Pa, respectively. A thermal bump is imposed as a surface heating element and centered in the spanwise direction as shown schematically in Figure 207. The surface heating element is modeled as a time-dependent step surface temperature rise $\Delta T_w$ with a monochromatic pulsing frequency $f$ and duty cycle (DC) as shown in Figure 208. For simplicity, it is assumed that $\Delta T_w = T_w - T_{w0}$, where $T_w$ and $T_{w0}$ are the wall temperature inside and outside of the heating region, respectively, and $T_{w0}$ is fixed at the adiabatic temperature ($T_{ad}$) as shown in Figure 207. The duty cycle is fixed at 0.5.

In all perturbed simulations, the heating element is placed immediately upstream of the first neutral point in the stability neutral curve which is obtained from the Langley Stability and Transition Analysis Codes (LASTRAC) (Chang, 2004). LASTRAC performs linear calculations and transition correlation by using the N-factor method based on linear stability theory. The N-factor is defined by $N = \int_{s_o}^{s_1} \gamma ds$ where so is the point at which the disturbance first begins to

grow, $s_1$ is the point at which transition is correlated, and $\gamma$ is the characteristic growth rate of the disturbance. The LASTRAC generated neutral stability curve for a Mach 1.5 flat plate adiabatic boundary layer is shown in Figure 209. For disturbances at $f = 100$ kHz, the first neutral point is located at $Re = 610$ based on the similarity boundary-layer length scale defined as $\eta = \sqrt{\nu_\infty x_\infty / u_\infty}$, where $\nu_\infty$ and $u_\infty$ are the dynamic viscosity and streamwise velocity at the freestream conditions, respectively. Thus the local Reynolds number based on the running distance from the leading edge of the plate is $Re_x = Re^2$. The solid squares and circles represent the leading edge of the heating element and the trailing edge of the flat plate in previous and

current studies, respectively. The nominal spanwise distance between bumps is determined from the most unstable mode, which for the present Mach number is oblique. The N-factor profile shown in Figure 210 for different spanwise wavelengths ($\lambda$) indicates that $\lambda = 2$ mm is the most unstable mode. Thus, the nominal distance between two adjacent heating elements is set to 2 mm to excite the most unstable wave. This is done by choosing the spanwise periodic condition based on a domain of 2 mm, at the center of which a bump is enforced. The distance between the leading edge of the bump and the plate is 7.65 mm, corresponding to $Re_x = 372,100$.
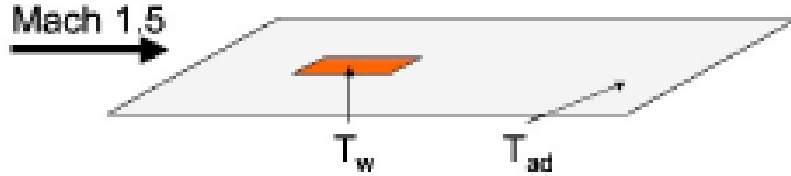


**Figure 207.  Flat Plate with Thermal Bump**
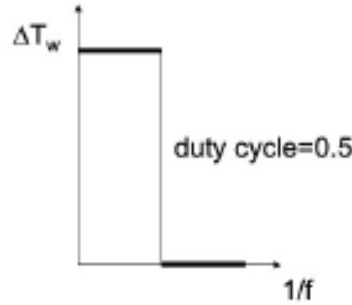


**Figure 208.  One Time Period of Surface Temperature Rise**

In addition to the no-heating flat plate boundary layer case, eight other cases are chosen to examine the effect of variation in $\Delta T_w$ and $f$ of the forcing, as well as bump characteristics (shape and width) as shown in Table 5. Case 2 considers a constant rectangular bump with the spanwise width of $w = 1$ mm and $\Delta T_w = 0.76T_{ad}$, and the streamwise length of the heating element is arbitrarily set as $l = 0.2$ mm. The principal pulsed case, Case 3, uses a rectangular element with $w = 1$ mm, $\Delta T_w = 0.76T_{ad}$, and $f = 100$ kHz. Cases 4 through 6 consider the variation of bump shape and width, while Cases 7 through 9 vary the disturbance amplitude and frequency. The circular bump used in Case 4 has the same geometric center and area as the rectangular one in the principal case, resulting in a diameter of 0.5 mm.
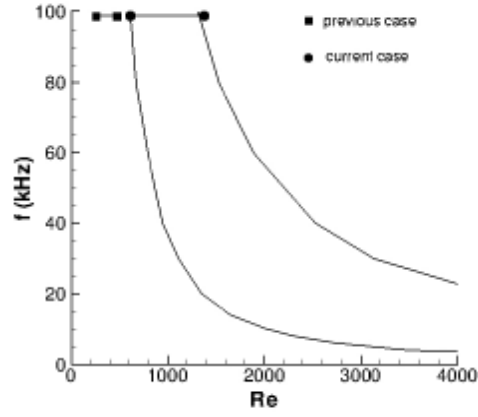
Figure 209.  Neutral Curve for Adiabatic Mach 1.5 Flat Plate Boundary Layer
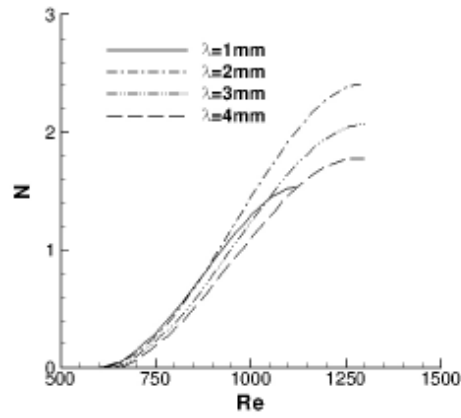


Figure 210.  Spanwise Wavelength

Table 5.  Cases Simulated

| Case | Shape | $w$ (mm) | $\Delta T_w$ (K) | $f$ (kHz) |
|------|-------|----------|------------------|-----------|
| 1 | no-heating | N/A | N/A | N/A |
| 2 | rectangular | 1 | $0.76T_{ad}$ | steady heating |
| 3 (principal case) | rectangular | 1 | $0.76T_{ad}$ | 100 |
| 4 | circular | diameter=0.5 | $0.76T_{ad}$ | 100 |
| 5 | rectangular | 0.5 | $0.76T_{ad}$ | 100 |
| 6 | rectangular | 2 | $0.76T_{ad}$ | 100 |
| 7 | rectangular | 1 | $0.3T_{ad}$ | 100 |
| 8 | rectangular | 1 | $2.52T_{ad}$ | 100 |
| 9 | rectangular | 1 | $0.76T_{ad}$ | 50 |

### 6.2.3 Numerical Model

The governing equations are solved by numerical discretization of space ($x,y,z$) and time ($t$). The Roe scheme (1981) has been incorporated together with the Monotone Upstream-Centered Schemes for Conservation Laws (MUSCL) (van Leer, 1979) to obtain up to nominal third order accuracy in space. Solution monotonicity is imposed with the harmonic limiter described by Van Leer (1979). Given the stringent time-step-size limitation of explicit schemes, an implicit, approximately factored second-order time integration method with a sub-iteration strategy is implemented for less computing cost. The time step is fixed at $8.4 \times 10^{-8}$ s for all the cases except Cases 4 and 8 in which the time step is $4.2 \times 10^{-8}$.

The computational domain is $L = 38$ mm long, $H = 20$ mm high and $W = 2$ mm wide and is determined by taking two factors into consideration. In the streamwise direction, the domain is long enough to capture 3D effects induced by heating and to eliminate the non-physical effects at the outflow boundary. Based on this constraint, the Reynolds number at the trailing edge of the plate is $Re_x = 1.8 \times 10^6$. In the vertical direction, the domain is high enough to avoid the effect of the reflection of the leading edge shock onto the surface. The upper boundary is positioned at $86\delta_L$ above the wall, where $\delta_L$ is the boundary layer thickness at the trailing edge of the plate.

The grid, comprised of 477x277x81 points in the $x$, $y$ and $z$ directions, respectively, is refined near the leading edge of the flat plate and near the heating element. Approximately 150 grid points are employed inside the boundary layer at the leading edge of the heating element to resolve the viscous layer and capture the heat release process. Previous results (Yan and Gaitonde, 2008) indicated that this is fine enough to capture the near-field effect of the thermal perturbation.

For boundary conditions, the stagnation temperature, pressure, and Mach number are fixed at the inflow. The non-slip condition with a fixed wall temperature is used on the wall. The pulse is imposed as a sudden jump shown in Figure 208. The symmetry condition is enforced at the spanwise boundary to simulate a spanwise periodic series of heating elements spaced $W$ apart. First-order extrapolation is applied at the outflow and upper boundaries.

### 6.2.4 Numerical Results

This discussion is organized as follows: first, the accuracy of the no-heating baseline flow is established by comparing it with theoretical compressible results and then the heating case is discussed in terms of the flow structures observed, as well as the disturbance quantities obtained.

#### 6.2.4.1 Steady Results with no Heating and Constant Heating

Figures 211 and 212 show the streamwise and vertical velocity profiles along the $y$-direction at $Re_x = 1.4 \times 10^6$, where the subscript $b$ denotes the baseline flow and $d$ is the local boundary layer thickness. Comparisons with compressible theoretical profiles are good. The fact that the profiles on the center and side of the plate collapse demonstrates the flow two-dimensionality as expected.

The heating element is turned on after the baseline flow is achieved. The sudden heat release acts as an isolated thermal bump on the surface, which produces pressure variations and disturbances of a three-dimensional nature. The steady heating case is first computed. Figure 213 shows the streamwise vorticity contours on the wall and four downstream cross sections. Two pairs of strong counter-rotating streamwise vortices are observed on the edges of the element. This disturbance penetrates into the freestream in the form of stretched vortical structures; however,

the disturbance strength decays significantly downstream. It is not clear at this time if higher values of steady thermal perturbation can yield disturbance growth in a manner similar to that observed with steady physical bumps of the type employed in an incompressible flat plate boundary layer (White, 2002).
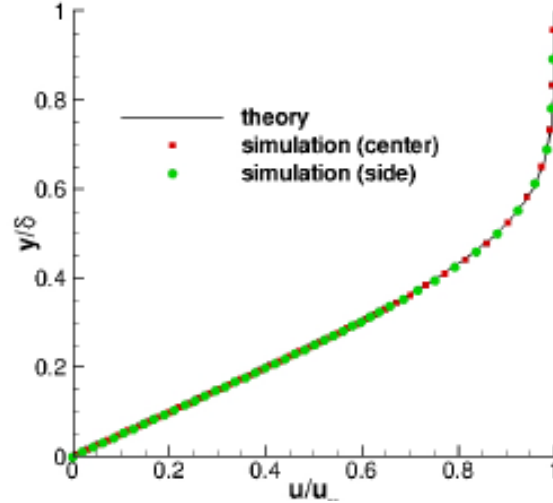


Figure 211. $u_b$ in the $y$-Direction (Baseline)
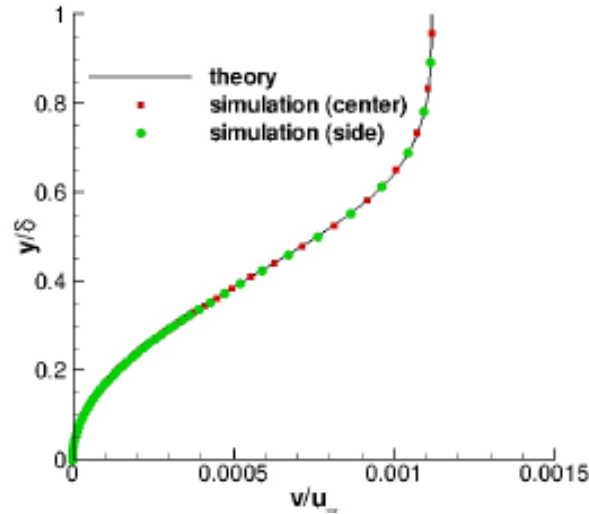


Figure 212. $v_b$ in the $y$-Direction (Baseline)

### 6.2.4.2   Unsteady Results with Pulsed Heating

In all the pulsed cases the solution is marched until an asymptotic unsteady state is obtained. This determination is made by monitoring all primitive variables at several points in the domain. Mean statistics are then gathered over numerous cycles until time invariant values are obtained.

The flow structures and instability generated by the thermal perturbation are described for the principal case (Case 3). The time-mean pressure ($\bar{p}$) contours are shown on the wall in Figure 214 and on the center plane in Figure 215, respectively. The surface pressure rise at the leading edge of the plate is caused by the leading edge shock due to the viscous interaction -- this effect has been further discussed by Hayes and Probstein (1959). The pressure variation is

observed in the vicinity of the bump due to the formation of a weak shock at the leading edge of the thermal bump, followed by the expansion waves at the trailing edge as shown in Figure 215. Further downstream, a series of expansion waves are formed at $Re_x = 1.5x10^6$ -- this feature is more intense around the center of the domain. Figure 216 shows the surface streamlines constructed by the streamwise and spanwise velocity components on the plane one grid-spacing above the wall. Numerous fluid particles across the entire span of the domain are seeded at the incoming flow, and then released to form the streamlines. The lines of coalescence and attachment are indicated on the plot. One attachment line is observed along the centerline and attachment occurs around $Re_x = 1.5x10^6$, corresponding to the streamwise location where the surface pressure decreases as shown in Figure 214. The difference of the time-mean skin friction coefficient between the pulsed and no-heating cases is shown in Figure 217. It is observed that the skin friction coefficient decreases below the laminar value inside the coalescence region, while it rises above the laminar value inside the attachment region as the new boundary layer is formed and generates a larger velocity gradient in the wall-normal direction. As discussed later in this section, strong non-linear vortex breakdown occurs around $Re_x = 1.5x10^6$ and vortical structures are concentrated around the center. This results in flow separation and attachment around the center as seen in Figure 216.
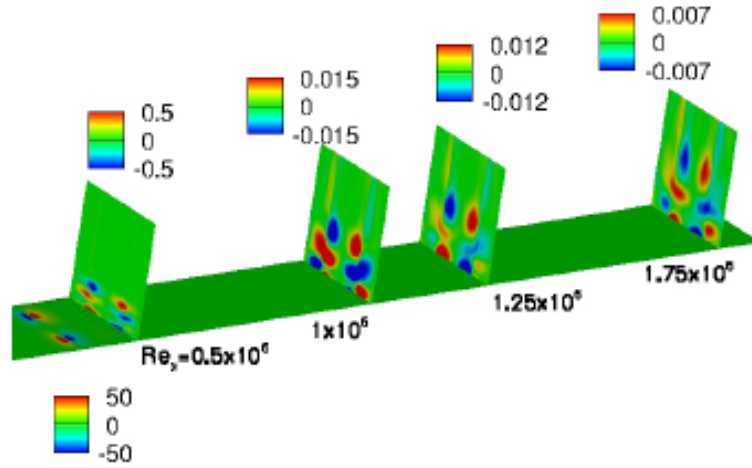


Figure 213. $\omega_x$ Contours on the Wall (Steady Heating)

214
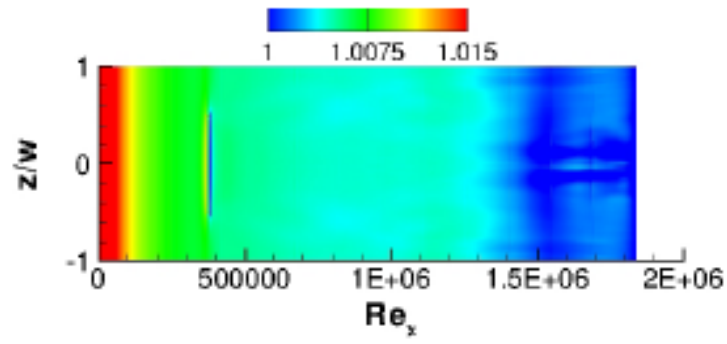
Figure 214. $\bar{p}$ Contours on the Wall (Principle Case)
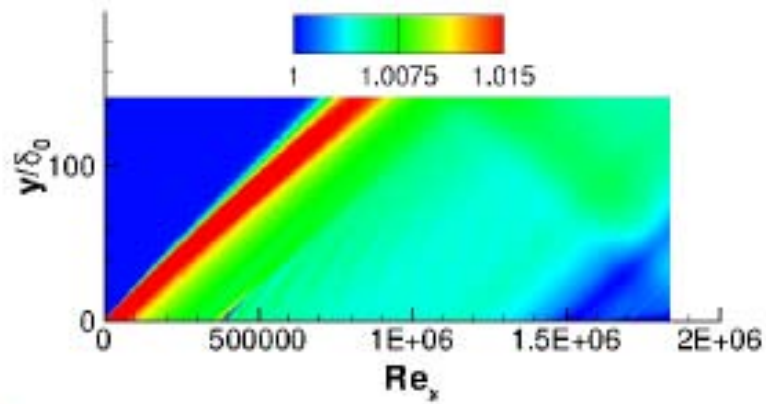


Figure 215. $\bar{p}$ Contours on the Center Plane (Principle Case)
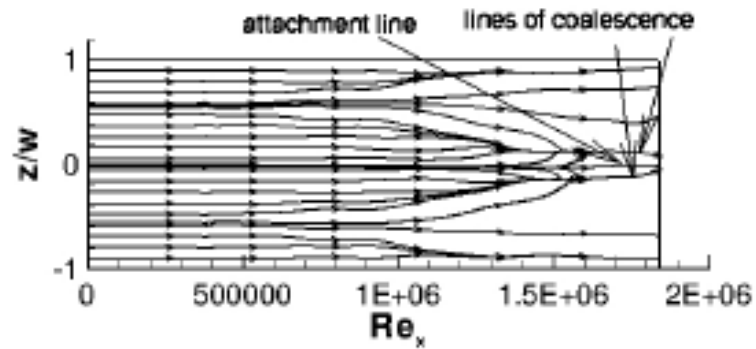


Figure 216. Time-Mean Surface Oil Flow (Principle Case)
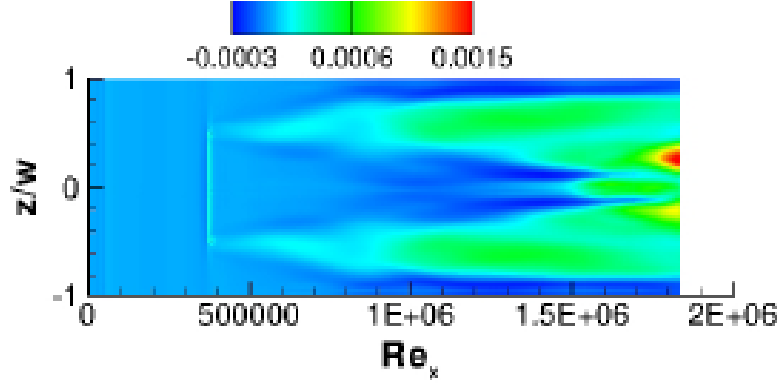
**Figure 217. Time-Mean Skin Friction Coefficient (Principle Case)**

Figure 218 shows the instantaneous streamwise vorticity contours on the wall and four cross sections. Two pairs of counter-rotating streamwise vortices are formed at the edges of the heating element. Examination of the individual terms in the expression for vorticity indicates that the dominant component arises from the variation of the spanwise velocity in the $y$-direction. These two pairs of vortices shed from their origins, forming a vortical pattern with alternating sign in the streamwise direction. They subsequently break into smaller eddies which are concentrated on the center after $Re_x = 1.5 \times 10^6$. The process is accelerated near the center, at about the location where the attachment of the mean flow is observed. Figure 219 shows the frequency spectrum of the streamwise velocity at $y = 0.9\delta_0$ at four different downstream locations, where $\delta_0$ is the boundary layer thickness at the leading edge of the element. The imposed frequency of $f = 100$ kHz dominates the unsteadiness and its component increases with the downstream distance, but higher harmonics are also observed at larger Reynolds numbers of $Re_x = 1.5 \times 10^6$ and $1.75 \times 10^6$, where as noted earlier, the boundary layer exhibits features of non-linear breakdown.
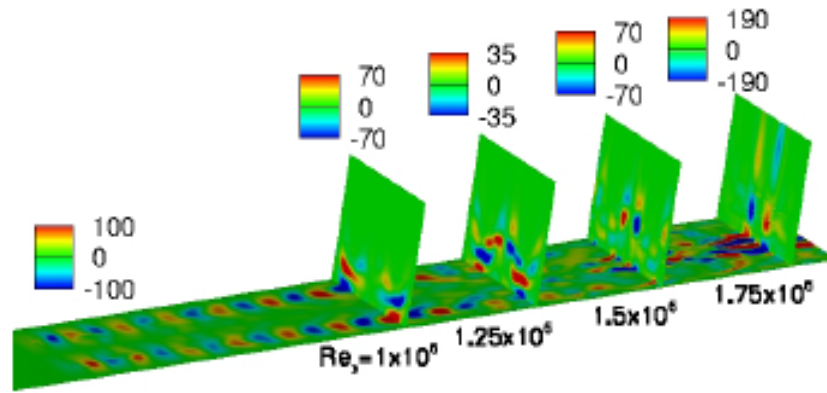


**Figure 218. Instantaneous $\omega_x$ Contours (Principle Case)**

216
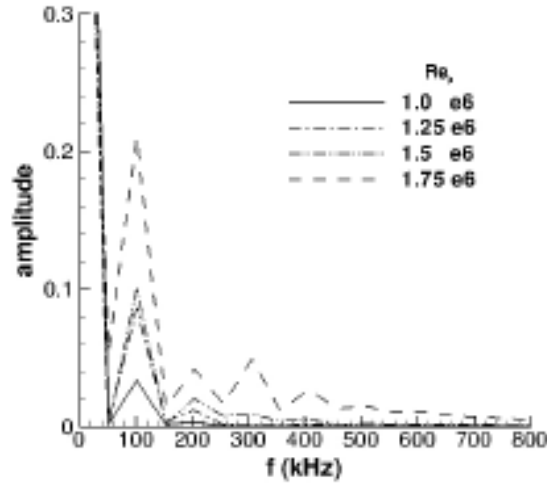
Figure 219.  Frequency Spectrum of *u* (Principle Case)

The effect of pulsing on the time-mean streamwise vorticity on the wall and four cross sections is shown in Figure 220. Spanwise-varying streaky structures are formed downstream with a concentration on the center which intensifies after $Re_x = 1.5 \times 106$. These results bear some similarity to free shear flow control with tabs. For example, Zaman et al. (1994) demonstrated with a comprehensive experimental study that the pressure variation induced by the tabs installed on the nozzle wall generated streamwise vorticity, which significantly enhanced the mixing downstream of the nozzle exit. The spanwise wavenumber in Figure 221 shows that the dominant spanwise wavelength is 1 mm, but higher wavenumbers appear further downstream. As noted earlier in the context of linear instability theory, the most unstable wavelength is 2 mm as shown in Figure 210. This suggests that non-linear instability mechanisms may play a significant role.
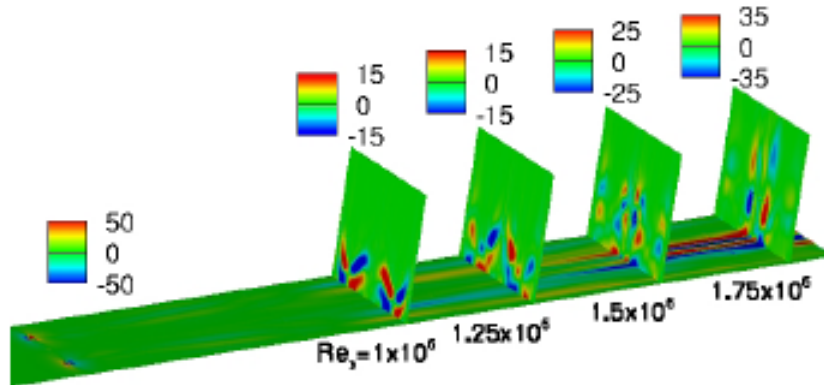


Figure 220.  $\bar{\omega}_x$ Contours (Principle Case)
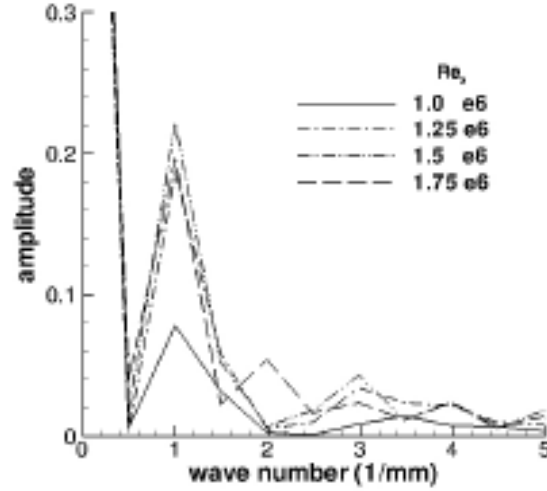
**Figure 221. Spanwise Wavenumber for $\bar{u}$ (Principle Case)**

The accumulated effect of the streamwise vorticity distorts the baseline flow in a nonlinear fashion. Figure 222 shows the streamwise perturbation velocity contours on four downstream cross sections. The quantity plotted is $\bar{u} - u_b$, where $\bar{u}$ is the time-mean value of the pulsed case. A velocity deficit is generated downstream of the center of the heating element, while an excess is observed on both sides of the deficit region. This behavior is similar to the observation in the flow over a shallow bump studied by Joslin and Grosch (1995). Proceeding downstream, the velocity distortion is amplified and the excess velocity regions begin to dominate in the vicinity of the wall, across the entire span of the domain, as the streamwise vortices bring the high-momentum fluid from the freestream towards the wall. This indicates that in the near-wall region along the centerline, the flow is first decelerated and then accelerated. This is consistent with the observation of an inflection point in Figure 223(a), which plots $\bar{u}$ and $\bar{u} - u_b$ along the $y$-direction at four downstream locations along the centerline. The intensity of the velocity excess in the near-wall region increases and reaches about 20% of $u_\infty$ at $Re_x = 1.75 \times 10^6$. Away from the centerline, the flow is accelerated across the entire boundary layer and no inflection points are observed (see Figure 223(b)). The different behavior between the center and sides suggests that the secondary flow instability due to the formation of the inflection points is initiated at the center.

218

a) $Re_x = 1.0 \times 10^6$

b) $Re_x = 1.25 \times 10^6$

c) $Re_x = 1.5 \times 10^6$

d) $Re_x = 1.75 \times 10^6$
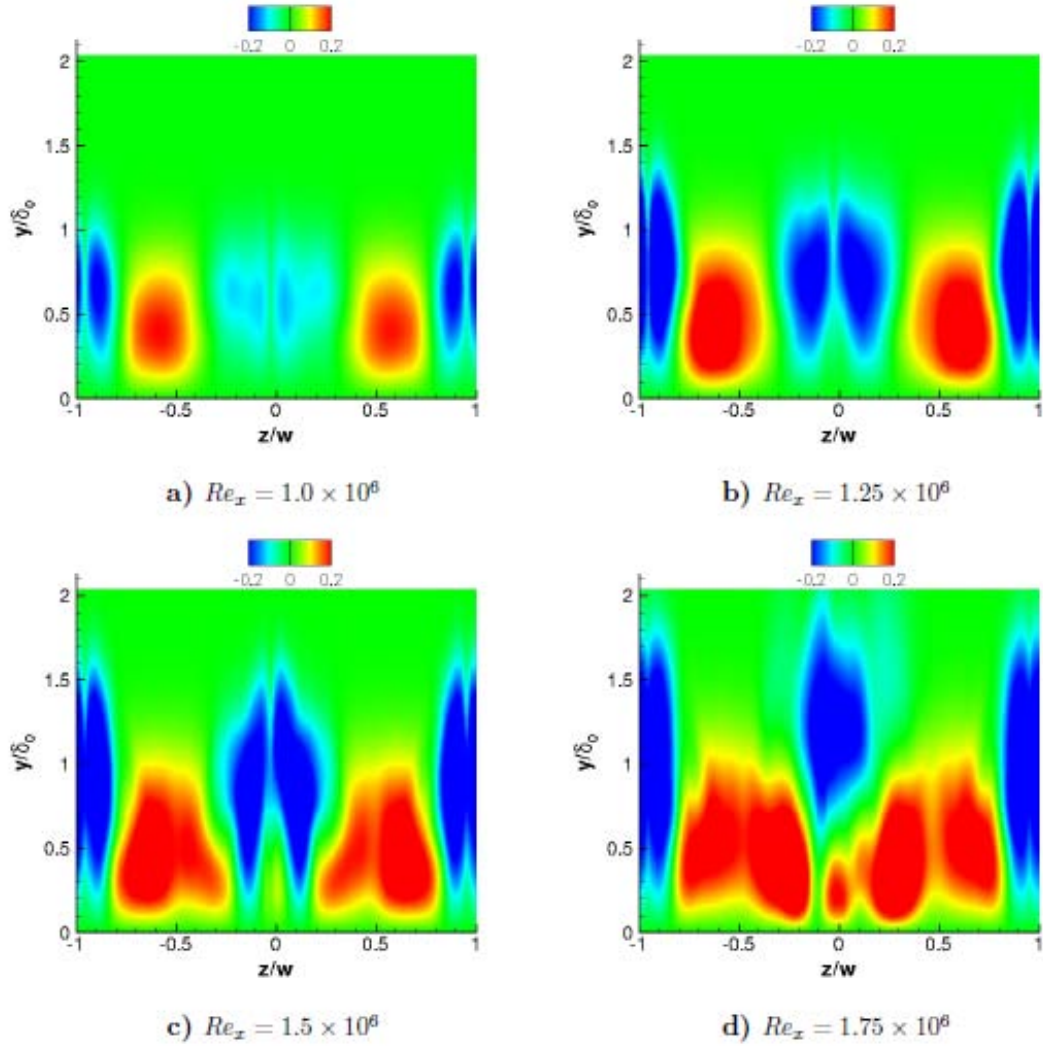
Figure 222. $\bar{u} - u_b$ Contours on Cross Sections (Principle Case)

a) at $z = 0$



b) at $z = -0.5w$
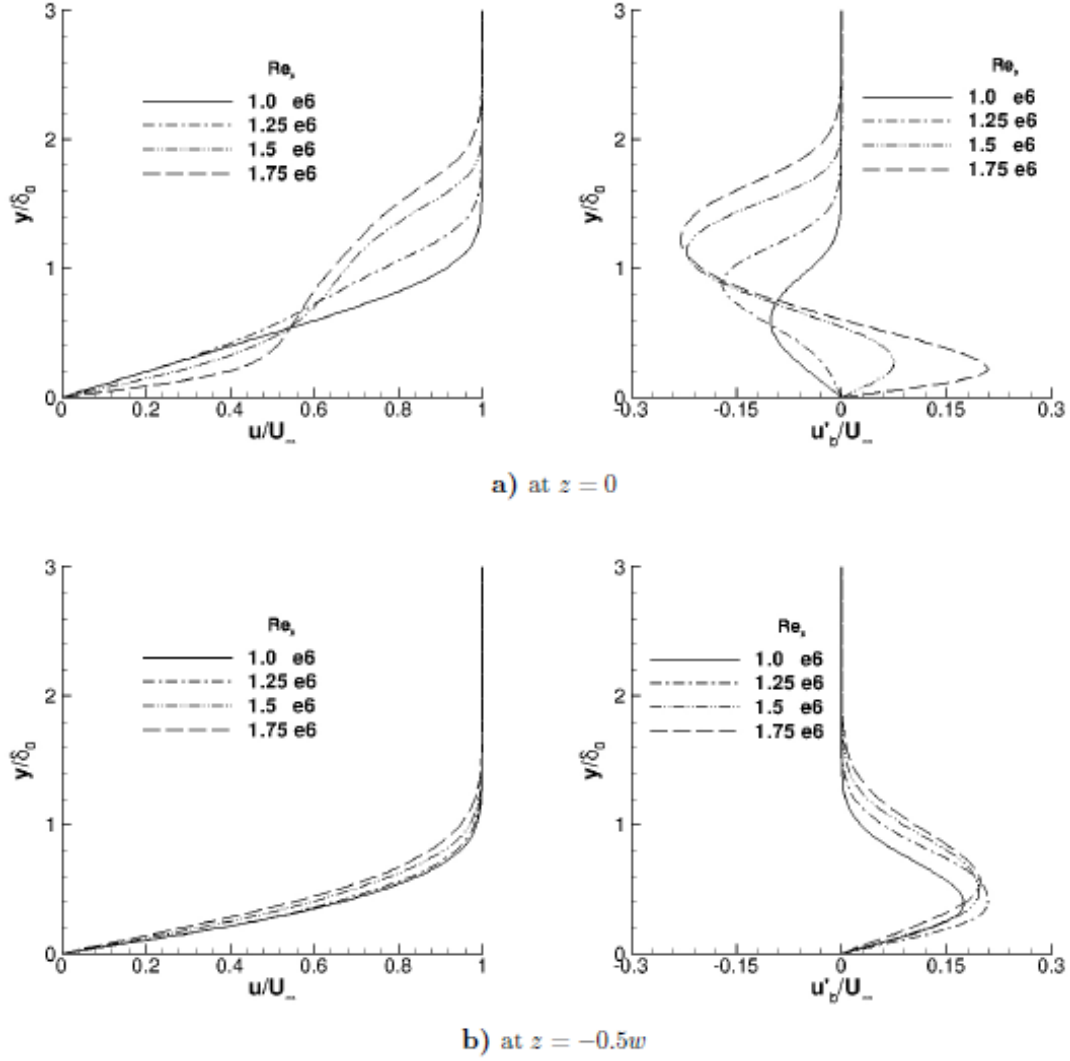
Figure 223. $\bar{u}$ and $\bar{u} - u_b$ Along the $y$-Direction (Principle Case)

The strength of disturbance energy growth is also measured by the energy norm proposed by Tumin and Reshotko (2001) as

$$E = \int_0^\infty \vec{q}^T M \vec{q} dy$$

(207)

where $\vec{q}^T$ and $M$ are the perturbation amplitude vector and diagonal matrix, respectively, and are expressed as

$$\vec{q} = (u', v', w', \rho', T')^T$$

(208)

and

$$M = diag[\rho, \rho, \rho, T/(\gamma \rho M_\infty^2), \rho/(\gamma(\gamma - 1)TM_\infty^2)]$$

(209)

where the superscript $'$ represents the deviation of the perturbed time-mean flow from the baseline flow. The first three terms represent the components of the kinetic disturbance energy denoted as $E_u$, $E_v$ and $E_w$, respectively and the last two represent the thermal disturbance energy as $E_\rho$ and $E_T$. The total disturbance energy is $E = E_u + E_v + E_w + E_\rho + E_T$. Figure 224 shows

220

the time-mean total disturbance energy contours. Streaky structures are observed after $Re_x = 1.0 \times 10^6$. A rapid energy growth is shown after $Re_x = 1.5 \times 10^6$, consistent with the non-linear breakdown shown earlier in Figure 218. To evaluate the overall effect, the spanwise-averaged disturbance energy is plotted in Figure 225. The initial growth rate of the total disturbance energy is small and becomes larger as the disturbances are amplified in $0.9 \times 10^6 < Re_x < 1.5 \times 10^6$. Then the disturbances saturate and reach the finite amplitude shown as a plateau in Figure 225(a). At this stage, the flow reaches a new state which becomes a base flow on which secondary instabilities can grow (Schmid and Henningson, 2001). The new baseline flow is represented by the appearance of an inflection point at $Re_x = 1.5 \times 10^6$ in the left plot of Figure 225(a). The disturbances grow more rapidly after $Re_x = 1.5 \times 10^6$ because the secondary instability is susceptible to high frequency disturbances and usually grow more rapidly than the primary instabilities. The thermal disturbance energy ($E_\rho$ and $E_T$) in Figure 225(b) shows a similar trend, except a spike in the vicinity of the thermal bump appears as expected. However, the thermal components are four orders of magnitude lower than the $E_u$, indicating that the heat is convected away efficiently by the flow.
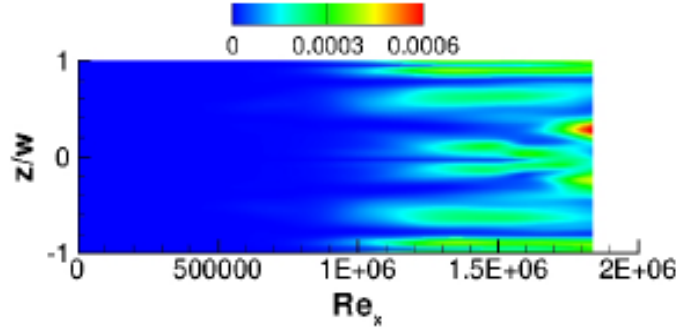


Figure 224. Total *y*-Integrated Disturbance Energy (*E*) Contours (Principle Case)

The observation that the streamwise kinetic disturbance energy ($E_u$) dominates the total disturbance energy ($E$) indicates that the instability mechanism is favorable to the growth of streamwise disturbances. The three-dimensional distribution of the streamwise kinetic disturbance energy is examined through $e_u$ which is defined as $e_u = \rho u'^2$, one component of the integrands in equation (207). Figure 226 shows the $e_u$ contours on the plane one grid-spacing above the wall and at four cross sections. Large energy growth is first observed downstream of the edges of the thermal bump as shown at $Re_x = 1.0 \times 10^6$ and $1.25 \times 10^6$. Downstream non-linear vortex breakdown distorts the mean flow significantly, resulting in the streaky structures and energy growth across the span as shown at $Re_x = 1.5 \times 10$ and $Re_x = 1.75 \times 10^6$.

a) $E$, $E_u$, $E_v$ and $E_w$

b) $E_u$, $E_v$ and $E_w$
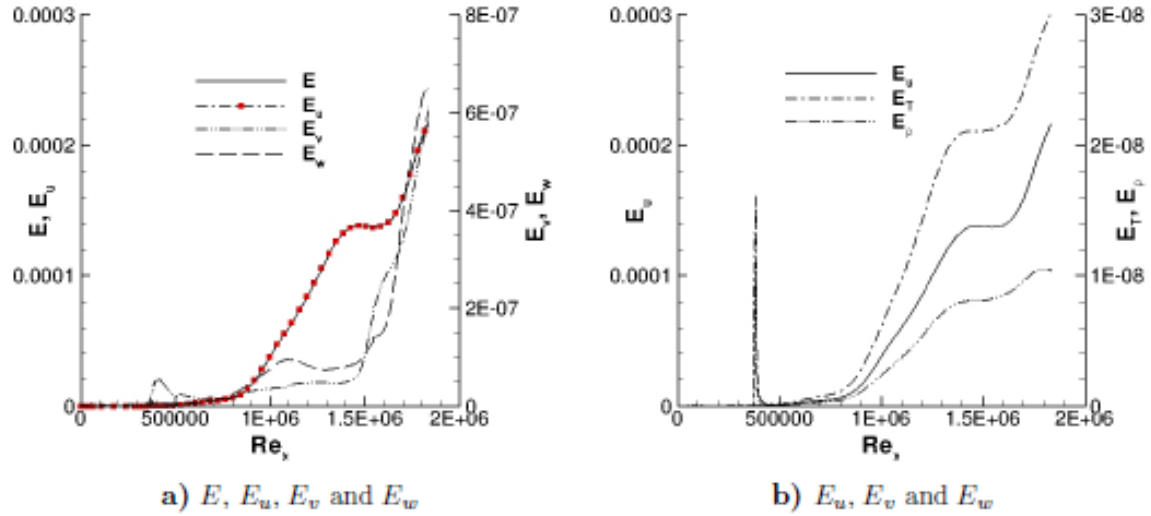
**Figure 225. Spanwise-Averaged Disturbance Energy Along $x$-Direction (Principle Case)**
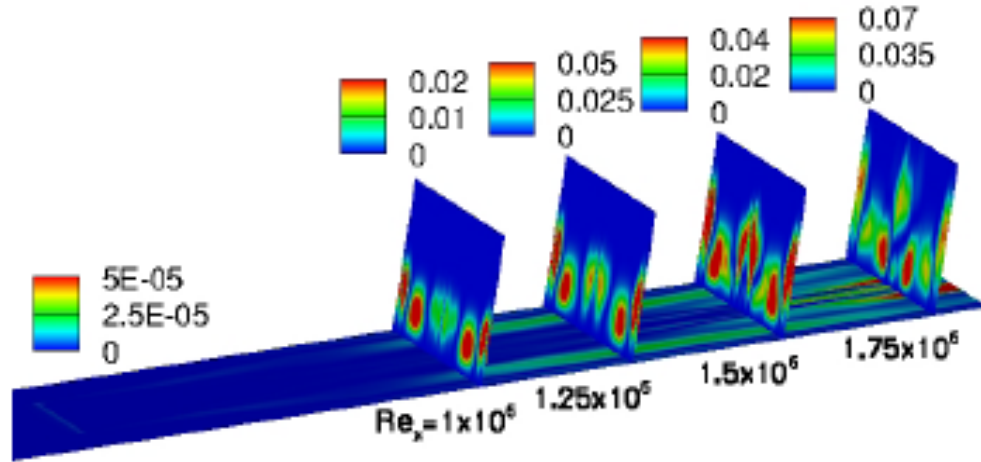


**Figure 226. Streamwise Kinetic Disturbance Energy ($e_u$) Contours (Principle Case)**

Effect of Geometry

To investigate the effect of heating element shape, a circular heating element (Case 4) is considered with the same area and geometric center as the rectangular one in the principal case. Two pairs of counter-rotating streamwise vortices are formed around the element with the same orientation as that in the rectangular element as shown in Figure 227(a). The pairs are closer to each other in the spanwise direction than in the principal case because the diameter of the circular bump is smaller than the width of the rectangular element. Unlike in the rectangular element case, the streaky structures arise near the sides of the plate and the time-mean total disturbance energy growth is more concentrated on the sides as shown in Figure 227(b).

222

a) $\overline{\omega_x}$ contours

b) $E$ contours
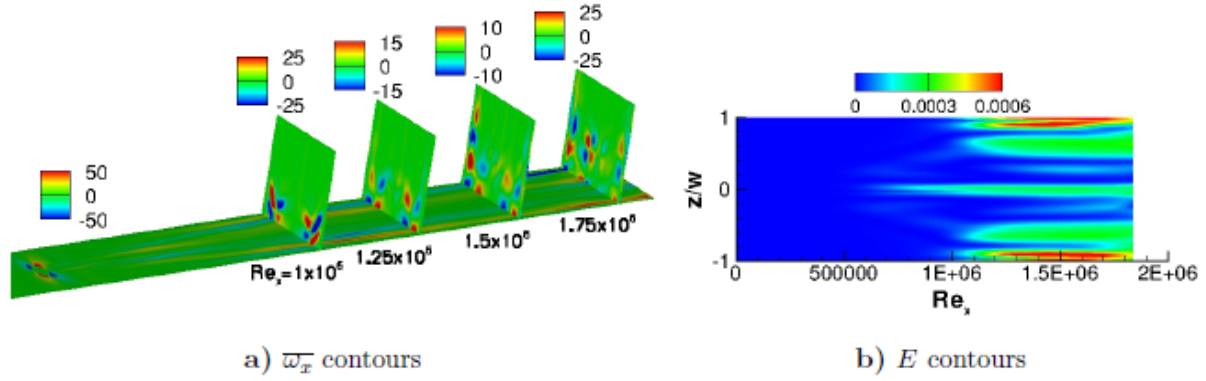
**Figure 227. Circular Element (Case 4)**

The effect of the spanwise width of the element is also examined by considering a full-span bump ($w = 2$ mm, Case 6), as well as one-half the width of the principal case ($w = 0.5$ mm, Case 5). Figure 228 shows the time-mean streamwise vorticity contours on the wall and at four cross sections and the total disturbance energy for $w = 0.5$ mm. Non-linear vortex breakdown occurs earlier, resulting in more streaks with high vorticity intensity downstream compared to the principal case. A larger energy growth region in span is observed after $Re_x > 1.5 \times 10^6$ compared to the principal case, leading to a significant increase in the disturbance energy growth. When the element is extended to the full span ($w = 2$ mm), the streaky structures occur only on half of the span, but at the same streamwise location ($Re_x = 1.5 \times 10^6$) as in other cases, as shown in Figure 229(a). The initial energy growth is much smaller than the principal case and larger growth occurs after $Re_x = 1.5 \times 10^6$ as shown in Figure 229(b).

Figure 230 shows the spanwise averaged energy profile to examine the effect of bump characteristics on disturbance growth. For the rectangular element, the shortest width provides the highest energy growth after $Re_x = 1.5 \times 10^6$. This indicates that shorter width is more effective with less energy input, which for fixed duty cycle and bump temperature varies directly as area is factored into consideration. The full span (the longest width) case has a delayed growth relative to other cases, but then rises rapidly and achieves values similar to the principal case. The reason for this is presently unclear. For the circular element, the initial growth is higher than its rectangular counterpart between $0.5 \times 10^6 < Re_x < 1.0 \times 10^6$, even though the energy input in the circular element is the same as the rectangular one. In the principal case ($w = 1$ mm), the energy growth is smaller after $Re_x > 1.5 \times 10^6$. This indicates that the rectangular element is more effective than the circular one in perturbing the flow.
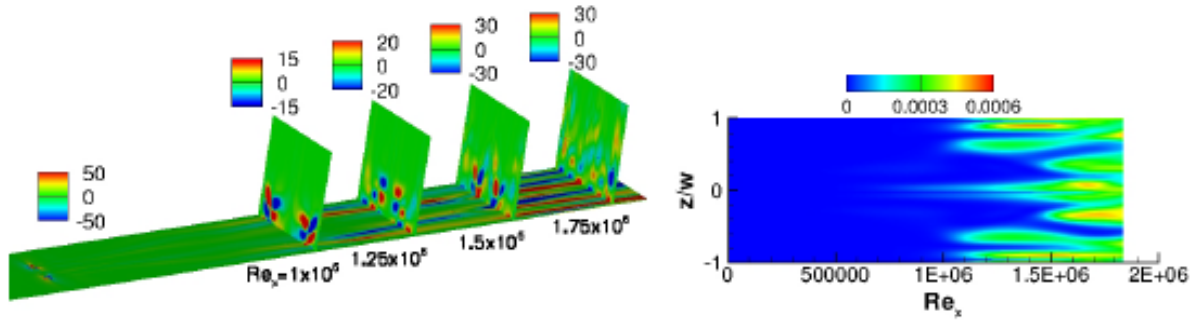
Figure 228.  $w = 0.5$ mm, (Case 5)



a) $\overline{\omega_x}$ contours

b) $E$ contours
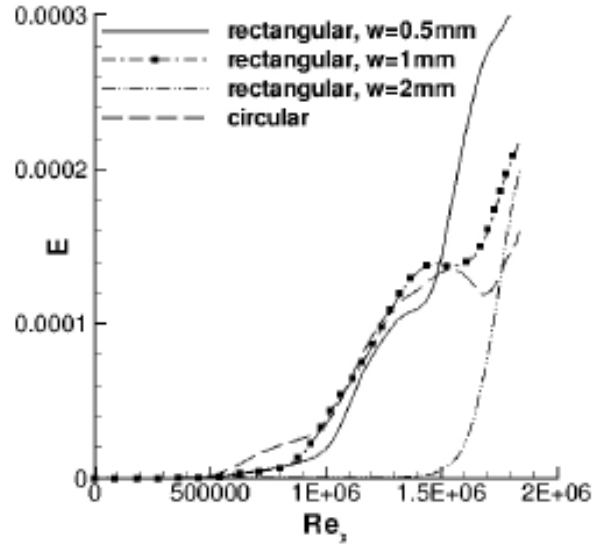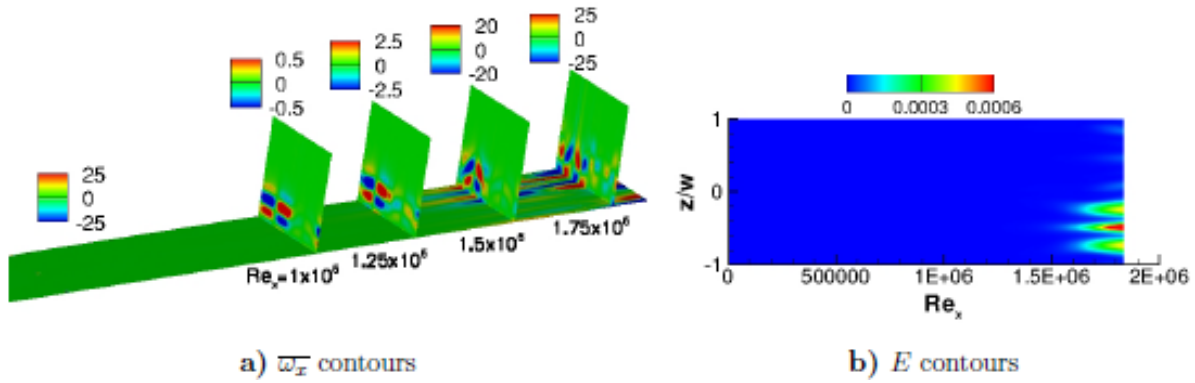


Figure 229.  Full-span, $w = 2$ mm, (Case 6)

Figure 230.  Spanwise Averaged $E$ Along the $x$-Direction (Geometry Effect)

## Effect of Pulsing Property

The effect of the initial disturbance amplitude has also been explored. Figures 231 and 232 show the time-mean streamwise vorticity contours on the wall at four cross sections and total disturbance energy for $\Delta T_w = 0.3T_{ad}$, and $2.52T_{ad}$ (Cases 7 and 8), respectively. Lower initial

disturbance amplitude produces weaker vortices and no distinct breakdown is observed downstream compared to the principal case. The energy streaks are symmetric about the centerline as shown in Figure 231(b). For the higher initial disturbance amplitude shown in Figure 232, stronger non-linear interaction leads to higher disturbance energy growth and the high energy region is narrowed on the center.

The effect of the pulsing frequency is also examined. As discussed earlier, the steady heating ($f = 0$) does not produce the energy growth. Figure 233 shows the time-mean streamwise vorticity contours on the wall at four cross sections and the total disturbance energy for $f = 50$ kHz (Case 9). Much weaker vortical structures are seen in Figure 233(a) compared to the principal case and result in the smaller energy growth downstream shown in Figure 233(b). More small vortical structures are observed on the cross sections (Figure 233(a)) than in the principal case (Figure 220). However, since these structures are essentially symmetric about the center plane, the dominant wavelength is half of the plate width (1 mm) and its component increases with the downstream distance, but higher wavenumbers are observed downstream as shown in Figure 234. This behavior is similar to the principal case; however, downstream the relative strength of the higher harmonics to the fundamental component is stronger than that in the principal case. This explains the distinct presence of the small vortices on the cross sections.
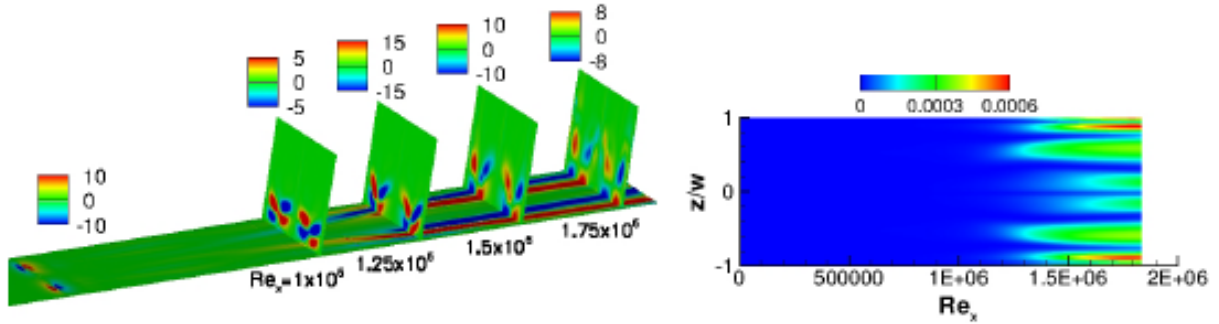


Figure 231. $\Delta T_W = 0.3\,T_{ad}$ (Case 7)
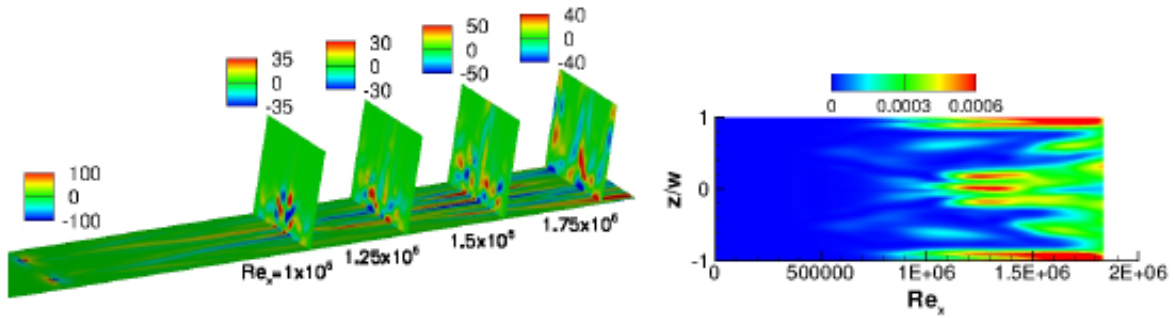


Figure 232. $\Delta T_W = 2.52\,T_{ad}$ (Case 8)

225
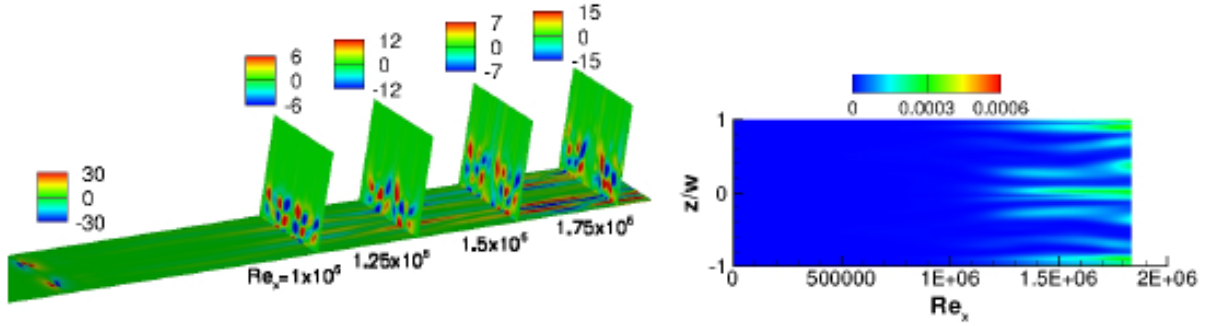
Figure 233. *f* = 50 kHz (Case 9)
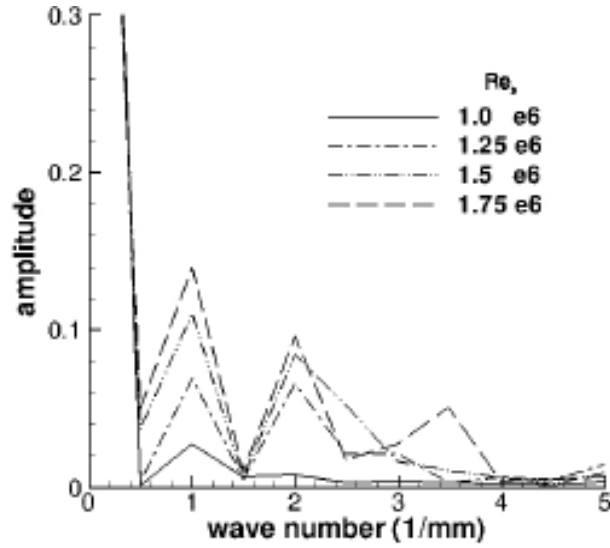


Figure 234. Spanwise Wavenumber for $\bar{u}$ (*f* = 50 kHz)

The dominant frequency is the imposed frequency (f = 50 kHz) as shown in Figure 235. Downstream the dominant component decays rapidly as opposed to the principal case, while higher harmonics are observed to grow. This implies that for the present configuration, the instability mechanism is favorable to higher frequency disturbances, such as *f* = 100 kHz in the principal case.

Figure 236 shows the spanwise-averaged total disturbance energy along the *x*-direction with the principal case marked with the solid squares. The disturbance energy grows with the increase of the initial disturbance amplitude. The highest amplitude produces the largest initial growth as seen between $0.5 \times 10^6 < Re_x < 1.0 \times 10^6$ and the largest plateau. After the plateau, the largest growth rate is observed for the highest amplitude. The lowest amplitude undergoes a delayed growth and no plateau is observed. This implies that non-linear disturbance growth has not reached the saturation stage. With decreasing pulsing frequency, the disturbance energy growth is reduced, emphasizing the importance of pulsing to initiate thermally-induced flow instability.

226
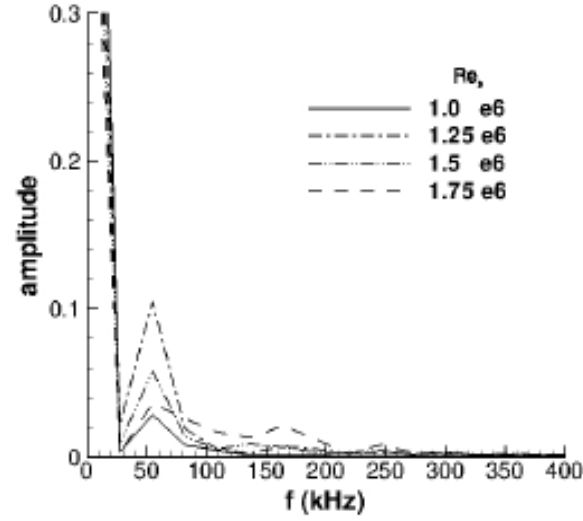
Figure 235.  Frequency Spectrum of *u* (*f* = 50 kHz)
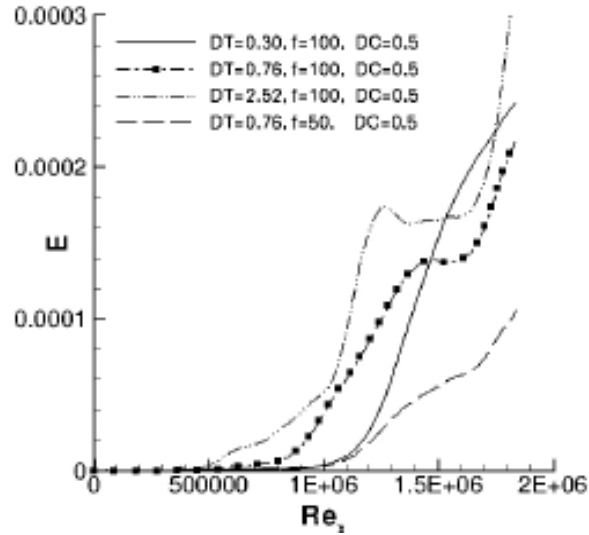


Figure 236.  Spanwise Averaged *E* Along *x*-Direction (Pulsing Effect)

### 6.2.5  Summary

The flow structures generated by a pulsed thermal bump were analyzed through three-dimensional simulations of a Mach 1.5 flat plate boundary layer. The no-heating baseline flow was accurately predicted and is in good agreement with the theoretical profiles. In heating studies, the flow stability characteristics are assessed by varying the geometry of the heating element (shape and spanwise width) and the pulsing properties (the initial disturbance amplitude and frequency). The vortex shedding from the heating element and vortex interactions between the pulses result in a complex vortical field, which gives rise to a secondary instability downstream and results in a rapid growth of disturbances. It is shown that the spanwise gradient of the streamwise velocity plays an important role in extracting the energy from the mean flow and energizing the disturbance. The rectangular element is more effective than its circular counterpart in perturbing the flow. The smaller width of the rectangular element produces higher disturbance energy, while full-span heating indicates delayed growth of the disturbances. This suggests the key role of three-dimensional disturbances. The disturbance energy increases with

227

the initial temperature variation as expected. The lower frequency produces less disturbance energy.

## 7.0 PAPERS PRODUCED

As part of the Plasma Modeling work the following papers were produced:

1.  Surzhikov S.T. and Shang, J.S., Two-Component Plasma Model for Two-Dimensional Glow Discharge in Magnetic Field, J. Computational Physics, Vol. 199, 2, Sept. 2004, pp. 437-464.

2.  Surzhikov S.T. and Shang, J.S., Supersonic Flow around Wing with Localized Surface Gas Discharge, AIAA 2005-0406, 43rd Aerospace Science Meeting and Exhibit, Reno NV, 10-13 January 2005.

3.  Shang, J.S. and Surzhikov, S.T., Kimmel, R., Gaitonde, D., Menart, J., and Hayes, J., Plasma Actuator for Hypersonic Flow Control, AIAA 2005-0562, 43rd Aerospace Science Meeting and Exhibit, Reno NV, 10-13 January, 2005.

4.  Kimmel, R., Hayes, J., Menart, J., and Shang, J., Application of Plasma Discharge Arrays to High-Speed Flow Control, AIAA 2005-0946, 43rd Aerospace Science Meeting and Exhibit, Reno NV, 10-13 January, 2005.

5.  Menart, J., Shang, J., Kimmel, R., Menart, J., Atzbach, C., Magoteaux, S., Slagel, M., and Billheimer, B., Total Drag and Lift Measurements in a Mach 5 Flow affected by a Plasma Discharge and a Magnetic Field, AIAA 2005-0947, 43rd Aerospace Science Meeting and Exhibit, Reno NV, 10-13 January, 2005.

6.  Surzhikov, S.T. and Shang, J.S., Viscous Interaction on a Flat Plate with a Surface Discharge in Magnetic Field, High Temperarure, Vol. 43, No. 1, 2005, pp.21-31.

7.  Surzhikov S.T. and Shang, J.S., Supersonic Flow Airfoil NACA-0012 with Localized Surface Gas Discharge, 6th Aeroplasma Dynamics Conference, Moscow Russia, May 2005.

8.  Surzhikov S.T. and Shang, J.S., The Quasi-Neutral Gas Discharge Plasma in Strong Magnetic Field and Hypersonic Gas Flow, 6th Aeroplasma Dynamics Conference, Moscow Russia, May 2005.

9.  Menart, J., Shang, J.S., Kimmel, R., and Hayes, J., Investigation of Heating and Lorentz Force Effects Caused by a Plasma and a Magnetic Field in a Mach 5 Flow, AIAA 2005-4783, 36th Plasmadynamics and Laser Conference, Toronto Canada, June6-9 2005.

10. Shang, J.S. and Chang, C.L., Magneto-Aerodynamic Interaction over Airfoil, AIAA 2005-5179, 36th Plasmadynamics and Laser Conference, Toronto Canada, June 6-9 2005.

11. Shang, J.S., Electromagnetic Field of Dielectric Barrier Discharge, AIAA 2005-5182, 36th Plasmadynamics and Laser Conference, Toronto Canada, June 6-9 2005.

12. Surzhikov S.T. and Shang, J.S., The Hypersonic Quasi-Neutral Gas Discharge Plasma in a Magnetic Field, Proceedings third MIT Conference on Computational Fluid and Solid Mechanics, June 14-17, 2005, pp1004-1005.

13. Shang, J.S. and Surzhikov, S.T., Magnetoaerodynamic Actuator for Hypersonic Flow Control, AIAA Journal Vol. 43, No. 8, August 2005, pp. 1633-1643.

14. Shang, J.S., Kimmel, R., Hayes, J., Tyler, C., and Menart, J., Hypersonic Experimental Facility for Magnetoaerodynamic Interactions, J. Spacecraft and Rockets, Vol. 42 No. 5, 2005, pp.780-789.

15.  Shang, J.S., Solving Schemes for Computing Magneto-Aerodynamics, Journal of Scientific Computing, Vol. 25, No. 1, Oct. 2005, pp. 289-306.

16.  Shang, J.S., Kimmel, R., Hayes, J., Tyler, C., and Menart, J., Mechanisms of Plasma Actuators for Hypersonic Flow Control, Progress in Aerospace Sciences, Vol. 41, No. 8, Nov. 2005, pp.642-668.

17.  Stanfield, S., Menart, J., and Shang, J., Application of a Spectroscopic Measuring Technique to Plasma Discharge in Hypersonic Flow, AIAA 2006-0559, Reno NV, January 2006.

18.  Shang, J.S., Electromagnetic Perturbation to Hypersonic Viscous-Inviscid Interaction, AIAA 2006-0709, Reno NV, January 2006.

19.  Kimmel, R., Hayes, J., Crafton, S., Fonov, S., Menart, J., and Shang, J., Surface Discharges for High-Speed Boundary-Layer Control, AIAA 2006-0710, Reno NV, January 2006.

20.  Shang, J.S., Menart, J., Kimmel, R., and Hayes, J., Hypersonic Inlet with Plasma induced Compression, AIAA 2006-0764, Reno NV, January 2006.

21.  Menart, J., Stanfield, S., Shang, J.S., Kimmel, R., and Hayes, R., Study of Plasma Electrode Arrangements for Optimum Lift in a Mach 5 Flow, J. Menart, S. Stanfield, J. Shang, R. Kimmel, and J. Hayes, AIAA 2006-1172, Reno NV, January 2006.

22.  Surzhikov, S. and Shang, J., Glow Discharge in Flow of Neutral Gas and External Magnetic Field, AIAA 2006-1371, Reno NV, January 2006.

23.  Shang, J.S., Chang, C.L., and Surzhikov, S.T., Simulating Hypersonic Magneto-Fluid-Dynamic Compression, AIAA 2006-2889, San Francisco CA, June 2006.

24.  Surzhikov, S.T. and Shang, J.S., "Anomalous" behavior of Glow Discharge in External Magnetic Field, AIAA 2006-3384, San Francisco CA, June 2006.

25.  Shang, J.S., Computing Simulation of Hypersonic Magneto-Fluid-Dynamic Interaction, Fourth International Conf. on CFD, Ghent Belgium, July 10-14, 2006.

26.  Kimmel, R.L., Hayes, J.L., Menart, J. A., and Shang, J., Effect of Magnetic Fields on Surface Plasma Discharges at Mach 5, J. Spacecraft & Rockets, Vol. 42, No. 6, 2006, pp.1340-1346.

27.  Shang, J.S., Menart, J., Kimmel, R., and Hayes, J., Experimental Investigation of Magneto-Fluid-Dynamic Compression in a Cylindrical Inlet, AIAA 2007-0399, Reno NV, January 2007.

28.  Surzhikov, S.T. and Shang, J.S., Normal Microwave Glow Discharge in Transversal Magnetic Field, AIAA 2007-0992, Reno NV, January 2007.

29.  Surzhikov, S.T. and Shang, J.S., Plasmadynamics of Glow Discharges in Hypersonic Internal Flows, AIAA 2007-0994, Reno NV, January 2007.

30.  Shang, J.S. and Chang, C.L., Hypersonic Magneto-Fluid-Dynamic Compression in Cylindrical Inlet, AIAA 2007-3885, Miami FL., June 2007.

31.  Shang, J.S., Chang, C., and Surzhikov, S.T., Simulating Hypersonic Magneto-Fluid Dynamic Compression, AIAA J. Vol. 45, No. 11, 2007, pp.2710-2720.

32. Stanfield, S., Menart, J., DeJoseph, C., Kimmel, R., and Hayes, J., (2007), "Rotational and Vibrational Temperatures for a Dielectric barrier Discharge in Air Using Emission spectroscopy," AIAA Paper No. 2007-3876, *38th AIAA Plasmadynamics and Lasers Conference,* Miami, FL, June 25 – 28, pp. 1 – 17.

33. Yan, H. and Gaitonde, D., "Effect of Energy Pulse on Edney IV Interaction", AIAA Journal, Vol. 46, No. 6, June 2008, pp. 1424-1431.

34. Yan, H. and Gaitonde, D., "E_ect of Thermally-Induced Surface Perturbation in Compressible Flow", AIAA-2009-0923, Jan 2009.

35. Yan, H. and Gaitonde, D., "Numerical Study on E_ect of a Thermal Bump in Super-sonic Flow Control", AIAA-2008-3790, June 2008.

36. Yan, H., Gaitonde, D. and Shang, J., "Supersonic Flow Control by Pulsed Thermal Bump", AIAA-2008-2607, April 2008.

37. Yan, H., Gaitonde, D. and Shang, J., "The E_ect of a Thermal Bump in Supersonic Flow", AIAA-2008-1096, January 2008.

38. Shang, J., Huang, G. and Yan, H., "Surface Direct Current Discharge for Hypersonic Flow Control", AIAA-2008-1352, January 2008.

39. Yan, H., Gaitonde, D. and Shang, J., "Numerical Investigation of Pulsed Thermal Perturbation in Supersonic Boundary Layer", AIAA-2007-3887, June 2007.

40. Yan, H., Gaitonde, D. and Shang, J., "Investigation of Localized Arc Filament Plasmas Actuator in Supersonic Boundary Layer", AIAA-2007-1234, January 2007.

41. Yan, H. and Gaitonde, D., "E_ect of Energy Pulse on Edney IV Interaction", AIAA Paper 2006-3344, June 2006.

42. Yan, H. and Gaitonde, D., "Control of Edney IV Interaction by Energy Pulse", AIAA-2006-0562, January 2006.

## 8.0 REFERENCES

Adelgren, R., "Localized Flow Control with Energy Deposition," Ph.D. dissertation, Dept of Mechanical and Aerospace Engineering, Rutgers University, September, Piscataway, New Jersey, 2002.

Adelgren, R., Yan, H., Elliott, G., Knight, D., Beutner, T., and Zheltovodov, A., "Control of Edney IV Interaction by Pulsed Laser Energy Deposition," *AIAA J.*, Vol. 43, No. 2, 2005, pp. 256-269.

Ames Research Staff, "Equations, Tables, and Charts for Compressible Flow," National Advisory Committee for Aeronautics, Report 1135, 1953.

Artana, G., D'Adamo, J., Leger, L., Moreau, E., Touchard, G., "Flow Control with Electrohydrodynamic Actuators," *AIAA J.*, Vol.40 No.9, 2002, pp. 1773-1779.

Biberman, L. M., Vorobev, V. S., and Yakuboy, I. T., *Kinetics of Nonequilibrium Low-Temperature Plasmas,* Consultants Bureau, New York, 1987.

Billig, F. S., "Shock-Wave Shapes Around Spherical- and Cylindrical-Nosed Bodies," *J of Spacecraft and Rockets*, Vol. 4, No. 6, 1967, pp. 822-823.

Bityurin, V.A., Bocharov, A.N., Klimov, A.I., and Leonov, S.B., "Analysis of Non-Thermal Plasma Aerodynamics Effects," AIAA Paper 2006-1209, Reno NV, January 2006.

Bityurin, V. A., Bocharov, A. N., and Lineberry, J. T., "Results of experiments on MHD hypersonic flow control," AIAA Paper 2004-2263, June 28 - July 1, 2004.

Bityurin, V. A., Bocharov, A. N., Lineberry, J. T., and Suchomel, C., "Studies on MHD interaction in hypervelocity ionized air flow over aero-surfaces," AIAA Paper 2003-4303, June 23-26, 2003.

Bityurin, V. A. and Klimov, A. I., "Non-thermal plasma aerodynamic effects," AIAA Paper 2005-0978, *43rd AIAA Aerospace Sciences Meeting and Exhibit*, Reno, NV, Jan. 10 – 13, 2005.

Bityurin, V., Kilmov, A., Leonov, S., Lutsky, A, Van Wie D., Brovkin, V., and Kolesnichenko, Yu., "Effect of Heterogonous Discharge Plasma on Shock Wave Structure and Propagation," AIAA Paper 99-4940, Norfolk VA, Nov. 1999.

Bobashev, S. V., Mende, N. P., Sakharov, V. A., Van Wie, D. M., "MHD control of the separation phenomenon in a supersonic xenon plasma flow. II." AIAA Paper 2004-0515, *42nd AIAA Aerospace Sciences Meeting & Exhibit*, Reno, NV, January 5-8, 2004.

Boeuf, J. P., and Pitchford, L. C., "Electrohydrodynamic force and aerodynamic flow acceleration in surface dielectric barrier discharge," *Journal of Applied Physics,* Vol. 97, May 2005.

Borghi, C.A., Carraro, M., and Cristofolini, A. "An Axi-symmetric Hall Configuration for the MHD Interaction in Hypersonic Flows," 2005-4785, Toronto Canada, June 2005.

Borghi, C. A., Carraro, M. R., Cristofolini, A., Veefkind, A., Biagioni, L., Fantoni, G., Passaro, A., Capitelli, M., Colonna, G., Bagatin, M., and Zuin, M., Experimental investigation on the magneto-hydrodynamic interaction in the shock layer on a hypersonic body," AIAA-2004-2265, *35th AIAA Plasmadynamics and Lasers Conference*, Portland, OR, June 28 – July 1, 2004.

Brackbill, J. U., and Barnes, D.C., The Effect of nonzero $\nabla \cdot B$ on the numerical solution of the Magnetohydrodynamic equations, *JCP*, Vol. 35, 1980, pp.426.

Bracken, R. M., Myrabo, L. N., Nagamatsu, H. T., Meloney, E. D., and Shneider, M. N., "Experimental investigation of an electric arc air-spike in Mach 10 flow with preliminary drag measurements," AIAA-2001-2734, *32$^{nd}$ AIAA Plasmadynamics and Lasers Conference*, Anaheim, CA, June 11 –14, 2001.

Breuer, K. S. and Haritonidis, J. H., "The Evolution of a Localized Disturbance in a Laminar Boundary Layer. Part I. Weak Disturbances," *J. Fluid Mech.*, Vol. 220, 1990, pp. 569-594.

Breuer, K. S. and Landahl, M. T., "The Evolution of a Localized Disturbance in a Laminar Boundary Layer. Part I. Strong Disturbances," *J. Fluid Mech.*, Vol. 220, 1990, pp. 595-621.

Brown, S.C. *Introduction to Electrical Discharges in Gases*, N.Y., Wiley, 1966.

Candler, G.V. and Kelley, J.D., "Effect of Internal Energy Excitation on Supersonic Air Flow," AIAA Paper 99-464, Norfolk, VA, 1–5 Nov., 1999.

Chang, C. L., "Langley Stability and Transition Analysis Code (LASTRAC) Version 1.2 User Manual," NASA/TM-2004-213233, 2004.

Chen, F.F., *Introduction to Plasma Physics*, Plenum Press, New York, 1974

Cheng, F., Zhong, X., Gogineni, S., and Kimmel, R., "Magnetic-field Effects on Second-mode Instability of a Weakly Ionized Mach 4.5 Boundary Layer," *Physics of Flui*ds, Vol. 15, no.7, July 2003, pp.2020-2040.

Chernyi, G.G., "Some Recent Results in Aerodynamic Applications of Flow with Localized Energy Addition," AIAA Paper 99-4819, Norfolk VA, Nov. 1999.

Chiper, A. S., Anita, V., Agheorghiesei, C., Pohoata, V., Anita,M., and Popa, G., "Spectroscopic Diagnostics for a DBD Plasma in He/Air and He/N$_2$ Gas Mixtures," *Plasma Processes and Polymers,* Vol. 1, 2004.

Corke, T. C., He, C. and Patel, M., "Plasma flaps and slats: An application of weakly-ionized plasma actuators," AIAA Paper 2004-2127, June 28 – July 1, 2004.

Corke, T.C., Jumper, E.J., Post, M.L., et al., "Application of Weakly-Ionized Plasmas as Wing Flow-Control Devices," AIAA Paper 2002-0350, 2002.

Cristofolini, A., Borghi, C.A., Carraro, M.R., Neretti, G., Biagioni, L., Fantoni, G., and Passaro, A., "Experimental Investigation on the MHD Interaction around a Sharp Cone in An Ionized Argon Flow." AIAA Paper 2006-3075, San Francisco CA, June 2006.

D'Ambrosio, D. and Giordano, D. Electromagnetic Fluid Dynamics for Aerospace Applications. Part I: Classification and Critical Review of Physical Models, AIAA Paper 2004-2165, Portland, OR, June 2004.

Edney, B., "Anomalous Heat Transfer and Pressure Distribution on Blunt Bodies at Hypersonic Speeds in the Presence of an Impinging Shock," The Aeronautical Research Institute of Sweden, FAA Report 115, 1968.

Edwards, J.R. and Liou, M.S., Low-Diffusion Flux-Splitting Methods for Flows at All Speeds. *AIAA J.*, 1998, Vol.36, No.9, pp.1610-1617.

Enloe, C. L., McLaughlin, T. E., Font, G. I., Baughn, J. W., "Parameterization of Temporal Structure in the Single-Dielectric-Barrier Aerodynamic Plasma Actuator,", *AIAA Journal*, Vol. 44, No. 6, 2006, pp. 1127-1136.

Enloe, C. L., McLaughlin, T. E., VanDyken, R. D., Kachner, K. D., Jumper, E. J., Corke, T. C., Post, M., and Haddad, O., "Mechanisms and Responses of a Single Dielectric Barrier Plasma Actuator: Geometric Effects," *AIAA Journal,* Vol. 42 No. 3, 2004a, pp. 595-604.

Enloe, C. L., McLaughlin, T. E., VanDyken, R. D., Kachner, K. D., Jumper, E. J., and Corke, T. C., "Mechanisms and Responses of a Single Dielectric Barrier Plasma Actuator: Plasma Morphology," *AIAA Journal,* Vol. 42, No. 3, March 2004b.

Fischer, P. and Choudhari, M., "Numerical Simulation of Roughness-Induced Transient Growth in a Laminar Boundary Layer," AIAA Paper 2004-2539 , June 2004.

Font, G. I., "Boundary-Layer Control with Atmospheric Plasma Discharges," *AIAA Journal,* Vol. 44, No. 7, July 2006.

Forghi, C. A., Carraro, M. R., Cristofolini, A., Veefkind, A., Biagioni, L., Fantoni, G., Passaro, A., Capitelli, M., Colonna, G., Bagatin, M., and Zuin, M., " Experimental investigation on the magneto-hydrodynamic interaction in the shock layer on a hypersonic body," AIAA Paper 2004-2265, June 28 – July 1, 2004.

Formin, V., Maslov, A., Malmuth, N., Formichev, V., Shashkin, A., Korotaeva, T., Shipyuk, A., and Pozdnyakov, G., Influence of a Counterflow Plasma Jet on Supersonic Blunt-Body Pressure, *J. AIAA*, Vol. 40, No. 6, 2002, pp. 1170-1177.

Gaitonde, D.V., Three-Dimensional Flow-Through Scramjet Simulation with MGD Energy-Bypass, AIAA Paper 2003-0172, January 2003.

Gaitonde, D. A High-Order Implicit Procedure for the 3-D electric Complex Magnetogasdynamic Simulations, *Computers & Fluids*, Vol. 33, 2004, pp.345-374.

Gaitonde, D.V., "Simulation of local and Global High-Speed Flow Control with Magnetic Field," AIAA Paper 2005-0560, Reno NV, January 2005.

Gaitonde, D. V. and Miller, J. H., "Numerical Exploration of Shock Interaction Control with Plasma- Based Techniques," AIAA Paper 2003-3483 , June, 2003.

Ganiev, Y., Gordeev, V., Krasilnikov, A., Lagutin, V., Otmennikov, V. and Panasenko, Aerodynamic Drag Reduction by Plasma and Hot-Gas Injection, *J. Thermophysics and Heat Transfer*, Vol. 14, No. 1, 2000, pp.10-17.

Gaster, M., Grosch, C. E., and Jackson, T. L., "The Velocity Field Created by a Shallow Bump in a Boundary Layer," *Phys. Fluids*, Vol. 6, No. 9, 1994, pp. 3079-3085.

George, C., Candler, G., Laux, C., Kruger, C., "Computational Analysis of Diffuse Discharge in Atmospheric Pressure Air," AIAA 2002-2223, 2002.

Georgievski, P. and Levin, V., "Unsteady Interaction of a Sphere with Atmosphere Temperature Inhomogeneity at Supersonic Speed," *Fluid Dynamics*, Vol. 28, No. 4, 1993, pp. 568-574.

Gershman, B.N., Eruhimov, L.M., Yashin, Yu., Y., Wave Phenomena in Ionosphere and Space Plasma. Moscow: "Nauka", 1984, 392 p. (in Russian).

Gilmore, F. R., Laher, R. R., Espy, P. J., "Franck-Condon Factors, r-Centroids, Electronic Transition Moments, and Einstein Coefficients for Many Nitrogen and Oxygen Band Systems", *J. Phys. Chem. Ref. Data*, Vol. 21, No. 5, 1992, pp.1005-1107.

Griem, H. R., *Principles of Plasma Spectroscopy,* Cambridge University Press, New York, 1997.

Griffiths, D., *Introduction to Electrodynamics*, Prentice-Hall, Englewood Cliffs, NJ, pp. 175-184, 1981.

Hayes, W. and Probstein, R*., Hypersonic Flow Theory*, Academic, New York, 1959.

Herzberg, G., *Molecular Spectra and Molecular Structure I. Spectra of Diatomic Molecules,* Van Nostrand, New Jersey, 1950.

Hoh, F.C., *Rev. Modern Physics*, 1962, Vol.34, p.267

Hornung, H., "Regular and Mach Reflection of Shock Waves," *Ann. Rev. Fluid Mech.*, Vol. 18, 1986, pp.33-58.

Howatson, A.M., *An Introduction to Gas Discharges*, 2nd Edition, Pergamon Press, Oxford, 1975.

Huang, J., Corke, T. C., and Thomas, F. O., "Unsteady Plasma Actuators for Separation Control of Low-Pressure Turbine Blades," *AIAA Journal,* Vol. 7, 2006, pp. 1477-1487.

Incropera, F. P. and DeWitt, D. P., *Fundamentals of Heat and Mass Transfer*, Wiley, New York, p. 394, 2002.

Ivanov, M. S., Markelov, G. N., Kudryavtsev, A. N., and Gimelshein, S. F., "Transition between Regular and Mach Reflection of Shock Waves in Steady flow," AIAA-1997-2511, June 1997.

Jacobsen, L.S., Carter, C.D., and Jackson, T.A., Toward Plasma-Assisted Ignition in Scramjets, AIAA Paper 2003-0871, January 2003

Joslin, R. D. and Grosch, C. E., "Growth Characteristics Downstream of a Shallow Bump: Computation and Experiment," *Phys. Fluids*, Vol. 7, No. 12, 1995, pp. 3042-3047.

Josyula, E., "Computational Study of Vibrational Relaxing Gas Past Blunt Body in Hypersonic Flows," *J. Thermophysics and Hear Transfer*, 2002, Vol.14, pp.18–26.

Kandala, R. and Candler, G., "Numerical Studies of Laser-Induced Energy Deposition for Supersonic Flow Control," *AIAA J.*, Vol. 42, No. 11, 2004, pp. 2266-2275.

Kimmel, R. L., Estevadeordal, J., and Gogineni, S., "Characterization of Flow Generated by Dielectric Barrier Discharges (DBD)", APS Presentation GH.59th Annual Meeting GH.000.10 of the APS Division of Fluid Dynamics, Miami, FL, 2006.

Kimmel, R., Hayes, J., Menart, J. and Shang, J., "Effect of surface plasma discharges on boundary layers at Mach 5," AIAA-2004-509*,* 42nd AIAA Aerospace Sciences and Meeting & Exhibit, Reno, NV , Jan. 5 - 8, 2004a.

Kimmel, R., Hayes, J., Menart, J. and Shang, J., "Effect of magnetic fields on surface plasma discharges at Mach 5," AIAA-2004-2661, *34th AIAA Fluid Dynamics Conference and Exhibit*, Portland, OR, June 28 – July 1, 2004b.

Kimmel, R.L., Hayes, J.R., Menart, J.A., Shang, J., and Henderson, S., "Measurements of a Transverse DC Discharge in a Mach 5 Flow," AIAA Paper 2003-3855, Orlando FL. June 2003.

Knight, D., Survey of Aerodynamic Flow Control at High Speed by Energy Deposition, AIAA Paper 2003-0525, January 2003.

Knight, D. "A selected survey of magnetogasdynamic local flow control at high speeds," AIAA-2004-1191, *42nd AIAA Aerospace Sciences Meeting & Exhibit*, Reno, NV, January 5 - 8, 2004.

Kogan, M. N. and Starodubtsev, M. A., "Reduction of Peak Heat Fluxes by Supplying Heat to the Free Stream," *Fluid Dynamics*, Vol. 38, No. 1, 2003, pp. 115-125.

Kolesnichenko, Y., "Selected Topics of Physics and Diagnostics of MV Discharge," AIAA Paper 2005-0405, Reno NV, January 2005.

Kolesnichenko, Y. F., Azarova, O. A., Brovkin, V. G., Khmara, D. V., Lashkov, V. A., Mashek, I. Ch., and Ryvkin, M. I., "Basics in beamed MW energy deposition for flow/flight control," AIAA-2004-0669, *42nd AIAA Aerospace Sciences and Meeting & Exhibit*, Reno, NV, January 5 – 8., 2004.

Kovacs, I., *Rotational Structure in the Spectra of Diatomic Molecules,* American Elsevier Publishing Company Inc., New York, 1969.

Kozlov, K.V., Wagner, H.E., Brandenburg, R. and Michel, P., "Spatio-temporally resolved spectroscopic diagnostics of the barrier discharge in air at atmospheric pressure," *J. Phys. D: Appl. Phys.,* Vol. 34, pp 3164-3176, 2001.

Kuo, S. P. and Bivolaru, D., "A physical mechanism of the plasma effect on shock waves," AIAA Paper 2003-0527, January 6-9, 2003.

Kuranov, A., and Sheikin, E., The potential of MHD Control for Improving Scramjet Performance, AIAA Paper 99-3535, June 1999.

Kurth, G., "Critical Physical Phenomena in Scramjet Propulsion", AGARD-CP-600, 2002, pp. C5.1- C5.11.

Laher, R. R., Gilmore, F. R., "Improved Fits for the Vibrational and Rotational Constants of Many States f Nitrogen and Oxygen", *J. Chem. Ref. Data,* Vol. 20, No. 4, 1991, pp.685-712.

Leonov, S., Bityurin, V., Savelkin, K., and Yarantsev, D., "Effect of electrical discharge on separation processes and shocks position in supersonic airflow," AIAA Paper 2002-0355, January 14-17, 2002.

Leonov, S., Bityurin, V., Savischenko, N., Yuriev, A., and Gromov, V., "Influence of surface electrical discharge on friction of plate in subsonic and transonic airflow," AIAA Paper 2001-0640, 2001.

Leonov, S, Bityurin, V., and Yarantsev, D. "The effect of plasma induced separation," AIAA Paper 2003-3852, *34th AIAA Plasmadynamics and Lasers Conference*, Orlando, FL, June 23-26, 2003.

Leonov, S.B., Yarantsev, D.A., Gromov, V.G., and Kuriachy, A.P., "Mechanisms of Flow control by near-surface Electrical Discharge Generation," AIAA Paper 2005-0780, Reno NV, January 2005.

Leonov, S., Yarantsev, D., Kuryachii, A., and Yuriev, A., "Study of friction and separation control by surface plasma," AIAA-2004-0512, *42nd AIAA Aerospace Sciences Meeting & Exhibit*, Reno, NV, January 5 – 8, 2004 .

Lifshits, E.M. and Pitaevskii, L.P., Physical Kinetics. Theoretical Physics. Vol. X. Moscow: "Nauka", 1979 (in Russian).

Luque, J., Kraus, M., Wokaun, A., Haffner, K., Kogelschatz, U., and Eliasson, B., "Gas temperature measurement in $CH_4/CO_2$ dielectric-barrier discharges by optical emission spectroscopy," *Journal of Applied Physics,* Vol. 93, No. 8, April 2003.

MacCormack, R.W., Three Dimensional Plasmadynamics – Flow Field Calculation, AIAA Paper 2003-0325, January 2003.

Macheret, S., Shneider, M., Miles, R., and Lipinski, R., "Electron-Beam-Generated Plasma Hypersonic Magnetohydrodynamics Channel," *AIAA J.*, Vol. 39, No 6, 2001, pp. 1127-1138.

Marr, G. V., *Plasma Spectroscopy,* Elsevier Publishing Company, New York, 1968.

McLaughlin, T. E., Munska, M. D., Vaeth, J. P., Dauwalter, T. E., Goode, J. R., and Siegel, S. G., "Plasma-Based Actuators for Cylinder Wake Vortex Control," AIAA Paper 2004-2129, 2004.

Menart, J., Henderson, S., Shang, J., Kimmel, R., and Hayes, J., "Study of Surface and Volumetric Heating Effects in a Mach 5 Flow," AIAA-2004-2262, June 28 – July 1, 2004a.

Menart, J., Henderson, S., Shang, J., Kimmel, R., and Hayes, J., "DC plasma discharge effects on a Mach 5 flow between small plate electrodes," AIAA-2004-2264, *35th AIAA Plasmadynamics and Lasers Conference*, Portland, OR, June 28 – July 1, 2004b.

Menart, J. and Shang, J., "Investigation of effects caused by a pulsed discharge and a magnetic field in a Mach 5 flow," AIAA Paper 2005-4783, *36th AIAA Plasmadynamics and Lasers Conference*, Toronto, Ontario, Canada, June 6 – 9, 2005.

Menart, J., Shang, J., Atzbach, C., Magoteaux, S., Slagel, M., and Bilheimer, B., "Total drag and lift measurements in a Mach 5 flow affected by a plasma discharge and a magnetic field," AIAA Paper 2005-0947, *43rd AIAA Aerospace Science Meeting and Exhibit*, Reno, NV, Jan. 10 – 13, 2005.

Menart, J.A., Shang, J.S., Henderson, S., Kurpik, A., Kimmel, R., and Hayes, J., "Survey of Plasma Generated in a Mach 5 Wind tunnel," AIAA Paper 2003-1194, Reno NV, January 2003a.

Menart, J, Shang, J., Kimmel, R. and Hayes, J. "Effects of magnetic fields on plasma generated in a Mach 5 wind tunnel," AIAA Paper 2003-14165*, 36th Plasma Dynamics and Lasers Conference*, Orlando, FL., June 23-26, 2003b.

Meyer, R., Chintala, N., Bystricky, B., Hicks, A., Cundy, M., Lempert, W. R., and Adamovich, I. V., "Lorentz force effect on a supersonic ionized boundary layer," AIAA Paper 2004-0510, *42nd AIAA Aerospace Sciences Meeting & Exhibit*, Reno, NV, January 5 - 8, 2004.

Mitchner, M. and Kruger, C., *Partial Ionized Gases*, John Wiley & Sons, New York, 1973.

Moratz, T.J., Pitchford, L.C. and Bardsiey, J.N., "Electron swarm behavior in nonuniform fields in nitrogen", *J. Appl. Phys.,* Vol. 61, No. 6, 1987, pp 2146-2151.

Oates, G.C., "Aerothermodynamics of Gas Turbine and Rocket Propulsion", 3rd edition, **AIAA**. 1997.

Pancheshnyi, S.V., Nudnova, M., and Starikovskii, A.Y., "Development of a cathode-directed streamer discharge in air at different pressures: Experiment and comparison with direct numerical simulation", *Phys Review E:* Vol. 71, 2005.

Pancheshnyi, S.V., Sobakin, S.V., Starikovskaya, S.M. and Starikovskii, A.Y., "Discharge Dynamics and the Production of Active Particles in a Cathode-Directed Streamer", *Plasma Physics Reports,* Vol. 26, No. 12, 2000, pp. 1054-1065.

Pancheshnyi, S.V., and Starikovskii, A.Y., "Two-dimensional numerical modeling of the cathode-directed streamer development in a long gap at high voltage", *J. Phys. D: Appl. Phys.,* Vol. 36, 2003, pp.2683-2691.

Pancheshnyi, S.V., Starikovskaia, S.M. and Starikovskii, A.Y., "Role of photoionization processes in propagation of cathode-directed streamer", *J. Phys. D: Appl. Phys.,* Vol. 34, 2001, pp. 105-115.

Poggie, J., "Plasma-Based Hypersonic Flow Control," AIAA Paper 2006-3567, San Francisco CA, June 2006.

Poggie, J. and Gaitonde, D.V., "Electrode Boundary Conditions in Magnetogasdynamic Flow Control," AIAA Paper 2002-0199, 2002.

Post, M., and Corke, T., "Separation Control on High Angle of Attach Airfoil Using Plasma Actuators," *AIAA Journal,* Vol. 42, No. 11, 2004 pp. 2177-2184.

Raizer, Yu. P., *Gas Discharge Physics*, Springer-Verlag, 1991.

Raizer, Yu. P. and Surzhikov, S.T., Two-dimensional Structure of the Normal Glow Discharge and the Role of Diffusion in Forming of Cathode and Anode Current Spots, *High Temperatures*, No. 3, Vol. 26, 1988.

Reshotko, E., "Transition Issues at Hypersonic Speeds," AIAA Paper 2006-0707, Reno NV, 2006.

Resler, E.L., Sears, W.R., "The Prospect for Magneto-aerodynamics," *J. Aero. Science*, 1958, Vol. 25, 1958, pp. 235-245 and 258.

Rizzetta, D. P. and Visbal, M. R., "Direct Numerical Simulations of Flow Past an Array of Distributed Roughness Elements," AIAA Paper 2006-3527, June 2006.

Roe, P., "Approximate Riemann Solvers, Parameter Vectors and Divergence Schemes," *J. Computational Physics*, Vol. 43, No. 2, 1981, pp. 357-372.

Roth, J.R., Sherman, D.M., and Wilkinson, S. P., "Boundary Layer Flow Control with a One Atmosphere Uniform Glow Discharge Surface Plasma," AIAA Paper 98-0328, January 1998.

Roth, J.R., Sherman, D.M., and Wilkinson, S.P., "Electrohydrodynamic Flow Control with a Glow-Discharge Surface Plasma," *AIAA J.*, Vol.38, No.7, 2000, pp. 1166-1172.

Rumsey, C., Biedron, R., and Thomas, J., "CFL3D: Its History and Some Recent Applications," NASA TM-112861, May 2007.

Samimy, M., Adamovich, I., Kim, J-H, Webb, B., Keshav, S. and Utkin, Y., "Active control of high speed jets using localized arc filament plasma actuators," AIAA-2004-2130, *2nd AIAA Flow Control Conference*, Portland, OR, June 28 – July 1, 2004.

Samimy, M., Kim, J.-H., I, A., J-H, K., Utkin, Y., and S, K., "Active Control of High Speed and High Reynolds Number Free Jets Using Plasma Actuators," AIAA Paper 2006-0711, 2006.

Schmid, P. J. and Henningson, D. S., *Stability and Transition in Shear Flows*, Springer-Verlag, New York, NY, 2001.

Shang, J.S., Recent Research in Magneto-Aerodynamics, *Progress in Aerospace Science*, Vol. 37, No.1, 2001, pp. 1-20.

Shang, J. S., Plasma Injection for Hypersonic Blunt Body Drag Reduction, *AIAA J.,* Vol. 40, No. 6, 2002a, pp. 1178-1186.

Shang, J., "Shared knowledge in computational fluid dynamics, electromagnetics, and magneto-aerodynamics," *Progress in Aerospace Science*, Vol. 38, 2002b, pp. 449-467.

Shang, J.S., "Electromagnetic Field of Dielectric Barrier Discharge," AIAA Paper 2005-5182, Toronto Canada, June 2005a.

Shang, J.S., Solving Schemes for Computational Magneto-Fluid-Dynamics, *Journal of Scientific Computing,* Vol. 25, No.1, Oct., 2005b, pp.289-306.

Shang, J.S., Chang, C.L., and Surzhikov, S.T., "Simulating Hypersonic Magneto-Fluid-Dynamic Compression," AIAA Paper 2006-2889, San Francisco CA, June 2006b.

Shang, J. S., Gaitonde, D. V., and Updike, G. A., "Simulating magneto-aerodynamic actuator for hypersonic flow control," AIAA-2004-2657, *35ᵗʰ AIAA Plasmadynamics and Lasers Conference*, Portland, OR, June 28 – July 1, 2004.

Shang, J.S. and Hankey, W.L., "Numerical Solution of the Navier-Stokes Equations for a Three-Dimensional Corner," *AIAA J.*, Vol. 15, No. 11, 1977, pp. 1675-1582.

Shang, J. S., Hayes, J., and Menart, J., Hypersonic Flow over a Blunt Body with Plasma Injection, *J. Spacecraft and Rockets*, Vol. 39, No. 3, 2002, pp. 367-375.

Shang, J., S., Hayes, J., and Wurtzler, K., "Jet-Spike Bifurcation in high-speed flows," AIAA-2000-2325, *AIAA Fluids Conference*, Denver, CO, June 19-22, 2000.

Shang, J. S., Kimmel, R., Hayes, J., and Tyler, C., "Performance of a low density hypersonic magneto-aerodynamic facility," AIAA Paper 2003-0329, January 6-9, 2003.

Shang, J.S., Kimmel, R., Hayes, J. Tyler, C., and Menart, J. "Hypersonic Experimental Facility for Magnetoaerodynamic Interaction," *J. Spacecraft and Rockets,* Vol. 42, No. 5, 2005a, pp. 780-789.

Shang, J.S., Menart, J., Kimmel, R., and Hayes, J., "Hypersonic Inlet with Plasma Induced Compression," AIAA Paper 2006-0764, Reno NV, 2006a.

Shang, J.S. and Surzhikov, S. T., Magneto-Fluid-Dynamics Interaction for Hypersonic Flow Control, AIAA Paper 2004-0508, Reno NV, January 2004.

Shang, J.S. and Surzhikov, S.T., "Magnetoaerodynamic Actuator for Hypersonic Flow Control," *AIAA Journal*, Vol. 43, No. 8, August 2005a, pp. 1633-1643.

Shang, J.S. Surzhikov, S.T., Kimmel, R. Gaitonde, D.V., Hayes, J.R., and Menart, J., "Plasma Actuator for Hypersonic for Flow Control," AIAA Paper 2005-0652, Reno NV. January 2005c.

Shang, J. S., Surzhikov, S. T., Kimmel, R., Gaitonde, D., Menart, J., and Hayes, J., "Mechanisms of Plasma Actuators for Hypersonic Flow Control," *Progress in Aerospace Sciences*, Vol. 41, 2005b, pp. 642-668.

Shcherbakov, Y.V. and Sigmond, R.S., "Subnanosecond spectral diagnostics of streamer discharges: I. Basic experimental results", *J. Phys. D: Appl. Phys.,* Vol. 40, 2007, pp. 460-473.

Shneider, M.N., "Hypersonic Aerodynamic Control and Thrust Vectoring by Nonequilibrium Cold-Air MHD Devices," AIAA Paper 2005-0979, Reno NV, January 2005.

Shneider, M. N., Macheret, S. O., Zaidi, S. H., Girgis, I. G., Raizer, Y. P., and Miles, R. B., "Steady and unsteady flow control with energy addition," *34th AIAA Plasmadynamics and Lasers Conference*, Orlando, FL, AIAA Paper 2003-3862, June 23-26, 2003.

Stanfield, S. A., Menart, J., Shang, J., Kimmel, R., Hayes, J., "Application of a Spectroscopic Measuring Technique to Plasma Discharge in Hypersonic Flow," AIAA Paper 2006-0559, January 2005.

Staats, G. E., McGregor, W. K. Jr., Sprouse, J. A., and Fröhlich, J. P., "Magnetogasdynamic experiments conducted in a supersonic plasma arc tunnel," AIAA Paper 2000-2566*,* June 19-22, 2000.

Surzhikov, S.T. and Shang, J.S., "Glow Discharge in Magnetic Field," AIAA Paper 2003-1054, Reno, NV, 2003a.

Surzhikov, S. and Shang, J., "Glow Discharge in Magnetic Field with Heating of Neutral Gas," AIAA Paper 2003-3654, 34th AIAA Plasmadynamics and Lasers Conference, 23-26 June 2003b, Orlando, Florida.

Surzhikov, S.T. and Shang, J.S., "Supersonic Internal Flows with Glow Discharge and External Magnetic Field," AIAA Paper 2003-3625, Florida, 2003c, 11p.

Surzhikov, S.T. and Shang, J.S., "Two-Component Plasma Model for Two-Dimensional Glow Discharge in Magnetic Field," *J. Comp. Phys,.* Vol. 199, No 2, Sept. 2004, pp. 437-464.

Takizawa, Y., Sato, S., Abe, T., and Koniforski, D., "Electro-magnetic effect on shock layer structure in reentry-related high enthalpy flow," AIAA-2004-2162, *35th AIAA Plasmadynamics and Lasers Conference*, Portland, OR, June 28 – July 1, 2004.

Thomas, J.L., Diskin, B., Brandt, A., "Textbook Multigrid Efficiency for Fluid Simulation," *Annual Review of Fluid Mechanics*, Vol. 35, January 2003, pp.317-340.

Toro, P. G. P., Nagamatsu, H. T., Minucci, M. A. S. and Myrabo, L. N., "Experimental pressure investigation of a "Directed-energy air spike" inlet at Mach 10," AIAA Paper 99-2844, July, 1999.

Toth, G., "The $\nabla \cdot B = 0$ Constraint in Shock-Capturing Magnetohydrodynamics Codes," *JCP*, Vol. 161, 2000, pp 605-652.

Toth, G. and Roe, P.L., "Divergence- and Curl-Preserving Prolongation and Restriction Formulas," *JCP*, Vol. 180, 2002, pp.736-750.

Trumble, K. A. and Candler, G. V., "Flow Control of Swept Fin Shock Interactions by Laser-Induced Plasmas," AIAA Paper 2006-405, 2006.

Tumin, A. and Reshotko, E., "Spatial Theory of Optimal Disturbances in Boundary Layers," *Phys. Fluid*, Vol. 7, No. 13, 2001.

Tumin, A. and Reshotko, E., "Receptivity of a Boundary-Layer Flow to a Three-Dimensional Hump at Finite Reynolds Numbers," *Phys. Fluid*, Vol. 17, No. 9, 2005, pp. 094101-1-094101-8.

Van Driest, E. R., "The Problem of Aerodynamic Heating," *Aeronautical Engineering Review*, Vol. 15, No. 10, 1956, pp. 26-41.

Van Leer, B., "Towards the Ultimate Conservative Divergence Scheme. V. A. Second Order Sequel to Godunov's Method," *J. Computational Physics*, Vol. 32, 1979, pp. 101-136.

Visbal, M.R., Gaitonde, D.V., and Roy, S., "Control of Transitional and Turbulent Flow Using Plasma-Based Actuators," AIAA Paper 2006-3230, San Francisco CA, June 2006.

Von Engel, A., and Steenbeck, M., *Elektrische Gasentladungen*, Vol. II, J. Springer, Berlin, 1932.

Wegener, P.P. and Buzyna, G., "Experiments on Shock Stand-Off Distance in Non-Equilibrium Flow," *J. Fluid Mech.*, 1969, Vol.37(2), pp.325–335.

White, E. B., "Transient Growth of Stationary Disturbances in a Flat Plate Boundary Layer," *Physics of Fluids*, Vol. 14, No. 12, 2002, pp. 4429-4439.

White, E. B. and Ergin, F. G., "Receptivity and Transient Growth of Roughness-Induced Disturbances," AIAA Paper 2003-4243, June 2003.

Wieting, A. R. and Holden, M., "Experimental Shock-Wave Interference Heating on a Cylinder at Mach 6 and 8," *AIAA J.*, Vol. 27, No. 11, 1989, pp. 1557-1565.

Wilcox, D. C., *Turbulence Modeling for CFD*, Second Edition, DCW Industries, Inc., 5354 Palm Drive, La Canada, California 91011, 1998.

Wilkison, S. P., "Investigation of an Oscillating Surface Plasma for Turbulent Drag Reduction," AIAA Paper 2003-1023, January 2003.

Williamson, J., and DeJoseph, Jr., C., "Determination of Gas Temperature in an Open-Air Atmospheric Pressure Plasma Torch from Resolved Plasma Emission", *Journal of Applied Physics*, Vol. 93, No. 4, 2003, pp. 1893-1898.

Worner, A., Rist, U., and Wagner, S., "Humps/Steps Influence on Stability Characteristics of Two- Dimensional Laminar Boundary Layer," *AIAA J.*, Vol. 41, No. 2, 2003, pp. 192-197.

Yan, H., Adelgren, R., Boguszko, M., Elliott, G., and Knight, D., "Laser Energy Deposition in Quiescent Air," *AIAA J.*, Vol. 41, No. 10, 2003, pp. 1988-1995.

Yan, H. and Gaitonde, D., "Control of Edney IV Interaction of Energy Pulse," AIAA Paper 2006-0562 , Jan, 2006.

Yan, H. and Gaitonde, D., "Numerical Study on Effect of a Thermal Bump in Supersonic Flow Control," AIAA Paper 2008-3790 , June, 2008.

Yan, H., Gaitonde, D., and Shang, J., "Investigation of Localized Arc Filament Plasma Actuator in Supersonic Boundary Layer," AIAA Paper 2007-1234 , Jan, 2007a.

Yan, H., Gaitonde, D., and Shang, J., "Numerical Investigation of Pulsed Thermal Perturbation in Supersonic Boundary Layer," AIAA Paper 2007-3887, June, 2007b.

Yan, H., Knight, D., Kandala, R., and Candler, G., "Effect of a Laser Pulse on a Normal Shock," *AIAA J.*, Vol. 45, No. 6, 2007c, pp. 1270-1280.

Zaidi, S. H., Smith, T., Macheret, S., and Miles, R. B., "Snowplow surface discharge in Magnetic field for high speed boundary layer control," AIAA paper 2006-1006, January 9 – 12, 2006.

Zaman, K., Samimy, M., and Reeder, M. F., "Control of an Axisymmetric Jet Using Vortex Generators," *Phys. Fluids*, Vol. 6, No. 2, 1994, pp. 778-793.

Zhong, X. L., "Application of Essentially Nonoscillatory Schemes to Unsteady Hypersonic Shock- Shock Interference Heating Problems," *AIAA J.*, Vol. 32, No. 8, 1994, pp. 1606-1616.

Zucrow, M. J. and Hoffman, J. D., *Gas Dynamics*, Volume I, Wiley, New York, pp. 356-364, 426-432, 1976.